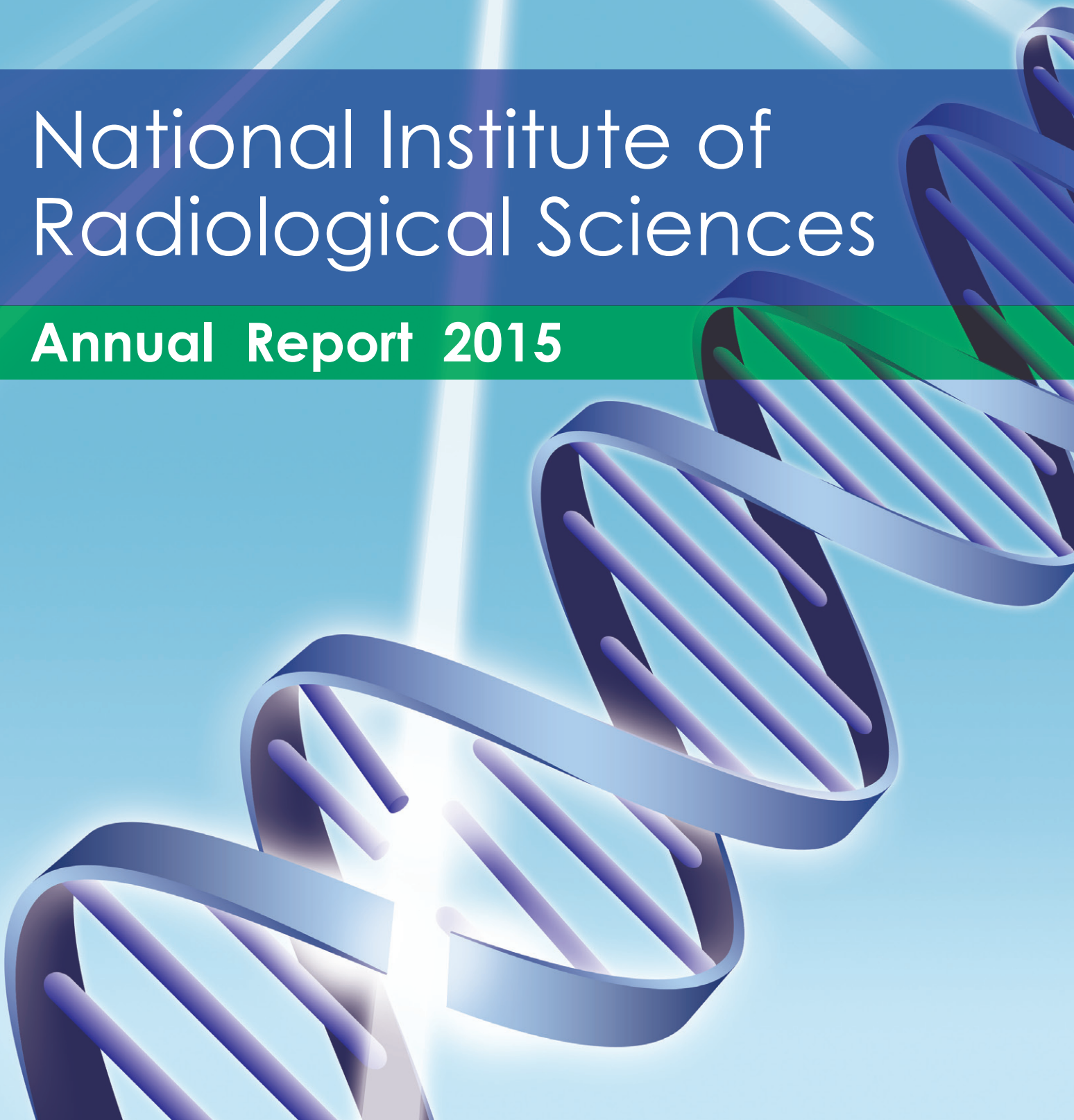


# National Institute of Radiological Sciences

**Annual Report 2015**



**Annual Report 2015**  
**(April 2015 - March 2016)**

NATIONAL INSTITUTE OF RADIOLOGICAL SCIENCES

Date of Publication      September 2016  
Editing and Publication      Research Information Section  
   Dept. of Information Technology  
   National Institutes for Quantum and Radiological  
   Science and Technology  
   Anagawa 4-9-1, Inage-ku, Chiba, 263-8555 Japan  
   Tel: +81-43-206-3485  
   Fax: +81-43-290-1112  
   Email: kagakujuhoka@qst.go.jp  
QST Homepage: <http://www.qst.go.jp/ENG/>  
NIRS Homepage: <http://www.nirs.qst.go.jp/ENG/>  
Full Text: <http://www.nirs.qst.go.jp/ENG/publication/annual/index.html>

Copyright ©2016 National Institutes for Quantum and Radiological Science  
and Technology All Rights Reserved

ISSN 2432-2229  
NIRS-54

## Editorial Note

On April 1 2016, National Institute of Radiological Sciences (NIRS) was unified with some units of the Japan Atomic Energy Agency (JAEA) to form a new organization, the National Institutes for Quantum and Radiological Science and Technology (QST). NIRS became one of the several institutes in QST, and continues to use the same institute name, NIRS.

This document presents the research and development results of NIRS for the fiscal year 2015, from April 2015 to March 2016. When the third mid-term plan of NIRS was begun in fiscal year 2011, we felt it was a good opportunity to revise the contents and format of the annual report. For the Annual Report 2015, we decided to follow this editorial policy and we have made a full-fledged revision of the contents. Our main revision was to publish summarized results on each research theme as "Highlights". Then, "Topics" sections were prepared that selected five results and outcomes with a technical research and development component.

We have included photographs of the contributing writers in a personal touch. We hope that the photos will make readers feel they already know us, when we meet at various conferences and events, or perhaps even at the NIRS campus in Chiba City. Readers with interests in specific Highlights and Topics should feel free to contact the respective writers. We look forward to hearing from you. Lastly, as an appendix we include the "List of original papers" for readers who are looking for more details.

We note that the Annual Report 2014 (published in 2015) is the final report to appear as a printed edition. NIRS published a printed edition every fiscal year prior to that and presented an electronic edition in addition on our website. We want to express our great appreciation to all the readers of the printed editions for utilizing these reports and for providing both NIRS researchers and us, the editorial staff, with much feedback with these print editions for many years. The present Annual Report 2015 becomes the first to appear as only an electronic edition which is released it on our website (<http://www.nirs.qst.go.jp/ENG/publication/annual/index.html>).

We hope that our printed edition readers will join those persons already utilizing the electronic edition and find it to be a handy resource describing what NIRS researchers have been doing. Finally, we thank all persons who worked on the production and English proofreading.

### Editorial Staff

Reiko ISHII  
Masanori OKAMOTO  
Takeo SHIMOMURA  
Katsumi UZAWA  
Kazuhisa YOSHIZAWA

# Contents

<b>Preface</b> .....	8
<b>■ Outline of Research Activities</b> .....	10
<b>■ Research on Cancer Therapy with Carbon Beams</b> .....	12
<Department of Accelerator and Medical Physics>	
Reliability monitoring for maintenance of HIMAC.....	14
Beam phase width in the NIRS-930 cyclotron.....	16
<Research on the Standardization and Clarification of Charged Particle Therapy>	
Carbon ion radiotherapy for sacral chordomas .....	18
<Research and Development on Medical Physics and Biology>	
Development of a superconducting rotating-gantry for carbon radiotherapy .....	20
Investigation of physical and clinical doses of charged-particle therapy in patients.....	22
<Basic Research on the Estimation of Effectiveness of Radiotherapy for Individual Cancer Patients>	
Solubilization of 2,2-diphenyl-1-picrylhydrazyl radical in water to evaluate the activity	
of water-soluble antioxidants.....	24
Study on the combination of carbon-ion radiation therapy and immunotherapy.....	26
<Research and Development for the International Promotion of Carbon Ion Radiotherapy>	
Gap-junction mediated bystander effects between carbon-ion irradiated tumor and	
non-irradiated normal cells .....	28
The Research Project with Heavy Ions at NIRS-HIMAC.....	30
<b>■ Molecular Imaging Research for Functional Diagnosis</b> .....	32
<Development and Production of PET Probes for Molecular Imaging>	
Striatal mGluR1 of rat accumulating A53T- $\alpha$ -synuclein dynamically changed during pathological	
progression of Parkinson's disease.....	34
Quantitative in vivo imaging of astrocytic energy metabolism in rat brain with radiolabeled benzyl acetate .....	36
<Research and Development of Advanced Bioimaging and Quantitative Analysis System>	
The DOI detector enables novel PET scanners .....	38
Development of a novel method for measurement of dopamine release in brain activation	
by positron emission tomography .....	40
<Research on Pathophysiological Diagnosis of Cancer and Other Diseases with Molecular Imaging>	
Clinical research on the PET/CT imaging of cancer hypoxia .....	42
Integrin $\alpha_6\beta_4$ -targeted imaging of pancreatic cancer model using a radiolabeled or	
fluorophore-labeled antibody .....	44
<Molecular Imaging Research on Neuropsychiatric Disorders>	
PET Quantification of tau pathology in human brain with $^{11}\text{C}$ -PBB3 .....	46
Brain circuits involved in vocal tic generation identified in the primate model of Tourette syndrome .....	48

<b>■ Research for Radiation Protection</b> .....	50
<Biospheric Assessment for Waste Disposal>	
Distribution differences of K and <sup>137</sup> Cs in leaf blade and petiole of herbaceous and woody plant leaves .....	52
The influence of ashing temperature on the determination of Pu in soil and biological samples .....	54
<Experimental Studies on the Radiation Protection of Children>	
Using genetic analysis to examine T cell lymphomas arising in mice irradiated with carbon ions or gamma rays .....	56
The influence of age at exposure on genetic alterations in radiation-induced mouse T-cell lymphomas .....	58
<Mechanistic Studies on the Reduction of Risks Relating to Radiation>	
Japanese sake is a modifier of radiation effects in mouse livers .....	60
Chronic restraint-induced stress seems to have little impact on radiation hematopoietic toxicity in mice .....	62
<Bridging the Gap between Scientific Knowledge and Society: Regulatory Sciences Research>	
Development of the retrospective animal archive and the international collaboration .....	64
<b>■ Research on Radiation Emergency Medicine</b> .....	66
<Research on Treatment and Diagnosis for Traumatic Radiation Damage>	
Mesenchymal stem cells protect against tacrolimus/radiation-induced cell death .....	68
Construction of a biodosimetric method for experimental low-dose irradiation in mice by the quantification of mRNAs using a drop of peripheral blood .....	70
<Research on the Development of Dosimetric Technology>	
Practical self-absorption correction method for various environmental samples in radioactivity measurements with HPGe detectors .....	72
The new low-cost metaphase finder .....	74
<b>■ Development of Fundamental Technologies in Radiological Science</b> .....	76
<Research Toward the Development of Fundamental Technologies that Support the Use of Radiation>	
Improvement of <i>in vitro</i> fertilization of inbred mice used for radiation research .....	78
<b>■ Fukushima Project Headquarters</b> .....	80
<Project for Environmental Dynamics and Radiation Effects>	
Research on characteristics of individual doses in Fukushima Prefecture after the Fukushima nuclear accident .....	82
<Project for Human Health>	
Reconstruction of early internal doses to Fukushima residents after Fukushima Daiichi NPP accident .....	84
<Radiation Effect Accumulation and Prevention Project>	
Effects of age at exposure on the life shortening and tumor incidence after low-dose-rate irradiation in mice .....	86

■ <b>Research on Evaluation of Medical Exposure</b> .....	88
<Medical Exposure Research Project>	
Physiologically-based pharmacokinetic model for calculating internal doses in <sup>18</sup> F-FDG examinations .....	90
■ <b>Topics</b> .....	92
Collaboration with IAEA to develop a training package for medical physicists in support of nuclear and radiological emergencies.....	92
Program of Research on the Standardization and Clarification of Charged Particle Therapy.....	94
Cooperation with WHO-REMPAN in radiation emergency medicine .....	96
■ <b>Organization Chart, Board Members, Activity of Center for Human Resources Development, International Collaboration, Budget, Personnel</b> .....	98
■ <b>Appendix: List of Original Papers</b> .....	108





# Preface

The National Institute of Radiological Sciences (NIRS) was established in 1957 as Japan's leading medical research institution dedicated to comprehensive research on radiation and human health. During more than a half century NIRS has carried out various scientific activities related to radiological science, ranging from basic and applied science to clinical medicine. In 2001, NIRS reformed its structure as an independent administrative institution, and has carried out its activities according to the 5-year mid-term plan approved by the Government. The fiscal year 2015 (April 2015 – March 2016) concludes the third mid-term plan (2011 – 2015), and this annual report summarizes the most recent accomplishments at NIRS.

NIRS aims to conduct scientific research and development by integrative efforts of a multidisciplinary approach. Based on the knowledge and technologies related to radiation and radiological science, NIRS continues to contribute to society through two approaches, i.e. promoting medical use of radiation to overcome health problems and protecting people from radiation injury. The third mid-term plan was started shortly after the severe nuclear accident at the Fukushima Daiichi Nuclear Power Plant that was triggered by the earthquake and tsunami on March 11, 2011. NIRS put its maximum efforts into activities for emergency medical procedures and radiation protection. In spite of coping with the effects of the accident, integrative efforts during the past five years have led to many successful scientific achievements.

The most intelligible outcome of these joint efforts can be seen for radiological protection in medical uses of radiation. NIRS has led collaborations among medical societies and experts involved in radiological science, and established the Japan Network for Research and Information on Medical Exposure (J-RIME), which provided the first diagnostic reference levels (DRLs) in Japan based on the latest nationwide surveys conducted by liaison organizations in 2015.

The development of cancer radiotherapy using carbon ion beams continues to be a major NIRS activity. Significant improvements have been accomplished during the past two decades in treatment planning, irradiation techniques and treatment in combination with chemotherapy, resulting in excellent treatment outcomes and better prognosis of patients. As a result, from the beginning of the fiscal year 2016, cancer radiotherapy using carbon ion beams will be covered partially by the Japanese National Health Insurance System. Molecular imaging research also requires the joint efforts of multi-disciplinary experts, including molecular imaging probes and instruments as the key elements for detection of abnormal function in the brain and tumor. These innovative research activities are strongly supported by basic research carried out at NIRS.

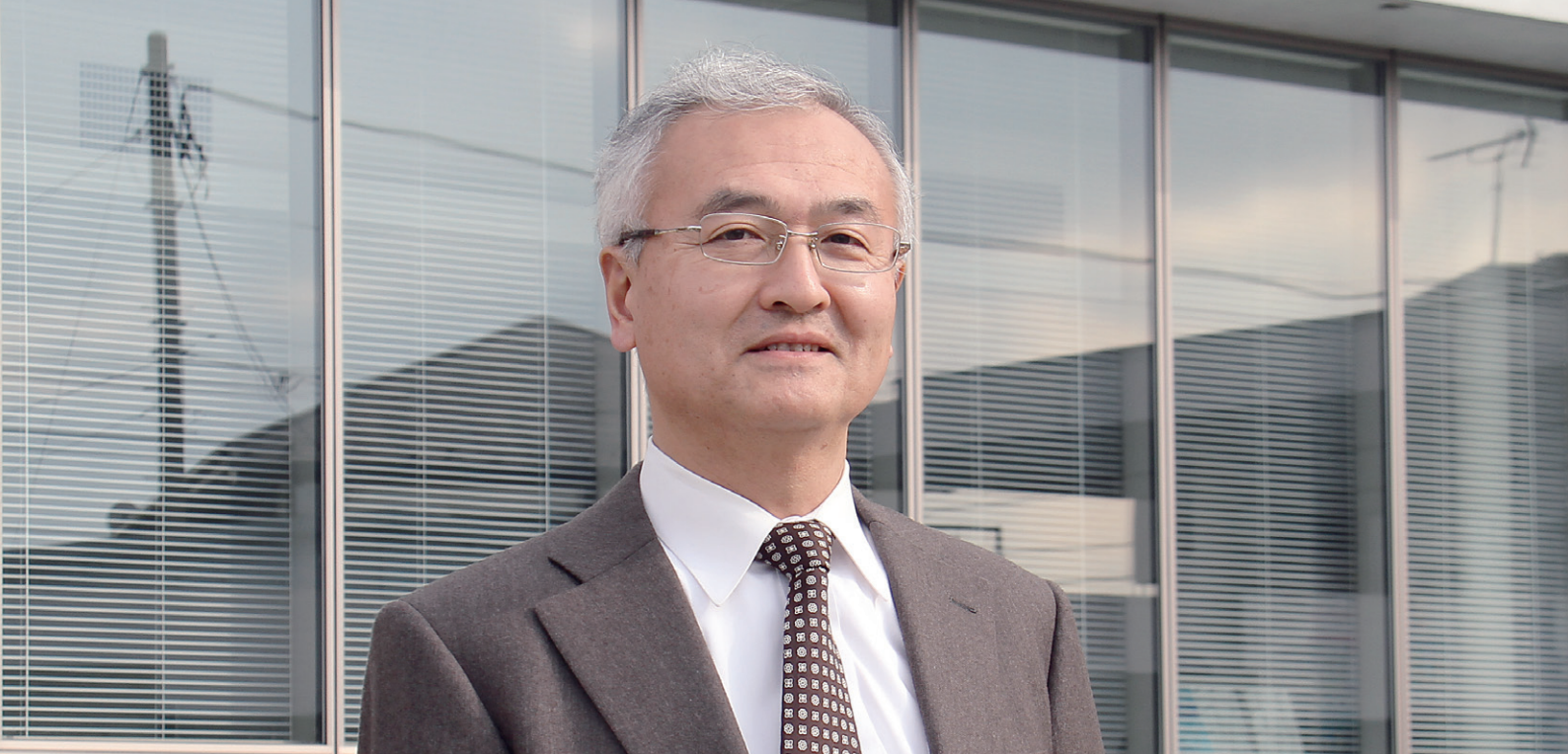
From April 2016, NIRS will function as a new organization to be known as the National Institutes for Quantum and Radiological Science and Technology (QST). With new opportunities and challenges, the researchers of the QST will continue their efforts to establish a solid base of comprehensive scientific research.

I would like to express my sincere appreciation to all the affiliated organizations, institutions, collaborators and friends for their valuable contributions and support given to the institute.

*March 2016*



**Yoshiharu Yonekura, M.D., Ph.D.**  
*President*



## Outline of Research Activities

**Makoto Akashi, M.D., Ph. D.**  
*Executive Director for Research*

Since re-organization as an independent administrative institution in April 2001, researchers at the National Institute of Radiological Sciences (NIRS) have been performing studies according to mid-term plans that have been revised every 5 years. The first mid-term plan was started in April 2001; the second, in April 2006; and the third, in April 2011. NIRS has four fields of research activities, heavy charged particle therapy, molecular imaging, radiation protection, and radiation emergency medicine, and a support system for radiation technology. The third mid-term plan was carried out by four research centers and one fundamental technology center. In May 2012, the program for recovery from the Fukushima Daiichi Nuclear Power Plant (NPP) accident was started as a new center. In March 2013, a new department was also established; the Radiation Emergency Medical Assistant Team (REMAT) now plays an important part in medical response to accidents including the after effects of the Fukushima NPP accident. In this report, the research activities at NIRS during the last year of the third mid-term plan (April 2015 to March 2016) are presented.

The Great East Japan Earthquake triggered tsunami with over 10-meter-high waves that damaged facilities of the Fukushima Daiichi NPP of Tokyo Electric Power Company (TEPCO), resulting in the severe nuclear accident. Since NIRS is the national core center for radiation emergency medicine, many NIRS researchers still continue to be involved in response activities to the accident, though 5 years have passed. Besides these activities many others are also being carried out and

251 original papers were published in FY 2015, in both international and domestic journals of high reputation. Furthermore, more than 81 proceedings were published for international and domestic scientific meetings, and 357 oral presentations and 34 patent applications were made. Collaborative studies and exchanges of researchers were also actively carried out: 103 collaborative studies were done, 363 researchers worked as visiting staff members at NIRS, and 136 students were accepted as trainees.

The Research Center for Charged Particle Therapy, as a leading research organization in this field, has been conducting clinical, biological and physics research studies using heavy ions generated from the heavy ion medical accelerator in Chiba (HIMAC). In FY 2015, 794 patients were treated. As well, the clinical trial team treated 7 tumor types of cancers: prostate, lung, head & neck, bone & soft tissue, liver, pancreas, and post-operative pelvic recurrence of rectal cancer. Scanning irradiation became available for the routine treatment of less mobile targets in the head & neck or pelvic region; more than one thousand patients could be treated with scanning at the new treatment research facility. Highlights of research progress are shown in detail in other sections.

The Molecular Imaging Research Center, consisting of four groups, has long experience with medical imaging technologies including positron emission tomography (PET), single photon emission tomography (SPECT), and magnetic resonance imaging (MRI). The Center

conducts basic science and technology studies for molecular imaging and also application studies for diagnosis and pathophysiology of oncology and psychiatry. Current projects include the development of molecular probes and radiopharmaceutical production techniques and the investigation of measurement techniques for PET and MRI, in addition to preclinical and clinical applications in oncology and psychiatric and neurological diseases. Details on these studies are presented later.

The Research Center for Radiation Protection has been providing a scientific basis for establishing regulations with global standards for radiation protection, security and safety, focusing on effects of low-dose and/or low-dose rate radiation derived from human activities and from natural environmental radiation. For this purpose, the results of basic radiobiological research have been provided to promote understanding of radiation effects and to encourage enactment of more rational regulations for the safe and secure use of radiation in daily life. Main research programs at this Center are to explore the mechanisms of radiation carcinogenesis, to investigate how lifestyle modifies radiation effects, and to study the effect of low dose-rate radiation exposure.

With the establishment of REMAT in 2010, the Research Center for Radiation Emergency Medicine became responsible for basic research. The Center is focusing its efforts on three projects: developing and modifying the most appropriate methodologies for evaluating radiation exposure, exploring and supplying effective drugs to reduce the radiotoxicity and metallic toxicity of internal contamination with radionuclides, and applying mesenchymal stem cells (MSCs) as regenerative medicine to treat radiation exposure injuries.

NIRS is the national center for radiation emergency medicine in Japan, providing direct or consultative services to local governments and hospitals in the event of a radiation incident. Services provided by REMAT include providing exposed victims (patients) with the most advanced radiation emergency medicine treatments possible and making dose assessments. REMAT especially is playing an important role in medical response to the Fukushima NPP accident. REMAT also carries out activities to maintain and strengthen the emergency preparedness system and has worked to establish three nation-wide network councils for medicine, bio-dosimetry with chromosome analysis, and physical dosimetry. REMAT has also introduced several international or domestic courses at NIRS on radiation emergency medical preparedness for medical professionals of the Asian region. In August 2015, NIRS was designated as an advanced center for radiation emergency medical assistance by the Nuclear Regulation Authority (NRA).

Since its designation as a collaborating Center of the World Health Organization (WHO) in September

2013, NIRS has been contributing to strengthening preparedness to radiation emergencies and Radiation Emergency Medical Preparedness and Assistance Network (REMPAN) activities, providing medical and technical assistance to WHO in response to radiation emergencies, carrying out biodosimetry, analyzing radiation protection for indoor radon exposure, and promoting radioprotection in the field of medical exposure to ionizing radiation, with the focus on risks assessment and risk management. Together, the Research Center for Radiation Protection and REMAT also have acted as a national hub in collaboration with international organizations including the International Atomic Energy Agency (IAEA), International Commission on Radiological Protection (ICRP), and United Nations Scientific Committee on the Effects of Atomic Radiation (UNSCEAR).

The Fundamental Technology Center, which was established to support various studies performed in NIRS using advanced fundamental technologies, has been carrying out maintenance and quality control of institute accelerators including the single particle irradiation system to cell (SPICE), the particle induced X-ray emission (PIXE) analysis and tandem accelerator (PASTA), and the neutron exposure accelerator system for biological effects experiments (NASBEE), as well as radiation measurement apparatuses for cosmic rays. Efforts have also been extended to establish and support experimental animal laboratories for internal and external researchers.

The program for recovery from the Fukushima Daiichi NPP accident started in May 2012 has four research projects and a system of cooperation. Research projects are the study for long-term and environmental effects of radiation, the health effect survey for emergency workers at the NPP, and the study of environmental dynamics of radionuclides and radiation in the ecosystems in Fukushima Prefecture. The program contributed to the external dose assessment of residents for 4 months after the accident.

Some other research programs have also been continued or were newly started with the support of funding agencies including the Ministry of Education, Culture, Sports, Science and Technology (MEXT), the Ministry of Economy, Trade and Industry (METI), the Ministry of the Environment (MOE), the Ministry of Health, Labour and Welfare (MHLW), and the NRA.

In this report readers will be able to learn about the substantial research that was performed in the 5th year of the third mid-term plan. I would like to conclude with heartfelt thanks for the cooperation and advice generously provided to us by all parties concerned.

# Research on Cancer Therapy with Carbon Beams – Development of Human Friendly Cancer Therapy with Carbon Ion Beams –

**Tadashi Kamada, M.D., Ph.D.**

*Director of Research Center for Charged Particle Therapy*

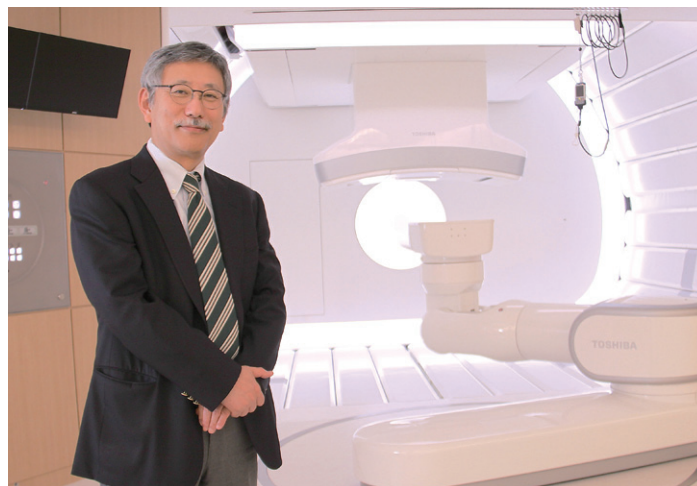
E-mail: kamada.tadashi@qst.go.jp

The Research Center for Charged Particle Therapy (hereafter, the “Center”) was established in 1993 when NIRS completed construction of the HIMAC. Since then it has been carrying out clinical, biological and physics research using heavy ions generated from the HIMAC. After accumulating clinical experiences of carbon ion radiotherapy in various types of malignant tumors, the Center was successful in obtaining approval from the Ministry of Health, Welfare and Labor for “Highly Advanced Medical Technology” in 2003. Thus in the meanwhile, carbon ion therapy achieved for itself a solid place in general practice of cancer treatment. The HIMAC has also served >700 researchers as a multi-user utilization facility for medical, biological and physics research, including more than 100 foreign researchers.

In 2011, when the Third Mid-Term Plan of NIRS was initiated, the Center was reorganized to conduct intensive research on heavy ion beams using carbon ions and development of more patient friendly next generation heavy ion treatment systems. This R&D will contribute to the long-term improvement of cancer treatment and quality of life of patients. For this aim, the Center is organized into four research programs, the department of physics (Director: Koji Noda, and the hospital (Director: Yutaka Ando). In the following, summaries from fiscal year (FY) 2015 on Progress of research and practice are presented for: 1) Research program for carbon ion therapy and diagnostic imaging (Program Leader: Hiroshi Tsuji); 2) Medical physics research program for development of a novel irradiation system for charged particle therapy (PL: Toshiyuki Shirai); 3) Advanced radiation biology research program (PL: Takashi Imai); 4) Research Program for the application of heavy ions in medical sciences (PL: Takeshi Murakami); and 5) Hospital.

## ① Research program for carbon ion therapy and diagnostic imaging (PL: Hiroshi Tsuji)

The Program of Research on the Standardization and Clarification of Charged Particle Therapy consists of the Clinical Trial Research Team, Applied PET Research Team, Applied MRI Research Team, and Clinical Database Research Team. All the teams are performing research and development on charged particle therapy. Progress of research in each team is summarized below. As of January 2016, a total of 9,716 patients had been treated with carbon ion beams at NIRS. Carbon ion radiotherapy of these patients was carried out as more than 60 different phase I/II or phase II clinical trials or advanced medicine (HAMT; Highly advanced medical technology). Six hundred



and ninety-five patients were treated as new patients from April 2015 to January 2016. This number will increase to about 750 at the end of March 2016 and will be comparable to that of last FY. Prostate, bone and soft tissue, head & neck, lung, and liver are the leading 5 tumors sites. Recently the numbers of pancreatic tumor and recurrent rectal cancer cases have increased significantly. Clinical trials for pancreas, esophagus, uterus and kidney cancer are being conducted and patient enrollment has progressed. As advancement of hypofraction of carbon ion therapy, the single session treatment for lung cancer and 12-fraction treatment for prostate cancer could be established and their application as advanced medicine was started. Scanning irradiation became available for the routine treatment of less mobile targets in the head & neck or pelvic region. Actually more than 1000 patients could be safely and efficiently treated with scanning at the New Treatment Research Facility. In addition, the clinical trial aiming to verify safety and steadiness of the respiratory-gated scanning system was carried out in 10 patients with a tumor in the chest or abdomen. The new working group, named J-CROS Japanese Carbon ion Radiation Oncology Study group, for the multi-institutional clinical trial of carbon ion therapy was established in 2014. It originally consisted of members from four operating carbon ion therapy facilities in Japan, the NIRS, the HIBMC in Hyogo, the GHMC in Gunma, and the HIMAT in Saga. A new institute i-ROCK in Kanagawa recently started carbon ion therapy and members of i-ROCK joined J-CROS last year. J-CROS performed data collection from the original four institutes for retrospective analysis and to plan a protocol for prospective clinical studies for major tumor sites.

## ② Medical physics research program for development of a novel irradiation system for charged particle therapy (PL: Toshiyuki Shirai)

This program consists of the Beam Delivery System Research Team, Treatment Planning System Research Team,

Radiation Effect Research Team, Experimental Therapy Research Team, and Image Guided Radiotherapy Research Team. We started the clinical trial of scanning irradiation for moving targets in March 2015. The number of the treated patients was 10 until January 2016 and the targets have been lung and liver. Treatment for the pancreas is being planned. We have used the fast rescanning irradiation system and the markerless fluoroscopic respiration gating system in the clinical trial. The transportation and the assembling of the rotating gantry with the superconducting magnets was started at NIRS in February 2015. The superconducting magnets was cooled down to 4K successfully in August 2015 and the construction was finished in September 2015. The beam commissioning has been carried out since November 2015 after receiving permission for the radiation control authority. The beam quality at the gantry iso-center is improved from that of the other treatment rooms and the beam spot size is about half that previously available with the low beam energy.

### ③Advanced radiation biology research program (PL: Takashi Imai)

This program consists of the Cancer System Biology Team, Cancer Metastasis Research Team, and Radio-Redox-Response Research Team. In this third Mid-Term Plan of the NIRS, we have studied mainly the following 4 subjects for the improvement of long-term survival. First, in order to improve our understanding about the mechanism of tumor recurrence after a course of radiation treatments, we established radiation resistant cancer cell lines by delivering repeated exposures to X-rays or C-ion beams. Furthermore, we established new radiation resistant tumor models *in vivo*. Local tumors on the NR-S1 grafted C3H mouse models were irradiated with a total dose of 180 Gy of gamma-ray and 90 Gy of C-ion beams, respectively. Characterization of these new *in vitro* and *in vivo* models is ongoing. Second, to obtain evidence for expansion of the range of application of combination therapy of C-ion irradiation and dendritic cell-immunotherapy, we evaluated the combination effects using several types of tumor/host models. A detailed report is highlighted elsewhere. Third, we have analyzed what causes invasion of some particular cancer cells after irradiation. We previously reported that C-ion enhanced invasion of one pancreatic cancer cell line, PANC-1, and one glioblastoma cell line, SF126, although they were very infrequent events. Most of the invaded PANC-1 cells exhibited nitric oxide (NO) production and activation of NOS-NO-PI3K-AKT-GIRDIN - (actin organization and lamellipodia formation) pathway. We showed that inactivation of any of these proteins in this pathway caused suppression of the irradiation-induced invasion. Finally, we have studied possible applications of radioprotective agents, such as anti-reactive oxygen species, to protect normal tissue surrounding tumor cells during radiation therapy. Detailed results of this study are also highlighted elsewhere.

### ④Research Program for the application of heavy ions in medical sciences (PL: Takeshi Murakami)

This program consists of the (1) Heavy-Ion Radiotherapy Promotion Team, (2) HIMAC Research Collaboration Team, (3) Cellular and Molecular Biology Research Team, and (4) International Radiotherapy Joint Research Team. The following main activities were carried out in FY 2015.

#### (1) Promotion of Carbon Ion Radiotherapy.

The wide range of knowledge and know-how is necessary for promotion of carbon ion radiotherapy. Research and analyses of technical developments, treatment procedures, and the social environment surrounding carbon ion radiotherapy were carried out. Procedures for transferring these results and know-how to new projects were also established. Contributions to new projects such as at Saga and Kanagawa were made. Training of human resources is also an important activity. Many kinds of training courses have been established, and more than 200 trainees, including Japanese and non-Japanese medical

doctors, medical physicists, technologists, etc., finished the courses during the past five years.

#### (2) Promotion of collaborative research, international as well as domestic.

Since 1994, HIMAC has accepted researchers from all over the world in the field of ion-beam sciences other than carbon ion radiotherapy. There are four experimental halls (Physics, Biology, Secondary beam and Medium-energy halls) as well as three treatment rooms at HIMAC. During the daytime from Tuesday through Friday, HIMAC is operated for patient treatments. At nights and weekends the four halls can be used for various experiments using various ion beams. The latter framework is specified as "The Research Project with Heavy Ions at NIRS-HIMAC". More than 120 proposals were accepted and carried out every year. The beam time of more than 5,000 hours per year was supplied to those research studies. The Research Project with Heavy Ions at NIRS-HIMAC is a centerpiece of collaborative research using heavy ions, and this program is deeply embedded in the operation of the whole project.

### ⑤Hospital, Research Center for Charged Particle Therapy (Director: Yutaka Ando)

The Research Center Hospital for Charged Particle Therapy of the NIRS is unique in its specialization in radiotherapy for cancer. The hospital is designed for radiotherapy especially carbon ion therapy and consists of the oncology department, diagnostic radiology department and dental department. The hospital has 100 beds for inpatients and sees 80 to 110 outpatients daily. The diagnostic radiology department has one CT-scanner with a 64-line detector, one 1.5 T MRI, one 3.0 T MRI, two PET/CTs, and one gamma camera. On the other hand, the oncology department is equipped with 5 fixed-beam treatment rooms for carbon ion therapy (one vertical beam room, one horizontal beam room and 3 rooms with both beams), one rotating gantry treatment room for carbon ion radiotherapy and one linear accelerator for x-ray therapy. The hospital performs radiotherapy using highly advanced medical technologies, carries out clinical studies mainly using radiotherapy and diagnosis, and has a role as a tertiary hospital for radiation emergency medicine. The highly advanced medical technology program started from 2003, the number of applications of this technology reached 6,234 and the number of clinical studies reached 3,532 at the end of March 2016. From 1994 to March 2016 we have treated 9,766 new patients with carbon ion therapy. In 2015 we treated 745 patients with carbon ion therapy. The gender distribution of the patients treated by the particle therapy was 527 males and 218 females. The ratio of males to females was 2.41 to one. Patients living in adjacent prefectures (Chiba, Ibaragi, Saitama and Tokyo) to the NIRS facility represented 54.2% of the total patients. In March 2012, we had implemented the Electronic Medical Record (EMR) system and developed a simple input method for the patient's findings, symptoms, tumor responses, and toxic reactions that should be estimated by the physician during the clinical interview. We improved the coordination among several database systems (Hospital Information System, Therapy Plan Database, Treatment Management System, PACS and Radiology Information System for Radiation Therapy). These systems are connected to each other and data are transmitted to the destination systems.

### ⑥Department of Accelerator and Medical Physics (Director: Koji Noda)

The department of accelerator and medical physics is one of the most active and leading departments of ion-beam radiotherapy related applied physics in the world. Reliable operation of the HIMAC accelerator and beam-delivery systems, and continuous development of novel techniques have been keeping us as the "center of excellence" in this field for many years. The highlights of research progress in FY 2015 are shown elsewhere.

Highlight

# Reliability monitoring for maintenance of HIMAC

**Shigekazu Fukuda**

E-mail: fukuda.shigekazu@qst.go.jp

### Introduction

A lot of experience, both as knowledge and as skills, has been accumulated by the many years of operating and maintaining the Heavy Ion Medical Accelerator in Chiba (HIMAC). Preventive maintenance has been performed to obviate the risk of a breakdown while operating HIMAC, including carrying out the component checks and replacements recommended by the component manufacturers. Manufacturers' recommendations assume use in a general environment, but it is well-known that the life of a component and its breakdown rate depends on conditions for use such as vibration, temperature and operating hours. The experience (experiential value) obtained from the actual environment is also becoming important to maintain appropriately medical accelerators that are required to be more stable and reliable than accelerators used in other ways.

To make use of the experience to achieve productive maintenance in addition to preventive maintenance, it is useful to implement the PDCA (Plan-Do-Check-Action) cycle. In the PDCA, the causes are investigated by collecting information on defected events occurring during operations and checks, the information is analyzed, and if needed, countermeasures are taken. The PDCA based on quality indicators is generally known as a reliability monitoring method. The quality indicators in reliability monitoring lead to "visualization" of the quality of maintenance quantitatively and are indispensable tools to monitor maintenance as a long-term trend. The final goal is the realization of more efficient and economical maintenance through this activity.

### Index parameters for reliability monitoring of HIMAC

At first, to construct the PDCA cycle for the maintenance of HIMAC, we defined three index parameters, that is, Availability, MTTR (Mean Time To Repair) and Failure Rate as quality indicators [1].

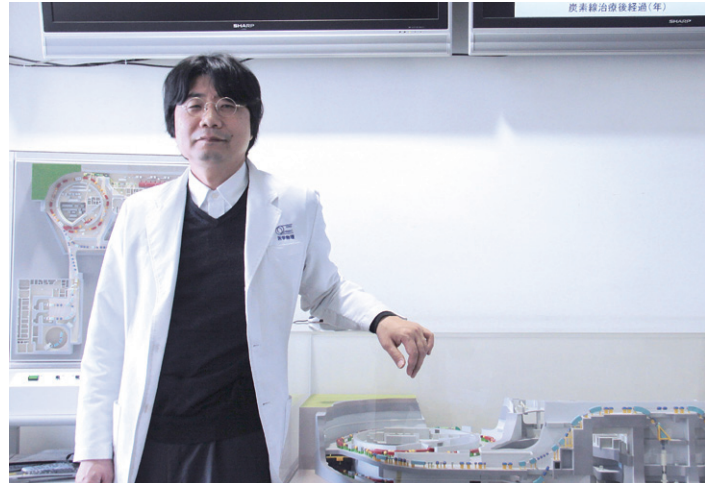
The Availability is the ratio of Operation Time and Machine Time,

$$\text{Availability} = \frac{\text{Operation Time}}{\text{Machine Time}} = \frac{\text{Operation Time}}{\text{Operation Time} + \text{Downtime}}$$

where Machine Time is composed of Operation Time and Downtime of HIMAC. MTTR is the ratio of the Total Repair Time and the Number of the Repaired Failures,

$$\text{MTTR} = \frac{\text{Total Repair Time}}{\text{Number of Repaired Failures}}$$

The Failure Rate is the ratio of the Total Number of Failures and



Operation Time,

$$\text{Failure Rate} = \frac{\text{Total Number of Failures}}{\text{Operation Time}}$$

We listed all failures that occurred in one month with the cause of each failure, the defective parts and the downtime to calculate the above index parameters. Furthermore, we categorized these failures into three classes according to the extent of the impact. Table 1 shows the relation between the class of failures and monitoring parameters. The parameters for accelerators including RFQ, DTL, synchrotron and beam transports and those for treatment rooms were calculated individually.

Table 1 Classification of failures and monitoring parameters.

Class of Failures	Definition	Monitoring Parameters
Interruption	Interrupt the beam supply or schedule.	Availability
Non-interruption	No interruption of the beam supply or schedule, but repair is necessary as soon as possible.	MTTR
Advisory	An advisory message. The failure should be fixed at the next scheduled maintenance.	Failure Rate

### Check and evaluation of parameters

Those parameters were checked and evaluated periodically to proceed to the next action of the PDCA cycle. A quality review meeting was held every month as an activity of the Quality Control Committee, QCC. The QCC consists of people from NIRS and the cooperating company (Accelerator Engineering Corporation). If the trend of parameters showed low quality, the causes were investigated and corrective actions were discussed in the meeting. The QCC also has a role of making rules about operation and maintenance for accelerators and treatment systems.

### Examples of reliability monitoring

We explain one example of what we could find from the reliability monitoring of HIMAC. Figure 1 shows the trend of availability for the accelerators from April 2014 to January 2015. The trend indicated that availability in September dropped to 93.5%, compared to the average availability of the same month in the previous fiscal year, 98.9%[2]. Figure 2 presents the distribution of kinds of accelerator failures in the same period. Two kinds of failures were dominant, those of RF systems and of control systems of the accelerator. Figure 3 shows the details of causes of breakdown related to RF failures. From this breakdown analysis, it was clear that the number of the failures related to RF protection systems increased from April to September (There were no failures in August because it was the maintenance period for HIMAC). Based on this analysis we investigated RF protection systems.

Electric Discharge Protection, EDP, is one of the RF protection systems and it was developed to protect against damage by electric discharge in an accelerator tank. The EDP disconnects the RF power when it senses a loss of vacuum in the accelerator tank. However, did not find that the RF power disconnections by the EDP had any correlation with the loss of vacuum. As a result of our investigation, the problem was caused by the high sensitivity of the EDP. After its threshold level was changed to the proper level in October, no problems with the EDP occurred.

Another example of reliability monitoring is shown in Fig.4. Figures (a) and (b) show the MTTR for the accelerators and for the treatment rooms. The green bars show the MTTR for interruption failures and the yellow bars show MTTR for interruption and non-interruption failures. The MTTR of interruption failures for the treatment rooms was smaller than for the accelerators. This was mostly because there are multiple treatment rooms. When one room has a failure, another room is available for treatment use.

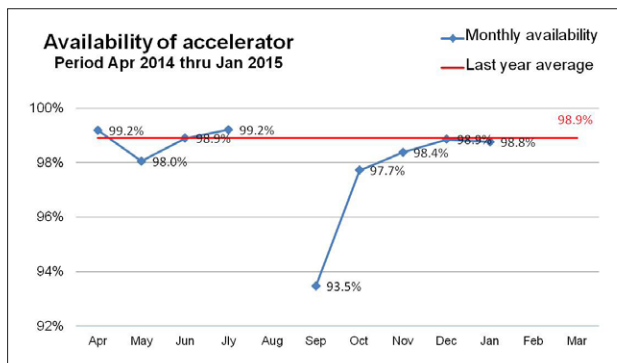


Fig.1 Availability of accelerators.

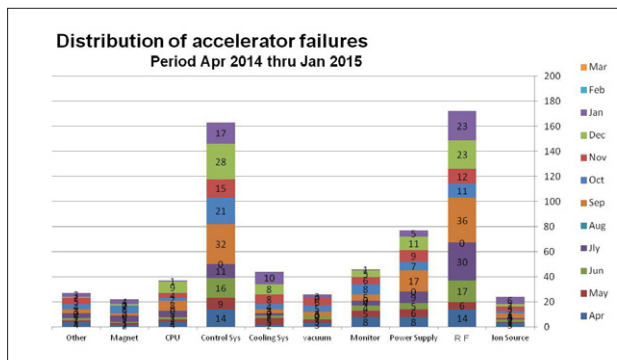


Fig.2 Distribution of accelerator failures.

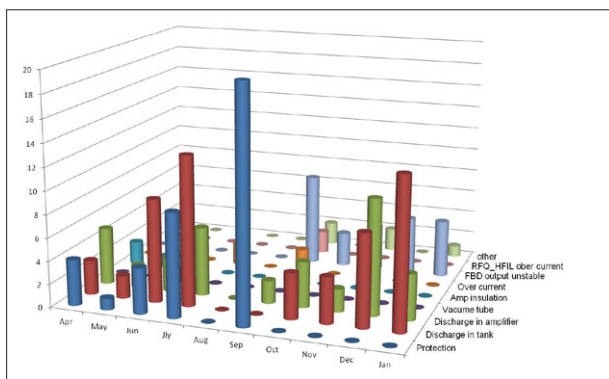


Fig.3 Causes related to RF failures.

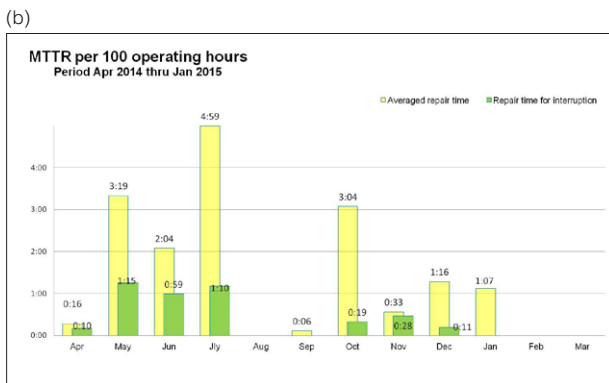
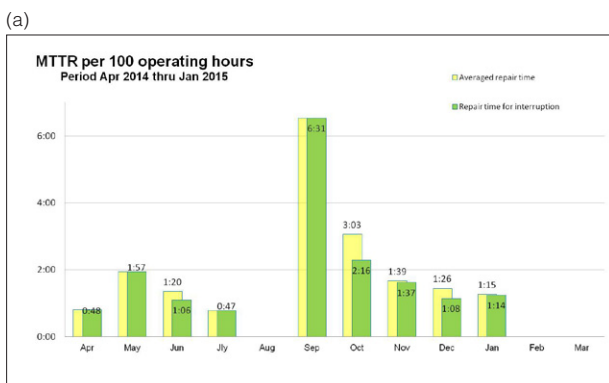


Fig.4 MTTR for accelerators (a) and treatment rooms (b).

### Conclusion

The index parameters for reliability monitoring of HIMAC were introduced to perform the PDCA cycle of maintenance and to improve reliability of the accelerators. We intend to realize more efficient and economical maintenance of HIMAC through this activity, and popularize this monitoring method of maintenance for facilities of particle therapy.

### References

[1] Fukuda S, *et al.*, The 12<sup>th</sup> Annual Meeting of Particle Accelerator Society of Japan Abstracts, 38, Tsuruga, 2015.  
 [2] Inokuchi H, *et al.*, [http://neutrons2.ornl.gov/conf/arw2015/presentations/G-Inokuchi-What can we find from failure data of the accelerator.pdf](http://neutrons2.ornl.gov/conf/arw2015/presentations/G-Inokuchi-What%20can%20we%20find%20from%20failure%20data%20of%20the%20accelerator.pdf), ARW2015.

# Beam phase width in the NIRS-930 cyclotron

**Takashi Wakui**

E-mail: wakui.takashi@qst.go.jp

## Introduction

The cyclotron facility at NIRS supports ongoing projects in molecular imaging and targeted radionuclide therapy (TRT) as well as detector development for satellites and nuclear physics. Major instrumentation includes the NIRS-930 cyclotron with the bending limit of 110 MeV for  ${}^4\text{He}^{2+}$  particles and the focusing limit of 90 MeV for protons, and the HM-18 cyclotron with the fixed energy of 18 MeV for protons and 9 MeV for deuterons.

The NIRS-930 cyclotron, commissioned in 1973, has both light and heavy ion capabilities. Protons and  ${}^4\text{He}^{2+}$  ions are available at intensities higher than 10  $\mu\text{A}$ . Other heavy ions through neon are accelerated to maximum energies defined by  $K=110 q^2/A$ . Here,  $q$  is the charge and  $A$  is the mass number. All the ions are produced by an electron cyclotron resonance ion source with permanent magnets [1]. The ion beams are delivered to users for 5 days/week and 1800 hours/year. The NIRS-930 cyclotron is more than four decades old, and consequently, the concern for its eventual failure is growing. However, its availability, defined as the ratio of the operated beam time divided by the scheduled beam time, consistently reaches 99% due to constant maintenance efforts.

In contrast, the HM-18 cyclotron, introduced in 1994, is dedicated to providing light ions. Because it accelerates negative ions, the available beam intensities are as high as 30  $\mu\text{A}$  for protons and 20  $\mu\text{A}$  for deuterons. The ions are used exclusively for the production of positron-emitting radionuclides, such as  ${}^{11}\text{C}$ ,  ${}^{15}\text{O}$ , and  ${}^{18}\text{F}$ , for positron emission tomography. The ion beams are provided to users for 5 days/week and 1600 hours/year. The availability is 98%.

TRT has been conducted as one of the main projects in NIRS and it is proposed in the next medium term plan (beginning in FY 2016). Radionuclides used for TRT have been produced using the NIRS-930 cyclotron and Table 1 summarizes their production reactions, beam energies, and provided beam intensities. To launch a clinical TRT trial, a higher beam intensity is indispensable for producing an applicable amount of radio-pharmaceuticals. The production of  ${}^{211}\text{At}$ , for instance, requires an intensity higher than 30  $\mu\text{A}$  for the 34 MeV  ${}^4\text{He}^{2+}$  beam [2]. To realize the beam intensity demands, our research effort has been focused on understanding the beam dynamics in the NIRS-930 cyclotron. The studies have involved not only a beam simulation [3], but also measurements of beam parameters such as the beam phase width. In this report, we describe the beam phase width measured for the NIRS-930 cyclotron.

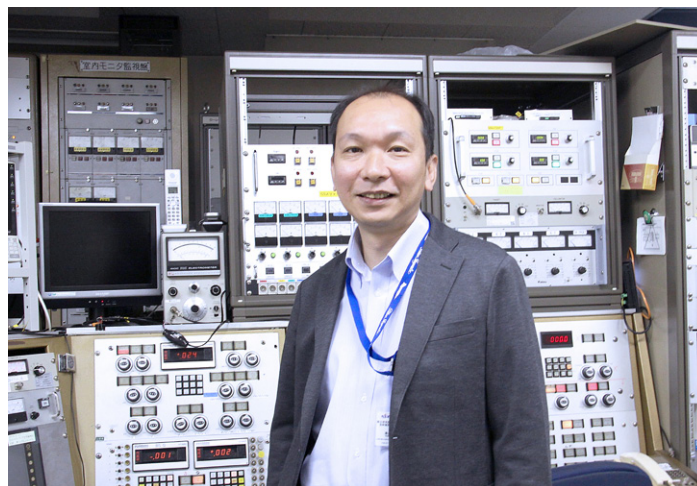


Table 1 Radionuclides produced using the NIRS-930 cyclotron.

Radionuclides	Reaction	Beam energy [MeV]	Beam intensity [ $\mu\text{A}$ ]
${}^{89}\text{Zr}$	${}^{89}\text{Y}(p, n){}^{89}\text{Zr}$	15	10
${}^{11}\text{C}$	${}^{14}\text{N}(p, \alpha){}^{11}\text{C}$	18	10
${}^{62}\text{Zn}/{}^{62}\text{Cu}$	${}^{\text{nat}}\text{Cu}(p, 2n){}^{62}\text{Zn}$	30	10
${}^{68}\text{Ge}$	${}^{\text{nat}}\text{Ga}(p, x){}^{68}\text{Ge}$	30	10
${}^{67}\text{Cu}$	${}^{68}\text{Zn}(p, 2p){}^{67}\text{Cu}$	60	5
	${}^{64}\text{Ni}(p, n){}^{67}\text{Cu}$	40	15
${}^{64}\text{Cu}$	${}^{64}\text{Ni}(p, n){}^{64}\text{Cu}$	24 ( $\text{H}_2^+$ )	10
${}^{124}\text{I}$	${}^{124}\text{Te}(p, n){}^{124}\text{I}$	27 ( $\text{H}_2^+$ )	10
${}^{177}\text{Lu}$	${}^{\text{nat}}({}^{176})\text{Yb}(d, n){}^{177}\text{Lu}$	20	10
${}^{43}\text{Sc}$	${}^{\text{nat}}({}^{40})\text{Ca}(\alpha, x){}^{43}\text{Sc}$	34	10
${}^{47}\text{Sc}$	${}^{44}\text{Ca}(\alpha, p){}^{47}\text{Sc}$	34	10
${}^{74}\text{As}$	${}^{\text{nat}}({}^{74})\text{Ge}(p, n){}^{74}\text{As}$	18	10
${}^{155}\text{Tb}$	${}^{\text{nat}}({}^{153})\text{Eu}(\alpha, 2n){}^{155}\text{Tb}$	34	10
${}^{186}\text{Re}$	${}^{185}\text{W}(d, n){}^{186}\text{Re}$	20	10
${}^{211}\text{At}$	${}^{209}\text{Bi}(\alpha, 2n){}^{211}\text{At}$	34	10
${}^{28}\text{Mg}$	${}^{27}\text{Al}(\alpha, 3p){}^{28}\text{Mg}$	75	10

## Measurement of the beam phase width

The beam phase width is a key parameter determining the beam quality and intensity. It can be roughly estimated from the injection efficiency without the beam buncher, and the estimated value is around 70 deg. However, a phase compression might take place in the acceleration. Thus, we measured the beam phase width in the acceleration for the NIRS-930 cyclotron.

Before the measurements, an isochronous field should be carefully formed by adjusting the currents of trim coils. The NIRS-930 cyclotron has twelve sets of trim coils. The magnetic field distribution for each coil as a function of the radius in the cyclotron is shown in Fig.1. The isochronism is confirmed by monitoring the phase excursion measured using a phase probe [4]. The phase probe consists of ten pairs of electrodes, whose positions are also indicated in Fig.1, and labelled P1 to P10. The beam phase is measured relative to the phase of the RF dee voltage. An example of the phase excursion measured for the 34 MeV  ${}^4\text{He}^{2+}$  beam is shown in Fig.2. The deviations of beam phases are kept within 3 deg., which is good enough for the measurements.

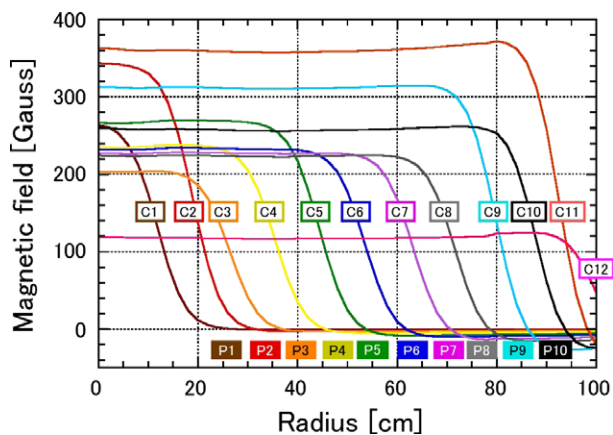


Fig.1 Magnetic field distribution of trim coils.

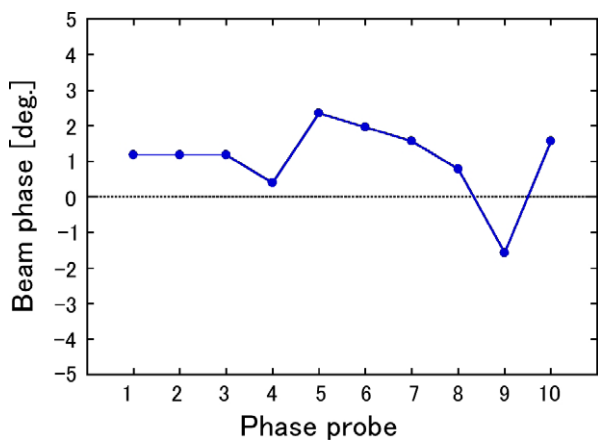


Fig.2 Relative phase excursion for 34 MeV  ${}^4\text{He}^{2+}$  beam.

For the measurements of the beam phase width, we have employed a method proposed in Ref. [5]. In this method, the beam currents at a certain radius in the cyclotron are measured by changing the frequency of the RF dee voltage,  $f_{rf}$ , from that of cyclotron resonance,  $f_0$ . The beam current will maintain its initial value at  $f_{rf} = f_0$  unless ions in a bunch enter the deceleration region where the energy gain per gap is negative. The beam current then decreases with further increase of the difference between  $f_{rf}$  and  $f_0$ . From the dependence of the beam current on the frequency difference, we can estimate the beam phase width in the acceleration.

The measurements of beam phase width have been carried out for 34 MeV  ${}^4\text{He}^{2+}$  beam, whose acceleration harmonics is 2. In the measurements,  $f_{rf}$  was changed from  $f_0 = 13650.0$  kHz in  $\pm 0.5$  kHz steps. The range of the frequency change was set within  $\pm 10$  kHz, which is sufficiently smaller than the automated

tuning range of 500 kHz by the use of a compensator. The beam current was measured using the main probe fixed at a radius of 860 mm from the center of the cyclotron. The position was slightly inside from the extraction radius. Figure 3 shows the results of the measurements. The open circles and solid circles denote the beam current measured with and without the beam buncher of the sinusoidal wave, respectively.

### Results

To obtain the beam phase width from Fig.3, we used the relation between the beam phase,  $\theta$ , and the frequency difference,  $\Delta f = f_{rf} - f_0$ , given in Ref. [5] as

$$\theta = \sin^{-1}\{1 - 2\pi fhN \frac{\Delta f}{f_0}\}.$$

Here,  $h$  is the acceleration harmonics and  $N$  is the minimum number of revolutions. We then assumed that the time distribution of ions in a bunch can be represented in terms of the normal distribution. Decreases in the beam current of 25% and 75% from the initial value are accordingly at  $0.67\sigma$  and  $-0.67\sigma$ , respectively. The  $\sigma$  can thus be derived from the beam phase  $\theta$  at the beam current reduction of both 25% and 75%. In the normal distribution, the relation between  $\sigma$  and the full width at half maximum,  $\Delta\theta$ , is  $\Delta\theta = 2.35\sigma$ . The  $\Delta\theta$  i.e. the beam phase width is thus deduced from the  $\sigma$ .

From the analysis above, the beam phase width without the beam buncher was obtained as  $28.9 \pm 0.5$  deg. in the acceleration. The beam phase width was compressed by a factor of 2.4 compared with the value estimated from the injection efficiency. The beam phase width with the beam buncher was also deduced to be  $23.7 \pm 1.1$  deg. This showed that a further compression occurred by using the beam buncher.

In this study, we found that the phase compression clearly took place in the NIRS-930 cyclotron. By combining this fact with the beam simulation, the measured beam phase width will bring us a better understanding of the beam dynamics in the NIRS-930 cyclotron. This will lead to an improvement in the beam intensity.

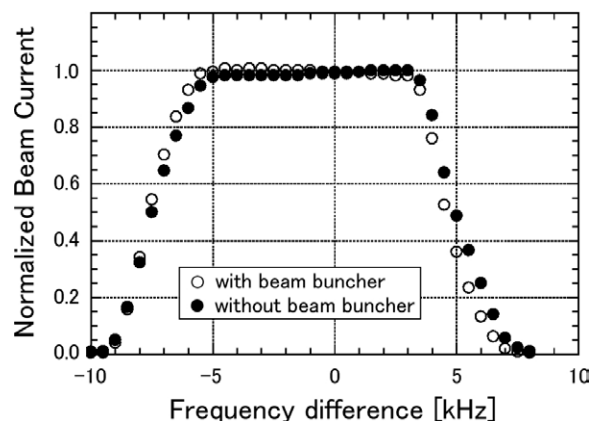


Fig.3 Normalized beam current measured by changing frequency of the dee voltage. The center frequency is 13650.0 kHz.

### References

- [1] Hojo S, et al., *Rev Sci Instrum*, 85, 02A959, 2014.
- [2] Nagatsu K, et al., *Appl Radiat Isot*, 94, 363, 2014.
- [3] Nakao M, et al., Proceedings of the 5th international particle accelerator conference, IPAC'14, 797, 2014.
- [4] Hojo S, et al., Proceedings of cyclotrons 2013, Vancouver, Canada, MOPPT008, 46-48, 2013, ISBN 978-3-95450-128-1.
- [5] Kurashima S, et al., *Rev Sci Instrum*, 81, 033306, 2010.

## Highlight

# Carbon ion radiotherapy for sacral chordomas

**Reiko Imai**

E-mail: imai.reiko@qst.go.jp

## Introduction

A clinical trial was first launched in 1996 to evaluate the safety and efficacy of carbon ion radiotherapy (C-ion RT) for bone and soft tissue sarcomas not suited for surgery. Through a dose escalation trial and a subsequent fixed dose trial, it was found that C-ion RT provided definite local control and offered a survival advantage without unacceptable morbidity for patients with bone and soft tissue sarcomas that were either difficult or impossible to cure using other modalities. As of March 2016, over 1000 patients had been treated with C-ion RT. The most treated sarcoma at NIRS was sacral chordoma, followed by high grade sarcomas.

Chordomas arise from notochordal remnants and are a rare tumor, between 1% and 4% of primary bone tumors. Approximately 50% of the chordomas originate from the sacrum [1, 2]. Surgery is the mainstay for treatment and complete resection is essential for good oncologic results. However, surgery is sometimes difficult because of the location and the size of the tumor. Surgery for chordomas in the proximal sacral bone like S1 can result in severe neurological deficits such as permanent gait, urinary and bowel dysfunctions. These seriously impair quality of life (QOL) of patients because most of the patients with sacral chordomas are elderly. Chordomas have poor sensitivity to photon radiotherapy or chemotherapy.

We published the first report on C-ion RT for unresectable sacral chordomas in 2004 [3]. As of 2015 over 200 chordomas had been treated with C-ion RT at NIRS. Our latest report has the largest number of patients with chordomas treated with charged particle therapy, including proton therapy that has ever been reported [4]. Here, we present some of our published clinical data regarding sacral chordomas treated with C-ion RT.

## Carbon ion radiotherapy for sacral chordomas

For axial tumors, 350 MeV/n and 400 MeV/n carbon ion beams were generally used. All patients were treated using a passive irradiating method. To immobilize patients, low-temperature thermoplastic shells and body rests were used. A set of computed tomography (CT) image slices 1-mm to 5-mm thick were acquired for treatment planning. Clinical Target Volume (CTV) was encountered as a margin of 5 mm of gross tumor volume (GTV). The planning target volume (PTV) was approximately 3–5 mm with the CTV margin. If the CTV was too close to critical organs such as the bowels, the CTV was modified. Irradiation was performed with a minimum of three ports, which included the posterior to anterior, left to right, and right to left directions. One port was used in one session per day, and treatment was performed on four consecutive days per week



from Tuesday to Friday. The total doses of 64.0 GyE, 70.4 GyE, or 73.6 GyE in 16 fractions (fr) were used in the clinical trials to determine a workable dose. After the 73.6 GyE/16 fr dose was employed, 70.4 GyE/16 fr was determined as a workable dose to avoid severe skin toxicity. In April 2007, we started to apply a total dose of 67.2 GyE because 15% of patients who had received 70.4 GyE experienced grade 2 and 3 neurological adverse events after a long follow-up period.

## Changes of Framework for Unresectable Bone and Soft Tissue Sarcomas

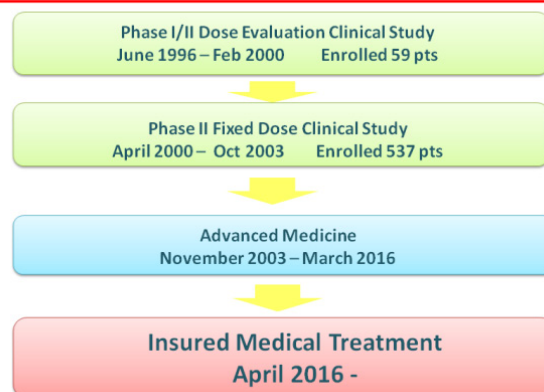


Fig.1 Changes of framework for unresectable bone and soft tissue sarcomas.

C-ion RT for unresectable sarcomas was started as a clinical trial and moved to advanced medicine (Fig.1); the treatment series for one patient with sarcoma cost 3140,000 JPY. From April 2016, the cost of C-ion RT for unresectable bone and soft tissue sarcomas will be covered by the Japanese health insurance system.

### Patients

Between June 1996 and March 2013, 188 patients with primary unresectable chordomas enrolled under the two C-ion RT protocols on bone and soft tissue sarcomas were evaluated in the study. The main eligibility requirements for the patients of the two protocols were the same: (1) the tumor was medically unresectable as judged by orthopedic surgeons; (2) the tumor was histologically confirmed as sarcoma; (3) the patient had not metastasized; (4) no metal instrumentation had been applied; and (5) the tumor had not received prior radiotherapy. Patients who refused surgery were included in our study. All patients signed an informed consent form, and the protocol studies were approved by the local Institutional Review Boards.

Median age was 66 years old. Median tumor size was 345 cm<sup>3</sup> and 73% of the tumors invaded at more proximal than the S2 level. The median prescribed dose was 67.2 GyE/16 fr (64.0–73.6).

### Results

The median follow-up period was 62 months (6.8–147.5 months). Figure 2 shows the overall survival (OS), local control (LC) and disease-free survival (DFS) curves for 188 patients. The 5-year (60-month) and 10-year (120-month) LC rates were 77.2% and 52.0%, respectively. Forty-one patients (22%) had a local recurrence. Among the 41 patients, recurrence in 12 patients (29%) occurred after 5 years. There was no significant prognostic factor for LC. Twenty-two patients with recurrent tumors received C-ion RT again under a clinical trial. The 3-year overall survival rates after local recurrence were 51.5%. The 5-year and 10-year overall survival rates were 81.1% and 66.8%, respectively. The 5-year and 10-year disease-free survival rates were 50.3% and 31.3%, respectively.

Regarding adverse events one patient underwent colostomy because of severe constipation caused by neurological toxicity. Twenty patients underwent colostomy before C-ion RT. Ten patients had sheets/silicon balloons inserted between the digestive tract and the tumors before C-ion RT. Among six patients with grade 3 peripheral nerve injuries, three patients received a total dose of 73.6 GyE. Ambulatory functions remained in 97% of the patients. Figure 3 shows the shrinkage of sacral chordoma for a 66-year-old male patient as a result of the C-ion RT.

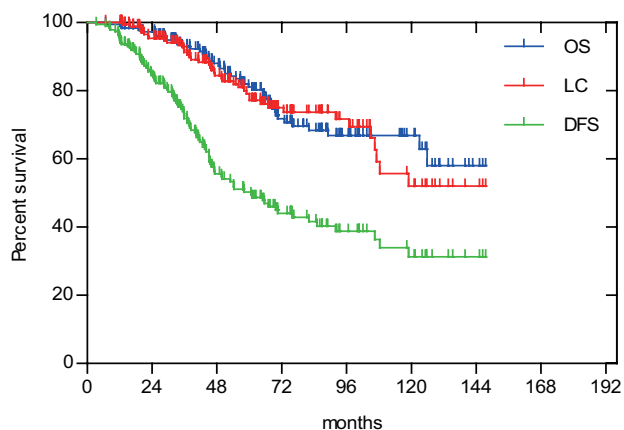


Fig.2 Overall survival (OS, blue line), local control (LC, red line) and disease-free survival (DFS, green line) curves for 188 patients.

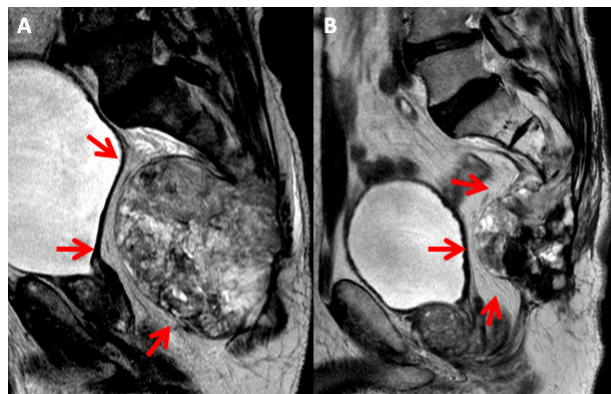


Fig.3 A sacral chordoma of a 66-year-old male. A) Before C-ion RT the large tumor reached the S2 level. B) 4 years after treatment the tumor had shrunk.

### Discussion

The local recurrence rate after surgery for sacral chordoma is approximately 35%–50% [2] Rates are higher for intralesional and marginal resections than for a wide resection. Generally, the higher the level of the sacral bones at which the tumor arises, the more difficult it is to achieve wide resection. In our study, there was no significant predictive factor for LC that was related to the tumor condition. This finding shows that C-ion RT may achieve the same results as for treatment of small tumors and tumors at a low spinal level, even if the tumor is at a high level in the sacrum and has a large volume. Furthermore, physiological stress and complications are less with C-ion RT than with sacrectomy as Nishida et al. [5] observed. This is an advantage of C-ion RT compared to surgery. Nishida et al. compared the results of surgery and C-ion RT for sacral chordomas. They found the results of both treatments were similar and patients treated with C-ion RT had better scores of emotional acceptance. The conclusive results from our study need further confirmation. We can say, however, that C-ion RT offers satisfying results for patients with unresectable sacral chordomas and will be a valuable alternative to surgery.

### References

- [1] Flanagan AM, et al. In: Fletcher CDM, Bridge JA, Pancras CW, Mertens F, eds. *World Health Organization (WHO) Classification of Tumours of Soft Tissue and Bone. Pathology and Genetics*. IARC Press, 328–329, 2013.
- [2] Ruggieri P, et al., *Clin Orthop Relat Res*; 468, 2939, 2010.
- [3] Imai R, et al., *Clin Cancer Res*, 10, 5741, 2004.
- [4] Imai R, et al., *Carbon ion radiotherapy for unresectable sacral chordomas*. *Int J Radiat Oncol Biol Phys*; 95(1):322, 2016.
- [5] Nishida Y, et al., *Int J Radiat Oncol Biol Phys*, 79, 110, 2011.

## Highlight

# Development of a superconducting rotating-gantry for carbon radiotherapy

**Yoshiyuki Iwata**

E-mail: iwata.yoshiyuki@qst.go.jp

## Introduction

In recent years, application of high-energy particle accelerators to cancer therapy has attracted much attention, and a number of medical particle accelerators have been constructed around the world. In particle radiotherapy, a rotating gantry is a powerful tool, and it is commonly used for proton therapy. However, it is very difficult to construct a rotating gantry for heavy-ion therapy, because the magnetic rigidity of carbon ions having an energy of 430 MeV/u is roughly three times higher than that for proton ions having an energy of 250 MeV/u, and therefore the size and weight of the entire gantry structure become considerably larger. There is only one carbon gantry, which was constructed at HIT in Heidelberg [1], and its total weight and radius are 600 tons and 7.0 m, respectively. To downsize the carbon gantry, we developed a compact superconducting rotating gantry [2]. The construction of the entire gantry was completed in September 2015, and commissioning is in progress. In this report, a design overview and current status of the gantry are presented.

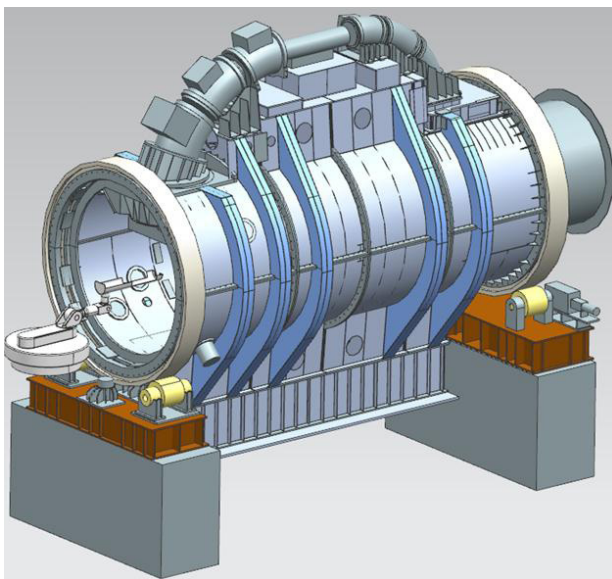
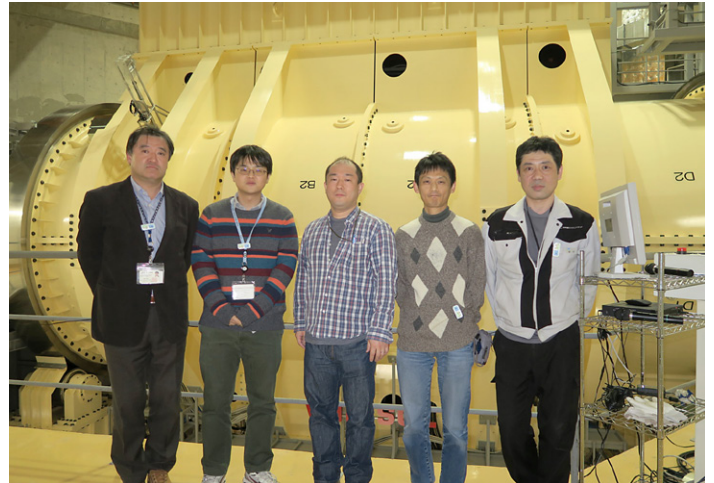


Fig.1 Schematic drawing of the superconducting rotating-gantry for carbon ion radiotherapy.



## Design and construction of the superconducting gantry

The compact superconducting rotating-gantry has a cylindrical structure with a beam-transport line, mounted on the structure, as schematically shown in Fig.1. The total length and the diameter of the cylindrical structure are approximately 14 m and 5.3 m, respectively. At both ends, two large rings having an outer diameter of 6.5 m are attached. The rings are placed on turning rollers, supporting the total weight of the entire structure, so as to rotate the entire structure along the central axis over  $\pm 180$  degrees.

This rotating gantry can deliver carbon ions having a kinetic energy of 430 MeV/u to the isocenter over  $\pm 180$  degrees, having the capability of performing three-dimensional raster-scanning irradiation. The beam line on the rotating gantry consists of ten superconducting magnets, a pair of scanning magnets, and three pairs of steering magnets as well as a beam-profile monitor, as illustrated in Fig.2. All of the ten superconducting magnets have a surface-winding coil-structure, and can provide both dipole and quadrupole fields, while BM07 and BM08 can provide only dipole field. The maximum dipole field was designed to be 2.9 T for BM01-06 and 2.4 T for BM07-10 with the maximum quadrupole field of 9.1 T/m for BM01-06 and 1.3 T/m for BM09-10. Having used the combined-function superconducting magnets, and optimized design of the beam optics, we could design a compact gantry, while keeping a large scan size at the isocenter. The length and the radius of the gantry beam-line are approximately 13 m and 5.5 m, respectively, which are comparable to those for the existing proton gantries, and the total weight of the gantry structure is estimated to be the order of 300 tons.

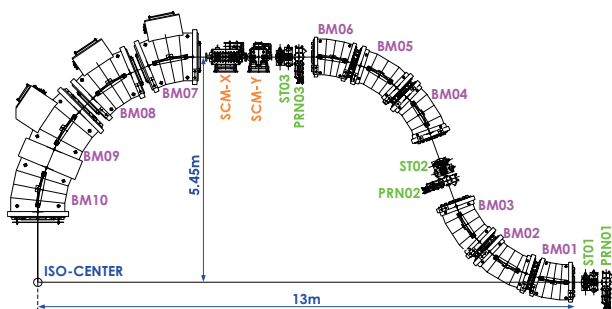


Fig.2 Layout of the beam transport line for the superconducting rotating gantry. The gantry consists of ten combined-function superconducting magnets (BM01-10), a pair of scanning magnets (SCM-X and SCM-Y), and three pairs of beam profile-monitor and steering magnets (ST01-03 and PRN01-03).

The superconducting magnets as well as components of the gantry structure were produced at the Toshiba Keihin Product Operations facility. Before transporting it to NIRS, the gantry structure was initially assembled in the factory. After a series of factory tests, the gantry structure was disassembled into components, and all the components were transported to NIRS beginning in February 2015. Since the gantry components are large in size, their transportation and installation as well as assembly of the gantry structure were done sequentially. All the construction and on-site tests of the gantry system (Fig.3) including the treatment room (room G; Fig.4) were completed at the end of September 2015. Treatment room G has the identical robotic couch to those used in treatment rooms E and F. With the unique caterpillar structure around the irradiation nozzle, the gantry floor can be kept flat, independently of the gantry angle.



Fig.3 A photo of the superconducting rotating gantry. The superconducting and scanning magnets are colored blue and red, respectively.

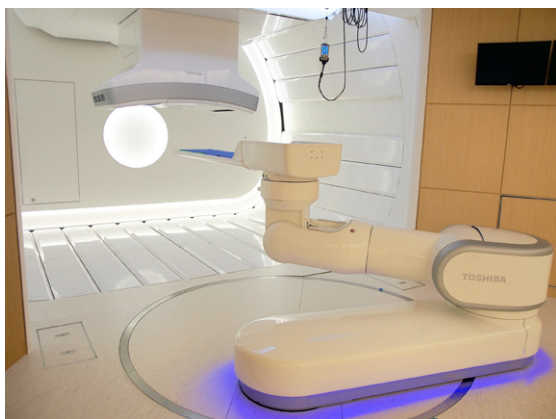


Fig.4 A photo of the gantry treatment room (treatment room G).

### Beam commissioning

Operations of the superconducting gantry and commissioning using the beam were initiated from October 2015. Carbon ions having the energies between 430–50 MeV/u, as accelerated by the upper synchrotron ring of the HIMAC, were successfully transported through the gantry, and beam spots at the isocenter were observed without any problems. Before using the gantry for treatments, the beam commissioning for combinations of various beam energies and gantry angles must be made. Since it is important to obtain stable and circular beam spots for scanning irradiation, we initially performed beam tuning of beam spots at the isocenter by finely tuning the superconducting quadrupoles. Some results of the beam tuning are given in Fig.5. As can be seen in the graphs, beam spots having a Gaussian shape were observed for the various gantry angles and beam energies.

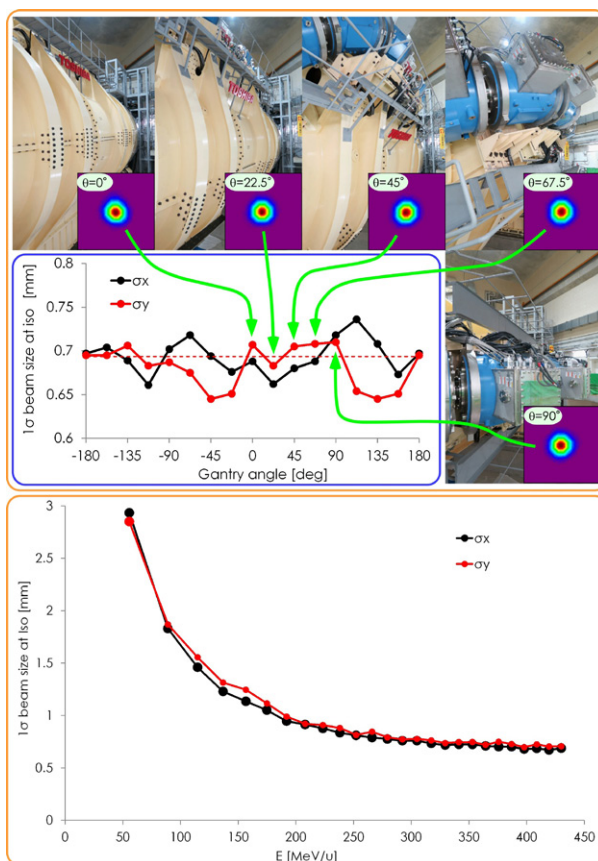


Fig.5 Measured  $1\sigma$  beam sizes of horizontal and vertical coordinates at the isocenter as functions of the gantry angle for the beam energy of 430 MeV/u (upper). Measured  $1\sigma$  beam size at the isocenter as a function of the beam energy (lower).

### Summary

We developed the superconducting rotating-gantry for carbon radiotherapy. The construction of the gantry was completed at the end of September 2015, and the beam commissioning is currently in progress. Treatment using the gantry is planned in FY 2016.

### References

[1] Eickhoff H, et al., *Proceedings of the 8th European Particle Accelerator Conference*, Paris, (EPS-IGA and CERN, Geneva), p. 2730, 2002.  
 [2] Iwata Y, et al., *Phys Rev ST Accel Beams*, 15, 044701, 2012.

## Highlight

# Investigation of physical and clinical doses of charged-particle therapy in patients

Taku Inaniwa

E-mail: inaniwa.taku@qst.go.jp

## Introduction

In the past 20 years, more than 8,000 patients with various tumors have been treated with passively scattered C-ion beams at NIRS, and the optimum dose-fractionation protocols have been established for the respective tumors through dose escalation studies. The favorable clinical results obtained at NIRS have encouraged several more facilities to initiate C-ion radiotherapy (RT) worldwide. To aid the ongoing development of C-ion RT, we started clinical treatments with pencil beam scanning, a new beam delivery method, in 2011. To exploit the advantages of the scanned C-ion RT fully, it is necessary to perform 3D treatment planning and optimization. A prerequisite for this is an algorithm for accurate and fast physical and clinical dose calculation. However, when the scanned C-ion RT was started at NIRS, there was no commercial treatment planning system (TPS) dedicated for this beam delivery method. Thus, we have developed a non-commercial TPS "XiDose" in which NIRS's original algorithms are interconnected to a TPS platform provided by Elekta AB, Sweden. Following our experience with the beam delivery method, the NIRS algorithms were transferred to several companies who have developed commercial products. In more recent years, our research efforts have been directed to better understanding of C-ion beams, improvement of physical and biological models, their integration into the TPS, and assessment of their influence on C-ion RT. In this report, we review our research articles published in FY 2015.

## Reformulation of clinical-dose system for carbon-ion radiotherapy treatment planning [1]

Through 20 years of clinical experience based on NIRS's original clinical-dose system, optimum dose-fractionation protocols have been established for various tumors, which may be considered as the standards in C-ion RT. Although the therapeutic appropriateness of the clinical-dose system has been widely demonstrated by clinical results, the system incorporates several simplifications such as the dose-independent RBE, empirical nuclear fragmentation model, and use of dose-averaged linear energy transfer to represent the spectrum of particles. We updated the clinical-dose system at the time we started clinical treatment with pencil beam scanning in 2011. The requirements for the updated system were to correct the simplifications made in the original system, while harmonizing with the original system to maintain the established dose-fractionation protocols. In the updated system, the radiation quality of the therapeutic C-ion beam was derived with Monte Carlo (MC) simulations, and its biological effectiveness was predicted with a theoretical model. We selected the most used C-ion beam with  $\alpha = 0.764 \text{ Gy}^{-1}$  and  $\beta = 0.0615 \text{ Gy}^{-2}$  as



reference radiation for RBE. The C-equivalent biological dose distribution is designed to allow the prescribed survival of HSG tumor cells in entire SOBP region, with consideration of the dose dependence in the RBE. This C-equivalent biological dose distribution is scaled to a clinical dose distribution to harmonize with our clinical experiences with C-ion RT. Designs of the original and the updated clinical-dose systems are shown in Fig. 1. Treatment plans were made with the two systems, and physical and clinical dose distributions were compared with regard to prescribed dose level, beam energy, and SOBP width. Both systems provided uniform clinical dose distributions in the targets consistent with the prescriptions. The mean physical doses delivered to targets by the updated system agreed with the doses by the original system within  $\pm 1.5\%$  for all tested conditions. The updated system reflects physical and biological characteristics of the C-ion beam more accurately than the original system, while allowing the continued use of the dose-fractionation protocols established with the original system at NIRS.

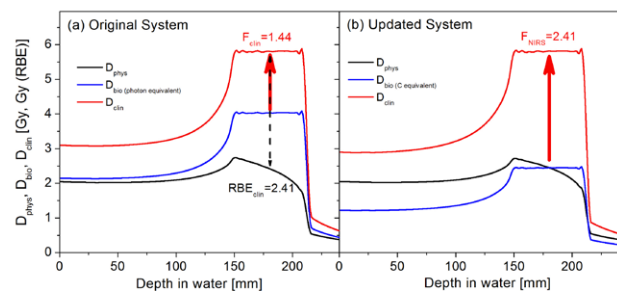


Fig. 1 Schematic designs of the original (a) and the updated (b) clinical-dose systems.

### Effects of beam interruption time on tumor control probability in single-fractionated carbon-ion radiotherapy for NSCLC [2]

C-ion RT treatment plans are designed on the assumption that the beams are delivered instantaneously, irrespective of the actual dose-delivery time structure in a treatment session. As the beam lines are fixed in the vertical and horizontal directions at our facility, beam delivery is interrupted in multi-field treatment due to the necessity of patient repositioning within the fields. Single-fractionated treatment for non-small cell lung cancer (NSCLC) is such a case, in which four treatment fields in multiple directions are delivered in one session with patient repositioning during the session. The purpose of this study was to investigate the effects of the period of dose delivery, including interruptions due to patient repositioning, on tumor control probability (TCP) of NSCLC. All clinical doses were weighted by RBE evaluated for instantaneous irradiation. The rate equations defined in the microdosimetric kinetic model (MKM) for primary lesions induced in DNA were applied to the single-fractionated treatment of NSCLC. Treatment plans were made for an NSCLC case for various prescribed doses ranging from 25 to 50 Gy (RBE), on the assumption of instantaneous beam delivery. These plans were recalculated by varying the interruption time  $\tau$  ranging from 0 to 120 min between the second and third fields for continuous irradiations of 3 min per field based on the MKM. The curative doses that would result in a TCP of 90% were deduced for the respective interruption times as shown in Fig.2. The curative dose was 34.5 Gy (RBE) for instantaneous irradiation and 36.6, 39.2, 41.2, 43.3 and 44.4 Gy (RBE) for  $\tau = 0, 15, 30, 60$  and 120 min, respectively. The biological effectiveness of the therapeutic C-ion beam decreased with increasing interruption time. These data suggest that the curative dose can increase by 20% or more compared to the planned dose if the interruption time extends 30 min or longer. These effects should be considered in C-ion RT treatment planning if a long dose-delivery time is anticipated.

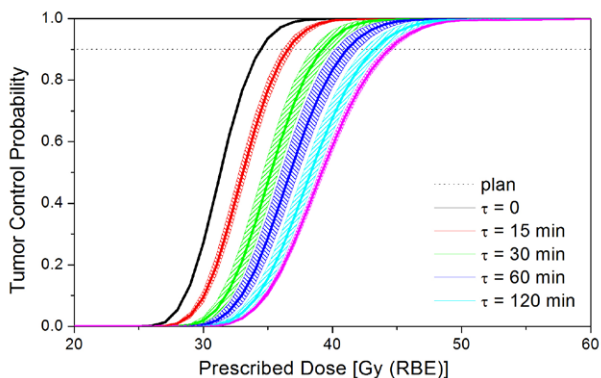


Fig.2 TCP curves of planned (black) and recalculated dose distributions for interruption times  $\tau$  of 0 min (red), 15 min (green), 30 min (blue), 60 min (light blue), and 120 min (pink) for an NSCLC case.

### Influence of nuclear interactions in body tissues on tumor dose in carbon-ion radiotherapy [3]

In C-ion RT treatment planning, the dose measured in water is applied to the patient dose calculation with density scaling using the stopping power ratio  $\rho_s$ . Since body tissues are different from water in composition, this dose calculation is subject to errors, particularly due to differences in non-elastic nuclear interactions. In recent studies, we proposed and validated a correction method for these errors. Dose calculation errors likely differ among different tumor sites as well as among patients. We thus assessed the influence of these errors on clinical cases in various tumor sites. Median dose corrections for the water non-equivalence of body tissues in nuclear interactions

were 0.2%, 0.0%, -0.3%, -0.1%, -0.1%, -0.4%, and -0.3% for the prostate, head & neck, bone & soft tissue, lung, liver, pancreas, and uterine cases, respectively. The largest correction of -1.6% in target average and -2.5% at maximum was observed in a uterine case as shown in Fig.3. In most clinical cases, the changes in dose would be marginal compared to the intrinsic uncertainties in treatment planning, patient setup, beam delivery, and clinical response. Nevertheless, in some extreme cases, the influence can be substantial. Thus, we recommend that the correction method should be routinely applied to treatment planning in clinical practice.

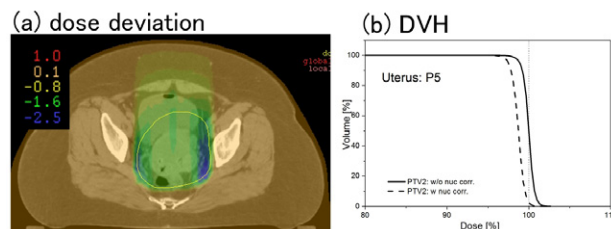


Fig.3 Dose deviation due to water non-equivalence of body tissues regarding non-elastic nuclear interaction in a uterine case (a), and the corresponding dose volume histograms (b).

### Correction for proton-nucleus interactions in non-water materials for proton radiotherapy treatment planning [4]

The water non-equivalence of body tissues regarding non-elastic nuclear interaction induces dose calculation errors in proton RT also. In this study, we proposed and validated an algorithm for correcting these errors. The dose in water is decomposed into three constituents according to the physical interactions of protons in water: the dose from primary protons continuously slowing down by electromagnetic interactions, the dose from protons scattered by elastic and/or inelastic interactions, and the dose resulting from non-elastic interactions. The proportions of the three dose constituents differ between body tissues and water. We determined correction factors for the proportion of dose constituents with MC simulations in various standard body tissues, and formulated them as functions of their  $\rho_s$  for patient dose calculation. The influence of nuclear interactions on dose was assessed by comparing the MC simulated dose and the uncorrected dose in common phantom materials. The influence around the Bragg peak amounted to -6% for polytetrafluoroethylene and 0.3% for polyethylene. The validity of the correction method was confirmed by comparing the simulated and corrected doses in the materials. The deviation was below 0.8% for all materials. The accuracy of the correction factors derived with MC simulations was separately verified through irradiation experiments with a 235-MeV proton beam using common phantom materials. The corrected doses agreed with the measurements within 0.4% for all materials. The influence on tumor dose was assessed in a prostate case. The dose reduction in the tumor was below 0.5%. Our results verify that this algorithm is practical and accurate for proton RT treatment planning, and will also be useful in rapidly determining fluence correction factors for non-water phantom dosimetry.

### References

- [1] Inaniwa T, et al., *Phys Med Biol*, 60, 3271, 2015.
- [2] Inaniwa T, et al., *Phys Med Biol*, 60, 4105, 2015.
- [3] Inaniwa T, et al., *Med Phys*, 42, 7132, 2015.
- [4] Inaniwa T, et al., *Phys Med Biol*, 61, 67, 2016.

## Highlight

# Solubilization of 2,2-diphenyl-1-picrylhydrazyl radical in water to evaluate the activity of water-soluble antioxidants

Ikuo Nakanishi, Emiko Sekine-Suzuki,  
Megumi Ueno, Minako Nyui,  
Ken-ichiro Matsumoto

E-mail: nakanishi.ikuo@qst.go.jp

## Introduction

It is known that about two thirds of the biological damage due to low linear energy transfer (LET) radiations, such as X-rays and the plateau region of heavy-ion beams, are caused by the hydroxyl radical ( $\cdot\text{OH}$ ), the most powerful reactive oxygen species (ROS), generated by the interaction of radiation energy with water molecules. Thus, antioxidants having an efficient ROS-scavenging activity have attracted much attention as promising candidates for radioprotective agents. In fact, we have recently demonstrated that natural antioxidants, such as (+)-catechin, resveratrol, caffeic acid, and quercetin, show an efficient protective activity against X-ray-induced apoptosis in rat thymocytes [1]. It is also known that the pH values of tumors (6.2–7.4) are slightly lower than those of normal tissues (7.0–7.4). Thus, if pH-responsive antioxidants, which can be activated in the pH range of 7.0–7.4, are available, normal tissues can be selectively protected without any protection of tumors during radiation therapy. In this context, the pH dependence of the activity of antioxidants is of considerable importance to develop such radioprotective agents. Since ROS are extremely unstable, relatively stable 2,2-diphenyl-1-picrylhydrazyl radical (DPPH $\cdot$ ) (Fig.1) has been frequently used as a reactivity model of ROS to evaluate the activity of antioxidants [2]. However, alcoholic co-solvents, such as methanol and ethanol, are required to use DPPH $\cdot$  in aqueous systems due to its insolubility in water. In such a case, concentrated buffer solutions cannot be used to control the pH of the reaction systems, because buffer salts are precipitated in the alcoholic reaction media. Cyclodextrins (CDs) are cyclic oligosaccharides that have a hydrophobic internal cavity and a hydrophilic external surface. Thus, CDs form inclusion complexes with a wide range of hydrophobic molecules and solubilize them in water. In this study, we investigated the solubilization of DPPH $\cdot$  in water using  $\beta$ -cyclodextrin ( $\beta$ -CD), which consists of 7 glucopyranoside units, in order to use DPPH $\cdot$  in aqueous buffer solutions.

## Results and discussion

15 mL of boiling water (Milli-Q) or a phosphate buffer solution (0.1 M, pH 7.4) was added to the mixture containing DPPH $\cdot$  (0.23 mmol) and  $\beta$ -CD (0.35 mmol), and the suspension was cooled to room temperature. The filtration of the suspension using a membrane filter (pore size: 0.22  $\mu\text{m}$ ) yielded a deep violet solution (Fig.2). This solution showed an absorption band at 527 nm, which is diagnostic of DPPH $\cdot$  (Fig.2). Thus, DPPH $\cdot$  could be solubilized in water by  $\beta$ -CD (Fig.1). A significant red shift of the band due to  $\beta$ -CD-solubilized DPPH $\cdot$  (DPPH $\cdot$ / $\beta$ -CD) as compared to those of free DPPH $\cdot$  in *n*-hexane (509 nm), methanol (516 nm), ethanol (517 nm), and acetonitrile (519 nm)

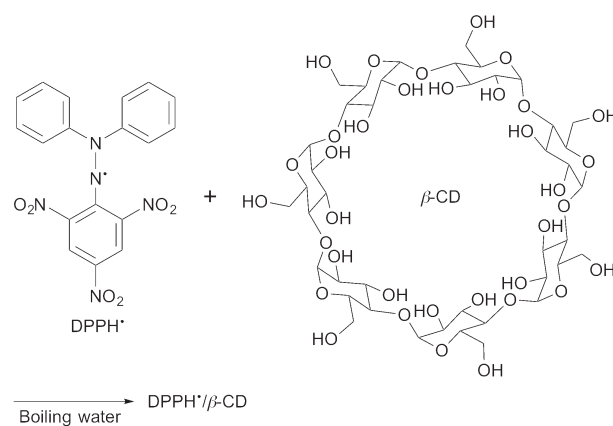


Fig.1 Solubilization of DPPH $\cdot$  in water by  $\beta$ -CD.

suggests that the  $>\text{N}-\text{N}\cdot$  moiety of DPPH $\cdot$  may exist outside of the  $\beta$ -CD cavity and strongly interact with water. In fact, an optimized structure of DPPH $\cdot$ / $\beta$ -CD by the density functional theory (DFT) (UB3LYP/3-21G:C-PCM solvation model parameterized for water) shows that the picryl moiety of DPPH $\cdot$  is incorporated into the hydrophobic cavity of  $\beta$ -CD (Fig.3) [3]. The concentration of DPPH $\cdot$  was estimated to be  $5.9 \times 10^{-5}$  M by using  $\epsilon$  value of 11000  $\text{M}^{-1} \text{cm}^{-1}$  determined for DPPH $\cdot$  in a 1:1 ethanol–buffer solution. DPPH $\cdot$ / $\beta$ -CD in water or the phosphate buffer solution (0.1 M, pH 7.4) is stable for at least several days at room temperature. When a boiling acetate buffer solution (50 mM, pH 4.4) was used instead of the phosphate buffer, DPPH $\cdot$  could also be solubilized by  $\beta$ -CD. On the other hand, a brown solution with absorption bands at 416 and 505 nm was obtained using the boiling borate buffer solution (14 mM, pH 9.1). This suggests that DPPH $\cdot$  is unstable under basic conditions.

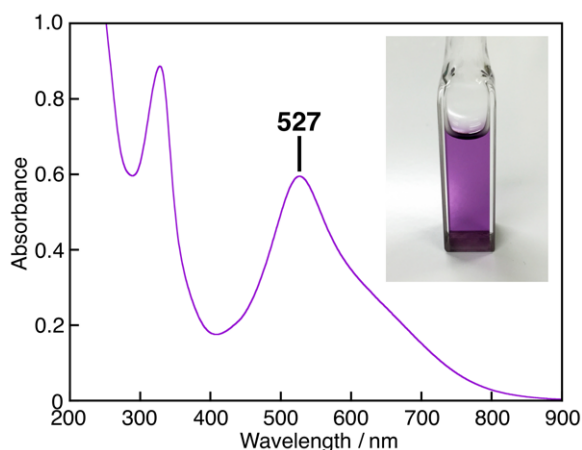


Fig.2 DPPH\*/ $\beta$ -CD in water and its UV-vis spectrum.

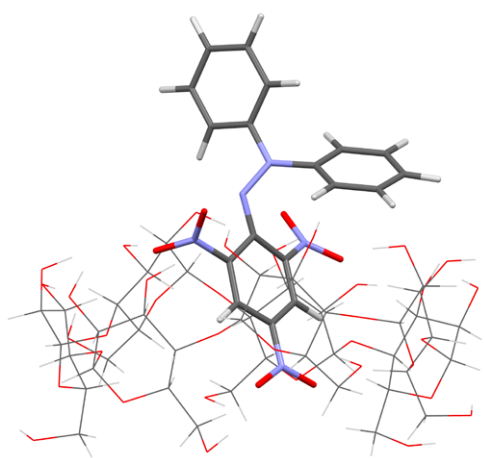


Fig.3 Optimized structure of DPPH\*/ $\beta$ -CD calculated by DFT.

The electron spin resonance spectrum of DPPH\*/ $\beta$ -CD observed in water at room temperature has the same  $g$  value (2.0036) and hyperfine coupling constant (7.8 G) as those of DPPH\* in methanol (2.0036 and 7.9 G, respectively).

When ascorbic acid (vitamin C) ( $\text{AscH}_2$ ) was added to the phosphate buffer solution (0.1 M, pH 7.4) of DPPH\*/ $\beta$ -CD, the band at 527 nm disappeared immediately with clear isosbestic points at 320, 338, and 431 nm. Since the  $pK_a$  value of  $\text{AscH}_2$  is reported to be 4.1,  $\text{AscH}_2$  undergoes deprotonation and exists in its anionic form,  $\text{AscH}^-$ , in phosphate buffer solution (0.1 M, pH 7.4). Thus, this spectral change indicates that  $\text{AscH}^-$  efficiently scavenged DPPH\* in phosphate buffer (eq. 1). When  $\text{AscH}^-$  was replaced by Trolox, a water-soluble analogue of  $\alpha$ -tocopherol (vitamin E), a similar spectral change was observed due to the scavenging reaction of DPPH\* by Trolox (eq. 2).



The decay of the absorbance at 527 nm monitored by a stopped-flow technique obeyed pseudo-first-order kinetics, when the  $\text{AscH}_2$  concentration ( $[\text{AscH}_2]$ ) was maintained at more than a 10-fold excess of DPPH\*/ $\beta$ -CD concentration (Fig.4). The pseudo-first-order rate constant ( $k_{\text{obs}}$ ) linearly increased with increasing  $[\text{AscH}_2]$ . From the slope of the linear plot of  $k_{\text{obs}}$  vs.  $[\text{AscH}_2]$ , the second-order rate constant ( $k$ ) for the scavenging of DPPH\*/ $\beta$ -CD by  $\text{AscH}_2$  was determined in a phosphate buffer (0.1 M, pH 7.4) to be  $7.2 \times 10^3 \text{ M}^{-1} \text{ s}^{-1}$ . The  $k$

value for Trolox was also determined in the same manner to be  $1.8 \times 10^4 \text{ M}^{-1} \text{ s}^{-1}$ , which is exactly the same as that measured in a 1:1 ethanol-phosphate buffer (pH 7.4) solution. Thus,  $\beta$ -CD does not inhibit the reaction of DPPH\* with the antioxidants.

The pH dependence of the  $k$  values for  $\text{AscH}_2$  was investigated using DPPH\*/ $\beta$ -CD in phosphate buffer solutions (0.05 M, pH 6.0–8.0). The  $k$  value increased with increasing pH as shown in Fig.5.

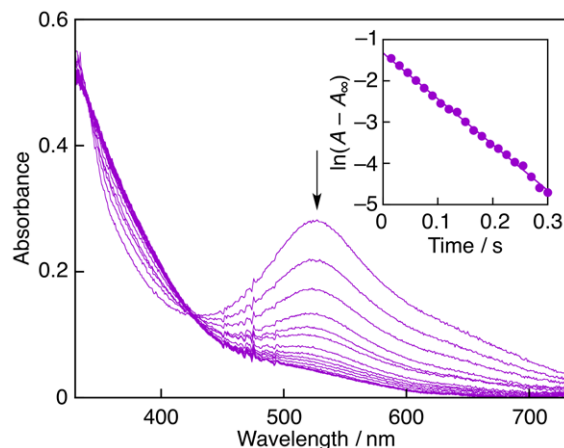


Fig.4 Spectral change (interval: 25 ms) observed during the reaction of  $\text{AscH}_2$  ( $1.4 \times 10^{-3} \text{ M}$ ) with DPPH\*/ $\beta$ -CD ( $2.6 \times 10^{-5} \text{ M}$ ) in phosphate buffer (0.1 M, pH 7.4) at 298 K. Inset: the first-order plot of the absorbance at 527 nm.

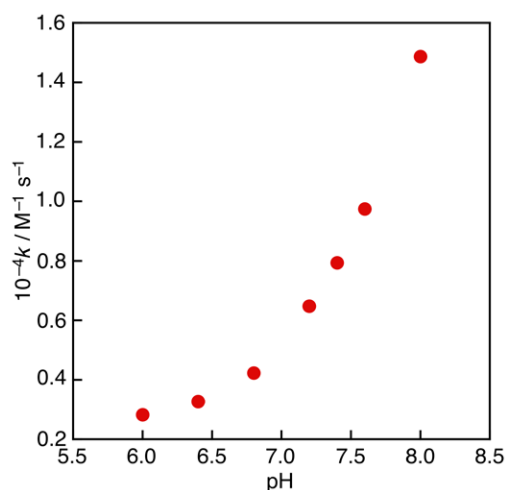


Fig.5 Plot of  $k$  vs. pH for the reaction of  $\text{AscH}_2$  with DPPH\*/ $\beta$ -CD.

## Summary

$\beta$ -CD-solubilized DPPH\* in water has been demonstrated to be a powerful tool to evaluate the antioxidative activity of antioxidants in aqueous media, especially in highly concentrated buffer solutions without precipitation of buffer salts as well as to develop pH-responsive antioxidants in order to selectively protect normal tissues during radiation therapy.

## References

- [1] Sekine-Suzuki E, *et al.*, *Anal Chem*, 85, 7650, 2013.
- [2] Waki T, *et al.*, *Chem Commun*, 49, 9842, 2013.
- [3] Nakanishi I, *et al.*, *Chem Commun*, 51, 8311, 2015.

## Highlight

# Study on the combination of carbon-ion radiation therapy and immunotherapy

**Takashi Shimokawa**

E-mail: shimokawa.takashi@qst.go.jp

## Background

Radiation therapy (RT) is one of the major cancer treatments, and it uses a physical strictness and difference of biological features between normal and cancer cells. Since RT is a non-invasive treatment, it results in a reduced physical burden for patients. In previous clinical reports, carbon ion (C-ion) RT showed a high local control rate and lower occurrence of adverse events. However, treatment-resistant cancer cells and distant metastasis are still important issues that need to be resolved. For C-ion RT in particular, metastasis control is required as a multidisciplinary therapy since micrometastasis, which is too small to detect by current technology, already exists at the time of the start of treatment in some cases.

In recent years, with the development of immune checkpoint inhibitors such as anti-PD-1 and anti-CTLA-4 antibodies, immunotherapy is receiving increasing attention. Immunotherapy has the potential to attack not only primary tumor cells, but also distant metastases. The features of immunotherapy and C-ion RT are complementary and the disadvantage of one is compensated for by the advantage of the other, so it has been expected that C-ion RT and immunotherapy might be an effectively combined for a multidisciplinary treatment. RT induces cell death of cancer cells in the patient body, and it is expected that the dying cancer cells are able to act as the source of a cancer antigen, which will be incorporated into antigen presenting cells and activate the immune system. However, basic research for such a multidisciplinary therapy is limited and insufficient.

Our research program has been conducting basic research for the purpose of solving the problems in the C-ion RT [1,2]. In particular, in our previous research aimed at metastasis control, the combination of C-ion irradiation and dendritic cell (DC) therapy drastically suppressed the lung metastases of the NR-S1 squamous cell carcinoma bearing C3H/He mouse model [1]. However, this combination effect was evaluated by only one type of mouse model, and it is unclear yet whether the underlying mechanisms of the different effects are due to the difference in radiation types, such as between photon beams or particle beams.

## Results and discussion

To obtain evidence for expansion of the application range of the combined therapy of C-ion RT and DC immunotherapy, we evaluated the combination effect by different models (Fig.1) [3]. Mouse osteosarcoma cell line, LM8, lung carcinoma cell line, LLC, and colon cancer cell line, Colon-26 were inoculated into the legs of C3H/He, C57BL/6J and BALB/c model mice, respectively. In the LM8 and LLC bearing mouse models, sig-

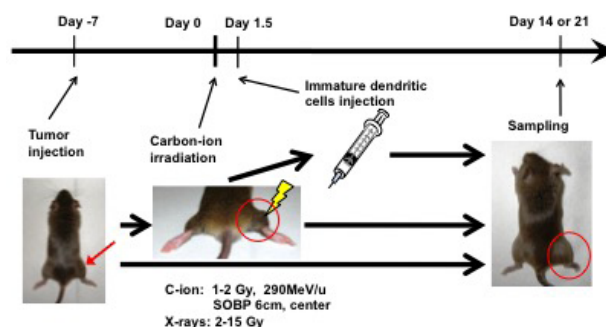


Fig.1 Experimental Schema.

Cancer cells are inoculated into right leg of 7 weeks-old female mice. At 1.5 day after irradiation, bone-marrow derived immature DC is injected intravenously. Lung metastasis is evaluated at day 14 or day 21 depend on mouse model.

nificant metastasis suppression was observed by the combination in the same manner as the previously reported NR-S1 bearing C3H/He model (Fig.2)[1]. On the other hand, we could not detect an enhanced metastasis suppressing effect by the combined treatment in the Colon-26 bearing BALB/c model. To elucidate the cause of the difference of such effects, we measured potential for DC activation by a co-culture with irradiated

cancer cells and immature DCs *in vitro* (Fig.3). If C-ion irradiation induces changes in cancer cells, which directly affect activation of immature DCs by being irradiated, and there is a difference in the change between the models, the difference should appear as efficiency of DC activation. When C3 H/He derived immature DCs were cultured with C-ion irradiated NR-S1 cells, a dose-dependent manner activation of DC cells was observed. A similar effect was also confirmed by the LM8 and LLC co-cultured with C3H/He and C57BL/6J derived DCs, respectively. On the other hand, for the combination of Colon-26 and BALB/c derived DCs, we could not detect activation of DC by irradiated cancer cells. These results indicate that the *in vitro* assay system reflects the model of *in vivo* and the difference among the models is caused by the process of DC activation by irradiated cancer cells.

In order to identify the mechanism of non-DC activation for the combination of Colon-26 and BALB/c derived DCs, we measured the DC-activating ability by changing combinations of cancer cells and DCs. Our results demonstrated that the difference of DC activation is not affected by the type of cancer cells, but it is determined by the mouse strain of the DC, which is connected to the genetic background of the mouse strain. Because all the DCs used in the experiment were confirmed to have an activating potential by LPS treatment, our results suggested that there is a functional variation among the DCs on the response to the irradiated cancer cells. On the other hand, we also found that C-ion irradiation is able to induce a change to allow DC activation on all investigated cancer cells.

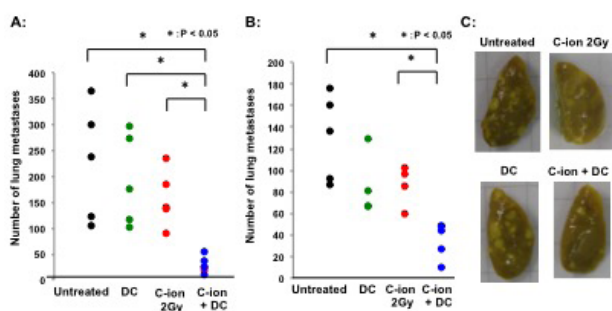


Fig.2 Repression of lung metastasis by the combination treatment. Number of lung metastasis of (A) LMB bearing C3H/He mouse model and (B) LLC bearing C57BL/6J mouse model evaluated at day 14 are showed. (C) Macroscopic images of Bouin stained lungs. Light yellow areas are metastatic nodules.

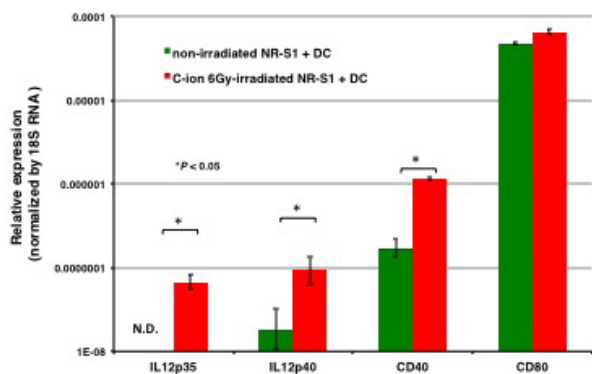


Fig.3 Maturation of DCs by co-culture with irradiated cancer cells. Gene expressions of DC maturation markers were analyzed by real-time PCR. Data are presented as a logarithmic plot of the 2- $\Delta\Delta Ct$  values (n = 3). The error bars indicate the standard deviation. ND, non-detected, the signal is below the sensitivity limit of the assay. \*, P<0.05 by Student's test.

In addition, we compared the effect of photon and C-ion beams by using the NR-S1 bearing C3H/He model. Based on the colony forming ability in *in vitro* assay, RBE of the NR-S1 cell line cell line was calculated to be 2. By the comparison at the equivalent dose (C-ion, 2 Gy and X-ray, 4 Gy), the combined effect was observed by C-ion irradiation, but not by the photon beam irradiation. However, at higher dose, such as 15 Gy, the combined effect occurred for the photon beam. It is suggested that there is an additional effect of C-ions which cannot be explained by only RBE.

As described above, our findings raise a question in the mechanisms of the metastasis inhibiting effect: Why is there a difference between the photon and C-ion irradiations, even though irradiated doses are equivalent for cytotoxicity based on colony formation assay? Therefore, we focused on differences in the form of induced cell death. Immunogenic cell death is a type of cell death form and it effectively elicits an immune response. There are several markers to measure the immunogenic cell death. In this time, we measured two markers, high-mobility group protein 1 (Hmgb1), which is known to be released into the extracellular space, and calreticulin (Calr), which is exposed to the cell surface. When comparing HMGB1 release and ecto-Calr in *in vitro* cell culture at the equivalent doses of C-ions and photons, there is no significant difference in the Hmgb1 release. Meanwhile the Calr exposure on the cellular surface was induced from a lower dose by C-ion irradiation compared with photon irradiation. This result was not consistent with the results of metastasis suppression in the mouse models.

Our results showed that C-ion irradiation has strong advantages as a partner combined with immunotherapy. Moreover, the results also indicated attention must be given to variation of individual patients to educe the full potential of the two therapies.

### Future perspective

Our findings showed the combination of C-ion RT and immunotherapy is effective to inhibit metastasis. However, to improve clinical outcome of C-ion RT, our final goal is controlling molecular mechanisms to regress distant metastasis (e.g. abscopal effect). If it is possible to induce antitumor effects by local C-ion irradiation on non-irradiated distant tumors, which are already engrafted and growing, we can expect to improve the overall survival rate. For this purpose, it is important to understand the underlying molecular mechanisms and to identify markers to select a suitable combination for an individual and to assess the therapeutic effect at an early stage.

### References

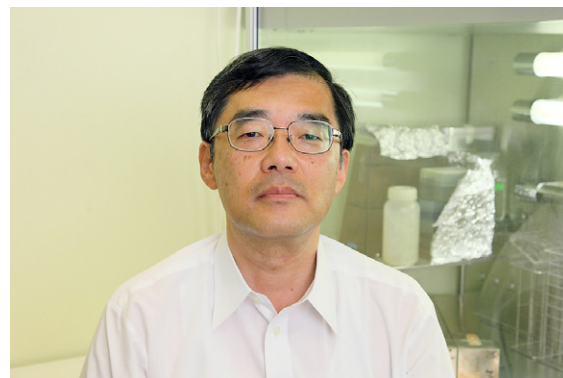
[1] Ohkubo Y, et al., *Int J of Radiat Oncol Biol Phys* 78, 1524-1531, 2010.  
 [2] Sato K, et al., *Radiat Res* 182, 408-419, 2014.  
 [3] Ando K, et al., *Int J of Radiat Oncol Biol Phys* 87, S642, 2013.

## Highlight

# Gap-junction mediated bystander effects between carbon-ion irradiated tumor and non-irradiated normal cells

**Masao Suzuki**

E-mail: suzuki.masao@qst.go.jp



A central paradigm in the research field of radiobiology has been that energy deposition from radiation tracks into a cell and/or water molecules causes either direct ionization or indirect ionization by hydroxyl radicals, eliciting radiobiological effects. This implies that the radiobiological consequences only affect the cells directly hit by the radiation and/or water radicals and that non-hit cells do not contribute to radiobiological effects. This paradigm is one of the important bases for the current system of risk estimation for radiation-induced biological consequences and, in particular, the risk of radiation-induced cancer after high and moderate doses which is relatively well known based on the data from detailed epidemiological studies of Japanese atomic bomb survivors in Hiroshima and Nagasaki [1]. However, the concept of radiation-induced biological effects has recently been challenged by so-called non-targeted effects, such as the bystander effect (Fig. 1).

The radiation-induced bystander effect can be explained as the ability of cells affected by some factors to convey manifestations of cellular damage to neighboring cells not directly hit by radiation. In the research field for both heavy-ion radiotherapy and radiation biology the bystander effect should play an important and essential role in the mechanism(s) of induced biological effects [2,3]. Especially because the volume of the tumor, which is the target for the medical treatment of radiation, is intertwined with both tumor and normal cells, communication between tumor and normal cells is one of the indispensable concerns for heavy-ion radiotherapy and it is necessary for further development of the current heavy-ion radiotherapy system to elucidate the mechanism(s) of the phenomena. Many reports have been published regarding bystander cellular effects after

exposure to low-fluence alpha particles from a plutonium-238 source or helium-ion microbeams. The studies mostly used the same cell line with both radiation-hit and non-hit bystander cells. However, only limited studies are available to understand bystander effects induced by heavier ions than helium ions, such as carbon ions, and that use a biological sample with different cell origins, such as normal and tumor cells.

This year we studied the bystander effect focusing on the communication of signaling events from carbon-ion irradiated tumor cells to non-irradiated bystander normal cells using the HIMAC-generated carbon ions with heavier atomic number than that of helium ions.

Human glioblastoma cell line (Resource No.: CRL1690, Resource name: T98G), which was distributed by the Health Science Research Resources Bank, was irradiated with mono-energetic carbon-ion beams (LET=73 keV/μm) with a single dose of 6 Gy in the HIMAC. Then normal human embryonic lung fibroblasts (Resource No.: RCB0523, Resource name: HFL-I), which were distributed by the RIKEN BioResource Center, were co-cultured with the irradiated T98G cells in the presence or absence of a gap-junction inhibitor (Lindane; 40 μM of γ-isomer

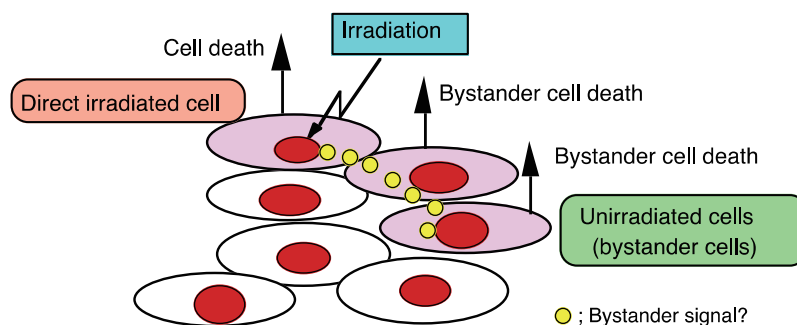


Fig. 1 The concept of the radiation-induced bystander effect. The bystander effect describes the ability of cells affected by irradiation to convey manifestations of damage to other cells not directly irradiated.

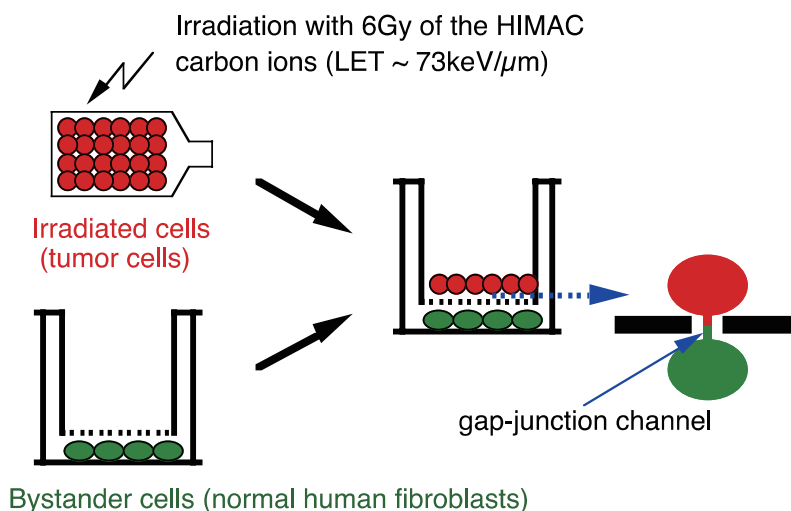


Fig.2 The co-culture method using the transwell permeable support system for the study of the bystander response via gap-junction mediated cell-cell communication. The advantages of this system for application to the present study are to make true bystander cells and to avoid the effects from secondary radiation.

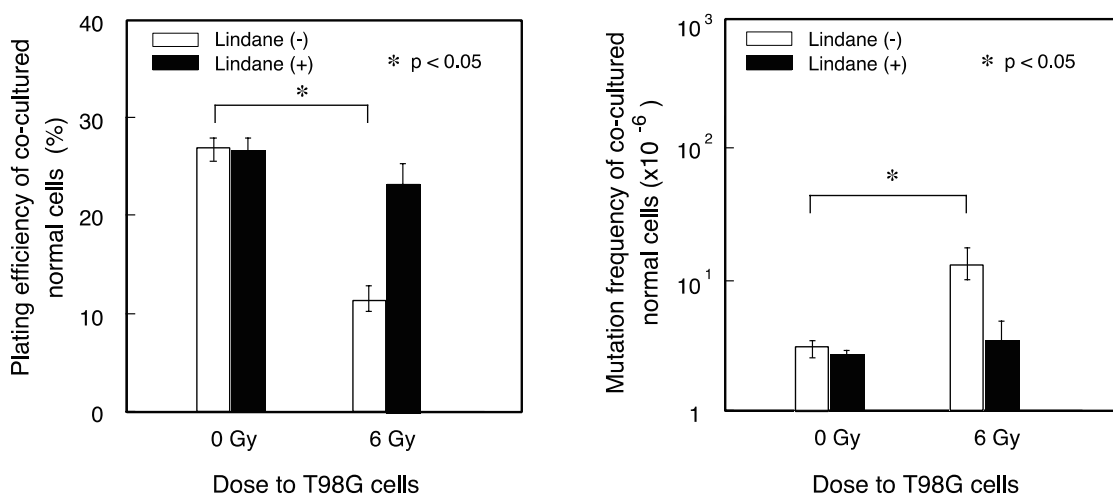


Fig.3 Bystander effect via gap-junction mediated cell-cell communication from carbon-ion irradiated tumor cells to non-irradiated normal cells. The left panel shows cell death and the right panel shows gene mutation. The results are the means and standard errors from 4 independent beam times (\*  $p < 0.05$ ).

of hexachloro-cyclohexane) using the transwell permeable support system (Fig.2). After 24 h, bystander HFL-I cells were then assayed for cell death using the colony-forming assay as a reproductive cell death and gene mutation at the hypoxanthine guanine phosphoribosyltransferase (*HPRT*) locus detected by 6-thioguanine resistant clones as one of the indicators for late biological effects in normal human cells.

The plating efficiency of the co-cultured bystander HFL-I cells with the carbon-ion irradiated T98G cells clearly decreased in the case of the absence of the gap-junction inhibitor, suggesting increased cell death. On the other hand, there was no statistically significant difference in the plating efficiencies of the co-cultured HFL-I cells between 0 Gy- and 6 Gy-irradiated T98G cells (Fig.3 left panel).

The mutation frequency of the co-cultured bystander HFL-I cells with the carbon-ion irradiated T98G cells was statistically higher than that with non-irradiated T98G cells in the absence of the gap-junction inhibitor, but the same level in the presence of the gap-junction inhibitor (Fig.3 right panel).

There is clear evidence that the irradiated tumor cells enable damage to be induced in the neighboring non-irradiated normal cells via the gap-junction mediated bystander effect.

In this study we focused on the bystander cellular effects via gap-junction mediated cell-cell communication. The transwell permeable support system is used to co-culture both the irradiated T98G cells growing in the wells and the bystander HFL-I cells growing in the inserts. It enables examination of bystander effects not only via gap-junction mediated cell-cell communication but also via factor(s) secreted into the culture medium from the irradiated cells. Now we have started to examine the bystander cellular effects between irradiated tumor cells and non-irradiated normal cells focusing on the effect of secreted factor(s).

#### References

- [1] Pierce D A, *et al.*, *Radiat. Res.* 154,178, 2000.
- [2] Autsavapromporn N, *et al.*, *Radiat. Res.*, 180, 367, 2013.
- [3] Autsavapromporn N, *et al.* *Mutat. Res.*, 756, 78, 2013.

## Highlight

## The Research Project with Heavy Ions at NIRS-HIMAC

### Tsuyoshi Hamano

E-mail: hamano.tsuyoshi@qst.go.jp

Since 1994 the Heavy-Ion Medical Accelerator in Chiba (HIMAC) at NIRS has been made available for use by researchers worldwide in the fields of ion-beam sciences and carbon-beam radiotherapy. There are four experimental halls (Physics, Biology, Secondary beam and Medium-energy beam caves) as well as five treatment rooms. During the daytime from Tuesday through Friday, HIMAC is operated for patient treatments. At night and on weekends the four halls can be used for various experiments with ion beams. The latter framework is specified as "The Research Project with Heavy Ions at NIRS-HIMAC". Table 1 shows typical beam characteristics which are available to users at the Physics cave.

NIRS accepts proposal submissions for the Research Project twice a year (basically in June and November). Information about the call for proposals can be seen on the NIRS website [1]. The Program Advisory Committee (PAC) for the Research Project reviews submitted proposals from the viewpoint of scientific merits and feasibilities. The Machine Time Committee allocates beam time in accordance with the review of the PAC, considering requests from proposers. The Program Coordinator Group supports researchers especially from external institutions. The researchers, whose accepted proposals employ HIMAC, are asked to make a report to NIRS including a list of publications of the work and to make a presentation at an annual meeting after the end of the fiscal year (FY).

Figure 1 shows the numbers of accepted proposals as a function of year. FY 2014 had 133 proposals from medicine, biology, physics and engineering etc. that were accepted and a total beam time of 5155 hours was supplied. Figure 2 shows



contents of accepted proposals: the physics pie chart (a) includes medical physics, accelerator, atom & nuclear physics, chemistry and space sciences; and the biology pie chart (b) includes fundamental studies for cancer treatment, response of normal tissue, cell biology and molecular biology. Registered participants from external institutions numbered 690 researchers, including 158 researchers from outside Japan. Figure 3 shows the numbers of scientific reports, including original papers, proceedings, theses and oral presentations. For more details, the annual report [2] of the Research Project (partly in English) is available from the Program Coordinator (book or CD-ROM) and at the NIRS website (PDF file). It includes submitted reports and publication lists.

Table 1 Typical characteristics of the beams available at HIMAC.

Ion	Energy (MeV/u)								Intensity pps (particles / second)
	100	180	230	290	350	400	430	-	
He	100	180	230	-	-	-	-	-	$<1.2 \times 10^{10}$
C	100	180	230	290	350	400	430	-	$<1.8 \times 10^9$
N	100	180	230	290	350	400	430	-	$<1.5 \times 10^9$
O	100	180	230	290	350	400	430	-	$<1.1 \times 10^9$
Ne	100	180	230	290	350	400	600	-	$<7.8 \times 10^8$
Si	100	180	230	290	350	400	600	800	$<4.0 \times 10^8$
Ar	-	-	-	290	-	400	650	-	$<2.4 \times 10^8$
Fe	-	-	-	-	-	400	500	-	$<2.5 \times 10^8$

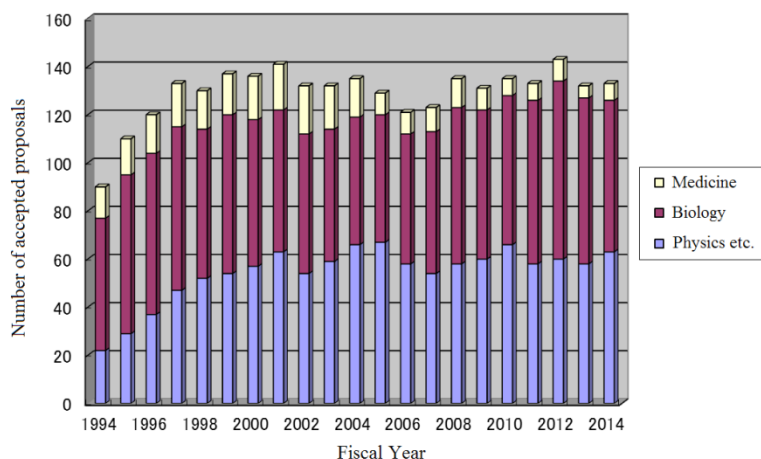


Fig.1 Numbers of accepted proposals as a function of fiscal year.

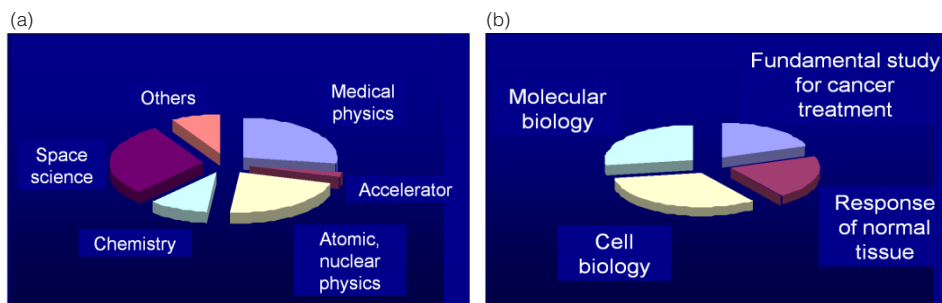


Fig.2 Contents of accepted proposals in physics (a) and biology (b) in FY 2014.

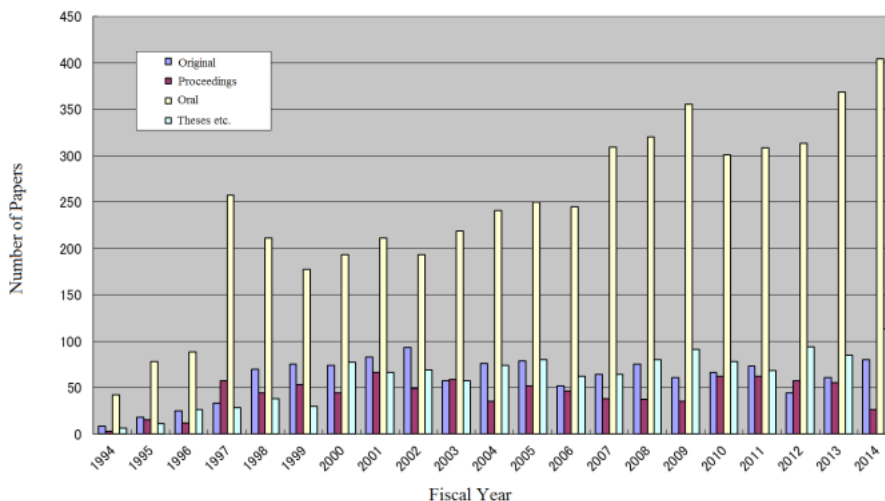


Fig.3 Number of scientific reports as a function of fiscal year.

**References**

- [1] NIRS, [http://www.nirs.qst.go.jp/information/application/28\\_himac2016.shtml](http://www.nirs.qst.go.jp/information/application/28_himac2016.shtml)
- [2] NIRS, 2014 Annual Report of the Research Project with Heavy Ions at NIRS-HIMAC, NIRS-M-285, Dec. 2015. <http://www.nirs.qst.go.jp/publication/irregular/02.html>

# Molecular Imaging Research for Functional Diagnosis

## Yasuhisa Fujibayashi, Ph.D., D.Med.Sci.

Director of Molecular Imaging Center

E-mail: fujibayashi.yasuhisa@qst.go.jp

NIRS has a long history of research and development in clinical applications of radiation, especially in the field of nuclear medicine including positron emission tomography (PET), single photon emission tomography (SPECT) and internal radiation therapy. Based on these accomplishments, the Molecular Imaging Center (MIC) was established in 2006. At present, research done at the MIC is based on collaboration among several diverse areas as follows:

- (1) Drug design for target-selective delivery (molecular probes), labeling of the molecular probes with suitable radioisotopes for diagnosis/therapy, and radionuclide production.
- (2) Development of three-dimensional quantum photon measurement systems such as PET and SPECT, including their hardware and software.
- (3) Basic evaluations and clinical applications for diagnosis/therapy of tumors, psychiatric and neurodegenerative disorders, and aging-related diseases such as inflammatory diseases.

The MIC also promotes research on magnetic resonance imaging (MRI), X-ray-CT imaging and optical imaging. These imaging techniques are an integral part of diagnostic imaging, and known as multimodal imaging. Recently, PET-MR has been approved for clinical medicine, and development of its clinical applications will be a key to further progress in this field.

### Molecular Probe Program

#### 1. Radiolabeling technique

We determined a reliable technique for producing [ $^{11}\text{C}$ ]carbon disulfide as a useful radioactive agent and constructed an automated synthesis system for producing [ $^{11}\text{C}$ ]carbon disulfide and synthesizing [ $^{11}\text{C}$ ]disulfiram as a PET probe for in vivo tumor imaging. To develop PET probes with various chemical functional groups, we used [ $^{11}\text{C}$ ]methyl iodide, [ $^{11}\text{C}$ ]phosgene, [ $^{18}\text{F}$ ]fluoroethyl bromide, and [ $^{18}\text{F}$ ]fluorine ion to label more than 10 novel compounds and to evaluate their potential applications both in vitro and in vivo.

#### 2. Development of novel molecular probes

We developed many novel PET probes for imaging of the brain, tumors and sites of inflammatory diseases etc. Among them, efficient synthetic methods of [ $^{18}\text{F}$ ]FEDAC, [ $^{18}\text{F}$ ]AMPBB3 and [ $^{11}\text{C}$ ]MePEPA have been determined. After preclinical evaluation, such as safety and dosimetry tests, these probes are being evaluated for clinical usefulness.



#### 3. Production of radionuclides for diagnosis/therapy of tumors

We determined techniques from irradiation to purification of Sc-47 and Re-186 and are performing a joint study on separation and purification of Ac-225 for cell and animal experiments. As well, we established an automated system for producing Cu-64 of > 300 mCi/day and we transferred amounts of this radionuclide to several facilities outside NIRS.

#### 4. Production of useful PET radiopharmaceuticals for clinical use

We are routinely producing more than 80 PET radiopharmaceuticals for clinical studies and for basic research in NIRS on cancers and brain functions also. This fiscal year, we established rapid and reliable production and quality control methods of three new PET radiopharmaceuticals including [ $^{11}\text{C}$ ]AIB, and we continued to provide documents and necessary information on techniques for producing several radiolabeled probes to PET facilities outside NIRS.

At the same time, we have obtained certification to produce PET radiopharmaceuticals that comply with the Japanese Society of Nuclear Medicine GMP standard for PET radiopharmaceuticals.

#### 5. Contribution to the quality control of clinical PET in Japan

We are routinely performing quantitative analysis and providing certificates for chemical impurities and residual solvents in several PET radiopharmaceuticals including [ $^{18}\text{F}$ ]FDG formulations which are produced in about 150 PET facilities in Japan.

## Biophysics Program

The Biophysics Program is aimed at development of the next generation PET technologies and the methods for quantitative analyses of in vivo imaging.

### 1. Imaging Physics

The Imaging Physics Team has carried out research and development of novel technologies for the next generation PET instrumentations and imaging algorithms. A depth-of-interaction (DOI) detector is a key device to get any significant improvement in sensitivity while maintaining high spatial resolution. DOI measurement has a potential to expand applications of PET to new fields because it allows for more flexible detector arrangement. Therefore we produced two innovations, OpenPET and “add-on” PET/MRI. OpenPET, which is our original idea for an open-type PET scanner, has led to implementation of PET imaging during treatment. At the end of this third 5-year project, we succeeded in developing a prototype OpenPET using the single-ring geometry to show a proof-of-concept of in-beam particle therapy imaging. On the other hand, recently developed semiconductor photodetectors, often referred to as silicon photomultipliers, have led us to develop a combined PET/MRI. We succeeded in showing a proof-of-concept of our original concept of an add-on PET/MRI, which is a MRI head coil with PET detectors. The prototype was applied to an existing MRI scanner.

### 2. Imaging Physiology

The Imaging Physiology Team has developed methods for the quantitative analyses of in vivo imaging obtained from PET, MRI, and optical imaging. In PET human brain studies, a novel method for measuring the dopamine release due to neuropsychological tasks was developed. This method shortened the scan period and improved the reproducibility of the estimation parameter representing the binding of neuroreceptors. In PET imaging for Alzheimer’s disease model mouse, we evaluated kinetic analysis methods for [<sup>11</sup>C]PIB, and established a quantitative index representing  $\beta$ -amyloid deposition. In the optical imaging of mouse, we developed a measurement system of two-photon laser scanning microscopy to trace degeneration of nerve cells caused by the deposition of tau protein over a long period. In addition, in autofluorescence imaging, we proposed a method to correct the decrease of fluorescence intensity due to the change of blood flow using simultaneously acquired optical intrinsic signals. This method can provide precise flavin-related fluorescence signals and should be useful for the evaluation of neural functions in small animals.

## Diagnostic Imaging Program

### 1. Basic and clinical research studies on pathophysiological imaging

We published two papers regarding the prognostic value of <sup>18</sup>F-FAZA PET/CT in patients with non-small cell lung cancer and head and neck cancer, and continued clinical PET research using <sup>11</sup>C-4DST, a marker of cellular proliferation, in patients with lung tumors. By using a metabolome analysis as a novel method to screen candidate probes, we succeeded in the selection and evaluation of novel PET probes for pancreatic cancer. We found that internal radiotherapy using <sup>64</sup>Cu-ATSM is effective against anti-VEGF Ab-resistant tumor, and we also confirmed the effectiveness of  $\alpha$ -emitting <sup>211</sup>At-labeled antibody in the radioimmunotherapy for the mouse model of peritoneal dissemination.

### 2. Development of antibody/peptide probes for targeted imaging and therapy of cancers

We proved the therapeutic efficacy of internal radiotherapy using a tetramer of cRGD labeled with <sup>64</sup>Cu/<sup>67</sup>Cu in the human glioma xenograft model. Human monoclonal antibody against  $\alpha_6\beta_4$  showing high accumulation in pancreatic cancer was labeled with  $\beta$ -emitting <sup>90</sup>Y and its therapeutic efficacy was tested in the mouse pancreatic cancer xenograft model. We labeled

an antibody against the tissue factor, a target expressed both on cancer cells and cancer stroma, with <sup>111</sup>In and succeeded in SPECT imaging of orthotopically implanted glioma in mice.

### 3. Development of MRI-based functional probes and nano-sized multi-functional probes and their application in various disease models

We published a paper on the development and evaluation of a nanoparticle responsive to relatively low dose  $\gamma$ -irradiation. The kinetic property of a soft nanoparticle was successfully modified by incorporating a quantum dot to show high accumulation in the tumor. A novel functional probe that can evaluate mitochondrial function was applied to various disease models including Parkinson’s disease and its usefulness was proved in the visualization of mitochondrial dysfunction. The resolution of MRI was improved by lowering it to 45  $\mu$ m, and, in combination with Mn-containing nano-micelles, we succeeded in detecting micrometastasis in the liver and also intratumoral heterogeneity.

## Molecular Neuroimaging Program

The Molecular Neuroimaging Program focuses on the pathophysiology of neuropsychiatric disorders including Alzheimer’s disease and depression, the evaluation of drug efficacy and the molecular mechanisms of human behavior. From basic research using transgenic mice to clinical studies, we use PET, MRI, and laser microscopes to analyze the molecular mechanism of disease onset and progression.

The major topic we pursued in 2015 was basic research to clarify the pathophysiology of vocal tics in Tourette syndrome which severely impact quality of life. Neural mechanisms underlying vocal tics remain unexplored because no established animal model representing the condition exists. We, in collaboration with NIH, reported that unilateral disinhibition of the nucleus accumbens (NAc) generates vocal tics in monkeys. Whole-brain PET imaging identified prominent, bilateral limbic cortico-subcortical activation. Local field potentials (LFPs) developed abnormal spikes in the NAc and the anterior cingulate cortex (ACC). Vocalization could occur without obvious LFP spikes, however, when phase-phase coupling of alpha oscillations was accentuated between the NAc, ACC, and the primary motor cortex. These findings contrasted with myoclonic motor tics induced by disinhibition of the dorsolateral putamen, where PET activity was confined to the ipsilateral sensorimotor system and LFP spikes always preceded motor tics. We have proposed that vocal tics emerge as a consequence of dysrhythmic alpha coupling between critical nodes in the limbic and motor networks.

In clinical studies, we continued the multicenter PET study of [<sup>11</sup>C]PBB3 in Japan to investigate the details of the binding characteristics of [<sup>11</sup>C]PBB3 using postmortem human brain. More than 200 PET scans have been executed for Alzheimer’s disease (AD) patients, non-AD dementia patients and healthy volunteers, and the comparison of PET images with histopathology of 6 brains derived postmortem are in progress. The quantification method of [<sup>11</sup>C] PBB3 accumulation with high precision in local brain regions of AD patients has been established using the reference tissue model (MRTMO) and standardized uptake value ratio (SUVR). The analysis of PET data from 60 patients with AD or mild cognitive impairment (MCI) confirmed that the increase in [<sup>11</sup>C]PBB3 accumulation was statistically significantly correlated with severity of AD progression, and it also revealed that pre-MCI and primary age-related tauopathy (PART) had already started even in healthy volunteers. We have developed the fluorinated PBB3 derivative and started the exploratory clinical trial.

## Highlight

# Striatal mGluR1 of rat accumulating A53T- $\alpha$ -synuclein dynamically changed during pathological progression of Parkinson's disease

Tomoteru Yamasaki

E-mail: yamasaki.tomoteru@qst.go.jp

## Objectives

Glutamate is the primary neurotransmitter involved in excitatory neurotransmission. Among the glutamate receptors, metabotropic glutamate receptor 1 and 5 (mGluR1 and mGluR5) are G protein coupled receptors classified into group I of the metabotropic glutamate receptor family and related to central nervous system (CNS) disorders including Parkinson's disease (PD) [1]. PD is the second most common chronic neurodegenerative disorder, following Alzheimer's disease (AD), and it is characterized by akinesia, tremors, rigidity, and poor balance. PD is believed to be caused by a combination of environmental and genetic factors leading to structural changes in the protein  $\alpha$ -synuclein (ASN). Aggregation of such abnormal ASN can affect many factors in synaptic transmissions [2].

PET is frequently used to monitor *in vivo* brain activity, and it allows for noninvasive assessment of longitudinal changes in target molecules. Here, we monitored longitudinal changes in striatal mGluR1 and mGluR5 expressions among chronic PD model rats with abnormal ASN aggregation by using selective radioligands and PET imaging [3].

## Materials and methods

### 1) Animals

As the PD model animal, Sprague-Dawley (SD) transgenic rats expressing human mutant A53T ASN (A53T-Tg) were chosen and purchased from Taconic Biosciences. The keeping of the animals and all experiments were approved by the Committee for the Care and Use of Laboratory Animals of the National Institute of Radiological Sciences.

### 2) Radioligands

Three radioligands (Fig.1) were synthesized in the laboratory of the Molecular Probe Program and used to monitor mGluR1, mGluR5, and dopamine transporter (DAT), a biomarker for dopaminergic neurons.

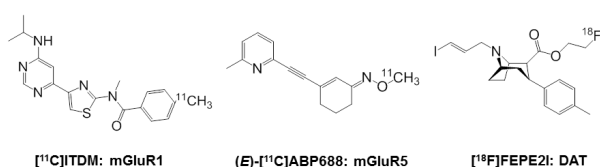
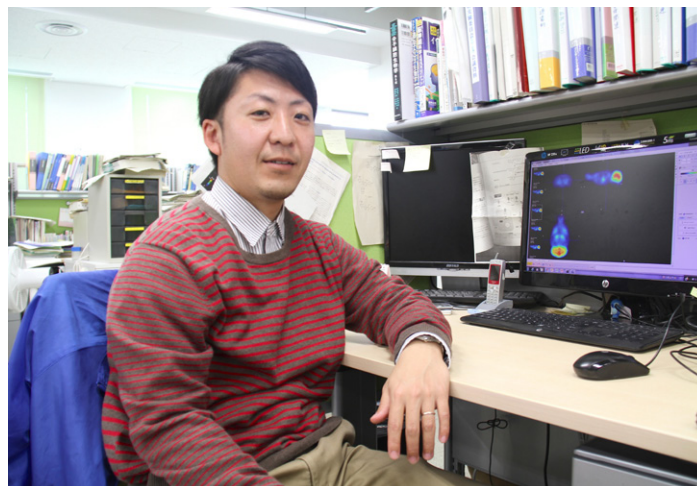


Fig.1 Chemical structures of radioligands used in this study.



### 3) Open-field test

To evaluate exploratory activity, the open-field test was performed using an acrylic box divided into 16 equal-area squares. The locomotion (the number of squares the four paws crossed) and rearing were measured as the indexes for general motor activities.

### 4) PET assessments

The dynamic emission scans were performed using a small-animal PET scanner (Inveon; Siemens Medical Solutions). Acquired PET dynamic images were analyzed, reconstructed with parametric images scaled by the binding potential ( $\text{BP}_{\text{ND}}$ ), and fused with the MRI template of rat brain. Kinetic models were chosen as follows: the Logan reference (for  $[^{11}\text{C}]$ ITDM) and the simplified reference tissue model (for (E)- $[^{11}\text{C}]$ ABP688 and  $[^{18}\text{F}]$ FEPE2I). Image reconstructions and kinetic analyses were performed by the PMOD software (PMOD Technology).

## Major findings

### 1) Decline of general motor activities in A53T-Tg rats

Locomotion and rearing scores tended to increase in 4 to 5 months old (mo) A53T-Tg rats, and then they dramatically decreased at older ages (Fig.2). A significant difference between noncarrier and A53T-Tg rats was found in locomotion scores ( $p$

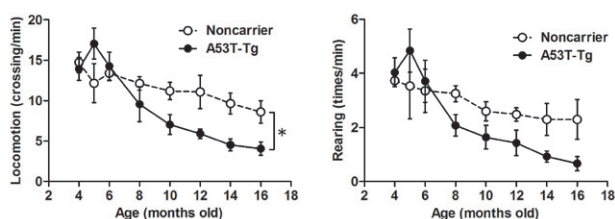


Fig.2 General motor activities (locomotion: left, rearing: right) in non-carrier and A53T-Tg rats. \* $p < 0.05$ : two-way ANOVA.

= 0.012). Locomotion and rearing scores in noncarrier rats also continually decreased with age during the present experimental period.

### 2) Dynamic changes of mGluR1 during progression of PD pathology

As shown in Fig.3, BP<sub>ND</sub>s for mGluR1 in the striatum of 4 mo A53T-Tg rats were higher than those of noncarrier rats, and dramatic decreases were subsequently shown in 8 to 16 mo A53T-Tg rats. Meanwhile, there was no difference in BP<sub>ND</sub>s for mGluR5 between noncarrier and A53T-Tg groups. In BP<sub>ND</sub>s for DAT, age-dependent decreases were shown in the striatum of A53T-Tg rats. Additionally, striatal signal area sizes also diminished with age.

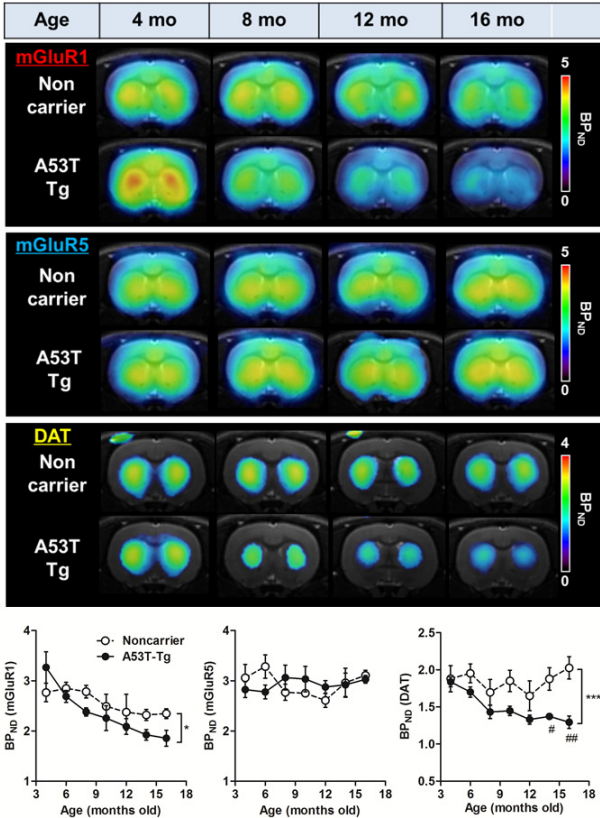


Fig.3 Representative parametric PET/MRI images for mGluR1 ( $^{11}\text{C}$ ]ITDM), mGluR5 ( $(E)$ - $^{11}\text{C}$ ]ABP688), and DAT ( $^{18}\text{F}$ ]FEPE2I) at 4, 8, 12, and 16 months in the striatum of the same noncarrier and A53T-Tg rats and dynamic changes in striatal BP<sub>ND</sub>s in 4 to 16 mo noncarrier and A53T-Tg rats. \* $p < 0.05$ , \*\*\* $p < 0.001$ : two-way ANOVAs; # $p < 0.05$ , ## $p < 0.01$ : Posthoc analyses.

### 3) High correlation between mGluR1 BP<sub>ND</sub>s and general motor activities

To confirm the relationship between BP<sub>ND</sub>s and general motor activities, scatter plot analyses were performed using each striatal BP<sub>ND</sub> (mGluR1, mGluR5, and DAT) and the general motor activities (locomotion and rearing). As shown in Fig.4, BP<sub>ND</sub>s for mGluR1 exhibited the highest correlation with motor activities, with correlation coefficients ( $r$ ) of 0.780 ( $p < 0.0001$ ) and 0.546 ( $p = 0.0008$ ) for locomotion and rearing, respectively. Relatively high correlations were also found between locomotion ( $r = 0.639$ ,  $p < 0.0001$ ) or rearing ( $r = 0.469$ ,  $p = 0.0034$ ) and BP<sub>ND</sub>s for DAT. In contrast, there was no correlation between BP<sub>ND</sub>s for mGluR5 and motor activities (locomotion:  $r = 0.007$ ,  $p = 0.9673$ ; rearing:  $r = -0.110$ ,  $p = 0.5492$ ).

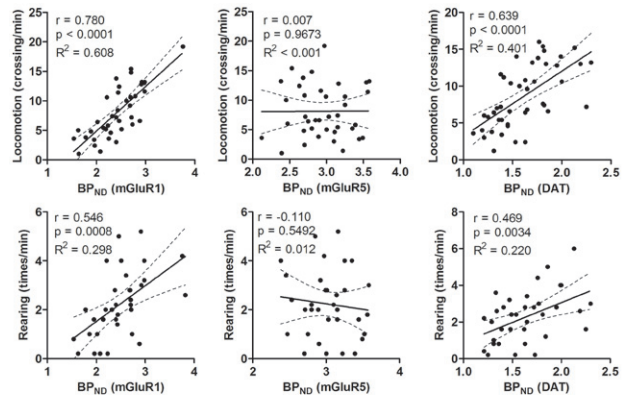


Fig.4 Scatter plots between general motor activities and each BP<sub>ND</sub> (mGluR1, mGluR5, and DAT). The regression lines in each graph show the 95% confidence intervals (dotted lines). Respective correlation coefficients ( $r$ ),  $p$  values, and  $R$  square values are given for each scatter plot.

### Discussion

In the present study, we demonstrated that dynamic changes occur in mGluR1, but not mGluR5 levels, in rat brains using a chronic-PD-model paradigm through longitudinal PET imaging. Interestingly, the changes in mGluR1 expression were strongly associated with the progression of PD pathology.

A53T is the most frequent mutation in familial Parkinsonism, and results in an earlier onset than that observed in most cases of sporadic PD. In this study, motor activities in A53T-Tg rats showed declines of approximately 50% at 10 months, and at 16 months, most A53T-Tg rats exhibited significantly lower motor activities. Besides, longitudinal PET studies showed dynamic changes with age in BP<sub>ND</sub>s for  $^{11}\text{C}$ ]ITDM, but not ( $E$ )- $^{11}\text{C}$ ]ABP688, in A53T-Tg rats. Interestingly, striatal  $^{11}\text{C}$ ]ITDM BP<sub>ND</sub>s were higher in A53T-Tg rats than noncarrier rats prior to onset of PD pathology, but subsequently decreased dramatically with age. These changes were highly correlated with dynamic changes in motor activities. These results suggest that the observed initial mGluR1 expression increase in 4 mo A53T-Tg rats was caused by the excessive glutamate release associated with abnormal ASN accumulation, and then these abnormalities would induce dopaminergic neuron degeneration.

In conclusion, in this longitudinal PET study, we have demonstrated for the first time that dynamic changes associated with PD progression occur in the expression of mGluR1, but not mGluR5, in a chronic PD model of rats, that mimics clinical pathology. We therefore suggest that mGluR1 is a useful in vivo biomarker to further the understanding of pathological mechanisms in PD. These findings may also facilitate the development of pharmaceuticals targeting mGluR1 for the treatment of PD and many other CNS disorders.

### References

- [1] Ribeiro FM, et al., *CNS Neurol Disord Drug Targets*, 9, 574, 2010.
- [2] Roberts HL, et al., *Biomolecules*, 5, 282, 2015.
- [3] Yamasaki T, et al., *J Neurosci*, 36, 375, 2016.

## Highlight

# Quantitative in vivo imaging of astrocytic energy metabolism in rat brain with radiolabeled benzyl acetate

Maki Okada

E-mail: okada.maki@qst.go.jp

## Introduction

Astrocytes, one of the glial cells, play important roles to protect and maintain neurons and they are associated with several neuronal diseases. Astrocytes use acetate as well as glucose as an energy fuel whereas neurons do not use acetate, which indicates acetate might be a specific marker for astrocytic energy metabolism. Therefore, acetate labeled with stable ( $^{13}\text{C}$ ) or radio isotope ( $^{11}\text{C}$  or  $^{14}\text{C}$ ) carbon atoms has been used in the studies for tracing and imaging of metabolic pathway of astrocytic energy metabolism [1-3]. Recently we developed  $^{11}\text{C}$  and  $^{14}\text{C}$  labeled benzyl acetate ( $^{11}\text{C}$ - and  $^{14}\text{C}$ -BA), lipophilic acetates, to improve the brain uptake, which resulted in higher brain uptake as measured by PET [2] and autoradiography [1] imaging in rat brain. Acetate enters into brain via a monocarboxylic acid transporter; this is the rate-limiting process for acetate measurement in brain, whereas benzyl acetate readily enters into brain because of its high lipophilicity and that is followed by a quick hydrolysis to acetate. Once it has entered the brain, acetate is transported to astrocytes selectively through the monocarboxylic acid transporter and metabolized to acetyl-CoA which subsequently enters the tricarboxylic acid (TCA) cycle. Acetate has two carbon atoms which have different metabolic fates; C-1 (carbonyl) acetate is more readily eliminated as carbon dioxide ( $\text{CO}_2$ ) than C-2 (methyl) acetate is. In this regard, C-1-labeled acetate seems to be a more suitable probe for oxidative energy metabolism than C-2-labeled acetate. These different characteristics between labeling positions might provide a useful marker for different types of neuronal diseases associated with abnormal astrocytic energy metabolism.

## Kinetics of [ $1\text{-}^{14}\text{C}$ ] and [ $2\text{-}^{14}\text{C}$ ]BA in mature rat brain

[ $1\text{-}^{14}\text{C}$ ] or [ $2\text{-}^{14}\text{C}$ ]BA were synthesized by the condensation of benzyl alcohol and [ $1\text{-}^{14}\text{C}$ ] or [ $2\text{-}^{14}\text{C}$ ]acetate under dicyclohexylcarbodiimide. The radioactivity derived from [ $1\text{-}^{14}\text{C}$ ] and [ $2\text{-}^{14}\text{C}$ ]BA decreased in a single-exponential manner and [ $2\text{-}^{14}\text{C}$ ]BA-derived radioactivity was significantly higher than that of [ $1\text{-}^{14}\text{C}$ ]BA in rat cortex, cerebellum, and pons (Figs. 1 A-C). The washout rates estimated from the slopes of the lines were higher in the rats injected with [ $1\text{-}^{14}\text{C}$ ]BA ( $0.043 \pm 0.006$ ,  $0.031 \pm 0.005$ , and  $0.028 \pm 0.005$  in cortex, cerebellum, and pons, respectively) compared with [ $2\text{-}^{14}\text{C}$ ]BA ( $0.013 \pm 0.003$ ,  $0.022 \pm 0.002$ , and  $0.027 \pm 0.003$ ), indicating [ $1\text{-}^{14}\text{C}$ ]BA was metabolized to [ $^{14}\text{C}$ ]CO $_2$  and exhausted faster than [ $2\text{-}^{14}\text{C}$ ]BA. Variou metabolite studies of stable or radio isotope-labelled acetate showed that acetate is metabolized to amino acids such as glutamine, glutamate, aspartate, and gamma-aminobutyric acid, as well as CO $_2$ . In particular, glutamate and glutamine are major metabolites of acetate in brain, which are produced via

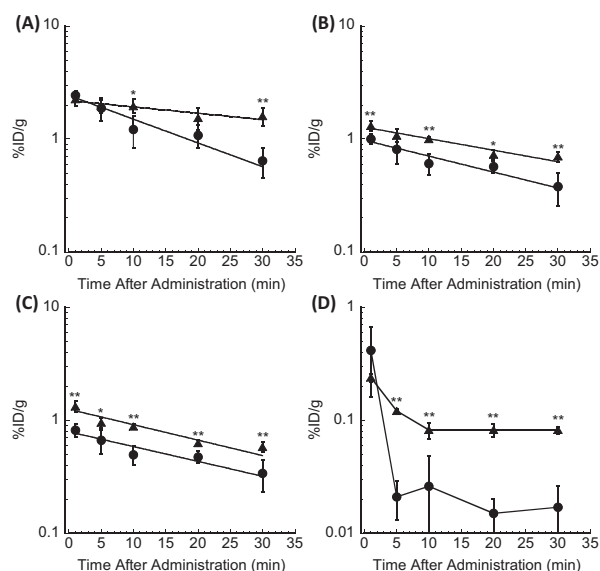
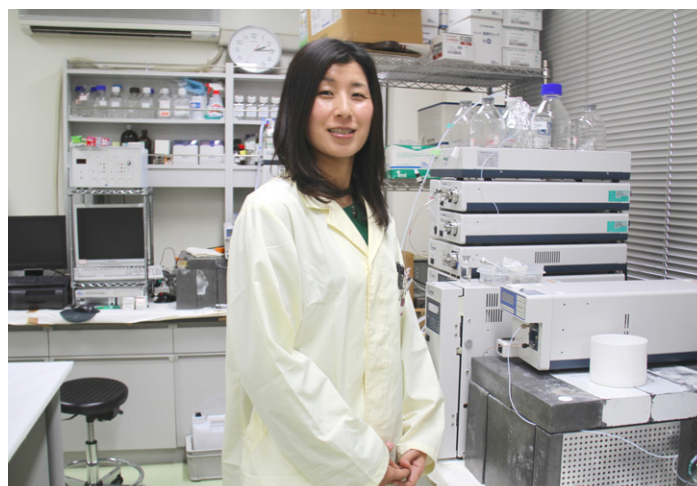


Fig.1 The time-radioactivity curves of [ $1\text{-}^{14}\text{C}$ ]BA (●) and [ $2\text{-}^{14}\text{C}$ ]BA (▲). (A) cortex, (B) cerebellum, and (C) pons. (D) The parent compound in the blood. %ID/g: % of injected dose/g tissue. Cited from [3].

$\alpha$ -ketoglutarate, the intermediate metabolite of the TCA cycle. The fates of acetate in brain are 1) metabolization to CO $_2$  and release from brain or 2) conversion to amino acids and accumulation in brain. Therefore, decrease of radioactivity from brain is reflected on CO $_2$  exhaustion (in other words, oxygen consumption), that is estimated as washout rate and retained radioactivity in brain seems to be in the form of amino acids.

The radioactivity derived from lipophilic parent compounds in blood obtained by a solvent extraction method was higher in [ $2\text{-}^{14}\text{C}$ ]BA than in [ $1\text{-}^{14}\text{C}$ ]BA as seen in brain (Fig.1 D). Almost all

the blood radioactivity of [1-<sup>14</sup>C]BA and [2-<sup>14</sup>C]BA disappeared quickly after injection. Radiometabolite analysis of [1-<sup>11</sup>C]BA in arterial plasma showed radiolabeled acetate, bicarbonate ion, glutamine, glutamate, and unknown metabolites but not [1-<sup>11</sup>C]BA even 1 min after injection (Fig.2). The radioactivity derived from metabolites detected in arterial plasma was extremely low and these metabolites seemed to slightly enter into brain. These analyses suggested that most of the radioactivities entered brain in the form of BA immediately after injection. Since C-1-labelled acetate metabolized into CO<sub>2</sub> within an earlier turn of the TCA-cycle than C-2-labelled acetate, [1-<sup>14</sup>C]BA seems to be a simpler indicator of CO<sub>2</sub> production for astrocytic metabolism.

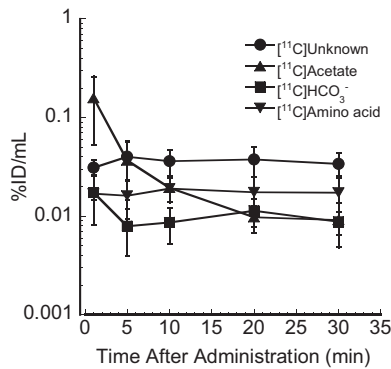


Fig.2 Kinetics of radiometabolites derived from benzyl [1-<sup>11</sup>C]acetate in arterial plasma. %ID/mL: % of injected dose/mL plasma. Cited from [3].

### Comparison study with immature rat by [1-<sup>14</sup>C]BA

The cerebral main energy fuel is converted from ketone bodies to glucose during an infant's development (post neonatal) and astrocytic oxidative metabolism might change in the development process. We compared the kinetics of [1-<sup>14</sup>C]BA in mature (8-week-old) and immature (3-week-old) rats. The radioactivity and washout rates of [1-<sup>14</sup>C]BA in brain tended to be lower in immature rats than in mature rats in all regions (Fig.3). Although additional detailed studies are needed using various age rats, this result implies that astrocytic oxidative metabolism is changing during the development process.

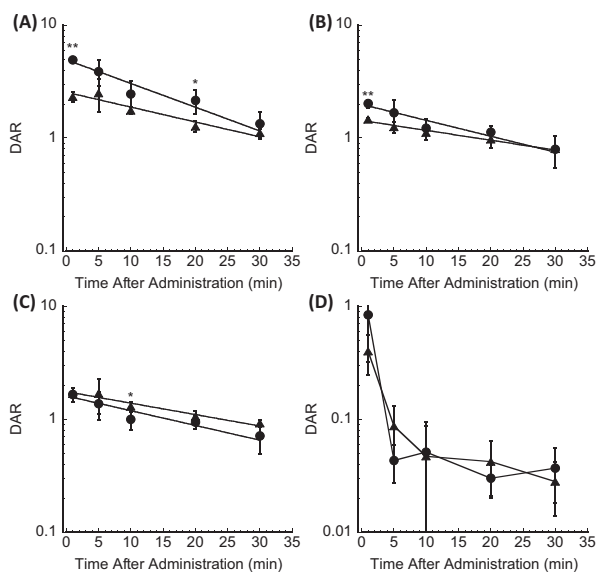


Fig.3 The time-radioactivity curves of [1-<sup>14</sup>C]BA in mature (●) and immature (▲) rats. (A) cortex, (B) cerebellum, and (C) pons. (D) the parent compound in the blood. DAR: % of injected dose/g tissue × body weight (g)/100. Cited from [3].

### The washout rate of [1-<sup>14</sup>C]BA in status epileptic model rat by simplified two-time point autoradiography

Astrocytic oxidative metabolism is associated with several neuronal diseases such as Alzheimer's disease, epilepsy, and ischemia. We measured the washout rate of [1-<sup>14</sup>C]BA in status epileptic (SE) model rat by a simplified two-time point quantitative autoradiographic method since the radioactivity of [1-<sup>14</sup>C]BA in normal rat brain decreased in a single-exponential manner. In several brain regions, SE model rats showed a higher radioactivity than control rats, although the washout rates were not different between the SE model and control rats in all regions studied except for the medial septal nucleus. Although SE model rats did not show any significant difference in washout rates, this method could be applied to other neuronal disease model animals to measure an abnormality resulting from disease.

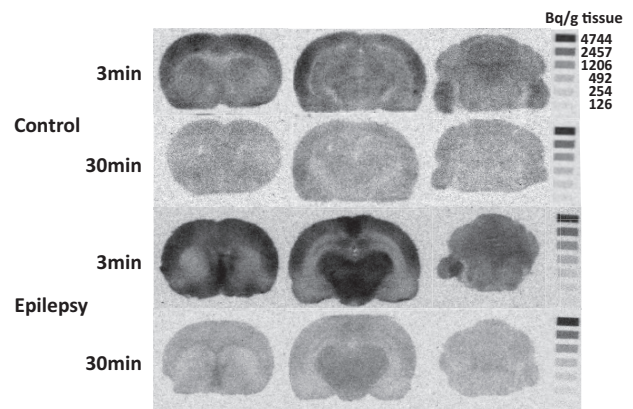


Fig.4 Typical quantitative autoradiograms of [1-<sup>14</sup>C]BA at 3 and 30 min after injection in control and SE model rats. Cited from [3].

### Conclusion

We compared the cerebral kinetics of [1-<sup>14</sup>C]BA and [2-<sup>14</sup>C]BA for quantitative assessment of astrocytic oxidative metabolism. [1-<sup>14</sup>C]BA showed single-exponential kinetics regardless of the labeling positions, but the washout rate of [1-<sup>14</sup>C]BA was higher than that of [2-<sup>14</sup>C]BA. Thus, [1-<sup>14</sup>C]BA appeared to be a potential radioprobe for estimating the astrocytic oxidative metabolism with washout rate in rat brain. On the other hand, C-2-labeled acetate might be a more suitable radioprobe for estimating accumulation of amino acids.

### References

- [1] Momosaki S, et al. *Nucl Med Bio*, 34, 939, 2007. doi: 10.1016/j.nucmedbio.2007.06.011
- [2] Okada M, et al., *Appl Radiat Isot*, 78, 102, 2013. doi: 10.1016/j.apradiso.2013.04.025
- [3] Okada M, et al., *J Cereb Blood Flow Metab*, 36, 442, 2016. doi: 10.1177/0271678X15606144

## The DOI detector enables novel PET scanners

**Taiga Yamaya**

E-mail: yamaya.taiga@qst.go.jp

Positron emission tomography (PET) plays important roles in cancer diagnosis, neuroimaging and molecular imaging research. However potential points remain for which big improvements of PET could be made, including spatial resolution, sensitivity and manufacturing costs. For example, the sensitivity of present PET scanners does not exceed 5%. This means that more than 95% of the gamma-rays emitted from a subject are not utilized for imaging. Therefore, research on next generation PET technologies remains a hot topic worldwide.

A depth-of-interaction (DOI) detector, for which various positioning methods have been studied, will be a key device to get any significant improvement in sensitivity while maintaining high spatial resolution (Fig.1). In order to maintain enough detection efficiency, the scintillation crystals should be 2 cm-3 cm long. In conventional detectors, the crystal thickness causes uncertainty in position identification, which results in degraded spatial resolution at the peripheral area of a field-of-view (FOV). On the other hand, the DOI detector can reduce the parallax error while maintaining the efficiency.

We have developed 4-layered DOI detectors based on the light sharing method [1][2]. One of the successful proofs-of-concept was done in the "jPET" project, in which we developed a brain prototype PET system with the DOI detectors; almost uniform spatial resolution of around 2 mm all over the FOV was obtained using iterative image reconstruction with the geometrically defined system matrix [3].

DOI measurement also has a potential to expand PET application fields because it allows for more flexible detector arrangement. This paper summarizes our development of some novel PET scanners.

### OpenPET: a future PET system for therapy imaging

OpenPET is our original idea to realize the world's first open-type 3D PET scanner for PET-image guided particle therapy such as *in situ* dose verification and direct tumor tracking. The principal of dose verification for particle therapy is based on the measurement of positron emitters which are produced through fragmentation reactions caused by proton or  $^{12}\text{C}$  ion irradiation. Even with a full-ring geometry, the OpenPET has an open gap between its two detector rings through which the treatment beam passes, while conventional positron cameras applied to particle therapy imaging have been basically limited to planner imaging with lower detection efficiency [4]-[6].

Following our initial proposal of the dual-ring OpenPET (DROP) in 2008 (Fig.2 (a)) [7], we finally developed a whole-body prototype of DROP (Fig.2 (b)). The prototype consisted of two detector rings, and each detector ring had two sub-rings of 40 detectors. Each detector consisted of the  $16 \times 16 \times 4$  array



of GSOZ crystals ( $2.8 \times 2.8 \times 7.5 \text{ mm}^3$ ). The portable gantry had a compact design; each detector ring had a 940 mm outer diameter and 171 mm thickness for the detector inner bore of 640 mm diameter and 113 mm axial FOV. Fig.2 (c) shows imaging results of a  $^{12}\text{C}$  beam irradiating a plastic phantom. We also succeeded in visualizing a 3D distribution of beam stopping positions inside the phantom with the help of radioactive beams ( $^{11}\text{C}$  beam and  $^{10}\text{C}$  beam) [8] used as primary beams.

### Helmet-chin PET: a super high-sensitive brain imager

To satisfy a potential demand for brain molecular imaging, prototypes of brain dedicated PET scanners have been developed. However, all previous developments were based on a cylindrical geometry, which is not the most efficient for brain imaging. Making the detector ring as small as possible is essential in PET, because sensitivity can be increased with a limited number of detectors. With appropriate DOI detectors, which reduce the parallax error caused by the thickness of the scintillators, spatial resolution can be maintained, or even improved by reducing the angular deviation effect. Therefore, in collaboration with ATOX Co., Ltd., we developed the world's first helmet-chin PET, in which DOI detectors are arranged to form a hemisphere, for compact, high-sensitivity, high-resolution, and low-cost PET imaging [9].

Our basic idea relies on the evidence that the average sensitivity of hemisphere PET is about 1.5-times higher than that of cylinder PET of the same radius and height, while the required number of detectors is the same for both geometries. In addition, our use of 12% more detectors for "chin detectors", which are placed like a chin strap, improves sensitivity especially

at the central area. In the prototype, 47 block detectors were used to form a hemisphere of 25 cm inner diameter and 50 cm outer diameter, and 7 block detectors were used for the chin strap (Fig.3 (a)). The total number of detectors was about 1/5 of the number to be used in whole body PET. Each detector block was a 4-layered DOI detector, which was the same as the detectors used for the OpenPET. The data acquisition system was developed based on collection of single events. An iterative reconstruction method with detector modeling was applied.

Measured sensitivity was 5% at the cerebellum region and 10% at the parietal region for a standard 400–600 keV energy window, which is more than 3 times higher than commercial scanners. Averaged FWHM of point sources was 3.0 mm (FBP) and 1.4 mm (iterative) (Fig.3 (b)), while commercial scanners have 5 mm or worse spatial resolution.

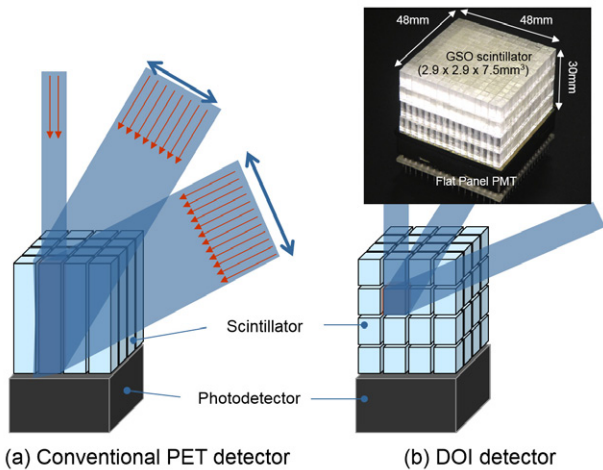


Fig.1 Comparison between a conventional PET detector (a) and our depth-of-interaction (DOI) detector (b). The DOI detector eliminates the parallax error, which is caused by the thickness of the crystals in conventional detectors.



(a)

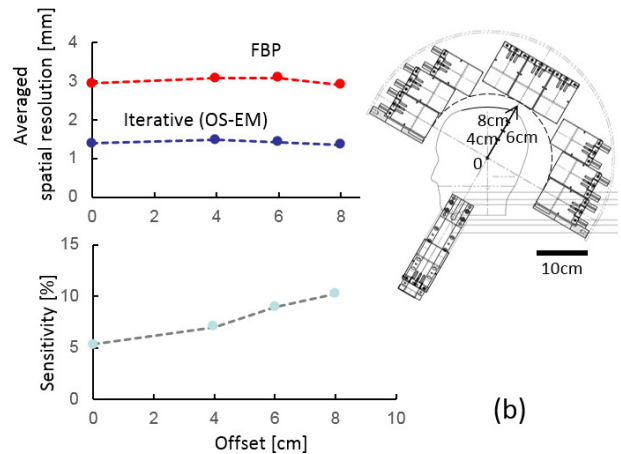


Fig.3 A prototype of the helmet-chin PET (a) for which we successfully obtained excellent sensitivity and resolution performance (b).

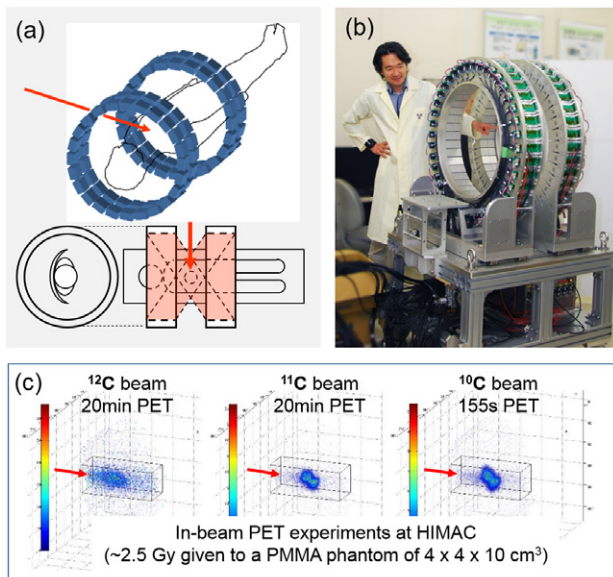


Fig.2 A conceptual sketch (a), the prototype (b) and experimental results (c) of the OpenPET.

**References**

- [1] Murayama H, et al., *IEEE Trans Nucl Sci*, 45, 1152, 1998.
- [2] Inadama N, et al., *IEEE Trans Nucl Sci*, 49, 629, 2002.
- [3] Yamaya T, et al., *IEEE Trans Nucl Sci*, 55, 2482, 2008.
- [4] Pawelke J, et al., *Phys Med Biol*, 41, 279, 1996.
- [5] Iseki Y, et al., *Nucl Instrum Methods Phys Res A*, 515, 840, 2003.
- [6] Nishio T, et al., *Med Phys*, 33, 4190, 2006.
- [7] Yamaya T, et al., *Phys Med Biol*, 53, 757, 2008.
- [8] Urakabe E, et al., *Japan J Appl Phys*, 40, 2540, 2001.
- [9] Tashima H, et al., *IEEE Nucl Sci Sym Conf Rec*, M11-11, 2013.

## Highlight

# Development of a novel method for measurement of dopamine release in brain activation by positron emission tomography

Yoko Ikoma

E-mail: ikoma.yoko@qst.go.jp

## Background and objectives

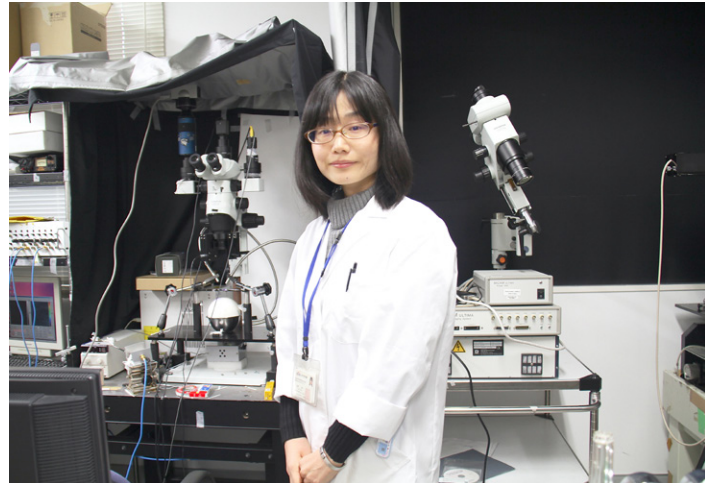
[<sup>11</sup>C]raclopride is an antagonist of dopamine D<sub>2</sub> receptors, and positron emission tomography (PET) with [<sup>11</sup>C]raclopride has been widely used for evaluating the density of dopamine D<sub>2</sub> receptors in the striatum. In addition, binding of administered [<sup>11</sup>C]raclopride to the dopamine D<sub>2</sub> receptors competes with endogenous dopamine. Therefore, regional dopamine release due to pharmacological challenges or neuropsychological tasks can be evaluated indirectly by measuring the changes in binding of [<sup>11</sup>C]raclopride between the baseline and the activated state using PET.

Methods for measuring the changes in binding of [<sup>11</sup>C]raclopride are roughly divided into two approaches. One is the bolus-plus-continuous infusion approach (B/I approach). In this method, after the bolus injection, [<sup>11</sup>C]raclopride is administered continuously to maintain the equilibrium state. The parameter binding potential (BP) represents the binding of [<sup>11</sup>C]raclopride to the dopamine D<sub>2</sub> receptors, and it is estimated by the radioactivity ratio of target and reference regions after a time-activity curve becomes flat, so the quantification process is simple. However, it is often difficult to design an injection protocol to maintain the equilibrium state individually. The other approach uses two independent PET scans with bolus injection in the baseline and activated state (dual-scan approach). In this method, it is not necessary to maintain the equilibrium state, so the injection protocol is easily designed. However, PET scans with bolus injections should be performed twice, before and after the activation, so a long study period is required. In addition, scans are often performed on separate days, so the physiological condition may change. Recently, to shorten the study period for the dual-scan approach, a novel method was developed to measure the changes in the BP by performing a single-session scan in conjunction with multiple injection of [<sup>11</sup>C]raclopride (multiple-injection approach) [1].

In this study, we designed a new PET scan protocol for the measurement of dopamine release using the multiple-injection approach, and we investigated the feasibility of this proposed method. As the first step, we investigated the reproducibility of BP obtained by the multiple-injection approach under rest conditions, and compared it with that of the conventional B/I approach.

## Theory of multiple-injection approach

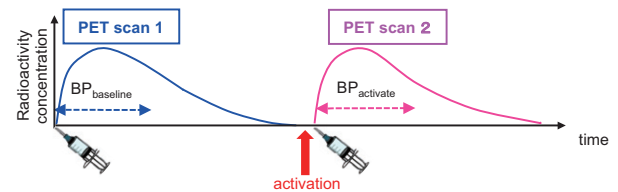
In the conventional dual-scan approach, two PET scans are carried out separately as the baseline and activated state, and the BP is generally estimated by the nonlinear least-square fitting with the model equation derived from the compartment model using the cerebellum as a reference region where the re-



ceptor binding is negligible (simplified reference tissue model; SRTM) [2]. A second PET scan must be performed after the disappearance of the [<sup>11</sup>C]raclopride administered in the first scan, so in general, pharmacological or neuropsychological activation and the subsequent second scan are performed a few hours after the first PET scan (Fig. 1A).

On the other hand, in the multiple-injection approach, the first injection is performed at the same time as scanning is started, and pharmacological or neuropsychological activation is performed 40–60 min after the first injection even though the radioactivity has not disappeared. Consecutively, the second injection is performed soon after the change of the binding

### (A) Dual-scan approach (conventional method)



### (B) Multiple-injection approach (proposed method)

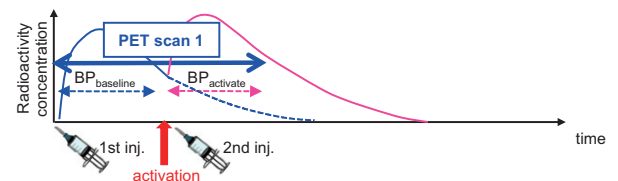


Fig. 1 PET scan protocol of a conventional approach with dual PET scans (A) and the proposed method by a single PET scan with dual injections of [<sup>11</sup>C]raclopride (B).

condition caused by the activation (Fig.1B). BP of the first injection, as the baseline, is estimated by the usual SRTM using data points measured before the activation, and  $BP_{ND}$  of the second injection, as the activated state, is estimated using data points measured after the second injection by taking account of the residual radioactivity of the first injection at the time of the second injection. In this estimation of the second injection, BP is estimated from the model equation which is the same as the usual SRTM, except that the initial condition at the injection time is not zero.

### PET human study

To evaluate the reproducibility of BP estimates by the multiple-injection approach, PET studies with [ $^{11}C$ ]raclopride were performed on ten healthy volunteers by both the multiple-injection approach and B/I approach under rest conditions (Fig.2). In the multiple-injection approach, BPs of the striatum as two rest conditions ( $BP_1$  and  $BP_2$ ) were estimated from frames for 0 to 40 min and 45 to 85 min using the SRTM that takes into account the residual radioactivity of the first injection after the second injection. Meanwhile, in the B/I approach,  $BP_1$  and  $BP_2$  were estimated from the striatum/cerebellum radioactivity ratio for 40 to 52 min and 68 to 100 min, respectively. In both approaches, the reproducibility of  $BP_{ND}$  was evaluated by the mean of the absolute difference (AD) (Eq. 1) between  $BP_1$  and  $BP_2$  for the ten healthy volunteers.

$$AD = \frac{|BP_1 - BP_2|}{(BP_1 + BP_2)/2} \quad (1)$$

Figure 3 shows typical time-activity curves (TACs) for the striatum and cerebellum obtained from the multiple-injection and B/I approaches.  $BP_1$  and  $BP_2$  were estimated from these curves. As a result, although both approaches gave a small value for the mean of AD (MAD) between  $BP_1$  and  $BP_2$ , the MAD of the multiple-injection approach was slightly smaller than that of the B/I approach (Table 1), and it was comparable to the MAD of two separate scans with a bolus injection reported previously [3]. BP values estimated by the multiple-injection approach agreed well with those by the B/I approach.

In the B/I approach, the TACs often had not reached equilibrium even after 40 min in spite of the continuous infusion of [ $^{11}C$ ]raclopride, resulting in lower reliability of BP estimates. On the other hand, in the proposed multiple-injection approach, although the nonlinear-least square fitting is required for the estimation of BP, the injection protocol is simpler and the scan period is shorter.

### Summary

We proposed a multiple-injection approach to estimate the changes in the binding of [ $^{11}C$ ]raclopride due to dopamine release from a single session of PET scanning. This approach provided reliable BP estimates with high reproducibility, suggesting a possibility of multiple-injection approach for evaluating the dopamine release due to neuropsychological tasks. We are now investigating the sensitivity of changes in the BP caused by the neuropsychological tasks using this multiple-injection protocol.

Table 1 Mean value of binding potential for the first and second resting state ( $BP_1$  and  $BP_2$ ) and mean absolute difference (MAD) between  $BP_1$  and  $BP_2$  for ten healthy volunteers.

	Multiple-injection approach	B/I approach
$BP_1$	$2.26 \pm 0.21$	$2.32 \pm 0.11$
$BP_2$	$2.26 \pm 0.22$	$2.32 \pm 0.15$
MAD (%)	$2.4 \pm 1.8$	$4.0 \pm 2.4$

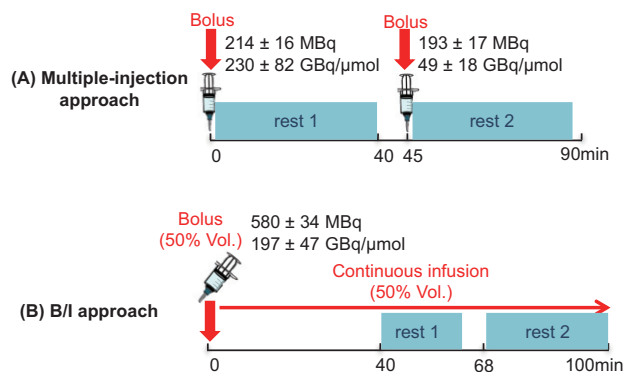


Fig.2 Injection protocol of multiple-injection approach (A) and B/I approach (B) for PET scans with [ $^{11}C$ ]raclopride for ten healthy volunteers.

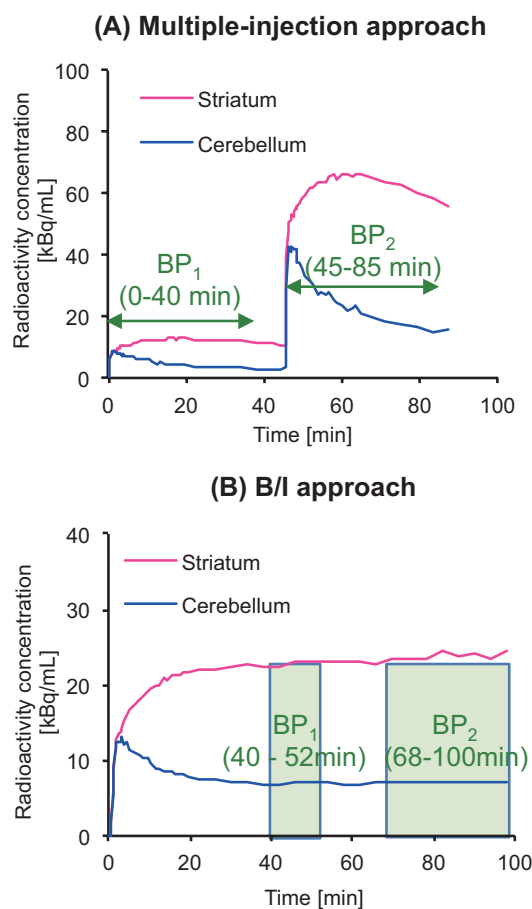


Fig.3 Time-activity curves for the striatum and cerebellum obtained by multiple-injection approach (A) and B/I approach (B).

### References

- [1] Ikoma Y, et al., *NeuroImage*, 47, 1639, 2009.
- [2] Lammertsma AA, et al., *NeuroImage* 4, 153, 1996.
- [3] Kodaka F, et al., *Eur J Nucl Med Mol Imaging*, 40, 574, 2013.

## Clinical research on the PET/CT imaging of cancer hypoxia

Tsuneo Saga

### Introduction

When cancer tissue outgrows its vascular supply, cancer cells are exposed to a hypoxic environment. The presence of hypoxic areas within cancer tissue is one of the major causes of resistance to treatment such as radiotherapy and anti-cancer agents. Furthermore, cancer cells acquire a more aggressive nature during their adaptation to the hypoxic environment. The information on cancer hypoxia, therefore, is very important for the management of cancer patients, such as the selection of appropriate treatment strategies depending on the grade of hypoxia and radiation treatment planning, in which a higher radiation dose is administered to hypoxic areas within the cancer tissue. Positron emission tomography/computed tomography (PET/CT) using hypoxia-seeking probes is suitable for the quantitative evaluation of cancer hypoxia in patients. At present two kinds of probes are mainly used for PET imaging of hypoxia in cancer patients; one is a nitroimidazole compound and the other one is Cu(II)-diacetyl-bis(*N*<sup>4</sup>-methyl-thiosemicarbazone) labeled with positron emitting copper radioisotopes. F-18 labeled fluoroazomycin arabinoside (FAZA, Fig.1) is a second generation nitroimidazole compound designed to have improved kinetic properties: faster uptake in hypoxic tissue and faster clearance from normoxic tissue. We have performed clinical research studies of PET/CT with FAZA in patients with lung cancer and head and neck cancer in order to evaluate the clinical value of FAZA uptake in tumors focusing on its prognostic impact.

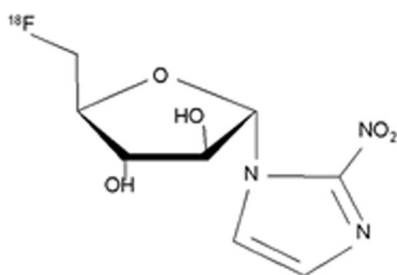


Fig.1 Chemical structure of FAZA.



### FAZA PET/CT for lung cancer patients

Clinical research on lung cancer patients was performed in collaboration with the Cancer Institute Hospital, Japanese Foundation for Cancer Research. Clinically suspected locally advanced non-small cell lung cancer (NSCLC) patients underwent PET/CT with FDG, a marker of accelerated glucose metabolism in cancer tissue, and with FAZA. Uptake of PET probes in the primary lesion and lymph node (LN) metastasis (maximum value of standardized uptake value for FDG and tumor-to-muscle uptake ratio (T/M) for FAZA) was compared with the outcome of the patients (progression-free survival: PFS) determined by clinical follow up. Various clinical parameters were also compared with the prognosis of the patients.

Figure 2 shows representative images of CT, FDG PET/CT and FAZA PET/CT indicating that intratumoral distribution patterns of FDG and FAZA are not identical to each other.

In all patients (stage III + stage IV), both the clinical stage (stage IV versus stage III,  $p = 0.017$ , Kaplan-Meier with log-rank test) and FAZA T/M in LN metastasis ( $T/M > 1.85$  versus  $T/M \leq 1.85$ ,  $p = 0.001$ ) were significant predictors of PFS. In contrast, FDG uptake parameters were not significant predictors of PFS. In a subgroup of patients with stage III NSCLC who were treated with chemoradiotherapy (CRT), FAZA T/M in LN metastasis was the only significant predictor of PFS ( $T/M > 1.85$  versus  $T/M \leq 1.85$ ,  $p = 0.016$ ). These results suggest that, in patients with advanced NSCLC having LN metastasis, FAZA uptake in LN metastasis, not in the primary lesion, is a prognostic indicator; these results also emphasize the importance of evaluating the character of LN metastasis in the case of advanced NSCLC [1]. Fig.3 reproduces CT and FAZA PET images for a patient with stage IIIB lung squamous cell carcinoma showing high FAZA T/M in LN metastasis who developed a recurrence after CRT and died of the disease.

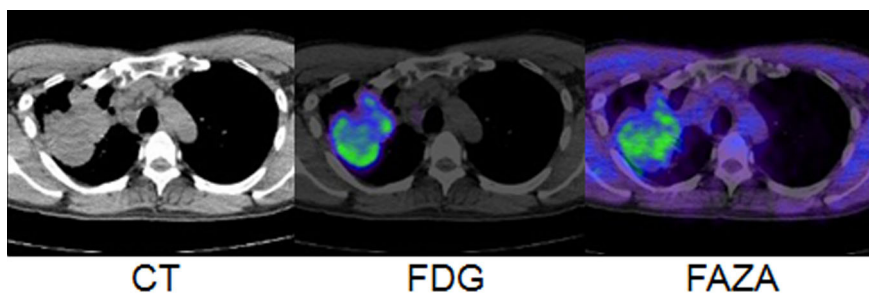


Fig.2 CT, FDG PET/CT and FAZA PET/CT images of a patient with large cell carcinoma of the right lung.

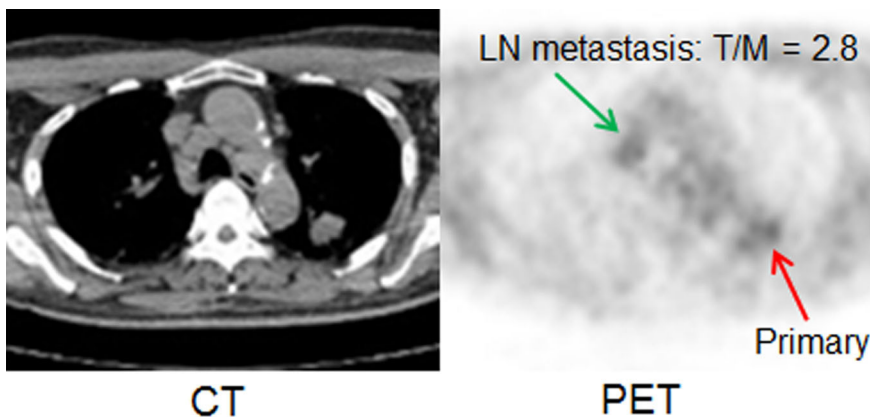


Fig.3 CT and FAZA PET images of a patient with stage IIIB lung squamous cell carcinoma.

#### FAZA PET/CT for head and neck cancer patients

Clinical research studies on head and neck cancer patients were performed in collaboration with the Department of Diagnostic Radiology and Radiation Oncology, Graduate School of Medicine, Chiba University. Patients with head and neck squamous cell carcinoma (HNSCC) underwent FAZA PET/CT before being treated with CRT. FAZA uptakes (T/M) in the primary lesions and LN metastasis were compared with various clinical parameters. FAZA and clinical parameters were then correlated with the PFS of the HNSCC patients.

FAZA T/M in the primary lesion showed a significant positive correlation with the maximum tumor diameter of the primary lesion and was significantly higher in stage IV lesions than in stage I – III lesions. Comparison of PET and clinical parameters with PFS showed that FAZA T/M in the primary lesion was the only significant predictor of PFS (T/M > 1.565 versus T/M ≤ 1.565,  $p = 0.010$ ). On the other hand, maximum tumor diameter and clinical stage were not significant predictors. These results suggest that, although the grade of hypoxia increased with the increase in tumor size and disease stage, FAZA uptake is a more reliable indicator of tumor hypoxia and is a useful predictor of treatment outcome [2].

Figure 4 reproduces FAZA PET/CT and PET images for a patient with high FAZA primary T/M who developed liver metastasis after CRT.

#### Conclusion

In conclusion, results from the present clinical studies on FAZA PET/CT for lung cancer and head and neck cancer patients have shown that the FAZA PET/CT performed prior to treatment can provide important information on prognostic

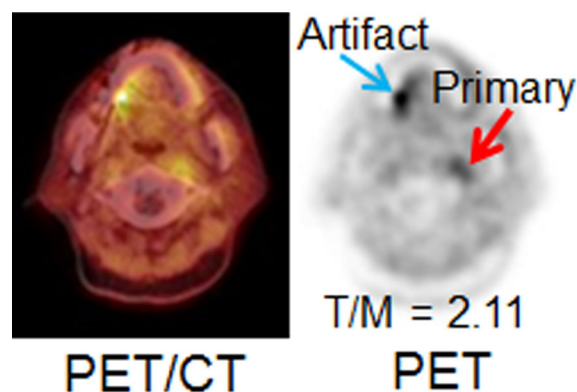


Fig.4 FAZA PET/CT and PET images of a patient with epipharyngeal cancer.

stratification of cancer patients that can be used for the selection of appropriate treatment strategies depending on the grade of cancer hypoxia.

#### References

- [1] Saga T, *et al.*, *Cancer Sci*, 106, 1554, 2015.
- [2] Saga T, *et al.*, *Ann Nucl Med*, 30, 217, 2016.

## Highlight

# Integrin $\alpha_6\beta_4$ -targeted imaging of pancreatic cancer model using a radiolabeled or fluorophore-labeled antibody

U Winn Aung

E-mail: winn.aung@qst.go.jp

## Background and objectives

Pancreatic cancer is a deadly malignancy because of its nonspecific symptoms, resulting in delayed diagnosis, and limited therapeutic options. The treatment outcomes of this disease are not yet fully satisfactory and the 5-year survival rate is low. Exploration of suitable molecular markers and imaging probes to assist in an early and specific diagnosis of pancreatic cancer is still necessary. An experimental imaging technique targeting these biomarkers would pave the way toward the development of therapeutic strategies and clinical management.

A family of adhesion molecules, integrins, form various heterodimer transmembrane proteins that mediate cell-cell and cell-extracellular matrix interactions, and they are involved in cancer progression, including adhesion, migration, invasion, proliferation, survival, and metastasis [1]. Among the integrins, we focused on integrin  $\alpha_6\beta_4$  ( $\alpha_6\beta_4$ ). According to the literature,  $\alpha_6\beta_4$  integrin is often highly expressed in pancreatic cancer cells, whereas it is rarely expressed in pancreatitis and normal pancreatic cells [2]. In addition,  $\alpha_6\beta_4$  overexpression is observed in early stages of pancreatic adenocarcinoma, termed as pancreatic intraepithelial neoplasias (PanINs), and has held high expectation as an early biomarker [2]. We recently isolated a fully human monoclonal IgG1 antibody against  $\alpha_6\beta_4$ , designated as ITGA6B4, from a large-scale human antibody library constructed using a phage-display system and screened using living pancreatic cancer cells [3]. In our study, we proposed the  $\alpha_6\beta_4$  integrin as a good target for pancreatic cancer and we realized two molecular imaging modalities using a radiolabeled or fluorophore-labeled ITGA6B4, and assessed their potential feasibility for pancreatic cancer imaging in an animal model. We labeled ITGA6B4 with indium-111 ( $^{111}\text{In}$ ) for single-photon emission computed tomography (SPECT) and near-infrared (NIR) fluorophore indocyanine green (ICG) for near-infrared fluorescence imaging.

## Integrin $\alpha_6\beta_4$ expression in human pancreatic cancer cell lines

Various levels of  $\alpha_6\beta_4$  integrin expression in four human pancreatic cancer cell lines were examined with Western blotting and flow cytometry (Fig. 1). Western blot analysis demonstrated a high expression of  $\beta_4$  and  $\alpha_6$  integrin subunits in BxPC-3 and AsPC-1 cell lines, a relatively low expression in MIAPaCa-1 and PANC-1 cell lines, and negligible expression in a mouse cell line A4. These results were consistent with membranous  $\alpha_6\beta_4$  expression measured by flow cytometry after overnight incubation with fluorescein-ITGA6B4. To provide the proof of concept, the BxPC-3 cell line which showed high expression of  $\alpha_6\beta_4$  was used as a representative  $\alpha_6\beta_4$ -positive cell line, and the A4 cell line was used as its negative counterpart.

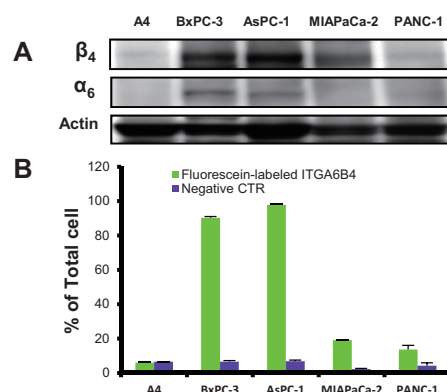


Fig. 1 (A) Expression of  $\beta_4$  and  $\alpha_6$  integrin subunits in 4 human pancreatic cancer cell lines, examined by Western blotting. Mouse cell line A4 was a negative control. (B) Percentages of  $\alpha_6\beta_4$  (+) cells are compared by flow cytometric analysis

## Cellular binding and biodistribution of $^{111}\text{In}$ -labeled antibody in tumor-bearing mice

We labeled ITGA6B4 with  $^{111}\text{In}$ , using a chelating agent CHX-A<sup>-</sup>-DTPA and evaluated its cellular binding. This probe highly and specifically bound to BxPC-3 cells but not to A4 cells. BxPC-3 cell binding increased in a cell concentration-dependent manner. According to the biodistribution results,  $^{111}\text{In}$ -DTPA-ITGA6B4 accumulation in BxPC-3 tumor was 2.28% ID/g at 1.5 hours after injection, gradually increased with time and reached 46.11% ID/g at 96 hours. Meanwhile,  $^{111}\text{In}$ -DTPA-ITGA6B4 accumulation in A4 tumor was 7.35% and 9.90% ID/g at 1.5 and 96 hours, respectively.

## Visualization of tumor by SPECT/CT imaging with $^{111}\text{In}$ -labeled antibody

We performed longitudinal SPECT imaging of the mouse bearing tumors at 1.5, 24, 48, 72, and 96 hours after injection

of  $^{111}\text{In}$ -DTPA-ITGA6B4. Markedly higher radioactivity was observed in BxPC-3 tumor compared to A4 tumor. At 48, 72, and 96 hours, BxPC-3 tumor uptakes were 28.4, 38.8, and 43.2% ID/g and A4 tumor uptakes were 10.0, 9.2, and 9.1% ID/g, respectively (Fig.2A). The probe accumulation patterns in tumors were in line with biodistribution results. Immediately after SPECT imaging at 96 hours after injection, a frozen section of BxPC-3 tumor displayed high radioactivity in autoradiography (ARG) (Fig.2B) and enhanced  $\alpha_6\beta_4$  immunohistochemical (IHC) staining in tumor cells, especially at the edge of the tumor-stromal interface (Fig.2C). No specific radioactivity and  $\alpha_6\beta_4$  staining were observed in the A4 tumor section. Taken together, these findings validated the probe specific binding to  $\alpha_6\beta_4$ .

### Visualization of tumor by NIR fluorescence imaging with ICG-labeled antibody

Mice bearing subcutaneous tumors were intravenously injected with ICG-ITGA6B4 and imaged at the indicated time points (1.5, 24, 48, 72, and 96 hours after injection). At 24 hours, the fluorescence intensities (FIs) of both tumors increased, and BxPC-3 tumors were more clearly visualized than A4 tumors. The BxPC-3 tumor FI was fairly well retained until 96 hours, whereas that of A4 tumors decreased during this period (Fig.3A). Moreover, in ex vivo imaging of tumors and tissues obtained from euthanized mice, BxPC-3 tumor FI was clearly identified and observed to be considerably higher than that of A4 tumors and other tissues. Post-imaging fluorescence microscopy of frozen sections confirmed the  $\alpha_6\beta_4$  specific binding of the probe in BxPC-3 tumors (Fig.3B).

### Summary and future expectations

When targeted molecular imaging approaches are used to detect and delineate pancreatic cancer lesions from the surroundings, the presence of adequate level of accessible tumor-specific targets is crucial. And, the expectation for increasing the pancreatic cancer cure rate depends on the early detection and eradication of preinvasive lesions such as PanINs. As mentioned,  $\alpha_6\beta_4$  is overexpressed and displays altered localization

in the early stages of PanIN. Thus, their earlier detection would raise the likelihood of a cure. Here, we could demonstrate a high expression of  $\alpha_6\beta_4$  integrin in certain pancreatic cancer cell lines, suggesting that  $\alpha_6\beta_4$  integrin is a desirable target for the diagnosis of pancreatic cancer, and  $\alpha_6\beta_4$  status could be detected by NIR imaging and nuclear imaging via ICG-labeled or radiolabeled antibody against  $\alpha_6\beta_4$ . The significantly increased accumulation of these probes in tumors might be specifically associated with  $\alpha_6\beta_4$  expression and specific binding of the probe.

Nowadays, radioimmunotherapy using an antibody labeled with an appropriate radioisotope ( $\beta^-$  and  $\alpha$  emitter) to deliver cytotoxic radiation to a target cell is increasingly acknowledged as useful for internal radiotherapy. Thus, a radiolabeled antibody directed against  $\alpha_6\beta_4$  would also be a favorable candidate for a theranostic agent. In like manner, photodynamic therapy is an advanced alternative molecular-targeted cancer therapy and an ICG-labeled antibody is attractive because ICG is one of the prospective dyes that could be used as an effective photosensitizer. Moreover, the ICG-labeled probe emits fluorescence signals in the NIR range (700–1000 nm). This is ideal for in vivo imaging because of the minimal light absorption, scattering, and autofluorescence in this range. Therefore, the ICG-labeled probe could be used in a real-time intraoperative or endoscopic/laparoscopic setting to facilitate the surgical removal of pancreatic cancer because it can delineate the tumor margin. Although radionuclide-based and NIR imaging techniques/probes still have their own pros and cons, the ability to noninvasively visualize and quantify the high tumor binding of our nuclear and optical probes with specific targeting to  $\alpha_6\beta_4$  in a pancreatic cancer model may provide a strong potential tool for diagnosis and selection of therapeutic strategies for personalized therapy in the future.

### References

- [1] Desgrosellier JS, et al., *Nature Rev Cancer*, 10, 9, 2010.
- [2] Cruz-Monserrate Z, et al., *Mod Pathol*, 20, 656, 2007.
- [3] Kurosawa G, et al., *Proc Natl Acad Sci USA*, 105, 7287, 2008.

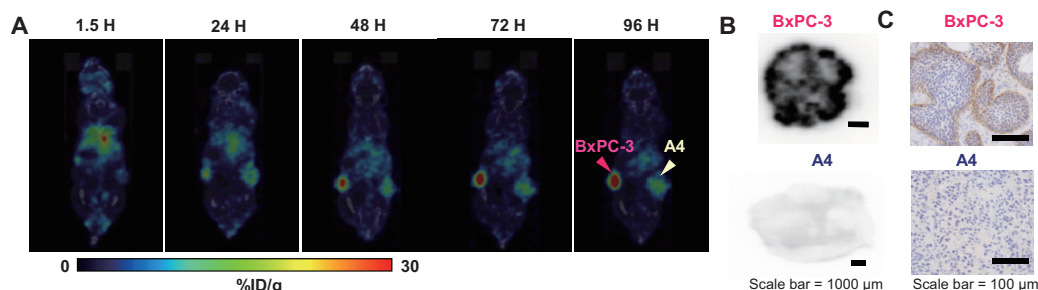


Fig.2 (A) Serial SPECT/CT images of a mouse bearing xenografted target tumor (BxPC-3, pink arrowhead) and nontarget tumor (A4, white arrowhead) (B) At 96 hours, a frozen BxPC-3 tumor section showed high radioactivity on the ex vivo autoradiographic image, whereas A4 tumor showed no specific radioactivity. (C) Immunohistochemical staining of adjacent sections displayed strong  $\alpha_6\beta_4$  staining in BxPC-3 tumor cells but not in A4 tumor cells.

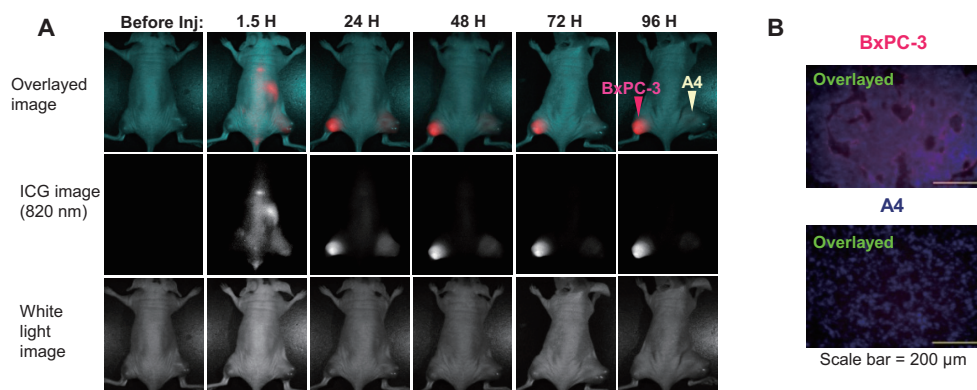


Fig.3 (A) Serial NIR fluorescence imaging of a representative mouse bearing xenografted target tumor (BxPC-3, pink arrowhead) and nontarget tumor (A4, white arrowhead) (B) At 96 hours after injection, fluorescence microscopy examination of a frozen tumor section was done by fusing the ICG fluorescence image (pink) and DAPI nuclear staining image (blue).

## Highlight

# PET Quantification of tau pathology in human brain with $^{11}\text{C}$ -PBB3

Yasuyuki Kimura, Masanori Ichise

E-mail: kimura.yasuyuki@qst.go.jp,

ichise.masanori@qst.go.jp

## Summary

- We have established methods for quantification of tau pathology using  $^{11}\text{C}$ -PBB3 considering entrance of radiometabolites into the brain.
- With blood data, a dual-input graphical analysis model successfully estimated binding potential,  $BP_{\text{ND}}^*$ , which reflects a regional amount of tau pathology.
- Without blood data, an original multi-linear reference tissue model ( $\text{MRTM}_0$ ) offers suitable quantification for  $^{11}\text{C}$ -PBB3 when a patient can be stably scanned for 60 min.
- If motion of a patient hampers the dynamic data, SUVR-1 estimated from 20-min scan data for 30–50 min can be used as an alternative method for the quantification.

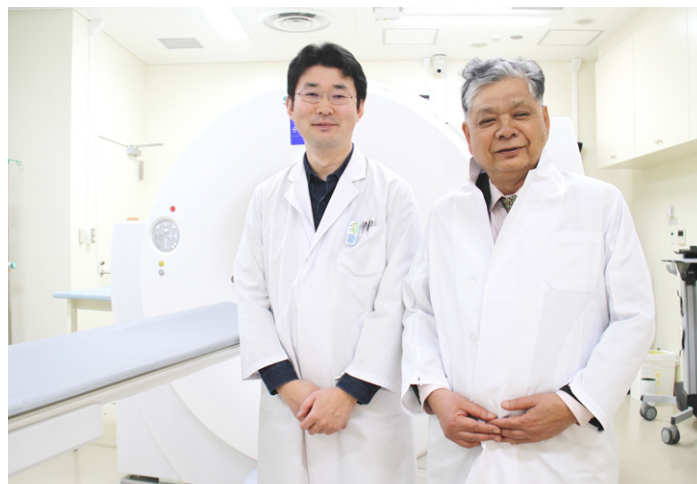
## Introduction

In Alzheimer's disease (AD) and other tauopathies, tau accumulation is a pathological hallmark in the brain. Tau pathology is closely related to the neural death and cognitive dysfunction in those diseases. Quantitative visualization of tau pathology in humans can be a powerful tool, both as a diagnostic aid and a monitor for potential therapeutic interventions.

For PET tau imaging, we developed a radioligand,  $^{11}\text{C}$ -PBB3 (2-((1*E*,3*E*)-4-(6-( $^{11}\text{C}$ -methylamino)pyridin-3-yl)buta-1,3-dienyl)benzo[*d*]thiazol-6-ol) [1].  $^{11}\text{C}$ -PBB3 binds reversibly to neurofibrillary tau tangles with high affinity and selectivity in vitro, and  $^{11}\text{C}$ -PBB3 PET studies have reflected the known pathological tau distribution at various stages of AD patients in vivo.

However,  $^{11}\text{C}$ -PBB3 studies in humans and mice indicated that  $^{11}\text{C}$ -PBB3 is rapidly converted to a major radiometabolite in plasma, and a significant amount of the radiometabolite has been shown to enter the mouse brain, which complicates quantitative PET data analysis [2].

We established methods of PET quantification of tau pathology with  $^{11}\text{C}$ -PBB3 considering the entrance of its radiometabolites into the human brain. We employed a dual-input model [3] that uses the unmetabolized parent and the radiometabolite in the plasma for input functions. We found that a parameter, the standardized uptake value ratio minus 1 (SUVR-1), and a reference tissue model binding parameter ( $BP_{\text{ND}}^*$ ) gave results that agreed with those of the dual-input model  $BP_{\text{ND}}^*$ , supporting the validity of these simplified models in quantifying tau pathology with  $^{11}\text{C}$ -PBB3 PET.



## Methods

Seven AD subjects and seven healthy (HC) subjects underwent dynamic  $^{11}\text{C}$ -PBB3 PET scanning. Arterial blood was sampled to obtain the parent and metabolite input functions. Quantification of  $^{11}\text{C}$ -PBB3 binding was performed using dual-input models that take the brain metabolite activity into consideration, traditional single-input models without such considerations, and a reference tissue model ( $\text{MRTM}_0$ ) and SUVR-1. The cerebellar cortex was used as the reference tissue for all methods.

## Quantification Models

### Dual-input model

We estimated  $^{11}\text{C}$ -PBB3 binding parameters,  $BP_{\text{ND}}^*$  (see below for its definition), in two ways using the dual-input graphical analysis model developed by Ichise et al. [3]. This graphical model is derived from the dual-input compartment model [3]. The graphical model has the following two operational equations both of which allow estimation of  $BP_{\text{ND}}^*$  when the system reaches transient equilibrium between the brain and plasma compartments:

$$\int_0^t C_b(t) dt = \alpha(t) \int_0^t \frac{C_a^P + C_a^M}{C_b(t)} dt + \beta(t), \text{ and} \quad \text{Eq. 1}$$

$$\int_0^t C_b(t) dt = \alpha^P \int_0^t \frac{C_a^P}{C_b(t)} dt + \alpha^M \int_0^t \frac{C_a^M}{C_b(t)} dt + \beta(t), \quad \text{Eq. 2}$$

where  $C_a^P$ ,  $C_a^M$  and  $C_b$  are the radioactivity concentrations of the plasma parent, radiometabolite, and brain, respectively.  $C_a^{P+M} = C_a^P + C_a^M$ . In Eq. 1,

$$\alpha = [1/(1+\delta)] \alpha^P + [\delta/(1+\delta)] \alpha^M, \quad \text{Eq. 3}$$

where  $\delta$  is the plasma metabolite/parent concentration ratio at equilibrium [3]. In Eqs. 2 and 3,  $\alpha^P$  and  $\alpha^M$  represent the total distribution volumes of the parent ( $V^P$ ) and radiometabolite ( $V^M$ ), respectively. Assuming that the non-displaceable distribution volume of the parent ( $V_{ND}^P$ ) or the radiometabolite ( $V_{ND}^M$ ) is the same in the target and reference tissues,  $BP_{ND}^*$  and plasma binding potential ( $BP_P$ ) are calculated from the  $\alpha$  values of the tau-rich target and tau-free reference tissues as

$$BP_{ND}^* = \frac{V_S}{V_{ND}^P + \delta V_{ND}^M} = \frac{\alpha_{\text{target}}}{\alpha_{\text{reference}}} - 1. \quad \text{Eq. 4}$$

Here, we define the parameter expressed by Eq. 4 as  $BP_{ND}^*$  with an asterisk to distinguish it from the original definition of  $BP_{ND}$ , because  $BP_{ND}^*$  includes an additional metabolite distribution volume term,  $\delta V_{ND}^M$ , in the denominator. We consider  $BP_{ND}^*$  as an extension of the definition of  $BP_{ND}$  because this  $BP_{ND}^*$  is also directly proportional to  $B_{\text{avail}}/K_D$ .

#### Reference tissue model

Reference tissue  $BP_{ND}^*$  estimated without blood data is the (tissue ratio-1) at equilibrium and it is theoretically equivalent to the dual-input  $BP_{ND}^*$  given by  $\frac{V_S}{V_{ND}^P + \delta V_{ND}^M}$ , if the metabolite enters the brain [3]. We used MRTM<sub>0</sub> to estimate  $BP_{ND}^*$  using region of interest (ROI) data and also to generate voxel-wise parametric images of  $BP_{ND}^*$  using the cerebellar cortex as the reference tissue. To evaluate the effect of shortening the scan length,  $BP_{ND}^*$  values from parametric images with truncated scan data (30, 40, 50, and 60 min) were calculated and compared to the  $BP_{ND}^*$  values from the full 70 min scan length.

#### Standardized uptake value ratio

We obtained (SUVR-1) ROI values from the summed PET images for 20–30, 30–50, and 50–70 min scan lengths normalized to the cerebellar cortex.

#### Results

The dual-input graphical model estimated the binding parameter ( $BP_{ND}^*$ ) stably ( $\sim 0.36$  in high binding regions). The MRTM<sub>0</sub>  $BP_{ND}^*$  matched the corresponding  $BP_{ND}^*$  by the dual-input graphical model ( $r^2 = 1.00$ , Figs. 1A and 2). MRTM<sub>0</sub> parametric images of the 60 min scan length showed slight underestimation of  $BP_{ND}^*$  values compared with those with 70 min scan data. SUVR-1 values from sets of 30–50 and 50–70 min scan data slightly overestimated MRTM<sub>0</sub>  $BP_{ND}^*$  values but correlated very well with them ( $r^2 > 0.97$ , Figs. 1B and 2).

#### Conclusions

The results obtained by the dual-input graphical model  $BP_{ND}^*$  were consistent with those by the reference tissue  $BP_{ND}^*$  and SUVR-1, suggesting that these parameters can accurately quantify binding of <sup>11</sup>C-PBB3 despite the entry of its radiometabolites into the brain.

#### Acknowledgements

This research was originally published in *JNM*. Kimura Y, Ichise M, Ito H, Shimada H, Ikoma Y, Seki C, Takano H, Kitamura S, Shinotoh H, Kawamura K, Zhang M-R, Sahara N, Suhara T, Higuchi M: PET Quantification of Tau Pathology in Human Brain with <sup>11</sup>C-PBB3. *J Nucl Med*. 2015;56:1359–1365. © by the Society of Nuclear Medicine and Molecular Imaging, Inc.

#### References

- [1] Maruyama M, et al., *Neuron*, 79, 1094, 2013.
- [2] Hashimoto H, et al., *J Nucl Med*, 55, 1532, 2014.
- [3] Ichise M, et al., *J Nucl Med*, 40, 1902, 1999.

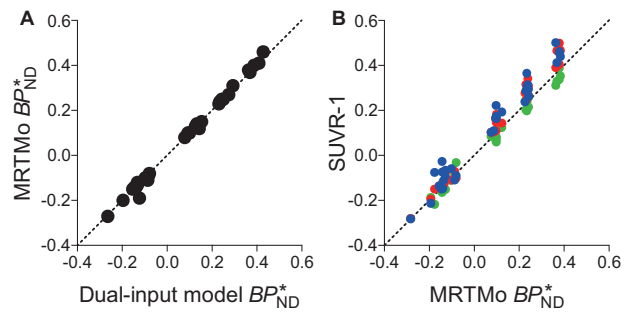


Fig.1 A Correlation of  $BP_{ND}^*$  values estimated by the dual-input graphical model with a combined plasma input and reference tissue model. The  $BP_{ND}^*$  estimated by the MRTM<sub>0</sub> analysis closely matched the  $BP_{ND}^*$  by the dual-input graphical model ( $r^2 = 1.00$ ). B Correlation of  $BP_{ND}^*$  estimated by MRTM<sub>0</sub> and SUVR-1 with the scan data of various lengths. SUVR-1 values with 50–70 min (blue), 30–50 min (red) and 20–30 min (green) data were plotted against  $BP_{ND}^*$  values estimated by MRTM<sub>0</sub> with 70 min data.

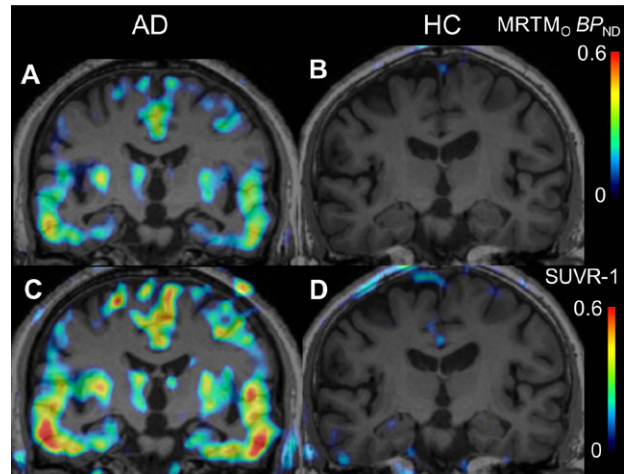


Fig.2 Coronal parametric images of AD and HC subjects. The MRTM<sub>0</sub> was used to estimate parametric  $BP_{ND}^*$  value images in ADs (A) and HCs (B). SUVR-1 images were created by averaging frames of the PET images for 30–50 min in AD (C) and HC (D) subjects.

## Highlight

## Brain circuits involved in vocal tic generation identified in the primate model of Tourette syndrome

Yuji Nagai, Kevin McCairn, Yukiko Hori,  
Erika Kikuchi, Tetsuya Suhara, Masayuki  
Matsumoto, Takafumi Minamimoto

E-mail: nagai.yuji@qst.go.jp,

minamimoto.takafumi@qst.go.jp

### Introduction

Tourette syndrome (TS) is a neurodevelopmental condition that affects about 1 in 100 school-aged children, as well as a significant number of adults. TS is defined by a complex pattern of (semi-)voluntary movements and sounds called “tics”. TS patients often suffer from irrepressible attacks of vocalization, called vocal tics, that range from simple sounds like throat clearing and grunting, to complex vocalization such as swearing (coprolalia), which severely impact quality of life. These symptoms are difficult to manage due to a lack of effective treatments. Although neural mechanisms underlying motor tics have been extensively investigated in macaque monkeys (i.e., motor tic models [1]), the mechanisms of vocal tics remain unexplored because no established animal model exists. For development of new therapies, an animal model that exhibits vocal tics is urgently needed to elucidate the neural mechanisms underlying vocal tic generation. Here we report an acute non-human primate model of vocal tics and identify the brain circuits involved in the symptom by using positron emission tomography (PET) imaging to monitor whole-brain activity during vocal tics [2].

### Disinhibition of the nucleus accumbens generates vocal tics in monkeys

Vocalization of nonhuman primates is controlled by two neural pathways. One pathway includes the anterior cingulate cortex (ACC) that belongs to the limbic loop and the other runs from the primary motor cortex (M1) that constitutes part of the sensorimotor loop. The ACC and M1 are important for vocal control because these regions display readiness potentials preceding voluntary utterances. As far as we know, no studies have generated vocal tics using animal models by affecting the sensorimotor loop in a consistent way. We therefore focused on the basal ganglia, especially the nucleus accumbens (NAc) that has a strong connection to the ACC. We injected a small amount of GABA antagonist bicuculline into the NAc in five monkeys while being guided by X-ray CT in order to disrupt physiological activity in the limbic network (Fig.1). After the injection, monkeys made abnormal and repetitive complex sounds that were comparable to vocalizations observed in normal monkeys described as “grunt” calls [3].

### Abnormal activation in the limbic loop regions during vocal tic manifestation

Next, we aimed at identifying the brain regions following disinhibition of the NAc, and we performed whole-brain PET imag-

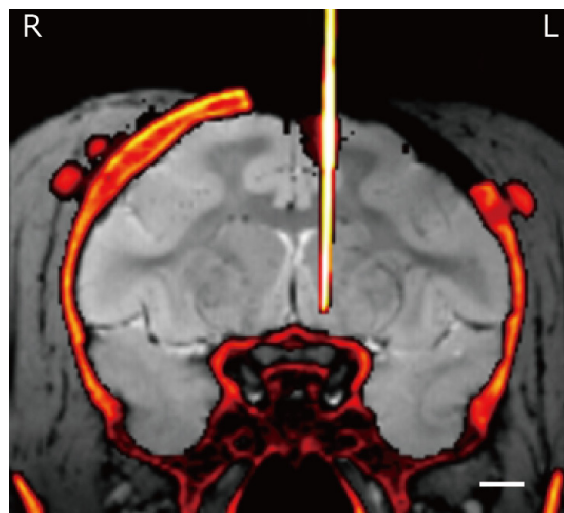


Fig.1 The location of the bicuculline injection cannula targeted as the NAc for inducing vocal tics is shown in a CT/MRI fusion image. Scale bar is 5 mm. R: right, L: left.

ing to measure the regional cerebral blood flow (rCBF) during a period of expression of each tic type in the monkeys. rCBF in the ACC, amygdala, and hippocampus, which are limbic loop regions, was significantly increased in the vocal tic model as compared with the motor tic model (Fig.2, top). On the other hand, the M1 and cerebellum in the motor tic model were significantly activated (Fig.2, bottom). The results were consistent with fMRI studies of TS patients that reported the ACC and

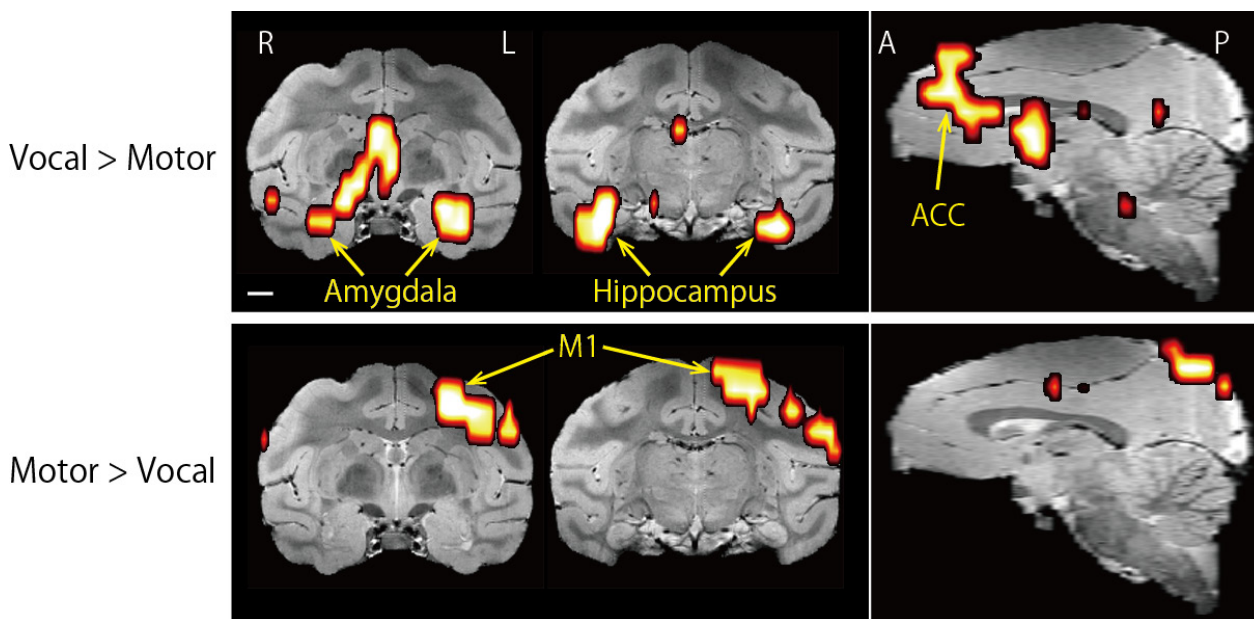


Fig.2 Increased regional cerebral blood flow following bicuculline injection into the NAc contrasted with injection into the putamen (Vocal > Motor, top), and the following bicuculline injection into the putamen contrasted with that into NAc (Motor > Vocal, bottom). The right top panel shows the activation to extend the ACC activation for each condition laid onto sagittal sections. Scale bar is 5 mm. R: right, L: left, A: anterior, P: posterior. Modified from [2].

amygdala are activated during premonitory urge and tic generation [4-6].

To investigate the physiological basis for the increased rCBF in the limbic regions of the vocal tic model, we recorded local field potentials (LFPs) at multiple sites including the NAc, ACC, and M1. After the bicuculline injection into the NAc, LFP spikes, which were defined as an electrophysiological marker of aberrant neuronal discharges, immediately appeared at the injection site and ACC (Fig.3, upper two rows). LFP spikes in the M1 were identified even though their amplitude was small (Fig.3, middle row). It is significant that LFP spikes in three regions had been synchronized. Furthermore, the timing of synchronized spike occurrence matched the timing of vocal tics (Fig.3). These findings led us to propose that vocal tics emerged as a consequence of dysrhythmic activity between critical nodes on the limbic and motor networks including the NAc, ACC, and M1.

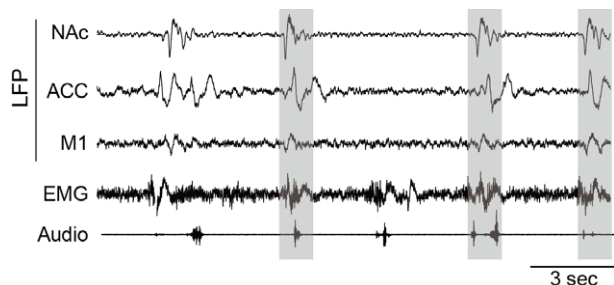


Fig.3 An example of LFP spikes in the NAc, ACC, and M1 recorded from the vocal tic model monkey as well as electromyogram (EMG) and vocal (audio) recordings. Repetitive abnormal neural activities were seen in three regions and vocal tics were evoked at the same time (gray shading).

## Summary

In the present study, we first demonstrated that disinhibition of the NAc by injection of bicuculline into the highly localized NAc of monkeys generated vocal tics acutely and reversibly. PET imaging revealed abnormal activity in the limbic network during the period of vocal tic expression. Electrophysiological investigations revealed that the LFP spikes in ACC, NAc, and M1 had been synchronized and matched the timing of vocal tics. We concluded that a key feature of vocal tic expression is synchronized dysrhythmia across the limbic network. This reproducible model of behaviors in TS provides a way to understand the detailed mechanism of the disease and a unique platform on which to develop new treatments.

This study was performed in an international collaboration (PI: Dr. Kevin McKarin, Korea Brain Research Institute) with researchers at the Primate Research Institute – Kyoto University, RIKEN, Kansai Medical University and Tsukuba University.

## References

- [1] McCairn KW, *et al.*, *Brain*, 132, 2125, 2009. doi: 10.1093/brain/awp142
- [2] McCairn KW\*, Nagai Y\*, *et al.*, *Neuron*, 89, 300, 2016. doi:10.1016/j.neuron.2015.12.025 (\*: co-first author)
- [3] Fukushima M, *et al.*, *J Neurosci*, 34, 4665, 2014. doi: 10.1523/JNEUROSCI.3969-13.2014
- [4] Bohlhalter S, *et al.*, *Brain*, 129, 2029, 2006. doi: 10.1093/brain/awl050
- [5] Neuner I, *et al.*, *Front Hum Neurosci*, 2014. doi: 10.3389/fnhum.2014.00362
- [6] Wang Z, *et al.*, *Am J Psychiatry*, 168, 1326, 2011. doi: 10.1176/appi.ajp.2011.09111692

# Research for Radiation Protection

## Yoshiya Shimada, Ph.D.

Deputy Director of Research Center for Radiation Protection

E-mail: shimada.yoshiya@qst.go.jp

### 1. Overview

The primary aim of the Research Center for Radiation Protection is to provide a scientific basis for radiation protection and safety. Toward this goal, radiation exposure from various sources is measured, the dose-effect relationships for various endpoints are examined, and the mechanisms underlying the effects are investigated. The Research Center disseminates its research results to promote public understanding of radiation effects and to encourage the enactment of more reasonable regulations concerning the use of radiation. The scope of its activities is not limited to Japan: the Center has been appointed as a Collaborating Center by the International Atomic Energy Agency and the appointment lasts until 2018.

The Research Center consists of the Planning and Promotion Unit, three research programs (Radiobiology for Children's Health Program, Radiation Risk Reduction Research Program, and Regulatory Science Research Program) and the R&D Team for Biospheric Assessment for Waste Disposal.

### 2. FY2015 activities

#### 2.1. Radiobiology for Children's Health Program

##### 1) Background and objectives of research

In this era of low birthrate and prolonged longevity in Japan, concerns about the safety of fetuses and children with respect to radiation protection have been growing. Progressive increases in the use of medical radiation for children have recently forced the ICRP, IAEA and WHO to draft global initiatives on radiation protection of children.

This program carries out studies using mice and rats to provide information on the risk of cancer due to radiation exposure during fetal and childhood periods. Our studies focus on the effects of high linear energy transfer (LET) radiations i.e., neutrons and heavy ions, on fetuses and children. The ultimate objective of this research group is to propose weighting factors for both age-at-exposure and radiation quality to support the framework of radiation protection.

##### 2) Main results

- The relative biological effectiveness of neutrons, from exposure during childhood, was determined experimentally for cancer risk of kidney and brain.
- Experiments were continued to investigate the effect of repetitive radiation exposure, giving reduction factors related to fractionation of radiation exposure for gamma rays.
- Novel findings were made on characteristic mechanisms of carcinogenesis associated with childhood exposure to



- radiation, including genetic mutations and early responses.
- Genomic analysis was conducted, for the first time in the world, on uranium-induced cancer in an animal model and a genetic alteration was found.
- Three articles, to which members of the Program had contributed as authors, were cited in ICRP Publication 131 *Stem Cell Biology with Respect to Carcinogenesis Aspects of Radiological Protection* (2015).

#### 2.2. Radiation Risk Reduction Research Program

##### 1) Background and objectives of research

Susceptibility to radiation-induced malignancies differs depending on the individuals. Variable efficiencies of the DNA repair function resulting from single nucleotide polymorphisms (SNPs) located in genes for DNA repair-related proteins are thought to be one of the factors that cause individual differences in radiation sensitivity. In addition, there is evidence suggesting that individual radiation sensitivity can be modulated by lifestyle practices. These practices include smoking habits which have been shown to elevate an individual's sensitivity to  $\alpha$ -particles. The purpose of this program is to identify factors, whether genetic or epigenetic, causing individual differences in radiation sensitivity, and also to present a possible way to reduce individual radiation risks by artificially regulating these factors.

##### 2) Main results

- More radiation-induced micronuclei were observed in mice administered Japanese rice wine (*sake*) than control mice, with varying degrees in induction of antioxidant activity in the liver depending on the grade of *sake*.
- Results were summarized on DNA damage repair factors Ku80 and Rad52 and candidates of protein markers of radio-sensitivity were listed.

- A combination of mild dietary restriction and radiation-induced adaptive response was effective in reducing genotoxicity of radiation.
- A research perspective was reported to OECD/NEA-CRPPH regarding modification of radiation sensitivity by lifestyle factors including dietary habits.

### 2.3. Regulatory Science Research Program

#### 1) Background and objectives of research

Objectives of this program are to investigate the necessary information for development of radiation safety standards and guidelines and to propose scientifically based measures for radiation regulation and policy aiming at a more reasonable system of radiation protection. For such purposes, the scientific knowledge is processed in a suitable form to apply each practice and to provide it to government regulatory agencies and to society.

#### 2) Results

- Twelve research articles were published regarding protection of radiation from natural sources.
- Information on research needs for the next mid/long-term plan was actively collected from international organizations including ICRP and IAEA.
- To establish grounds for deployment in research and other activities, agreements were concluded on research collaboration with overseas organizations and partnerships were strengthened with governmental administration and educational organizations.
- Experts were dispatched to national councils and other meetings to support setting of standards for radiation safety. For example, in a cross-ministerial meeting on safety of participants in offsite disaster prevention, a proposal was made on training of disaster prevention workers during normal times, which was adopted in the final report.

### 2.4. R&D Team for Biospheric Assessment for Waste Disposal

#### 1) Background and objectives of research

The aim of the team's current project is to provide environmental transfer parameters for radiation dose assessments from radionuclides released from radioactive waste disposal sites. To obtain suitable parameters for the Japanese biosphere, this team has been carrying out three tasks: (1) constructing the database of environmental transfer parameters ( $TF$  and  $K_d$ ) considering climate change; (2) estimating the effects on microbial activities for the transfer parameters of carbon-14 in soil-plant systems; and (3) collecting the environmental transfer parameters of important radionuclides (Pu, Am, Th and Cl) by ultra-high sensitivity analysis.

#### 2) Main results

- Regarding development of analysis methods for trace radionuclides, the recommended temperature for soil sample ashing in the nitric acid leaching method was determined for plutonium, which is applicable to other artificial radionuclides (e.g. strontium-90 and americium-241) in soil samples; for seaweed samples, there is no limitation for the ashing temperature.
- Concentrations of cesium-137 and potassium-40 were measured in leaves of several perennial herbaceous and woody plants and it was clarified that these two radionuclides do not behave similarly in the leaf blade and petiole.

## 3. Summary of main results of the mid-term plan

### 3.1. Experimental research for radiation protection of children

- Information for age-weighting factors of radiation risk was collected through experiments on age dependence of the relative biological effectiveness of carbon ions and neutrons

on life shortening and incidence of breast cancer and on age dependence of the relative biological effectiveness of neutrons on induction of lung cancer, myeloid leukemia, renal cancer and brain tumor.

- Reduction factors related to fractionation of radiation exposure was experimentally determined regarding life shortening of young animals exposed to gamma rays or carbon ions.
- Persistence of uranium exposed during infancy was clarified in a rat model; a novel model was developed in which exposure to uranium induces renal carcinogenesis with an identified genetic mutation.
- As biological grounds for age-weighting factors for radiation risk, distinct mechanisms of carcinogenesis were revealed between infant and adult animals.
- These and other results were presented in international meetings including the WHO Collaboration Center Symposium and the International Congress of Radiation Research and cited in important publications issued by UNSCEAR, ICRP, NCRP and WHO (a cumulative total of 11 citations).

### 3.2. Mechanistic studies aiming at risk reduction

- High calorie diets, drinking alcohol and hormones were shown to be factors that may modify radiosensitivity of mice.
- Two amino acids of Ku80 and 8 amino acids at the C terminus of Rad52 were shown to be candidates of biomarkers for individuals with high susceptibility to radiation-induced carcinogenesis.
- Dietary conditions were identified to be factors that modify efficiency of radiation-induced adaptive response.
- Artemis, a protein for non-homologous end joining, was shown to have a function that may increase mutation frequency in DNA damage response after low-dose radiation exposure.
- Regarding modification of radiation sensitivity by lifestyle factors including dietary habits, future research needs were summarized as a proposal to OECD/NEA-CRPPH.

### 3.3. Regulatory science for bridging the gap between scientific findings and society

- As the main sources of radiation exposure in Japan have been medical radiation and natural radiation even after the Fukushima Daiichi nuclear power plant accident, the current status of, and countermeasures to, natural radiation exposure in Japan were clarified and information on management measures and requirements thereof were conveyed to the regulation authorities.
- Regarding the important issue of risk of radiation at low dose and low dose rate, mathematical models and pooled analysis were used to more precisely estimate radiation risks, by incorporating the latest epidemiological information and parameter values for the Japanese population.
- To support risk communication activities conducted nationwide after the Fukushima Daiichi nuclear power plant accident, information sources and methodologies were developed and published.
- Regarding the environmental effect of the Fukushima Daiichi nuclear power plant accident, exposure levels of wild life and the dose rate of no observed effect were estimated, presenting IAEA with scientific grounds for judging the necessity of environmental protection measures.

## Highlight

# Distribution differences of K and $^{137}\text{Cs}$ in leaf blade and petiole of herbaceous and woody plant leaves

Keiko Tagami, Shigeo Uchida

E-mail: tagami.keiko@qst.go.jp

## Introduction

Large areas in Eastern Japan were contaminated with radiocesium ( $^{134}\text{Cs}$  and  $^{137}\text{Cs}$ ) after the Fukushima Daiichi Nuclear Power Plant (FDNPP) accident. Because of the similar chemical reactivities of Cs and potassium (K),  $^{40}\text{K}/^{137}\text{Cs}$  ratios in aboveground plant tissues are similar. Therefore, it was widely thought that to predict the behavior of radiocesium in plants, K could be used as an analogue of radiocesium for any plant species after uptake through the roots. However, Ban-nai et al. [1] reported that radiocesium concentrations in petiole of three leafy vegetables (lettuce, spinach and komatsuna) were smaller than that in the leaf blade. On the other hand, for sycamore tree, the K concentration in the petiole was found to be higher than that in the leaf blade [2]. These results suggested that petiole and leaf blade would have different K/Cs ratios, which means the elements have different roles in leaves.

In this study, we collected leaves of several perennial herbaceous and woody plants and measured  $^{137}\text{Cs}$  and  $^{40}\text{K}$  concentrations of their leaf blade (LB) and petiole (P) tissues to clarify whether the two elemental distributions were the same or not in other plant species.

## Materials and method

The following plants grown wild on the NIRS campus in Chiba City located ca. 220 km south from the FDNPP were collected at various times from 2012 until 2015: giant butterbur (*Petasites japonicus*, LB and P); Japanese knotweed (*Fallopia japonica*, LB and P); Japanese dock (*Rumex japonicus*, LB and P+S (petiole+stem)); ginkgo (*Ginkgo biloba*, deciduous tree, LB and P); Someiyoshino cherry (*Cerasus × yedoensis* (Matsum.) A.V.Vassil. 'Somei-yoshino' deciduous tree, LB and P); and mochi tree (*Ilex integra*, evergreen tree, LB and P). We have in particular collected giant butterbur regularly since 2012 in the spring. For comparison, we also collected two wild herbaceous plants in Fukushima Prefecture, that is, giant butterbur (LB+P) and *momijigasa* (*Parasenecio delphinifolius*, LB and P+S) in 2013 and 2015, respectively.

Immediately after the collection, plant specimens were transferred to a laboratory and then, each tissue part was separated as shown in Fig. 1. They were separately washed with tap water to remove dust from the surface; this was done in a washing bowl by changing the water 5 times, and then, finally, the samples were rinsed with reverse osmosis water. All samples were oven-dried to a constant weight at 80°C in an electric oven for at least 2 d to decrease the sample volume. Each oven-dried sample was pulverized and mixed well, and then transferred to a 100-mL plastic container.



Radioactivity concentration in each sample was measured by a Ge detecting system (Seiko EG&G) using 50,000–150,000 s counting intervals. A mixed gamma standard solution (Amersham, QCY-46) was used for an efficiency correction. The  $^{137}\text{Cs}$  activity was decay corrected to the sampling date. Potassium analysis was done based on  $^{40}\text{K}$  because the radionuclide is a nearly perfect indicator of stable K.

Concentration ratios for  $^{137}\text{Cs}$  (CR\_Cs) and  $^{40}\text{K}$  (CR\_K) were defined as

$$\text{CR}_{\text{Cs}} = C_{\text{LB-Cs}} / C_{\text{PS-Cs}} \quad \text{.....(1)}$$

$$\text{CR}_{\text{K}} = C_{\text{LB-K}} / C_{\text{PS-K}} \quad \text{.....(2)}$$

where  $C_{\text{LB-Cs}}$  is  $^{137}\text{Cs}$  concentration in LB,  $C_{\text{PS-Cs}}$  is  $^{137}\text{Cs}$  concentration in P (+S),  $C_{\text{LB-K}}$  is  $^{40}\text{K}$  concentration in LB and  $C_{\text{PS-K}}$  is  $^{40}\text{K}$  concentration in P (+S). Then the discrimination ratio (D) of  $^{40}\text{K}/^{137}\text{Cs}$  of LB to P (+S) was calculated as  $\text{CR}_{\text{K}} / \text{CR}_{\text{Cs}}$ , that is,

$$D = (C_{\text{LB-K}} / C_{\text{PS-K}}) / (C_{\text{LB-Cs}} / C_{\text{PS-Cs}}) \quad \text{.....(3)}$$

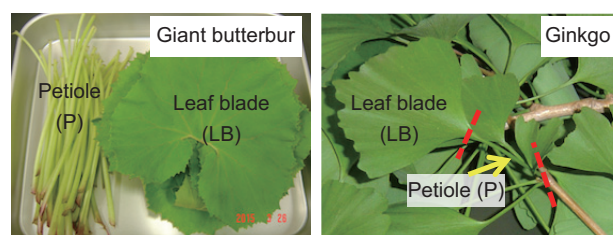


Fig. 1 Leaf blade and petiole samples for giant butterbur and ginkgo.

## Results and discussion

We judged the source of  $^{137}\text{Cs}$  in plants collected at NIRS to be mostly from the FDNPP accident because global fallout  $^{137}\text{Cs}$  in plants was low in Japan before 2011. Since March 2011, we have been able to measure  $^{134}\text{Cs}$  in many plant samples. In this highlight, however, we only report  $^{137}\text{Cs}$  and  $^{40}\text{K}$  results.

The measured concentrations of  $^{137}\text{Cs}$  and  $^{40}\text{K}$  in LB and P samples for giant butterbur are shown in Fig.2 on a dry weight basis. The  $^{137}\text{Cs}$  decreased for both LB and P in 2012–2014, because bioavailability of radiocesium added to the soil should decrease with time after the deposition due to the aging effect. We previously reported the effective half-lives of  $^{137}\text{Cs}$  in giant butterbur tissues from 2011–2014 and found the average value of 446 d [3]. However, when we compared the data from 2014–2015, no statistical differences were observed, that is,  $^{137}\text{Cs}$  concentrations did not decrease from 2014 to 2015. Thus we assumed that the bioavailable  $^{137}\text{Cs}$  amount in the soil did not change much between 2014–2015.

From the results of Fig.2, we saw  $^{137}\text{Cs}$  concentrations in LB were higher than those in P, however  $^{40}\text{K}$  showed a different tendency. Specifically, CR\_Cs and CR\_K were calculated using eqs. (1) and (2), respectively, and the results are shown in Fig.3. The CR\_Cs values were from 1.2 – 2.1, while the CR\_K

values were from 0.49 – 0.70. Then we calculated the discrimination ratio D using eq. (3). If D values are equal to one then the leaf blade and petiole or stem do not discriminate Cs from K, and if the value is lower than one then the leaf blade concentration of K is decreased and/or Cs is enhanced in. The D values were from 0.23 – 0.47 with an average value of 0.35. Thus apparently, K and Cs discrimination was observed in the leaf components, LB and P. One of the reasons for the different  $^{137}\text{Cs}$  and K distributions in these leaf parts might be soil re-suspension onto the plant; however, our previous study of plant tissues from the same sampling sites showed that  $^{137}\text{Cs}$  concentration did not increase by re-suspension of soil onto the giant butterbur LB and P [4]. Therefore, the soil re-suspension effect should be negligible.

To allow us to compare the giant butterbur results with other plant species, further measurements were carried out and the results are shown in Table 1. The only exception was found for mochi tree, an evergreen tree species. Because evergreen tree leaves generally have a longer life than deciduous tree leaves or herbaceous plants have, they might have different physiological chemistry and, consequently, the concentration difference may not be clear between the leaf blade and petiole. Therefore, data for mochi tree leaves are not considered further here.

The CR\_Cs values for plant species were higher than 1 (1.2 – 4.1). The tendency was the same not only for the plant samples collected at NIRS but also for samples collected in Fukushima Prefecture. We also used reported data [1] and calculated the CR\_Cs for comparison; the value ranged from 1.4 – 2.1 showing the same tendency as the present study.

For  $^{40}\text{K}$ , on the other hand, CR\_K values were lower than 1, not only for giant butterbur but also for other plant species, and K concentrations in P were higher than those in LB. The D values were calculated to be lower than 1. These results suggested that Cs and K did not behave similarly in these specific areas of leaf tissues, leaf blade and petiole. We previously reported Cs and K distribution differences between stems and leaves of perennial herbaceous plants; thus Cs and K roles in a plant might be different. From these results we concluded that to understand the detailed radiocesium fate in plants, K measurement results should not be used as an analogue.

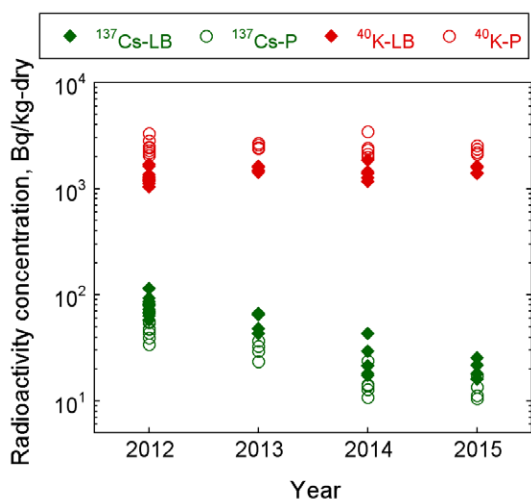


Fig.2  $^{137}\text{Cs}$  and  $^{40}\text{K}$  concentrations change in leaf blade (LB) and petiole (P) in giant butterbur samples collected at NIRS from 2012 to 2015.

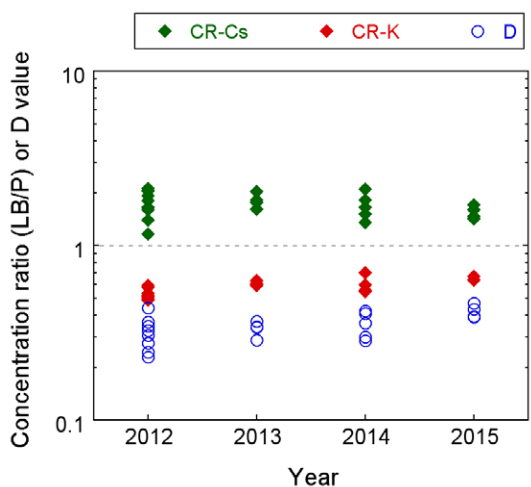


Fig.3 CR\_Cs, CR\_K and D values of giant butterbur from 2012 to 2015.

Table 1 CR\_Cs, CR\_K and D values of seven plant species.

Plant name	Collection date	CR_Cs LB/P(+S)	CR_K LB/P(+S)	D
Japanese Knotweed	3-Sep-14	-	0.40	-
Japanese dock	1-May-15	1.3	0.54	0.41
Giant butterbur <sup>a</sup>	27-Apr-15	1.3	0.84	0.62
Momijigasa <sup>a</sup>	24-May-13	1.2	0.44	0.38
Ginkgo	30-Sep-15	4.1	0.68	0.17
Ginkgo	19-Jul-13	1.2	0.52	0.44
Ginkgo	10-Jul-14	-	0.54	-
Ginkgo	27-Apr-15	-	0.54	-
Someiyoshino cherry	17-Jun-14	2.1	0.95	0.46
Mochi tree	17-Jun-14	0.71	1.0	1.4

<sup>a</sup>Samples were collected in Fukushima Prefecture.

## References

- [1] Ban-nai T, et al., *J Radiat Res* 36, 143, 1995.
- [2] Guha MM, Mitchell RL, *Plant Soil* 24, 90, 1966.
- [3] Tagami K, Uchida S, *J Environ Radioactiv* 141, 138, 2015.
- [4] Tagami K, Uchida S, *Hosyakagaku* 28, 1, 2013.

## Highlight

# The influence of ashing temperature on the determination of Pu in soil and biological samples

Zhongtang Wang, Jian Zheng,  
Keiko Tagami, Shigeo Uchida

E-mail: wang.zhongtang@qst.go.jp

## Introduction

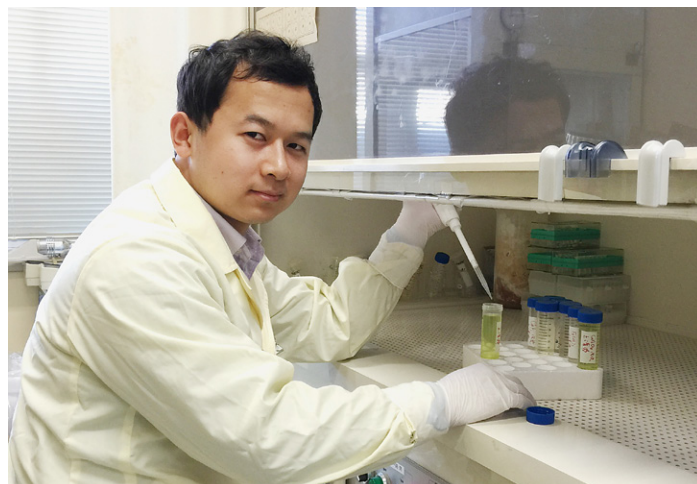
Plutonium is the second element in the transuranium element series. The current existence of Pu in the natural environment is due to human nuclear activities, such as nuclear weapon test explosions, nuclear industry operations and accidental releases. Global fallout, resulting from extensive atmospheric nuclear weapon tests in the last century, is the dominant Pu source in the environment. In recent years, there has been considerable concern regarding the behavior of global fallout Pu in the environment because of the radiotoxicity associated with its alpha-emitting radioisotopes ( $^{239}\text{Pu}$ ,  $^{240}\text{Pu}$ ).

Attention has also been given to using Pu as a tracer to study geochemical processes, for example, soil erosion, sediment dating and desertification studies. In all these applications, an inevitable analytical operation is to transfer Pu from environmental samples (e.g. soil, sediment and biological samples) into a liquid which is compatible with the subsequent chemical treatment. In the literature, many methods have been presented to achieve this, such as, the nitric acid leaching method, total digestion method and alkali fusion method. Among these methods, nitric acid leaching is the most popular one because it is simple, fast and effective. Normally, the nitric acid leaching analytical method consists of four steps: ashing, acid leaching, Pu separation and Pu measurement. The ashing step is intended to destroy any organic matter in the samples that would have a negative impact on the Pu separation step. Different ashing temperatures, from 400 to 900°C, have been used by different researchers. Various ashing temperatures may cause additional uncertainty in Pu analysis. For example, low temperatures may not decompose the organic matter thoroughly, while high temperatures may produce some refractory particles. Therefore, an appropriate ashing temperature should be identified and accepted by researchers to improve the reliability and accuracy of the nitric acid leaching method.

Thus, in this study, efforts were made to investigate the effect of ashing temperature on accurate determination of Pu using the nitric acid leaching method, for soil and biological samples. Furthermore, an optimum temperature was recommended for sample ashing.

## Experimental

One seaweed (IAEA-446) and two soil (IAEA-soil-6 and IAEA-375) standard reference materials were used to in the experiment. 1.5 – 2 g soil samples and approximately 5 g seaweed samples were weighed and ashed in a muffle furnace (FUW 253PA, Tokyo). The ashing temperature was set from 375 to 600°C, and each temperature was used to ash three replicate samples for analysis. After ashing, a well-established



two stage anion chromatographic chemical separation method was utilized for sample preparation [1]. Specifically, 20 mL conc.  $\text{HNO}_3$  was used to leach Pu from a soil sample by heating the sample- $\text{HNO}_3$  mixture in a closed PTFE vessel at 160°C for 4 h. After filtration and adjusting Pu to the tetravalent state, the sample was loaded onto a preconditioned 2 mL AG 1 × 8 resin column, which was subsequently washed with 50 mL 8M  $\text{HNO}_3$  and 30 mL 10 M HCl to remove U, Fe, Pb and Th. Pu was eluted from AG 1 × 8 with 40 mL 0.1 M  $\text{NH}_4\text{I}$ -8.5 M HCl solution, followed by sample evaporation, organic matter decomposition (adding 1 mL aqua regia and heating to dryness, repeated twice) and dissolution in 4 mL conc.  $\text{HCl}/\text{H}_2\text{O}_2$  solution. The sample was then transferred to a preconditioned 2 mL AG MP-1M resin column, where matrix elements like U and Th were further removed by washing with 20 mL 8M  $\text{HNO}_3$  and 8 mL 10 M HCl. Afterwards Pu was eluted from AG MP-1M resin with 16 mL conc. HBr. After the sample was heated to dryness, 1 mL ultrapure  $\text{HNO}_3$  was added and heated to dryness again to remove any trace of HBr. Finally, the residue was dissolved in 0.8 mL 4%  $\text{HNO}_3$  for ICP-MS measurement [2].

## Results and discussion

For soil samples, the Pu analytical results of IAEA-soil-6 and IAEA-375 are plotted in Fig.1 and Fig.2, respectively [3]. In Fig.1, for samples ashed at temperatures not exceeding 450°C, the  $^{239+240}\text{Pu}$  activities were generally consistent with the reported range: 0.96 – 1.11 mBq/g. As the ashing temperature increased, however, an obvious decreasing trend of  $^{239+240}\text{Pu}$  was observed. The lowest activity was found in samples ashed at 600°C, in which only 62% of the Pu was recovered, compared to the certified  $^{239+240}\text{Pu}$  activity (1.035 mBq/g). In contrast to the  $^{239+240}\text{Pu}$  activities, the  $^{240}\text{Pu}/^{239}\text{Pu}$  atom ratios plotted in Fig.1 did not show any significant difference at various ashing temperatures, and all the ratios were within the reported range. This may indicate that no isotopic discrimination occurred during

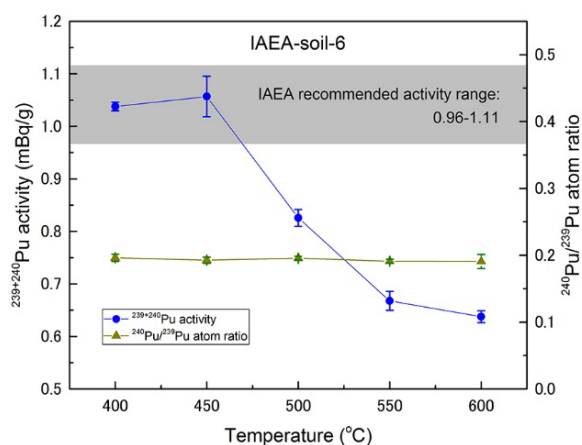


Fig.1 Pu analytical results of IAEA-soil-6 samples treated by the conc.  $\text{HNO}_3$  leaching method (ashed at 400 – 600°C)

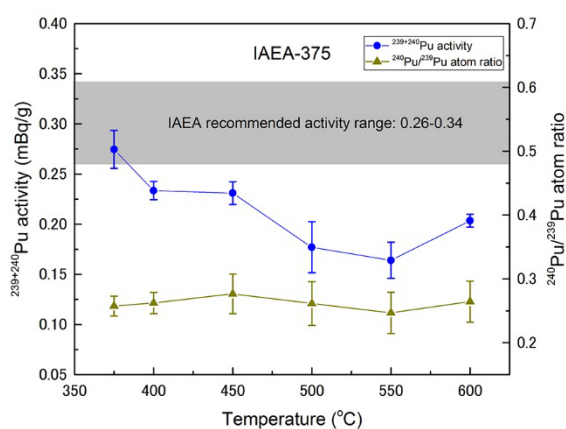


Fig.2 Pu analytical results of IAEA-375 samples treated by the conc.  $\text{HNO}_3$  leaching method (ashed at 375 – 600°C)

ashing, and all Pu isotopes were lost at the same rate. For the IAEA-375 samples, similar tendencies were observed, with the exception of the 600°C ashed samples, which might be slightly influenced by hot particles that had been released from the Chernobyl accident [3]. The lowest Pu activity was found for the 550°C ashed samples, in which only 60% of the Pu was recovered, compared to the certified activity of IAEA-375 (0.30 mBq/g).

As discussed above, both soil standard reference materials had a decreasing trend for  $^{239+240}\text{Pu}$  activity when the ashing temperature exceeded 450°C, indicating that a smaller Pu content was measured in these samples. Since all the experimental conditions were the same except ashing temperature, it was hypothesized that the Pu loss in these soil samples may be attributed to high temperature ashing by forming some refractory fractions in which some portion of the Pu was trapped and could not be leached out by  $\text{HNO}_3$ . To verify this hypothesis, X ray diffraction (XRD) analysis was performed to examine the chemical composition change in soil samples after ashing. The XRD results of non-ashed, 400°C ashed and 600°C ashed soil samples showed that new crystalline phases were generated in the 600°C ashed samples. These new phases were further identified as plagioclase-like silicate materials which are known to be insoluble in  $\text{HNO}_3$ .

To validate the hypothesis, various combinations of leaching/ digesting conditions, including conc.  $\text{HNO}_3$ ,  $\text{HNO}_3\text{-HF}$ , and  $\text{HNO}_3\text{-HF-HClO}_4$ , were utilized to treat IAEA-soil-6 samples after ashing at 550°C. The  $^{239+240}\text{Pu}$  activity obtained from the conc.  $\text{HNO}_3$  leaching method was  $0.67 \pm 0.02$  mBq/g, significantly lower than the reported range: 0.96 – 1.11 mBq/g. For the  $\text{HNO}_3\text{-HF}$  leaching and  $\text{HNO}_3\text{-HF-HClO}_4$  digestion methods, silicate fractions formed during ashing were dissolved by HF, resulting in the  $^{239+240}\text{Pu}$  activity being within the reported range:  $0.96 \pm 0.03$  mBq/g for  $\text{HNO}_3\text{-HF}$  leaching; and  $0.99 \pm 0.02$  mBq/g for  $\text{HNO}_3\text{-HF-HClO}_4$  digestion. Consequently, based on the above discussion, it was confirmed that high ashing temperatures (500 – 600°C), can lead to formation of some refractory silicates which remain insoluble in conc.  $\text{HNO}_3$ , and that results in Pu loss in the  $\text{HNO}_3$  leaching method.

For seaweed samples, only two temperatures were assessed (450 and 600°C), with the results shown in Table 1. For both temperatures, the Pu activities and atom ratios were all consistent with the certified values, indicating that no ashing temperature effect was observed. The contradictory behavior to that of soil samples might be attributed to the different silicate concentrations in soil and seaweed materials. Soil is well to be rich in silicon, with the proportion up to one third, while the silicon fraction in the investigated seaweed sample is only 0.042%. Therefore, for seaweed samples, high temperature ashing (> 450°C) does not lead to Pu loss for the conc.  $\text{HNO}_3$  leaching method.

Overall, the results of soil samples showed less Pu extractability with  $\text{HNO}_3$  when the ashing temperature exceeded 450°C, due to the formation of plagioclase-like refractory fractions. The findings of this study suggest that the temperature for soil sample ashing in the  $\text{HNO}_3$  leaching method should be controlled below 500°C, and 450°C is recommended. This suggestion is also useful for the determination of other artificial radionuclides (e.g.  $^{90}\text{Sr}$ ,  $^{241}\text{Am}$ ) in soil samples. But for seaweed samples, there is no limitation for the ashing temperature.

Table 1 Pu analytical results of the ashing temperature experiment for IAEA-446 seaweed samples (n=3)

Ashing temperature	450°C	600°C	Certified value
$^{239+240}\text{Pu}$ activity (mBq/g)	$0.026 \pm 0.001$	$0.025 \pm 0.003$	$0.024 \pm 0.002$
$^{240}\text{Pu}/^{239}\text{Pu}$ atom ratio	$0.222 \pm 0.003$	$0.230 \pm 0.007$	$0.220 \pm 0.006$

#### References

- [1] Bu W T, Zheng J, Guo Q J, Aono T, Tazoe H, Tagami K, Uchida S, Yamada M, *Environ Sci Technol*, 48, 534, 2014.
- [2] Zheng J, Yamada M, *Talanta*, 69, 1246, 2006.
- [3] Wang Z T, Yang G S, Zheng J, Cao L G, Yu H J, Zhu Y B, Tagami K, Uchida S, *Anal Chem*, 87, 5511, 2015.

## Highlight

# Using genetic analysis to examine T cell lymphomas arising in mice irradiated with carbon ions or gamma rays

Benjamin J. Blyth



## Introduction

One of the key advantages of carbon ion radiotherapy is the reduction of radiation deposition in normal tissue ahead of the target volume. The reduction in second cancer risk associated with this dose reduction is, however, dependent on the relative cancer risk associated with this radiation exposure compared to traditional radiotherapy modalities. In this project [1], we examined T cell lymphomas which arose in mice exposed starting from 1 week old to a mono-energetic carbon ion beam (290 MeV/u) produced at the Heavy Ion Medical Accelerator at Chiba (HIMAC) at the NIRS, such that the whole-body received the low LET (13 keV/μm) deposition ahead of the Bragg Peak recapitulating the exposure of normal tissue ahead of an irradiated tumour. We examined both single exposures of 4 – 4.8 Gy as well as the same total dose delivered over four once-weekly fractions. Our aim was to determine whether the radiation-induced tumours from these exposures showed different cancer-initiating events from tumours arising following a standard gamma ray exposure at the same dose.

## Induction of Lymphomas by Gamma or Carbon Irradiation

When comparing a single exposure of 4 Gy, carbon ions induced a significantly increased frequency of T cell lymphomas (cancer of the thymus originating from immature T cells), with a significantly reduced T cell lymphoma-free lifespan, an indication of a higher RBE for carbon ions, even at the low LET relevant for normal tissue exposure (Fig. 1). The effect of

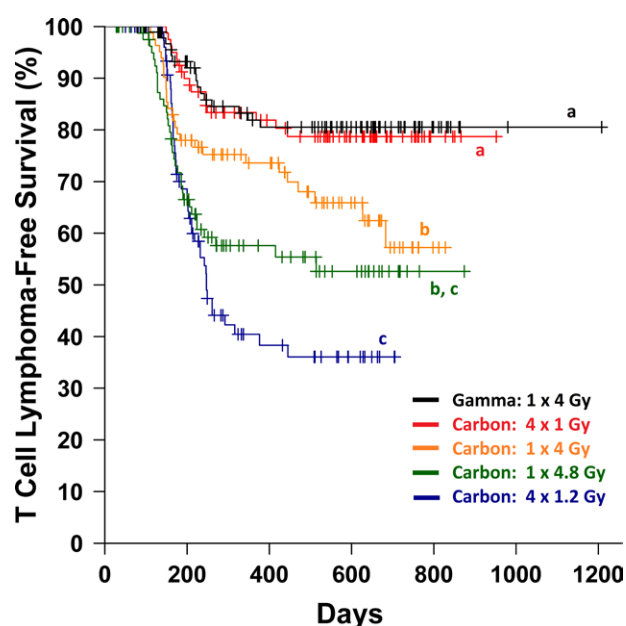


Fig. 1 T cell lymphoma-free survival of mice irradiated with gamma rays or carbon ions. The Kaplan-Meier estimator is plotted for the five irradiation groups with censored cases (causes of death other than TL) marked with crosses. Curves sharing the same letter designation (a, b or c) are not significantly different by pairwise log-rank tests ( $P > 0.05$ ).

fractionation for carbon ion irradiation was complex, with the 4 Gy and 4.8 Gy doses at the inflection point for efficient induction of early lymphomas instead of late-occurring solid tumours. However, when the 4 Gy carbon dose was fractionated mimicking a clinical regimen, the risk was the same as for a single dose of gamma rays, suggesting that normal tissue can be partially protected from second cancers using this method that is routinely employed to prevent acute tissue reactions.

### Genetic Analysis of Tumour Suppressor Genes

We selected T cell lymphomas from a cohort of 100 carbon ion irradiated mice, based on records in J-SHARE (Japan-Storehouse of Animal Radiation Experiments) an experimental and pathology archive of lifetime radiobiology experiments at NIRS. For comparison, we also examined 16 tumours from gamma irradiated mice.

A selection of the carbon tumours (n=20) and all of the gamma tumours (n=16) were examined by whole genome DNA copy number analysis to identify regions of the genome which had suffered deletions or amplification events. Identifying which regions of the genome had been lost allowed us to characterise candidate tumour suppressor genes within the deleted regions. In both carbon and gamma tumours, deletions were identified over regions containing known T cell tumour suppressor genes, including Pten, Bcl11b, Ikzf1, Trp53, Cdkn2a/Cdkn2b and Notch1.

Allelic loss on the chromosomes harbouring Pten, Bcl11b, Ikzf1 and Trp53 genes was then examined across the whole cohort of tumours. Those genes which are known to frequently suffer DNA mutations were also screened by sequencing of mRNA transcripts via reverse-transcription PCR. Many of these gene alterations were mutually exclusive, as they converge on important T cell developmental networks, removing any advantage from multiple hits to the same pathway. Although some significant differences were observed in the frequency of the competing inactivation modes (loss of a Bcl11b allele was more common in carbon tumours, while Pten loss was more common in gamma tumours), on the whole, both radiation types showed cancer-initiating mutations in canonical T cell lymphoma genes.

### Interstitial Chromosomal Deletions

Many of the DNA copy number aberrations were small (less than a few million basepairs) and often occurred within tumour suppressor genes, resulting in loss of gene expression. These are known to arise in many cases by illegitimate recombination events, whereby cryptic signal sequences are recognised by the cell's normal gene rearrangement machinery and undergo unintended recombination events. Larger events included whole chromosome loss, or loss of a chromosome at a break-point to the end of the chromosome. However, it was observed that large interstitial deletions, or a loss of more than 5 million basepairs of DNA from within the chromosome, was more common in the carbon tumours than those from mice irradiated with gamma rays (Fig.2). These deletion events are more complex, requiring the DNA to be broken in two distant locations and for the intervening DNA to be lost before repair of the distant ends. Genes in the middle of a chromosome are normally more resistant to deletion, yet it appears that even at the lower LET in the plateau region, heavy ion irradiation is more effective at inducing these lesions.

Interestingly, most of these large interstitial deletions did not involve any of the T cell lymphoma tumour suppressor genes and are likely hallmarks of the heavy ion radiation exposure, but are not the causal events. This is consistent with radiation acting as a genotoxin to introduce cancer-initiation mutations, as well as a promoter of cells harbouring DNA damage to expand in tissues which need to recover from large-scale radiation-induced cell death.

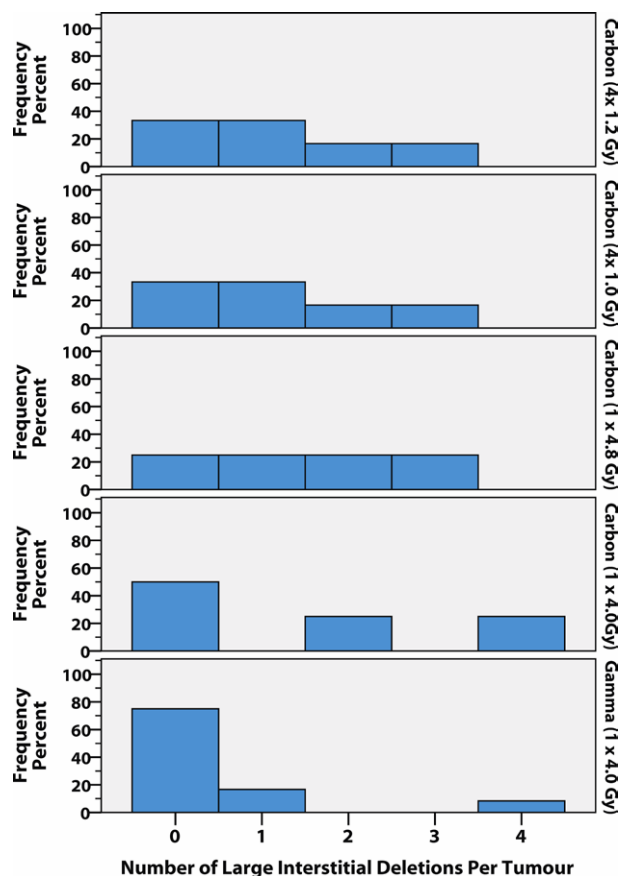


Fig.2 Distribution of large interstitial deletion frequency by irradiation group. The number of large interstitial deletions (>250 kb) per tumour is shown for each treatment group as a percentage of the number of tumours examined by array CGH (n = 4 – 6 per carbon group, n = 12 gamma group).

### Conclusions

The efficacy of strategies to use heavy ion irradiation to spare normal tissues from acute radiotoxicity may also reduce the risk of future second cancers in surrounding normal tissues. However, the benefit depends not only on the dose reduction, but also on the biology of how the heavy ions interaction with healthy tissues to increase cancer risk. We showed here that even at low LET, carbon ions were more effective at causing radiation-induced tumours in a mouse model, and that they may harbour unique signatures of the exposure. However, we also saw that for this tumour type, the initiating events were similar to those after photon irradiation, and that large interstitial deletions might be an additional risk for second cancer induction, but was not the primary cause of tumour suppressor gene loss. Future studies in other tumour types and for alternative exposure parameters will help establish these lesions as bone fide markers of heavy ion exposure.

### Reference

[1] Blyth BJ, *et al.*, *PLOS ONE* 2015. doi: 10.1371/journal.pone.0130666

## Highlight

# The influence of age at exposure on genetic alterations in radiation-induced mouse T-cell lymphomas

Masaaki Sunaoshi



## 1. Introduction

It has been considered that children are more sensitive to radiation-induced cancer than adults, because i) children's tissues and organs are growing and developing rapidly, and ii) they have more time for radiation-induced tumors to manifest. Epidemiology studies of the atomic bomb survivors from Hiroshima and Nagasaki show that the risk of radiation carcinogenesis is higher in exposed children than adults, with leukemia showing the greatest modification by age. Our animal experiments assessing radiation risk depending on age at exposure show similar results to the human studies. However, the mechanism of the age dependency is still unclear, making it necessary to reveal the molecular mechanisms which increase the risk of radiation carcinogenesis at a young age. However, due to the small number of tumors associated with childhood radiation exposure available for study, the inability to distinguish radiation-induced tumors from spontaneous tumors, and the retrospective nature of such human studies, very little is actually known about molecular characteristics associated with age at exposure. In this study, we examined radiation-induced T-cell lymphomas, a mouse model of human acute lymphoblastic leukemia, as a way to investigate any molecular mechanisms that might be dependent on the age at exposure.

In this highlight, we show that age at irradiation might influence the targets and mechanisms of tumor suppressor gene inactivation in radiation-induced T-cell lymphomagenesis, or favor particular tumor pathways due to age-specific selection pressures [1].

## 2. Results

### 2.1. T-cell lymphoma incidence

To characterize age-specific molecular changes in tumors, we analyzed T-cell lymphomas induced by 1.2 Gy whole-body X-ray irradiation of female B6C3F1 mice for 4 consecutive weeks starting at 1, 4 or 8 weeks of age (Fig. 1). As the thymus continues to grow between birth and puberty, and then begins to atrophy, the three age groups chosen represent the respective growth stages of the thymus and correspond to the infant (1–4 weeks old), adolescent (4–7 weeks old), and young-adult (8–11 weeks old) periods in B6C3F1 mice. The incidences of T-cell lymphoma in infant-, adolescent-, and young adult-irradiation groups were 26% (16/62), 34% (17/50) and 22% (11/50), respectively. The incidence was the lowest in the oldest age group, although the differences among the three age groups (all of which were still young when compared with the average B6C3F1 lifespan of about 124 weeks) were not statistically significant. Furthermore, comparison of other metrics such as lifespan of mice with lymphoma, tumor latency, and tumor

weight did not show statistically significant differences among the three groups.

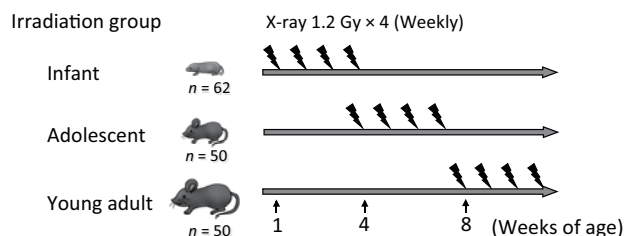


Fig. 1 Experimental design of T-cell lymphoma induction.

Mice were observed daily until moribund, when they were sacrificed by exsanguination under terminal isoflurane anesthesia, and they were assessed for the incidence of T-cell lymphoma.

### 2.2. Age at exposure-dependent distribution of LOH and copy-number alteration in lymphomas

Since loss of heterozygosity (LOH) is frequently accompanied by inactivation of tumor suppressor genes in radiation induced tumors, we determined the frequency of LOH at microsatellite markers flanking the *Cdkn2a* (chromosome 4), *Ikaros* (chromosome 11), *Bcl11b* (chromosome 12) and *Pten* (chromosome 19) candidate tumor suppressor genes implicated in radiation-induced T-cell lymphoma in our previous studies [2]. LOH can occur as a result of chromosomal deletion (with loss of DNA copy number) or recombination/mis-segregation (without copy number change). Thus, to reveal the LOH mechanism, we used array-based comparative genome hybridization (CGH) to distinguish between copy number loss- and copy number neutral-LOH on these chromosomes. In particular, we noted that the nearest markers of *Cdkn2a*, *Ikaros* and *Pten* showed LOH frequencies that differed between infant and young-adult groups ( $P = 0.12$ ,  $P = 0.12$  and  $P = 0.04$ , respectively) (Fig. 2). Since the *Cdkn2a*, *Ikaros* and *Pten* loci showed signs of the

LOH frequency changing with age at exposure, the LOH analysis was extended to markers along the length of chromosomes 4, 11 and 19. Conversely, the *Bcl11b* locus did not show any age-dependent changes in LOH frequency, and thus was not studied further.

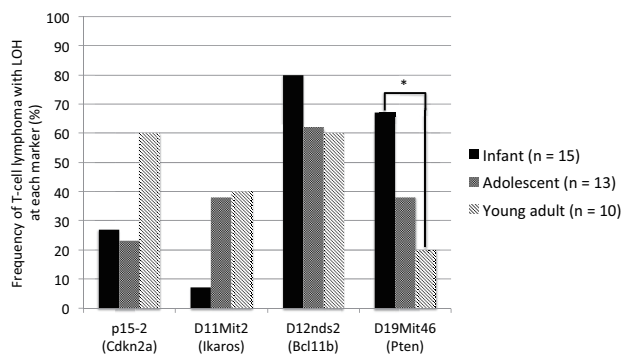


Fig.2 The frequency of LOH at microsatellite markers flanking (downstream) the *Cdkn2a*, *Ikaros*, *Bcl11b* and *Pten* loci. \*Showing significant difference between infant- and young adult-irradiation group ( $P = 0.04$ ).

LOH on chromosome 4 always included the marker nearest *Cdkn2a* and was either by interstitial deletion (of one or both copies) or copy number-neutral LOH along the whole chromosome. The frequency of LOH or deletions including the *Cdkn2a* locus was higher in the young adult-irradiation group than in both of the younger groups. LOH on chromosome 11 always included the *Ikaros* locus, predominantly by large interstitial deletion (of one or both copies) or deletion extending to the most centromeric marker examined; although, LOH in some tumors was by retention of two copies of chromosome 11 from a single parent. The frequency of LOH or deletions involving *Ikaros* was higher in both of the older groups than in the infant-irradiation group. In all but one tumor, LOH on chromosome 19 always included the *Pten* locus. Interestingly, LOH on chromosome 19 was predominantly via retention of two copies from a single parent, either along the length of the chromosome, or extending from near the *Pten* locus down to the most telomeric marker examined; although, smaller interstitial deletions (of one or both copies) centered on the *Pten* locus were also observed. In contrast to the *Cdkn2a* and *Ikaros* loci, the frequency of LOH at the *Pten* locus was higher in the infant-irradiation group than in the two older groups.

### 2.3. Expression and mutation of IKAROS and PTEN

We examined the expression and sequence of *Ikaros* and *Pten* transcripts by RT-PCR and measured protein levels by western blotting. Mutation frequencies of *Ikaros* (including inactivation of both alleles, a single dominant-negative mutation or unexplained lack of expression) were 33% (5/15), 31% (4/13) and 50% (5/10) in the infant-, adolescent-, and young adult-irradiation groups, respectively. Lack of IKAROS protein was observed in the young adult-irradiation group in particular. In contrast, the mutation frequencies of *Pten* (including inactivation of both alleles or unexplained lack of protein), were 60% (9/15), 38% (5/13) and 30% (3/10) in the infant-, adolescent-, and young adult-irradiation groups, respectively. There were no significant associations between the status of *Ikaros* and *Pten* across the tumors that would indicate either coincidence or exclusivity of the mutation events.

### 2.4. Aberrations in other genes

In contrast to *Cdkn2a*, *Ikaros* and *Pten*, the *Trp53* mutation frequency in lymphomas from all three irradiated groups was low in accordance with previous reports showing a low frequency of *Trp53/TP53* mutation in mouse T-cell lymphoma and human leukemia. Furthermore, frequency of site-specific copy-number alteration did not show any other significant differences depending on age at exposure among the three-irradiation groups. Activating deletions in *Notch1*, deletion of *Bcl11b*, and trisomy of chromosome 15 were frequent events in all three irradiation groups. Copy-number alteration at the various T cell receptor gene loci, indicative of V(D)J recombination-induced rearrangement, was in keeping with the developing T-cell origin of the tumors.

### 3. Summary

The incidence of mouse T-cell lymphoma showed no difference depending on age-at-irradiation. Nevertheless, our findings demonstrate that while deletions on chromosomes 4 and 11 affecting the *Cdkn2a* and *Ikaros* loci are a prominent feature of young adult irradiation-induced T-cell lymphoma, tumors arising after infant irradiation suffer a second hit in the *Pten* gene by chromosome mis-segregation or recombination (Fig.3). This is the first report showing an influence of age-at-exposure on genomic alterations of tumor suppressor genes and their relative involvement in radiation-induced T-cell lymphoma. These data are important for considering the risks associated with childhood exposure to radiation and suggest that the mechanism of carcinogenesis can vary even where cancer incidence does not change.

➤ There was no difference in incidence of T-cell lymphoma among three irradiation groups.

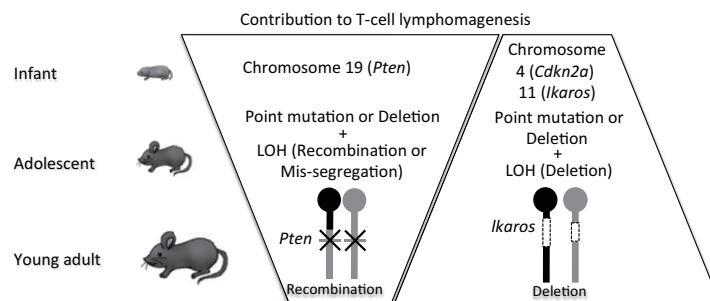


Fig.3 Scheme of contribution of *Pten* and *Ikaros* mutations to T-cell lymphomagenesis. While the incidence of T-cell lymphoma did not show significant difference between three groups, the causal genes and the status of mutation depended on age at irradiation.

### References

- [1] Sunaoshi M, et al., *Mutat Res*, 779, 58-67, 2015.
- [2] Shimada Y, et al., *Radiat Res*, 154, 293-300, 2000.

## Highlight

# Japanese *sake* is a modifier of radiation effects in mouse livers

Tetsuo Nakajima, Guillaume Vares,  
Bing Wang, Mitsuru Neno

E-mail: nakajima.tetsuo@qst.go.jp

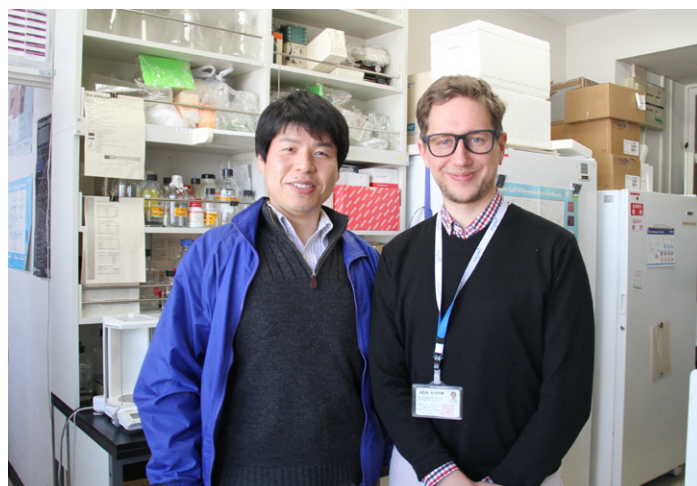
## Introduction

Diet habits or nutrient factors have been demonstrated to influence radiation effects [1, 2]. However, among diet habits, how alcohol drinking habits modify radiation effects remain unclear. Many types of alcohol beverages are consumed worldwide. *Sake* is a traditional alcoholic beverage in Japan that is gaining popularity worldwide. Although *sake* is reported to have beneficial health effects, it is not known whether the habit of drinking *sake* modulates health risks due to radiation exposure or other factors. The liver is the main organ involved in detoxification of harmful substances, including alcohol and it is susceptible to radiation damage. Alcohol is metabolized in the liver, and the resulting metabolic byproducts can impair liver function and cause tissue damage. For this reason, liver metabolites are useful indicators of health status. Here, the effects of chronic administration of *sake* on radiation-induced metabolic alterations in the livers of mice and metabolic markers in serum were evaluated [3].

## Metabolome analysis on effects of sake & 15% ethanol solution on mouse livers

*Sake* (*junmai-shu*) was administered daily to female mice (C3H/He) for one month, and the mice were exposed to fractionated doses of X-rays (0.75 Gy/day) for the last four days of the *sake* administration period. For comparative analysis, another group of female mice were administered 15% (v/v) ethanol in water instead of *sake*, and these mice were exposed to fractionated doses of X-rays (0.75 Gy/day) for the last four days of the 15% ethanol administration period. Metabolites in the liver were analyzed by capillary electrophoresis-time-of-flight mass spectrometry (CE-TOFMS) one day after the last exposure to radiation. In the analyses, a total of 230 metabolites (87 anions and 143 cations) and 245 metabolites (81 anions and 164 cations) were identified in the livers of mice administered *sake* and 15% ethanol, respectively. Principal component analysis (PCA) was performed to reveal differences in the metabolite profiles of the four treatment groups, which consisted of the control, radiation, *sake*, and the combination of *sake* administration and radiation (Fig.1). In the PCA score plot, the group that received a combination of radiation and *sake* was clearly separated from the other three groups by the second principal component (PC2, 18.9% proportion; Fig.1). The metabolite profiles of mice chronically administered *sake* in combination with radiation showed marked changes. On the other hand, in the case of 15% ethanol administration, the group that received a combination of radiation and 15% ethanol was not clearly separated from the other groups along either PC1 or PC2[3].

Using the correlation coefficients between the PC scores



and variables for factor loading, we identified liver metabolites in irradiated mice were affected by *sake* administration. Metabolites that reached significant levels ( $p < 0.01$ ) in the evaluation of positive and negative correlations using the correlation coefficients were selected from the PC2 data from mice treated with a combination of radiation and *sake*. In the selected metabolites, seven metabolites (3-dephospho-CoA, GSH, nicotianamide, cysteine glutathione disulfide, GMP, UMP, and sedoheptulose 7-phosphate) were significantly modulated in the livers of mice treated with radiation and *sake* compared to the levels in the control, and *sake* and radiation alone-treated mice.

We have also demonstrated changes in several metabolites, including methionine and valine, were induced by radiation alone, but they were not detected in the livers of mice who received chronic administration of *sake* [3].

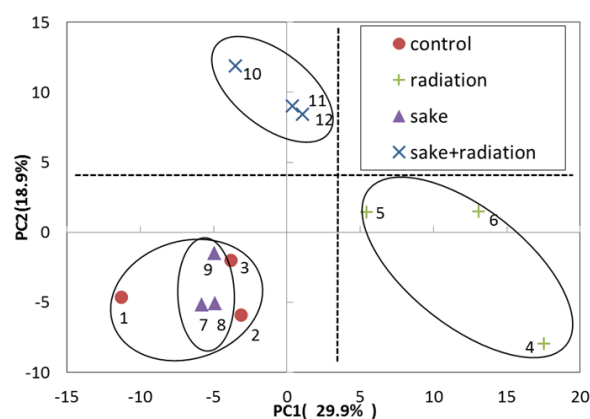


Fig.1 PCA of metabolic data for the combined effects of *sake* and radiation on mouse livers.

### Sake induces anti-oxidative activities in livers

Among the seven selected metabolites that were significantly modulated in the livers of mice treated with radiation and *sake*, GSH is an important regulator of redox homeostasis and GSH/GSSG (glutathione disulfide) is considered to be the major redox couple that determines anti-oxidative capacity. GSSG is the oxidized form of GSH, and the GSH/GSSG ratio is often used as an indicator of the cellular redox state. Here, the levels of GSH and GSSG significantly increased and decreased, respectively, in the livers of mice treated with a combination of radiation and *sake* (Fig.2). The changes in these metabolites were not observed in mice administered 15% ethanol instead of *sake* (Fig.2), suggesting that glutathione metabolism is specifically influenced by the consumption of *sake*.

### Sake and radiation induce decrease in TG

Changes in the serum levels of several metabolic biochemical markers that were accompanied by alterations in liver metabolism in the four treatment groups were also evaluated [3]. In this experiment, the amount of *sake* administered to mice seemed to be excessive because a significant increase of serum TG (triglycerides) in mice administered *sake* alone was observed compared to control mice (Fig.3). Although radiation

alone induced a slight reduction of TG levels, the serum TG level in the treatment group that was administered *sake* was greatly reduced by radiation to the level of the control mice.

The observed reduction of TG by radiation in mice administered *sake* may be in part due to an induction of anti-oxidative responses, as indicated by the increase of GSH in the liver because the alcohol-induced accumulation of TG can reportedly be mitigated by a diet including foods that contain factors that promote anti-oxidative responses.

### Conclusions

Chronic Japanese *sake* consumption induces specific metabolic alterations in the liver in response to irradiation. Although excess *sake* consumption may induce adverse effects on the liver, *sake* intake has the potential to promote anti-oxidative stress activities following radiation exposure in the liver. As many other aspects in the biological modulation of radiation effects by drinking *sake* have to be evaluated more, the findings presented here suggest that moderate *sake* consumption may promote anti-oxidative activity following exposure to stress such as radiation at least in the liver, thereby limiting the adverse effects typically associated with these stresses.

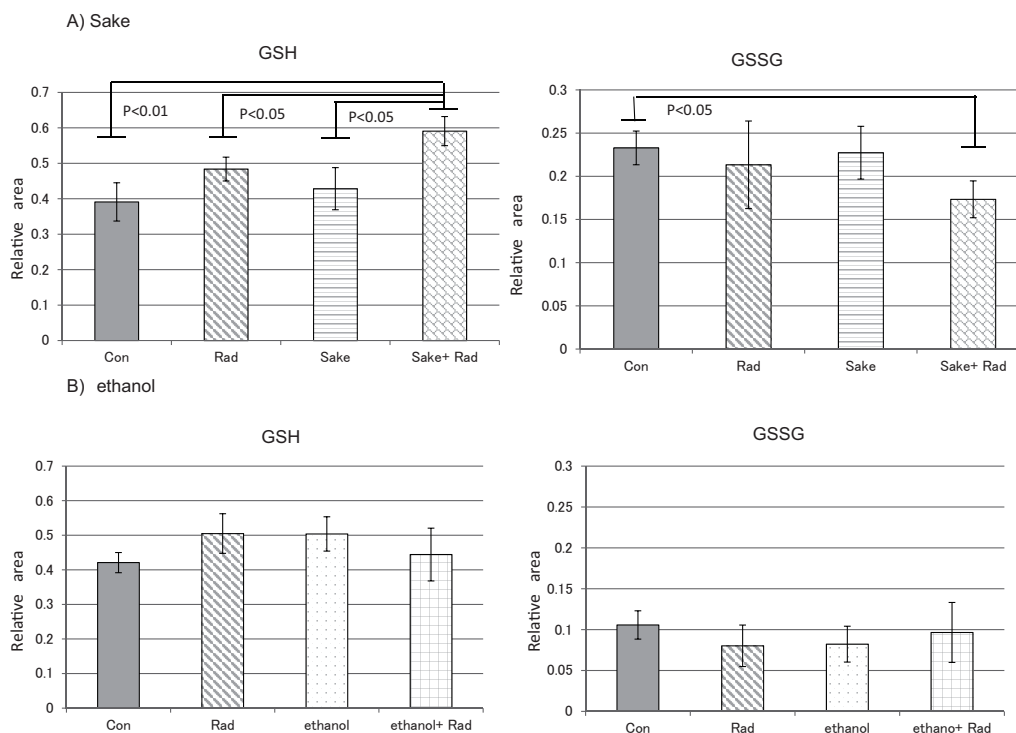


Fig.2 Effects of *sake* or ethanol on radiation-induced changes of GSH and GSSG in mouse livers.

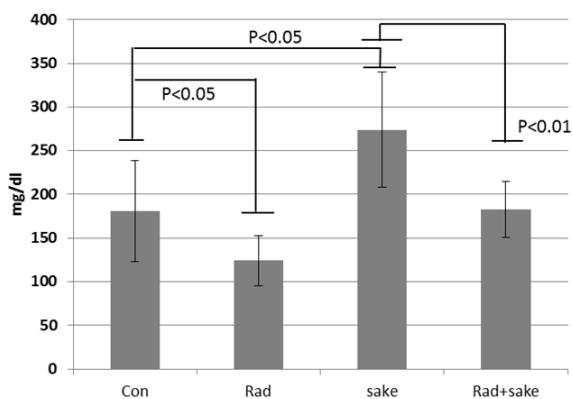


Fig.3 Effects of *sake* on TG (triglycerides) in the serum of irradiated mice.

### References

- [1] Vares G, *et al.*, PLoS One, 9, e0106277, 2014. doi: 10.1371/journal.pone.0106277
- [2] Nakajima T, *Med Sci Monit*, 21, 1721, 2015. doi: 10.12659/MSM.893234
- [3] Nakajima T, *et al.*, PLoS One, 11, e0146730, 2016. doi:10.1371/journal.pone.0146730

## Highlight

## Chronic restraint-induced stress seems to have little Impact on radiation hematopoietic toxicity in mice

Bing Wang, Kaoru Tanaka, Takanori Katsube,  
Yasuharu Ninomiya, Guillaume Vares,  
Tetsuo Nakajima, Mitsuru Neno

E-mail: wang.bing@qst.go.jp

### Introduction

Both ionizing radiation (IR) and stresses cause detrimental effects on humans [1]. Besides possible health effects resulting directly from exposure to IR, a nuclear plant accident is a cause of social psychological stresses (PS). Using a mouse PS model, a recent study showed that chronic restraint-induced stresses (CRIS) attenuated *Trp53* functions and increased carcinogenesis (predominantly lymphomas and sarcomas) susceptibility of *Trp53* heterozygous (*Trp53*<sup>+/-</sup>) animals to total-body  $\gamma$ -irradiation, having a big impact on the academic world and a sensational effect on the public, especially residents living in areas contaminated by radioactive materials from such an accident. It is important to investigate the possible modifying effects from CRIS on IR-induced health consequences in *Trp53* wild type (*Trp53*<sup>wt</sup>) animals. Prior to a carcinogenesis study, effects of total-body X-irradiation (TBXI) on the hematopoietic system under CRIS were investigated on hematological abnormality in the peripheral blood and residual damage in the bone marrow erythrocytes using a mouse PS model [2].

### Materials and Methods

Four-week-old male *Trp53*<sup>wt</sup> C57BL/6J mice were purchased from SLC, Inc., Japan. The mice were acclimatized to the laboratory conditions for 1 week as an adaptation period before use: they were maintained in a clean conventional animal facility under a 12-h light/12-h dark photoperiod. The mice were housed in autoclaved cages with sterilized wood chips, and allowed free access to acidified water (pH = 3.0  $\pm$  0.2) and a standard laboratory chow MB-1 (Funabashi Farm Co., Japan). The mice at postnatal age 5 weeks were randomly assigned to 4 experimental groups, namely, the "control group (C-Gr)" receiving neither restraint nor TBXI, the "restraint group (R-Gr)" receiving only restraint, the "TBXI group (IR-Gr)" receiving only TBXI, and the "restraint and TBXI group ((R+IR)-Gr)" receiving both restraint and TBXI. For the mice in R-Gr and (R+IR)-Gr, the mouse restraint system (Flat Bottom Rodent Holder, RSTR541, Kent Scientific Co., USA) was used for chronic periodic restraint on a daily basis of 6 hours for 28 consecutive days. Individual mice were placed in the strainer and the restrained mice were maintained horizontally in their home cage during the 6-h restraint session (9:30 a.m. to 3:30 p.m.) daily, then the animals were released into the same cage and allowed to access food and water during the free session (3:30 p.m. to 9:30 a.m. the next day). The animals in C-Gr and IR-Gr received no restraint but they were kept from food and water from 9:30 a.m.



to 3:30 p.m. each day. For the mice in IR-Gr and R+IR Gr, they were given an acute TBXI (4 Gy) on the 8<sup>th</sup> day. X-rays were generated with an X-ray machine (Pantak-320S, Shimadzu, Japan) operated at 200 kVp and 20 mA, using a 0.50-mm Al + 0.50-mm Cu filter. The dose rate was at 0.25 Gy/min. The body weight gain of the animals in each experiment group was recorded daily. At the end of the restraint regimen, the animals were euthanized. The peripheral blood hemogram was assessed and the bone marrow micronucleus test was carried out accordingly [3]. Bone marrow smears prepared from both femurs were processed for the enumeration of micronucleated polychromatic erythrocytes (MNPCEs) and micronucleated normochromatic erythrocytes (MNNCEs). The slides were coded to avoid any observer bias. The micronuclei were scored using a light microscope at a magnification of 1000 $\times$ . At least 5000 cells per mouse were counted and the data for each experimental point were from at least 5 mice. All experimental protocols involving mice were reviewed and approved by the Institutional Animal Care and Use Committee of the National Institute of Radiological Sciences (NIRS). The experiments were performed in strict accordance with the NIRS *Guidelines for the Care and Use of Laboratory Animals*. Statistical evaluation of the body weight data was done by 2-way ANOVA. For the other data Student's *t*-test was used except for the micronucleus data where the  $\chi^2$  test was performed. Statistical significance was assigned to a value of P of <0.05.

## Results

Significantly reduced body weight gain by CRIS appeared one day after onset of the restraint, which resulted in the lowest body weight on the 3rd day (Fig.1). After TBXI, significant reduction of body weight gain was observed on the following day in both IR-Gr and (R+IR)-Gr while no interaction (namely, neither synergistic nor antagonistic effect) between the restraint and TBXI was observed. The recovery of body weight gain appeared late in the animals that received the restraint (R-Gr and (R+IR)-Gr). In general, there was a statistically significant difference in the mean body weight between the groups that received the restraint and the groups that received no restraint 1 day after the onset of restraint regardless of the TBXI.

CRIS alone induced a marked decrease in red blood cell (RBC) and white blood cell (WBC) counts, while TBXI caused significant low counts of RBCs, WBCs and blood platelets, and low concentration of hemoglobin regardless of CRIS (Fig.2). CRIS alone did not show any significant effect on erythrocyte proliferation and on induction of micronucleated erythrocytes, while TBXI markedly inhibited erythrocyte proliferation and induced a significant increase in the incidences of micronucleated erythrocytes regardless of CRIS (Fig.3).

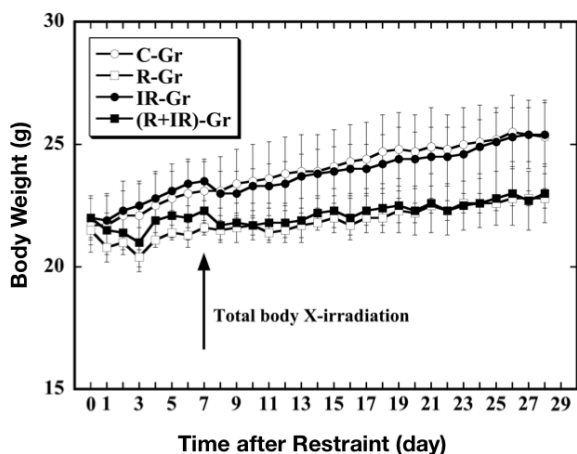


Fig.1 Effect of CRIS and TBXI on body weight gain of mice. Group mean  $\pm$  SD levels of the control group (C-Gr, open circles), the restraint group (R-Gr, open squares), the TBI group (IR-Gr, solid circles), and the restraint and TBXI group ((R+IR)-Gr, solid squares).

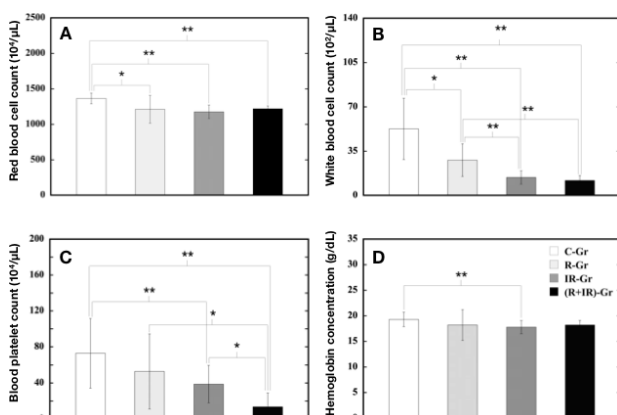


Fig.2 Effect of CRIS and TBXI on the peripheral blood hemogram of mice. Group mean  $\pm$  SD levels of RBC count (A), WBC count (B), PLT count (C), and hemoglobin concentration (D). “\*\*” and “\*\*\*” indicate a significant difference between two groups compared at  $P < 0.05$  and  $P < 0.01$ , respectively.

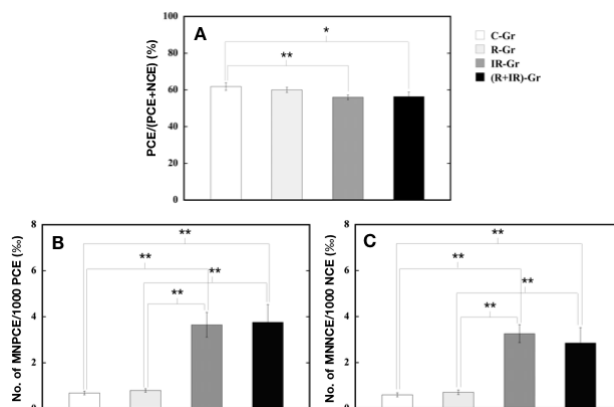


Fig.3 Effect of CRIS and TBXI on the femur bone marrow erythrocytes of mice. Group mean  $\pm$  SD of the percentage of PCEs to the sum of PCEs and NCEs (A), the number of MNPCEs per 1000 PCEs (B), and the number of MNNEs per 1000 NCEs (C). “\*\*” and “\*\*\*” indicate a significant difference between two groups compared at  $P < 0.05$  and  $P < 0.01$ , respectively.

These findings suggest that CRIS does not have a significant impact on radiation-induced detrimental effects on the body weight gain and the hematopoietic system in *Trp53wt* mice.

## Discussion and Conclusion

Results obtained in the present study are consistent with the report on increased susceptibility induced by CRIS for *Trp53<sup>-/-</sup>* mice to radiation carcinogenesis. It should be noticed that although the mice used were of the same strain, *Trp53wt* animals were used in this work. It is known that chronic stresses-induced susceptibility to pathogens and toxicological assaults including IR on health is dependent on the genetics of the exposed organism. Based on these studies and the results obtained in the present work, it was suggested that CRIS would have little influence on sensitivity of *Trp53wt* mice to radiation effects on the hematopoietic system, including the genotoxic effect. The possibility still could not be excluded that the methodology of the present work is not sensitive enough to detect the influence of CRIS on the genotoxic effect in this experimental system. To improve the sensitivity for detection of genomic damage, further study using the fluorescence in situ hybridization technique for detection of chromosome aberrations in splenic cells is in progress.

In summary, the present findings suggest that CRIS does not have a significant impact, neither synergistic nor antagonistic, to modify the radiation-induced detrimental effects on the hematopoietic system in young *Trp53wt* mice under the experimental setup used here. For most people, especially those living in radioactively contaminated areas, the present work may partially allay their concern that stresses could increase the cancer susceptibility to radiation.

## References

- [1] Wang B, et al., *J Radiat Res* (in press. doi: 10.1093/jrr/rw035).
- [2] Wang B, et al., *J Radiat Res* 56, 760-767, 2015.
- [3] Wang B, et al., *J Radiat Res* 54, 45-51, 2013.

## Highlight

# Development of the retrospective animal archive and the international collaboration

**Shin Saigusa**

E-mail: saigusa.shin@qst.go.jp

## Introduction

It is well known that radiation health risk estimations for radiation protection are based on the epidemiological data from the LSS (Life Span Study) of atomic bomb survivors. However, these health effect data are the results of the single- and acute-exposure to relatively high-dose and high-dose rate radiation, and therefore, they require an extrapolation to low-dose and low-dose rate using a reduction factor to apply these values to the practical doses of radiation protection, i.e., over ten mSv order. Though there are no suitable epidemiological data at present, the reduction factor for this purpose is estimated by long-term animal experimental data and numerical model analysis. Therefore, the storage of animal exposure experimental data and the reposition of derivative biomaterials of both previous and present studies are valuable and important.

Archival activities may be categorized into two types, prospective archiving and retrospective archiving. In short, the former includes the archiving activity which is concurrently proceeding with the ongoing studies. Conversely, the latter includes the activity which is archiving the data and materials of terminated studies. The activities described in this report are mainly focusing on the retrospective type of archiving.

The retrospective type of archival and repository activities to digitalize and store the data/materials of long-term animal experiments was started in the early 1990's in institutes of both the US and Europe. These archival activities included the collection and digitalization of the primary data and information (detailed exposure protocols, animal data and pathological diagnosis, etc.) and storage of the experimental materials (paraffin embedded tumor blocks, derivative slides). Data and exposed materials have been correlating to each other by using a common data registry format.

Long term animal experiments have become considerably difficult to perform on a large-scale, because research grants have been reduced and the numbers of investigators, particularly radiation pathologists, have dropped as well. According to the national intellectual infrastructure development plan, NIRS has started to archive its research products as well as the measurement standards.

## Scientific background

Differences between animal data and models adopted in research organizations are reflected on the resulted risk estimates, e.g., National Academy of Sciences – National Research Council estimated the DDREF (Dose and Dose Rate Effectiveness Factor) as 1.5 in its 2006 BEIR VII Report [1] and ICRP (International Commission on Radiological Protection) estimated it as 2 in its 2007 Recommendations [2].



In the early 1990's, in order not to lose valuable information, U.S. and European scientists started an international collaborative project to collect data and store exposed biomaterials. This project, with the cooperation of Japan, has been followed up with a series of successive projects of the EU (e.g., ERA, ERA-PRO, and STORE shown in Fig.1 and the US (Janus Tissue Archive).

Accumulated archival data have been used for radiation risk reanalysis [3] or meta-analysis by compiling different data sets from previous studies and the exposed materials are being provided for checking by recent molecular analysis techniques.

## Development of international network

To enhance the international collaboration, the 1st International Workshop on Sample/Tissue Archiving of Radiobiology (STAR2015) was organized as a satellite meeting of the International Congress on Radiation Research in Kyoto (ICRR 2015) on 24-25 May 2015 and NIRS co-chaired this meeting. The purpose of this workshop was to provide researchers with information about the structure of archive systems worldwide, technology for research analysis of archived materials, and the future possibility to organize an academic network and international research collaboration for sustainability of the archives as the property for the next generation. A total of 26 participants from 4 countries joined this workshop and 14 presentations were made. Table 1 shows the archives and databases introduced in this meeting. It was concluded that this workshop will be organized regularly every 4 years.

## Development of International Radiobiology Archives

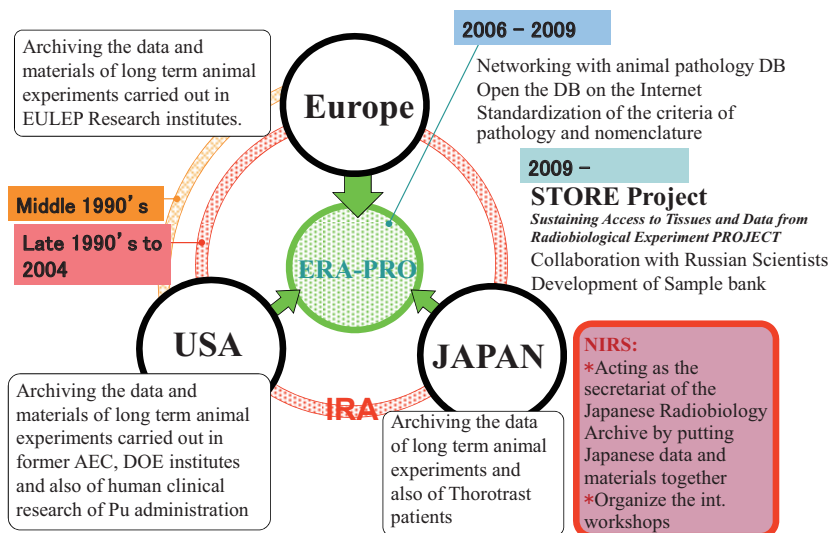


Fig.1 Development of International Radiological Archive.

Table 1 Archives and databases in the world.

Archive	Organization / Country
STORE	Univ. Cambridge, UK
Janus Tissue Archive	Northwestern Univ., USA
The National Human Radiobiology Tissue Repository	USTUR, USA
Chernobyl Thyroid Tissue Bank	CTTB
J-SHARE	NIRS, Japan
Fukushima accident abandoned domestic animals organ archive	Tohoku Univ., Japan
Database on Thorotrast Patient in Japan	Tohoku Univ., Japan
Biological Resources of Radiation Effects Research Foundation	RERF, Japan
Storage of Biosamples from Atomic Bomb Survivors at Nagasaki Univ.	Nagasaki Univ.
Institute for Environmental Sciences	IES, Japan

### Legacy materials to be archived

As a result of reorganization of NIRS, some of the legacy data and biomaterials of the long term animal experiments carried out for well over a decade are expected to be released from the storage management by the institute. Such data and materials are the results of the following studies:

- (1) Radiation-induced myeloid leukemia in C3H/He mice and the effect of prednisolone acetate on leukemogenesis;
- (2) Radiation-induced myeloid leukemia in C3H/He mice calorie restriction reduces the incidence of myeloid leukemia induced by a single whole-body radiation in C3H/He mice;
- (3) Radiation-induced myeloid leukemia in mice exposed to the low dose rate radiation; and
- (4) Radiation-induced tumor in mice exposed to fast neutrons, heavy particle beams and gamma rays.

It is planned that data and materials related to the above studies will be digitalized and redeposited as a part of the retrospective archive in the near future.

### Conclusion

NIRS is now planning to take over several research departments of JAEA (Japan Atomic Energy Agency) and rebuild them into the new organization on 1 April 2016. This reorganization is expected to be accompanied by a wide range of restructuring in both administrative systems and research environments. Such re-organization of the institutions and the related transfer / retirement of the investigators will result in the disposal of the research deliverables. It is important to archive the legacy materials of the past studies systematically and reproduce them for the next generation.

### References

- [1] Committee to Assess Health Risks from Exposure to Low Levels of Ionizing Radiation, National Research Council, Health Risks from Exposure to Low Levels of Ionizing Radiation: BEIR VII Phase 2. National Academy Press, 2006.
- [2] International Commissions on Radiological Protection, 2007 Recommendations of the International Commission on Radiological Protection. *Annals of the ICRP*, Vol.37/No.2-4. Elsevier, 2008.
- [3] Haley BM, et al., *PLoS One*, 10, Dec 9, 2015. doi:10.1371/journal.pone.0140989

# Research on Radiation Emergency Medicine

**Yasuhisa Fujibayashi, Ph.D., D.Med.Sci.**

*Director of Research Center for Radiation Emergency Medicine*

E-mail: fujibayashi.yasuhisa@qst.go.jp

## Introduction

The aim of the Research Center for Radiation Emergency Medicine is to propose and provide the best treatment methods to anyone who becomes involved in a radiation accident, anytime and anywhere. All of our efforts are made to attain this ultimate goal. Specifically, we are focusing on three projects (Fig. 1). The first project is directed toward the establishment of the most appropriate methodologies for evaluating radiation exposure, especially from contamination with actinides accompanied by trauma. The term “actinide” refers to 14 heavy-metal elements (atomic numbers 90 – 103) with unique characteristics, including high radioactivity and alpha-ray emission. The second project is aimed at exploring and supplying effective drugs to reduce the radiotoxicity and metallic toxicity of actinides that have been taken in internally. In Japan, NIRS is the only institution which is authorized to perform these two research projects using actinides including uranium and plutonium. The third project is targeted at possible applications of mesenchymal stem cells (MSCs) as regenerative medicine to treat radiation exposure injuries. MSCs can differentiate into various normal tissues and support regeneration of damaged tissues. Tissue regeneration failure is a characteristic of radiation injuries, and therefore, the application of MSCs to treat these injuries is plausible.

### 1. Research project to evaluate radiation exposure

Accurate dose evaluation in radiation exposure accidents is essential to treat patients and estimate their prognosis. One of the challenging issues in this is dose evaluation in the case of internal contamination with actinides such as uranium, plutonium and americium. Most of these actinides are alpha emitters and they have long effective half-lives in the body. For this reason, the actinides are likely to give significant doses even with a small amount and it is also difficult to quantitatively determine the doses in a short time. Bioassay (radiochemical analyses of excreta samples) is practically the only method to evaluate internal doses from actinides. Therefore, we have developed rapid bioassay procedures for the actinides with high and stable recovery yields and applied these procedures in international intercomparison programs. We have also developed other related techniques for internal dose evaluation and actinide decontamination measures in this research plan period (Fig.2).

Chromosomal analysis is also a useful method for evaluating radiation exposure. This method is used to evaluate specific chromosomal translocations as eventual outcomes from biologic reactions derived from radiation exposure. Chromosomal translocation may be stable in peripheral blood cells for a long period of time, and thus exposure doses can be retrospectively evaluated. We have developed an automatic system that achieves simpler handling and shorter handling time.

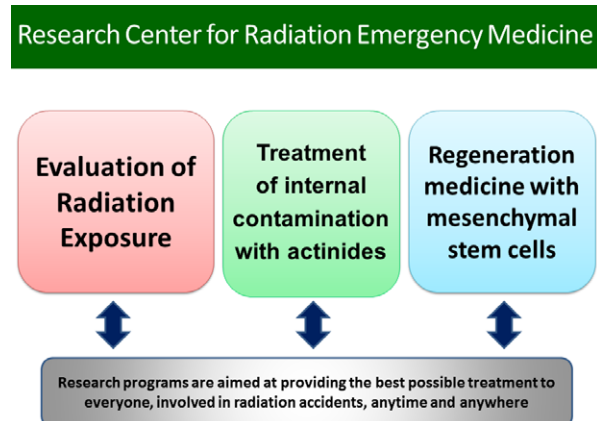
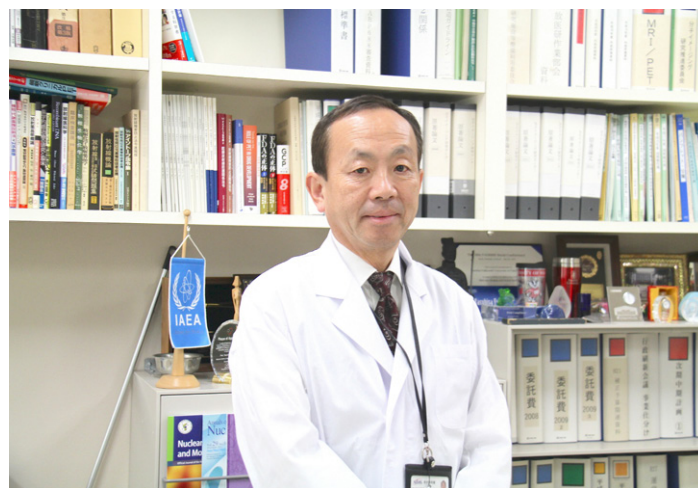


Fig.1 Outline of Research Center for Radiation Emergency Medicine.

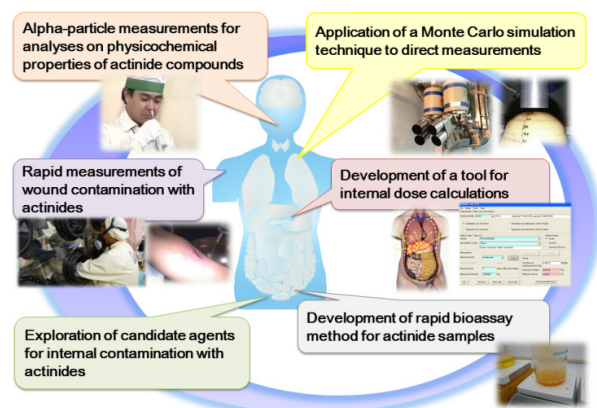


Fig.2 Research Project for Radiation Dosimetry.

## 2. Research project on the treatment of actinide exposure

Once an actinide enters into the body, it is retained in the target organ and induces radiologic as well as metallic toxic effects for a long time. The treatment strategy is usually comprised of two or three steps (Fig.3). The initial step is removal of the actinides by decontamination. This is not always possible, especially when contamination occurs widely or deeply or in unresectable body areas. In such cases, only treatment with chelating reagents such as diethylenetriaminepentaacetic acid (DTPA) is currently available. The pharmacokinetics of free-DTPA indicates that it has a short half-life in peripheral blood (about 1 hour) and it is poorly distributed into intracellular spaces. We have found new drug candidates for actinide-related accidents from commercially available reagents.

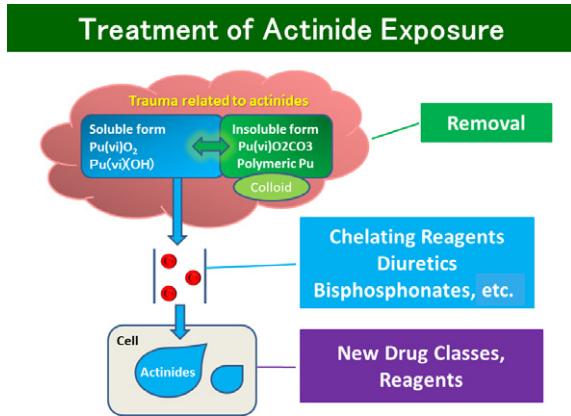


Fig.3 Research Project on the Treatment of Actinide Exposure.

## 3. Mesenchymal stem cells protect against tacrolimus/radiation-induced cell death

Intestinal thrombotic microangiopathy (I-TMA) is a critical complication of stem cell transplantation. Although the precise cause of I-TMA is not yet fully elucidated, several factors—including graft versus host disease (GVHD), total body irradiation (TBI), calcineurin inhibitors such as cyclosporine A (CsA), tacrolimus, and infection—are suggested to play a role in its etiology. I-TMA has attracted particular attention as a cause of preventable, non-relapse mortality, which has rates of 10%–70%. Investigations of I-TMA pathogenesis have mainly focused on intestinal endothelial injury caused by calcineurin inhibitors, which induce various types of dysfunction in human umbilical vein endothelial cells (HUVECs). Prompt withdrawal or reduction of calcineurin inhibitor administration in patients with I-TMA is recommended based on case studies. Approximately 50% of patients respond to a tapered schedule, but complete withdrawal is not advisable for patients with severe GVHD, for whom novel therapeutic strategies are required.

TBI or abdominal radiation therapy can induce gastrointestinal (GI) syndrome in patients, which is characterized by nausea, vomiting, diarrhea, or sometimes life-threatening microangiopathy or bacterial translocation and for which there is no definitely effective prophylactic or therapeutic treatment. Although the precise link between microvascular endothelial cell apoptosis and epithelial cell loss in GI syndrome is still debated, calcineurin inhibitors and radiation may commonly attack both cell types. Histopathologic features of I-TMA mimic those of GI syndrome, suggesting common pathological mechanisms.

MSCs are promising tools for cell-based therapy, and in clinical settings, commercially produced MSCs have been used to treat resistant intestinal GVHD. In addition, in radiation-induced intestinal injury models, MSCs limit radiation damage and contribute to tissue regeneration via release of beneficial

pleiotropic factors, although the underlying mechanisms are not well understood. MSCs release various neurotrophic factors, which improve radiation-induced myelopathy and protect against ischemic brain damage by preventing neuronal apoptosis and improving microcirculation. Furthermore, their over-expressing MSCs reduce infarct size and promote functional recovery in a rat model of brain infarction. They also protect HUVECs against damage induced by tumor necrosis factor  $\alpha$  or interleukin-1. However, whether they have positive effects on irradiated intestinal epithelial cells remains unknown.

Recent studies have found that combination therapy with MSCs and tacrolimus attenuates ischemic brain damage, while tacrolimus may increase a specific neurotrophic factor expression in astrocytes subjected to ischemia, suggesting a possible link between tacrolimus and its expression in MSCs. Based on these findings, we hypothesized that MSCs and released neurotrophic factors have beneficial effects on intestinal epithelial and endothelial cells exposed to radiation, and may be useful for the treatment of patients with I-TMA or GI syndrome.

However, for therapeutic application of MSCs, more detailed knowledge of the effects of tacrolimus and MSCs on epithelial and endothelial cells with or without irradiation is required. Given the difficulties in investigating relationships between I-TMA, GI syndrome, and the cells or molecules involved in vivo, in the present study we established an in vitro system (Fig.4A) to analyze these interactions and examined the mechanistic basis for the effects of MSCs on intestinal epithelial cells in order to provide answers to these basic questions that can benefit future in vivo studies (Fig.4B).

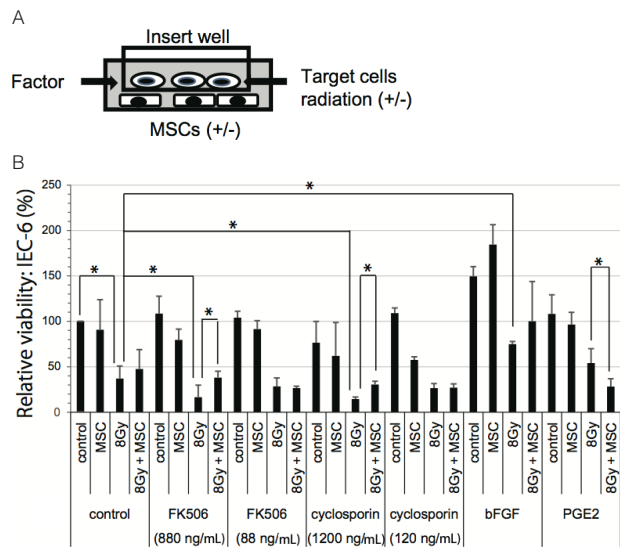


Fig.4 In vitro evaluation system.

4A: Schematic illustration of the in vitro system for evaluating the relationship between MSCs, target cells (IEC-6 cells or HUVECs), radiation, and various factors. The system is comprised of an insert well containing target cells ( $1.5 \times 10^5$ /well) with or without 8 Gy radiation exposure and an external well with or without MSCs ( $1.0 \times 10^5$ /well) supplied with or without factors in a 1.5 mL culture medium. After culturing for 48 h, target cells were harvested and viability was assessed by the Trypan Blue exclusion test. Mean survival was determined by counting eight randomly selected non-overlapping fields containing viable and non-viable cells.

4B: Interactions between various factors, radiation, MSCs, and IEC-6 cells. Values represent mean  $\pm$  SD. The value in target cells without application of MSCs, radiation, or factors (control group) was set as 100%. Relative viability of each group to the control was evaluated for 48 h. Interaction experiments were repeated three times. \* $p < 0.05$  by Student's t-test.

## Highlight

## Mesenchymal stem cells protect against tacrolimus/radiation-induced cell death

**Kenichi Tomiyama, Masaharu Hazawa,  
Ai Saotome-Nakamura, Chizuka Obara,  
Takaya Goto, Takeshi Yasuda,  
Katsushi Tajima**

E-mail: [tomiyama.kenichi@qst.go.jp](mailto:tomiyama.kenichi@qst.go.jp)

Intestinal thrombotic microangiopathy (I-TMA) is a critical complication of stem cell transplantation. Although the precise cause of I-TMA has not yet been fully elucidated, several factors—including graft versus host disease (GVHD), total body irradiation (TBI), calcineurin inhibitors such as cyclosporine A (CsA), tacrolimus, and infection—are suggested to play a role in its etiology. I-TMA has attracted particular attention as a cause of preventable, non-relapse mortality, which has rates of 10%–70%. Investigations of I-TMA pathogenesis have mainly focused on intestinal endothelial injury caused by calcineurin inhibitors, which induce various types of dysfunction in human umbilical vein endothelial cells (HUVECs). Prompt withdrawal or reduction of calcineurin inhibitor administration in patients with I-TMA is recommended based on case studies. Approximately 50% of patients respond to a tapered schedule, but complete withdrawal is not advisable for patients with severe GVHD, for whom novel therapeutic strategies are required.

TBI or abdominal radiation therapy can induce gastrointestinal (GI) syndrome in patients, which is characterized by nausea, vomiting, diarrhea, or sometimes life-threatening microangiopathy or bacterial translocation and for which there is no definitely effective prophylactic or therapeutic treatment. Although the precise link between microvascular endothelial cell apoptosis and epithelial cell loss in GI syndrome is still debated, calcineurin inhibitors and radiation may commonly attack both cell types. Histopathologic features of I-TMA mimic those of GI syndrome, suggesting common pathological mechanisms.

Mesenchymal stem cells (MSCs) are promising tools for cell-based therapy, and in clinical settings, commercially produced MSCs have been used to treat resistant intestinal GVHD. In addition, in radiation-induced intestinal injury models, MSCs limit radiation damage and contribute to tissue regeneration via release of beneficial pleiotropic factors, although the underlying mechanisms are not well understood. MSCs release various neurotrophic factors, which reduce symptoms of radiation-induced myelopathy and protect against ischemic brain damage by preventing neuronal apoptosis and improving microcirculation. Furthermore, their overexpressing MSCs reduce infarct size and promote functional recovery in a rat model of brain infarction. They also protect HUVECs against damage induced by tumor necrosis factor  $\alpha$  or interleukin-1. However, whether they have positive effects on irradiated intestinal epithelial cells remains unknown.



Recent studies have found that combination therapy with MSCs and tacrolimus attenuates ischemic brain damage, while tacrolimus may increase a specific neurotrophic factor expression in astrocytes subjected to ischemia, suggesting a possible link between tacrolimus and its expression in MSCs. Based on these findings, we hypothesized that MSCs and released neurotrophic factors have beneficial effects on intestinal epithelial and endothelial cells exposed to radiation, and may be useful for the treatment of patients with I-TMA or GI syndrome.

However, for therapeutic application of MSCs, more detailed knowledge of the effects of tacrolimus and MSCs on epithelial and endothelial cells with or without irradiation is required. Given the difficulties in investigating relationships between I-TMA, GI syndrome, and the cells or molecules involved in vivo, in the present study we established an in vitro system to analyze these interactions and examined the mechanistic basis for the effects of MSCs on intestinal epithelial cells in order to provide answers to these basic questions that can benefit future in vivo studies.

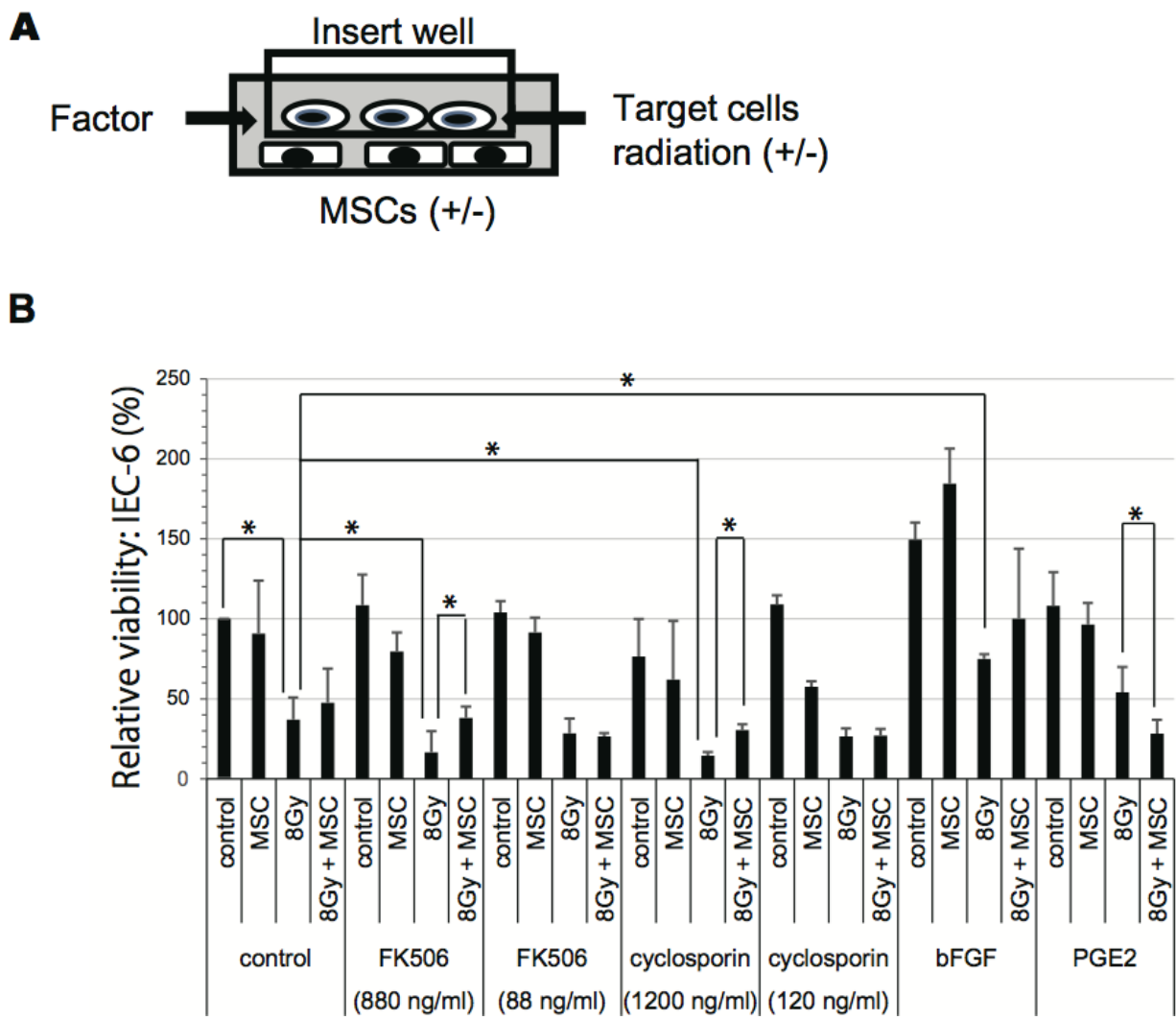


Fig.1 In vitro evaluation system. (A) Schematic illustration of the in vitro system for evaluating the relationship between MSCs, target cells (IEC-6 cells or HUVECs), radiation, and various factors. The system comprises an insert well containing target cells ( $1.5 \times 10^5$ /well) with or without 8 Gy radiation exposure and an external well with or without MSCs ( $1.0 \times 10^5$ /well) supplied with or without factors in a 1.5 ml culture medium. After culturing for 48 h, target cells were harvested and viability was assessed by the Trypan Blue exclusion test. Mean survival was determined by counting eight randomly selected non-overlapping fields containing viable and non-viable cells. (B) Interactions between various factors, radiation, MSCs, and IEC-6 cells. Values represent mean  $\pm$  SD. The value in target cells without application of MSCs, radiation, or factors (control group) was set as 100%. Relative viability of each group to the control was evaluated for 48 h. Interaction experiments were repeated three times. \* $p < 0.05$  by Student's t-test.

## Highlight

# Construction of a biodosimetric method for experimental low-dose irradiation in mice by the quantification of mRNAs using a drop of peripheral blood

Izumi Tanaka, Hiroshi Ishihara

E-mail: tanaka.izumi@qst.go.jp,

ishihara.hiroshi@qst.go.jp

## Objectives

Various irradiation situations can be simulated by in vivo experiments using animals. Biodosimetry using living cells provides direct evidence of the cellular damage in a body. At present, biodosimetric methods by the measurement of chromosomal damage in lymphoblasts by high-dose irradiation have been established. However, the method is not suitable for quantification of low-dose radiation below 500 mGy. To investigate biological effects by the exposure to low-dose radiation, quantitative indicators reflecting a weak level of damage are useful. If such indicators are found, they can be applied to study in various models including continuous exposure at low-dose rate and internal contamination. Here, we established an example of the biodosimetric method to measure low-dose radiation below 500 mGy by the use of mRNA in white blood cells from irradiated mice [1].

## Results and discussion

### Quantification method of irradiation dose-dependent increase in mRNA in avoidance of strong effect of circadian rhythms

As a biological sample for biodosimetry, the use of small amounts of peripheral blood collected from a body by a low-invasive method has an advantage in various situations of animal experiments. It is believed that small amounts of undifferentiated or proliferating cells are included in white blood cells in circulating blood. Because blood cells are more sensitive against radiation than other somatic cells, they are used as a highly sensitive indicator in the body. After irradiation, such undifferentiated or proliferating blood cells are expected to trigger early apoptotic mechanism, with induction of mRNA for early apoptotic genes such as *Bax*. In fact, we have reported that mRNAs for DNA damage-induced genes including *Bax* are increased dose-dependently in peripheral blood after whole-body irradiation of C3H/He inbred mice [2].

Messenger RNA for a house keeping gene, glyceraldehyde-3-phosphate dehydrogenase (*Gapdh*), is expressed in all the living cells and is widely used as an internal standard for quantitative analysis of inducible mRNAs, because of its constant expression after addition of various inducers on gene expression. Concentration of white blood cells in circulating blood in mice changes diurnally [1]. There is a possibility that the ratio of the cells which express *Bax* mRNA in response to irradiation also fluctuates by the circadian rhythm. The possibility is similar that the rate of non-responsive cells containing *Gapdh* mRNA without *Bax* mRNA fluctuates simultaneously. If so, the mRNA rates of *Bax/Gapdh* change diurnally after irradiation. In fact, the levels in the mRNA rates in blood collected from mice 4h



after whole-body exposure at a dose of 500 mGy of kinetic energy released per unit mass (air-kerma) in a daytime irradiation was 2 times higher as compared with the levels in a nighttime irradiation (Fig.1., blue line).

For the practicable use of mRNA quantification in blood for biodosimetry, we focused on protooncogene *c-myc* (*Myc*) mRNA which is known to be expressed in undifferentiated white blood cells as well as in proliferative cells. If undifferentiated or proliferating cells in circulating white blood cells continuously keep the intracellular levels of the *Myc* mRNA and induce *Bax* mRNA after irradiation, the circadian change is expected to be minimized. In fact, the mRNA rates of *Bax/Myc* were not affected by the irradiation clock time (Fig.1., red line). Therefore, the RNA rate of *Bax/Myc* was suggested to be useful as a biodosimetric indicator in animal experiments.

### Radiation dose-dependent increase in the mRNA rate of *Bax/Myc* in white blood cells

To use the mRNA rate of *Bax/Myc* as a biodosimetric indicator, the levels have to increase depending on the irradiation doses. We examined the mRNA rate in blood collected 4h after whole-body exposure at X-ray doses of 0, 100, 200 and 500 mGy (air-kerma) to mice in their active time (Fig.2., red). The mRNA rates were increased proportionally to the irradiation doses. Similarly, blood samples from mice in their resting time gave a similar regression line (Fig.2., purple). Slopes of the two lines were closely similar and their coefficients of correlation were too. Because the relationships between mRNA rates and exposed doses were kept among different production batches of C3H/He inbred mice [1], we concluded that the mRNA rate of *Bax/Myc* can be used for the biodosimetric method.

### Application of the mRNA rate of *Bax/Myc* in white blood cells in the model of internal contamination

The mouse irradiation model mentioned above simulates a single whole-body irradiation at high-dose rate (0.5 Gy/min). As an internal contamination model with continuous irradiation at

low-dose rate, we injected a beta emitter of  $^{32}\text{P}$ -phosphate to mice. When injected doses of  $^{32}\text{P}$  were 200 or 80 MBq/kg, the estimated absorbed dose rates to water were 80 or 32 mGy/h, respectively. Because total absorbed doses in mouse are accumulated every hour, linear increases in the levels of the mRNA rates of *Bax/Myc* were calculated. The 95% confidence intervals of the predicted increases after 80 or 32 mGy calculated by the single irradiation model are shown as gray bands in Fig.3. The actual mRNA rates of *Bax/Myc* in blood collected 4h and 8h after injection of phosphate were measured (red, orange and blue symbols). All the data (red and orange symbols) were included in the predicted ranges (gray bands). Therefore,

we concluded that the biodosimetric method is applicable to internal contamination experiments and the continuous irradiation model.

### Perspectives

Here we showed an example of the mRNA ratio of *Bax/Myc* in peripheral blood as a biodosimetric indicator following low-dose radiation. Similarly, we have previously found that mRNA ratios of *Bbc3/Myc* and *Cdkn1a/Myc* were also applicable [1]. When these indicators are used for biodosimetry in low-dose exposure experiments, more precise analysis is expected by the simultaneous measurements of these 3 sets of indicators.

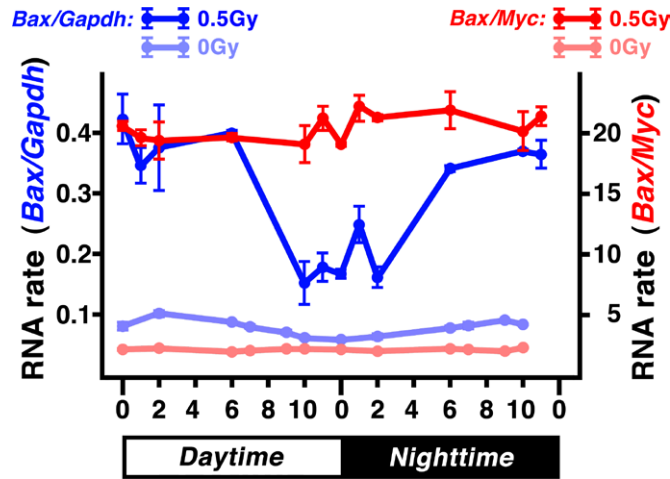


Fig.1 Messenger RNA rates in white blood cells from mice irradiated at different clock-times. Four mice per group were whole-body X-irradiated in a dose of 0.5Gy (air-kerma) or 0Gy at the indicated time (x-axis). Four hours after the irradiation, a drop of blood was collected and the mRNA levels were measured by accurate quantitative RT-PCR [2]. Clock time-dependent fluctuation in the averages and standard errors (s.e.s) of *Bax/Gapdh* mRNA rates in blood from irradiated mice (blue line) and sham-irradiated mice (light blue line) were observed. The fluctuation became the minimum in the averages and s.e.s of *Bax/c-Myc* mRNA rates in blood from the irradiated mice (red line) and the sham-irradiated mice (light red line).

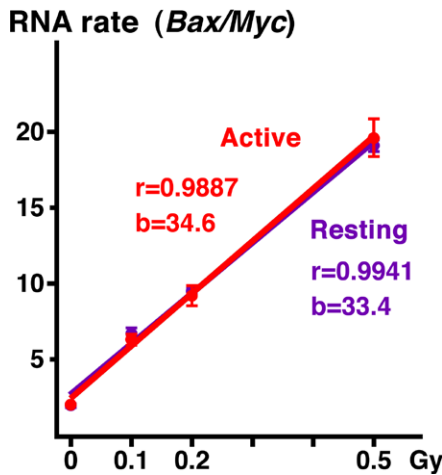


Fig.2 Correlation between the *Bax/Myc* RNA ratios and exposed doses of X-ray. Four mice per group were used for X-irradiation at doses of 0, 0.1, 0.2, or 0.5 Gy (air-kerma). Mice in active time were whole-body irradiated at nighttime 02:00 and blood was collected 4 h later (red dots and line). Blood from mice in resting time were collected 4h after irradiation at daytime 02:00 (purple dots and line). Averages, s.e.s, and regression lines, and correlation coefficients (r) and slopes of the lines (b) are indicated.

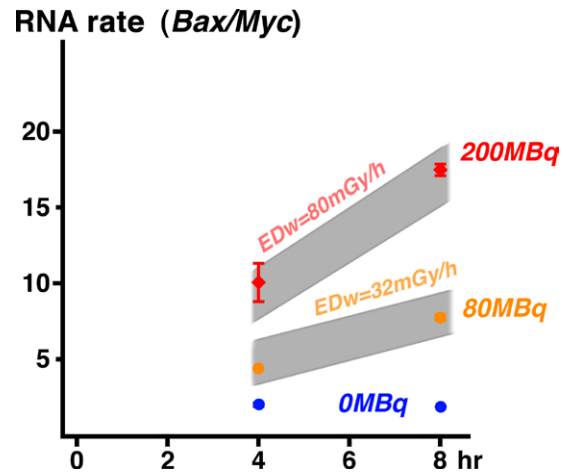


Fig.3 Dose-dependent increase in *Bax/Myc* RNA rates in an internal contamination model. Four mice per group were injected with a  $\beta$ -emitter,  $^{32}\text{P}$ -phosphate, at a dose of 200 MBq/kg (red diamonds), 80 MBq/kg (orange closed circles), or 0 Bq/kg (blue closed circles). Areas shaded in gray indicate predicted 95% confidence intervals of the time-dependent increase in the RNA ratio corresponding to the estimated absorbed dose to water, which were calculated from the data obtained from the single  $\gamma$ -irradiation experiment [1]. Averages and s.e. among 4 mice per group are shown as symbols and bars, respectively.

### References

- [1] Ishihara H, et al., *J Radiat Res*, 57, 25, 2016.
- [2] Ishihara H, et al., *J Radiat Res*, 51, 265, 2010.

## Highlight

# Practical self-absorption correction method for various environmental samples in radioactivity measurements with HPGe detectors

Osamu Kurihara, Hidesuke Itadzu\*

\*SEIKO EG&G Co., Ltd.

E-mail: kurihara.osamu@qst.go.jp

## Introduction

Radioactivity measurements of various environmental samples have been performed by many institutes. In these measurements, the gamma-ray spectrometry using High-Purity Germanium (HPGe) detectors is commonly used. A significant advantage of this method is its easiness and promptness although targeted radionuclides are limited to gamma-emitters. Meanwhile, a large number of NaI(Tl) detectors with poor energy resolution have been newly installed to cope with extensive inspections of samples including food products after the Fukushima Daiichi Nuclear Power Plant (FDNPP) accident. Additional inspections using the HPGe detectors have been also requested for the samples exceeding screening levels.

For accurate radioactivity determinations in these measurements, the efficiency calibration of the detector used should be made under the same conditions as those for the sample. However, a major difficulty in this is to prepare a standard source with the same chemical composition and density as the sample to be measured. Thus, we addressed the problem of obtaining a self-absorption correction factor for accurate activity determinations without the preparation of standard sources for samples in 1000 cm<sup>3</sup> re-entrant containers (known as Marinelli containers) that have been widely used for the additional inspections after the FDNPP accident. We also demonstrated the validity of the proposed self-absorption correction factor through an intercomparison test among laboratories that owned different-sized HPGe detectors.

## A semi-empirical self-absorption correction factor for Marinelli containers

The self-absorption correction factor for the sample is given by

$$\varepsilon_x(E, \mu_x) = \frac{f(\mu_x)}{f(\mu_{ref})} \cdot \varepsilon_{ref}(E, \mu_{ref}) \dots (1)$$

where,  $\varepsilon_x(E, \mu_x)$  is the peak efficiency for the sample with  $\mu_x$  at a photon energy  $E$ , and  $\varepsilon_{ref}(E, \mu_{ref})$  is the peak efficiency for the reference source.  $f(\mu)$  is the self-absorption correction factor as a function of the linear attenuation coefficient.

Regarding  $f(\mu)$ , many studies have suggested theoretically calculated or empirical formulae for the Marinelli containers. The gamma-ray spectrometry guidelines [1] also provide the following empirical formula:

$$f(\mu) = \frac{1}{1 + a \cdot \mu + b \cdot \mu^2} \dots (2)$$

where,  $a$  and  $b$  are the constants that depend on the size of the Marinelli container.



This formula has been commonly used especially in Japan. The values of the two constants are provided in the guidelines for the 700 cm<sup>3</sup> and 2000 cm<sup>3</sup> Marinelli containers; however, not for the 1000 cm<sup>3</sup> container. In addition, the accuracy of the formulae has not been fully studied for a wide range of the linear attenuation coefficient.

## Materials and methods

Monte Carlo simulations were employed to determine the  $a$  and  $b$  constants in the self-absorption correction factor. The MCNP5 code was used for this task. Figure 1 shows the simulation model for the HPGe detector used in this study coupled to the 1000 cm<sup>3</sup> Marinelli container. The thicknesses of the dead layers that exist at outer surfaces of the crystal were chosen based on the information from the manufacturer without estimating the actual thickness.

In the simulation, photons were uniformly generated within the source region in the model and each energy deposition event in the active volume of the crystal was scored using a pulse height tally. Peak efficiencies were then determined from the resulting pulse height spectra. The matrix in the container was the source region, which was virtually set as SiO<sub>2</sub>. The simulations were individually performed for each peak energy from the reference source used for efficiency calibration of the HPGe detector, while changing the density of the source region from 0 (void) to 4 g cm<sup>-3</sup> in 1 g cm<sup>-3</sup> steps. One million histories were performed in each simulation to reduce the statistical standard deviation (1 $\sigma$ ) less than 1%.

Equation (1) can be modified as follows:

$$\frac{\varepsilon_c(E, \mu_c)}{\varepsilon_{void}(E, 0)} = \frac{f(\mu_c)}{f(0)} = f(\mu_c) = \frac{1}{1 + a \cdot \mu_c + b \cdot \mu_c^2} \dots (3)$$

where,  $\varepsilon_c(E, \mu_c)$  and  $\varepsilon_{void}(E, 0)$  are the calculated peak efficiencies for SiO<sub>2</sub> with a non-zero  $\mu_c$  and the void ( $\mu=0$ ). We note that  $f(\mu)$  is one in the case of the void. The two constants in the factor were determined by the least-squares method based on the calculated  $f(\mu)$  values.

The self-absorption correction factor was validated using a set of four test sources comprising different matrices with densities ranging from 0.7 to 3.0 g cm<sup>-3</sup>. These sources contained the following nine radionuclides: <sup>109</sup>Cd (88 keV), <sup>57</sup>Co (122 keV, 136 keV), <sup>139</sup>Ce (320 keV), <sup>51</sup>Cr (168 keV), <sup>113</sup>Sn (392 keV), <sup>85</sup>Sr (514 keV), <sup>137</sup>Cs (662 keV), <sup>88</sup>Y (898 keV, 1836 keV) and <sup>60</sup>Co (1173 keV, 1332 keV). As a result, this set provides a wide range of linear attenuation coefficient values from 0.0357 cm<sup>-1</sup> to 0.929 cm<sup>-1</sup>. Linear attenuation coefficients of matrices were calculated using the XCOM database and the reference data of the density and elemental weight fraction.

We also performed an interlaboratory comparison to evaluate the validity of the factor by providing two identical test samples made of brown rice with certified radioactivities of <sup>134</sup>Cs and <sup>137</sup>Cs. These samples were placed in two 1000 cm<sup>3</sup> Marinelli containers. Five laboratories participated in this test.

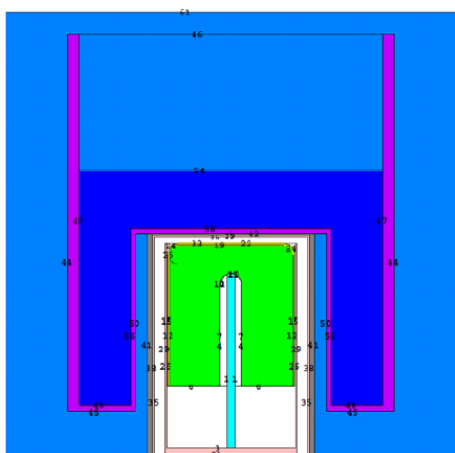


Fig.1 Simulation model for the HPGe detector and 1000 cm<sup>3</sup> Marinelli container.

### Results and discussion

Figure 2 shows the self-absorption correction factors for the 1000 cm<sup>3</sup> Marinelli container as a function of the linear attenuation coefficient. Each point in the figure corresponds to the  $f(\mu_c)$  values calculated by Monte Carlo simulations. As a result, the constants  $a$  and  $b$  were determined to be 1.362 and 0.6774, respectively.

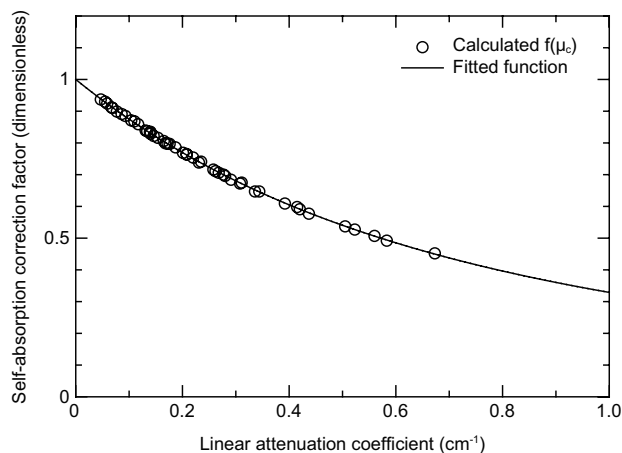


Fig.2 Self-absorption correction factor for a 1000 cm<sup>3</sup> Marinelli container.

Figure 3 demonstrates the ratios of the quantified radioactivity to the certified radioactivity for each peak energy from the test sources: panels (A) and (B) are the ratios without and with the self-absorption correction, respectively. The error bars of the symbols in the figure denote the combined uncertainty ( $k=2$ ) of the sources used for calibration and quantification) and counting statistics. The figure shows that the self-absorption correction factor enabled accurate radioactivity determination of the test sources over a wide range of the linear attenuation coefficient ( $\mu$ : 0.05 – 1.0 cm<sup>-1</sup>), whereas the absence of corrections resulted in significant underestimations for  $\mu > 0.2$  cm<sup>-1</sup>.

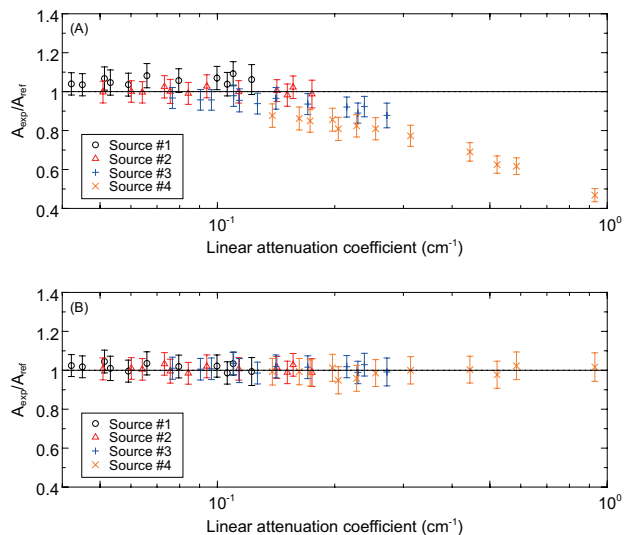


Fig.3 Ratios of quantified to certified radioactivities of the test sources. Panel (A): no correction, Panel (B): correction.

The interlaboratory comparison also validated the proposed self-absorption correction factor although the relative efficiency and crystal size of the 11 HPGe detectors of the laboratories were different. Details of the results for this report have been described elsewhere [3].

### References

- [1] JP. MEXT, Gamma-ray spectrometry using a germanium semiconductor detector (Radiation Measurement Methods Series #7), 1992.
- [2] Berger M J *et al.*, XCOM: Photon Cross Section Database, 2010. Available at <http://www.nist.gov/pml/data/xcom/index.cfm>
- [3] Itadzu H *et al.*, *Radioisotopes*, 64, 661-671, 2015.

## The new low-cost metaphase finder

**Akira Furukawa**

E-mail: furukawa.akira@qst.go.jp

### Introduction

Biological dosimetry is used to estimate an individual's dose by biological phenomena. The most popular and "gold standard" phenomenon is the appearance of dicentric chromosomes in the metaphase (Fig.1) in white blood cells [1]. The metaphase finder is a tool for biological dosimetry that finds metaphase cells on glass slides. It consists of an automated microscope, auto-focus system, X-Y stage, camera, and computer. It does the image diagnosis of the microscopic images of the glass slides, and displays the positions of metaphase cells. The metaphase finder was used to determine the radiation doses received by emergency personnel who worked at Fukushima Daiichi Nuclear Power Plant during the accident. There are several commercially available metaphase finders, and we also have developed an automated optical microscope system [2]. But, these systems are usually expensive and inconvenient to fit to the various chromosome preparations. We have already reported a previous model of the low-cost metaphase finder system [3], but this was still inconvenient. Then, we planned a new project with a software company to make our previous system faster. The aims of the new system were 1) to be adapted not only for metaphases, but also for PCC cells; 2) to take less than 20 minutes per slide; 3) to have a false positive rate of less than 5%; 4) to have a compact system including a microscope, power supplies, a small PC and a display; 5) to have a retail price below 8 million JPY; and 6) to use all domestically made components (except the OS). Figure 2 shows a photo of the completed system.

### The new optical microscope

The previous metaphase finder system consisted of the following components: an optical microscope, a motorized sample stage, and an auto-focusing unit. But, the new system combined these components into one automated microscope. This enabled reduction of the size and cost of the total system. The new high-definition camera made it possible to use 4x objective lens. The image recognition software for detecting metaphases in the microscope image was ordered to be supplied by the software company based on the our previously developed program at the author's laboratory.

### Metaphase detection

The most significant feature of the software of this metaphase finder is its use of mathematical morphology filters in most the image recognition process. The mathematical morphology filters for grey-level images were also used in as the previous 2008 version. First, the captured image is adjusted by the background subtraction (Fig.3A). Next, the "dilation" and

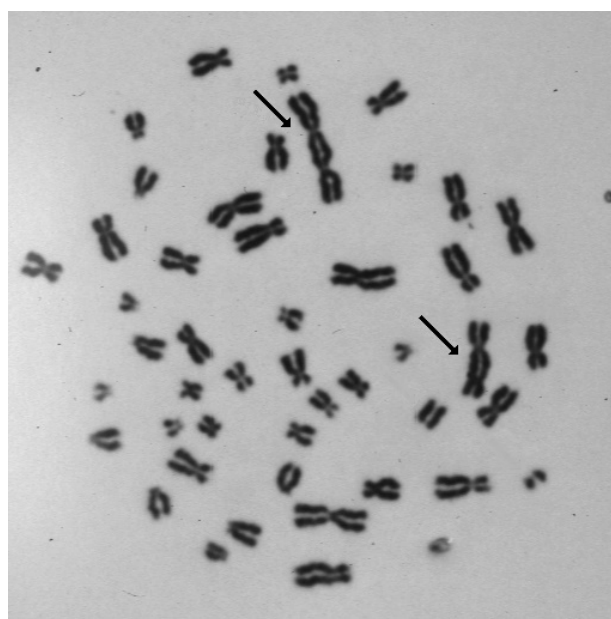


Fig.1 Microscope image of a metaphase cell. Arrows are dicentric chromosomes.

"erosion" were applied several times to this color image for several times to eliminate the small objects like chromosomes (Fig.3B). In this process, "erosion" was applied once more than "dilation" was applied, to make fringes of remained the remaining objects bigger than the original image. This image is subtracted from the original image to make small objects appear small objects that had been removed by the previous

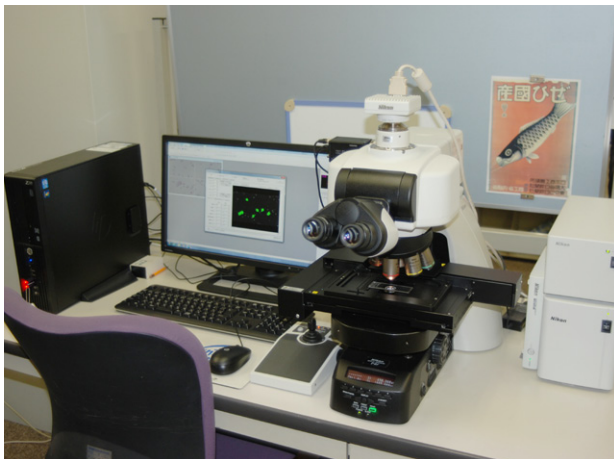


Fig.2 The new metaphase finder.

process (Fig.3C). Then, this image is then binarized to black pixels and white pixels (Fig.3D), by a user-selected threshold value. ThenNext, extraction of the particles whose sizes are comparable with chromosomes from the binary image is done by using the “opening” (Fig.3E) and “closing” (Fig.3F) the filters. The sizes, the shapes (roundness, aspect ratio, etc.) and the darkness of the clusters of the particles are measured and the clusters with appropriate values were are finally determined to be the metaphases. The XY coordinates of each metaphase on the slide are calculated from the position of the metaphase in the image and the scanning position on the slide.

#### Performance test

The metaphase finder system’s speed was determined by scanning one whole slide. It took 13 minutes and 56 seconds per slide, while capturing 1,333 images. And, the false positive rate was below 5%. These values satisfied the aims of the project.

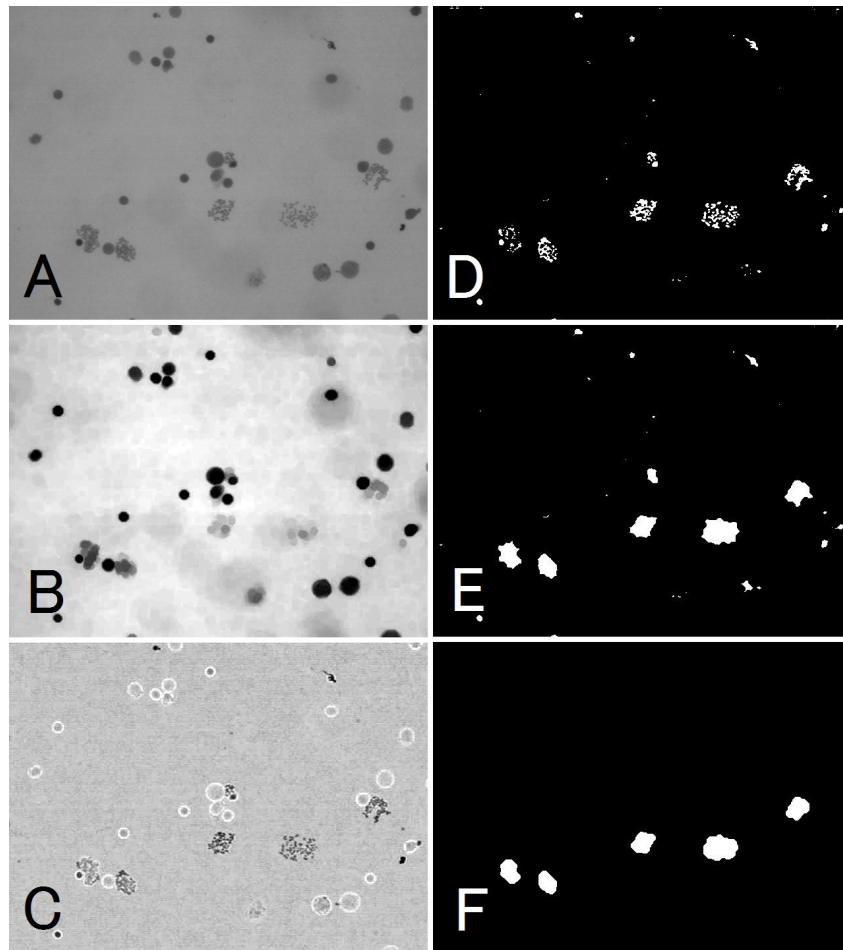


Fig.3 Image processing for metaphase detection. A: Original image. B: Dilation and erosion of A. C: Subtract B from A. D: Binarize C. E: Closing of D. F: Opening of E.

#### References

- [1] International Atomic Energy Agency: *Cytogenetic analysis for radiation dose assessment, a manual, Technical Reports Series 405*. International Atomic Energy Agency, 2001.
- [2] Furukawa A, *et al.*, *Cytometry Res* 7, 1, 1997.
- [3] Furukawa A, *et al.*, *Health Phys* 98, 269, 2010.

# Development of Fundamental Technologies in Radiological Science

## Shinichi Kuroki

*Director of Research, Development and Support Center*

### Research, Development and Support Center

The Research, Development and Support Center was established in 2011 to support and promote research activities of NIRS.

This center performs basic and advanced research and development necessary for the activities of NIRS such as R&D in technologies for radiation generators, radiation detection, and radiation biology. It also supports researchers by providing users a comfortable environment in which they make use of research facilities such as the radiation generators and in supplying experimental animals, and so on. In addition to these activities, it maintains safety of all working environments and manages buildings in the NIRS campus, the NIRS computer network system and the NIRS library.

This center consists of one unit and three departments: the Planning and Promotion Unit, Department of Technical Support and Development, Department of Safety and Facility Management, and Department of Information Technology. The unit and each department are briefly introduced as follows.

### Planning and Promotion Unit

The Planning and Promotion Unit functions as the secretariat of the center and it is the hub linking all the sections of the center with the NIRS administrative sections such as the Department of Planning and Management and the Department of General Affairs and the other centers.

### Department of Technical Support and Development

The Department of Technical Support and Development provides services to users for performing various experiments such as management of the facilities for radiation generators and the many devices used for experiments. This department also develops radiation detectors employing new technologies, carries out fundamental research in radiation biology, and supports researchers in conducting animal experiments of the highest level quality.

This department has three sections: Radiation Engineering Section, Radiation Measurement Research Section and Laboratory Animal and Genome Sciences Section.

The Radiation Engineering Section maintains the facilities for radiation generators and many of the devices which are used for experiments. There are seven gamma-ray generators, six X-ray generators and two Cockcroft-Walton accelerator systems which consist of proton accelerators and beamlines. One of the Cockcroft-Walton accelerator systems is used to generate neutron fluxes for research experiments on the biological effects of low dose radiation (NASBEE; a neutron exposure accelerator



system for biological effect experiments). The other Cockcroft-Walton accelerator system has three beamlines; two beamlines are used as atomic element analyzers (PASTA; PIXE analysis system and tandem accelerator) and the third beamline is used to deliver a single particle proton targeting an individual cell (SPICE; single particle irradiation system to cell). In 2015, the micro-PIGE (Particle Induced Gamma-ray Emission) method using the  $^{19}\text{F}(p,p'\gamma)^{19}\text{F}$  nuclear reaction to analyze fluorine distribution was developed in PASTA. In SPICE, a new stage system was designed and fabricated in order to improve the irradiation speed to cells.

The Radiation Measurement Research Section develops various radiation detectors. After the Fukushima Dai-ichi Nuclear Power Station accident occurred, the section began developing some detectors for surveying high level radiation areas in Fukushima Prefecture: In 2015, a small, lightweight and low cost radiation camera which can selectively detect radiation from the radioisotope  $^{137}\text{Cs}$  was tested in Fukushima; it was improved by working together with an instrument manufacturing company for commercial use. A dose assessment method of secondary particles for proton beam radiotherapy was also developed. A visualize technique of dose distribution by means of combining autoradiographic methods using solid state chips and evaluation techniques of local doses was established.

The Laboratory Animal and Genome Sciences Section supports researchers in conducting animal experiments of the highest level quality. Seven species of animals for animal experiments are available. In this section, more than 12,000 mice and 1,100 rats are bred each year, and genetically modified mice have been developed in order that researchers can conduct even more advanced experiments. Since some mice and rats are bred in SPF conditions, it is very important to sterilize the area periodically and keep it clean all the time. The SPF areas are controlled very strictly. In 2015, our developed

genetically modified mice systemically expressing GFP-Dcp1a, an indicator of processing bodies (P-bodies), were deposited with and are available from RIKEN BioResource Center (Tsukuba, Japan) and CARD (Kumamoto, Japan). Normal fertilization *in vitro* using both fresh and frozen-thawed sperm of inbred mice used for research has been further improved and well adapted to practical applications. Finally, it was found that point mutations in iPS cell genomes arise during reprogramming from somatic cells to iPS cells.

### R&D Infrastructure Platform Program

In 2013, the research subject proposed by NIRS, "Business use of various radiation fields related to humans", was selected as the R&D Infrastructure Platform Program by the Ministry of Education, Science and Technology (MEXT). This Platform Program is aimed at two purposes: promoting usage of advanced research equipment and facilities of universities and public research institutes by researchers from industry-government-academia and supporting formation of networks.

Under this program, advanced facilities of NIRS such as PASTA, SPICE, NASBEE and the other radiation generators are provided for use by industry-government-academia researchers with steadfast support. This program will strengthen research activities in the fields of life science, human science, and human environment related science. In 2015, the number of user themes under the program increased to 14 from 10 in 2014.

### Department of Safety and Facility Management

The Department of Safety and Facility Management is responsible for keeping working environments safe and providing safe and comfortable conditions for all research activities. It has four sections: Safety and Risk Management Section, Safety Control Section, Radiation Safety Section, and Facility Management Section.

The Safety and Risk Management Section is in charge of planning and promoting safety, providing NIRS's employees with educational training for maintaining safety and security, and maintaining general safety on the NIRS campus and in buildings and facilities. In particular, it is responsible for risk management including making and revising the Emergency Preparedness Plan of NIRS and implementing drills for nuclear and radiological emergencies in Japan. In 2014, a more systematic risk management structure at NIRS was established under the risk management committee.

The Safety Control Section is in charge of such activities as safety for genetic modification of experimental animals, safety for handling chemical agents and harmful substances, safety in the workplace, protection of the environment, and prevention and extinguishing of fires.

About 1,800 persons including direct employees of NIRS, researchers from outside NIRS, and contracted workers are registered as radiation workers who can work in the 20 radiation controlled areas in NIRS. NIRS must instruct them regarding radiation safety and security before entering a radiation-controlled area for the first time. There are more than 400 kinds of radioisotopes used for experiments on radiobiology, radiation medicine and so forth. And NIRS also has many radiation generators. All items concerned with radiation have to be controlled strictly by rules. The Radiation Safety Section is charged with controlling all of them in accordance with the rules.

The Radiation Emergency Medicine Cooperative Research Facility (REMCRF) has one building in which the use of actinide nuclei is allowed for research on radiation emergency medicine. This facility is the only one of its kind in Japan in which researchers can use, for instance, plutonium in animal experiments. Therefore, this building has to be strictly controlled to keep the inside of the building at a negative pressure according to the radiation safety law. In this case, the ventilation system of the building is maintained by the Radiation Safety Section in cooperation with the Promotion Section for REMCRF

in accordance with the strict rules.

There are about 50 buildings on the NIRS campus. The Facility Management Section maintains the buildings and their equipment such as elevators, air conditioners, etc., and the campus infrastructures such as electric power lines, telephone systems, gas lines, water supply lines, and so on. NIRS was established in 1957, so some buildings are very old and a few were damaged considerably in the March 2011 earthquake. Some of them have had to have seismic strengthening. Construction of a new building used for human resource development and a new one used for environmental radiation research were completed under the supervision of this section and these buildings were opened in 2013 and 2014, respectively. This section has been managing the renewal of a high voltage electric booster station, which will be completed in 2018.

### Department of Information Technology

The computer network system is one of the main infrastructures of NIRS. This network system has more than 1,400 daily users and about 4,300 computers are connected to it. The Department of Information Technology is responsible for maintenance and development of the computer network system. This department has two sections: Information Systems Section and Research Information Section.

The Information Systems Section has established and continuously revised the computer network system. In these five years, mainly two important missions have been accomplished: (1) to secure the system and data on it; and (2) to save space and energy using virtual machine technology. Revising related regulations, periodical instruction for users and self-check of daily actions are included in the PDCA cycle to improve the overall security of the system. In addition, security instruments such as firewalls, access control systems and inspection software were replaced or newly installed. Virtual machine technology was applied to some small but important servers and some websites to save energy, space and management load.

The Research Information Section is responsible mainly for other information system-related matters especially user support of the system. The administrative sections have many computer-aided service systems, for instance, personnel management, accounting procedures, patent databases, etc. These service systems are maintained by the relevant section in principle, but the Research Information Section has undertaken various jobs such as improving the service systems and their coordination or adding new functions to them. This section also has developed an institutional repository to replace the conventional database system used for registration of achievements of NIRS research activities. Since this repository was released worldwide in October 2014, as of February 2016 more than 212,000 accesses have been received for 23,000 items. In addition, this section is also managing the library of NIRS and publications such as research reports, proceedings and so on prepared at NIRS.

## Highlight

# Improvement of *in vitro* fertilization of inbred mice used for radiation research

Seiji Kito

E-mail: kito.seiji@qst.go.jp

Assisted reproductive technologies (ARTs) in laboratory mice, such as cryopreservation, *in vitro* embryo production, embryo transfer and micromanipulation, have been playing essential roles to accelerate progress of biomedical research including radiation biology and medicine. These technologies not only enable scheduled mass production of mice and efficient maintenance of animals by frozen embryos and gametes, but they also lead to a reduction in the number of animals used for research. Of the ARTs, one of the most important techniques is *in vitro* fertilization (IVF), by which a large number of fertilized embryos can be produced for subsequent cryopreservation, embryo transfer or micromanipulation. *In vitro* fertilization in mice was first reported in 1971 using outbred mice [1]. From the late 1990s, many bio-resource programs in which various mice with an inbred genetic background have been distributed as frozen embryos for research purposes were started in many countries all over the world and efficient production of embryos by IVF became inevitable. However, IVF conditions used then were limited only for outbred and a few inbred strains and there were many strains which could not be fertilized *in vitro*, such as 129, BALB/c, C3H/He and genetically-modified and mutant strains bred from these inbred mice. These strains were also often used in various radiation research conducted in NIRS and it became urgent in embryo production by IVF and embryo cryopreservation to back-up important strains in the event of catastrophes such as natural disasters and microbiological infection.

For IVF, sperm need to be pre-incubated for 1-2 h to interact with eggs and fertilize, the so-called process of 'capacitation'. Only these capacitated sperm can fertilize with eggs in IVF medium. During the 2nd mid-term plan, we successfully improved IVF conditions for the BALB/c strain and found that successful fertilization was obtained by using the modified Krebs-Ringer's bicarbonate solution called TYH for the capacitation medium and modified human tubal fluid (mHTF) for the fertilization medium, and that one of the important factors for successful fertilization is increasing the calcium concentration from 1.71 to 5.13 mM [2]. These conditions have been successfully applied to other inbred strains such as C57BL/10, C3H/He, 129 and BALB/c [3].

However, recently we further found that in the C3H/He strain, increased calcium concentration resulted in a significant increase in the incidence of abnormal fertilization, or inhibition of extrusion of the second polar body (PBII) [4]. These abnormal eggs have two female and one male pronuclei (Fig.1). In addition, such abnormal eggs are still able to undergo cleavage division to the blastocyst stage, but they are unable to develop to term because of aneuploidy. Thus, use of such IVF conditions

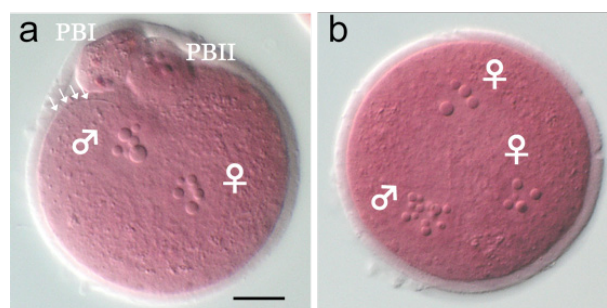


Fig.1 Images of normal and abnormal C3H/He fertilized eggs at 5 h PI. Scale bar indicates approximately 20  $\mu$ m. PBI: the first polar body. PBII: the second polar body. ♀ : female pronucleus (PN). ♂ : male pronucleus (PN). In normal fertilized egg fertilized in 1.71 mM calcium (a), single female PN, male PN, PBII and sperm tail (arrows) are clearly observed. In egg without PBII extrusion fertilized in 6.84 mM calcium (b) two female PNs and single male PN associated with a single sperm tail (out of focus) were observed.

has to be avoided and abnormal embryos have to be removed prior to subsequent manipulation.

Then, we have examined the details about this phenomenon of inhibition of PBII extrusion by high calcium in C3H/He [4] in the last few years. By increasing calcium from 1.71 mM to 6.84 mM, significant percentages of eggs failed PBII extrusion in a dose-dependent manner (Fig.2). The most sensitive time window against high calcium level was observed at 2-3 h post-insemination (PI). This calcium effect was somewhat alleviated by cumulus cells surrounding the eggs which connected with the egg cell through gap junctions and may have modified the microenvironment around the eggs during fertilization.

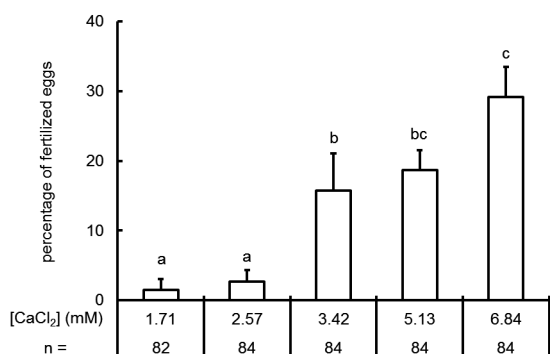


Fig.2 Percentages of PBII extrusion of C3H eggs under various concentrations of calcium during *in vitro* fertilization coincubation. After 1.5-2.0 h capacitation of sperm, eggs were inseminated in HTF with 1.71-6.84 mM calcium. At 5 h PI, eggs were examined under a microscope. Error bars indicate standard errors of mean. Letters above bar indicate significant difference at  $P < 0.05$ .

This phenomenon was specific to C3H/He because reciprocal IVF by changing sperm and egg between C3H/He and B6D2F1, whose egg is not influenced by a high calcium level at all, showed that failure of PBII extrusion under high calcium level was observed only when C3H/He eggs were used irrespective of sperm strains. However, when eggs were parthenogenetically activated by ethanol and incubated under high calcium, an unexpected result was obtained, that is, PBII extrusion was not disturbed, indicating that sperm are still involved in this phenomenon.

We hypothesized that the cytoskeletal organization was disturbed under high calcium level. Eggs were examined at

1-4 h PI and actin filaments and microtubules were stained for observation under confocal microscopy. In normally fertilized egg, the meiotic spindle anchored at the cortex rotates from horizontal to perpendicular against oolemma during the second meiosis and microfilaments form the contractile ring around the equatorial plate of the spindle to extrude the PBII (Fig.3a-c). In eggs with disturbed PBII extrusion, the spindle rotation was inhibited and microfilaments aggregated without forming the ring structure, or sometimes the ring structure were found in the center of the ooplasm (Fig.3d-f). In addition, distribution of two isotypes of actin molecules in egg with disturbed PBII extrusion were found different from normal egg. Because the dynamics of the meiotic spindle during fertilization is coordinated by various cytoskeletal components, these results suggested that high calcium level may disrupt the machineries involved in the dynamics of the meiotic spindle during fertilization.

Based on the above results, for IVF of C3H/He we decided not to use the medium with high calcium level that has been successfully applied to other strains. Various studies, including our own [3] indicate that conditions of IVF are different among inbred strains, and that optimal IVF conditions have to be examined on a strain by strain basis at least for frequently used strains in individual institutes. Our research about ARTs has been well applied to our routine work to obtain large numbers of embryos at a time and has played an important role in conducting animal research in NIRS. Currently, our research has moved to improve IVF conditions for frozen-thawed sperm which are often damaged by the freezing process and may require somewhat different conditions from fresh unfrozen sperm.

#### References

- [1] Toyoda Y, et al., *Jpn J Anim Reprod*, 16, 147, 1971.
- [2] Kito S, Ohta Y, *Zygote* 16, 249, 2008.
- [3] Kito S, et al., *Comp Med*. 54, 564, 2004.
- [4] Ohta Y, et al., *Zygote* 24, 603, 2015. doi:10.1017/S096719941500060X.

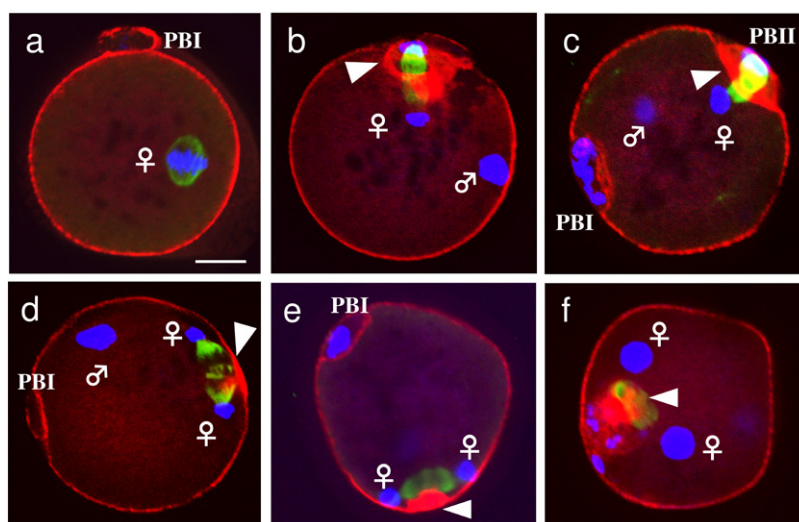


Fig.3 Confocal images of cytoskeletal organization of C3H/He eggs fertilized in 1.71 or 6.84 mM calcium. The scale bar indicates approximately 20  $\mu\text{m}$ . PBI: the first polar body. PBII: the second polar body. ♀: egg chromosome(s) or female PN(s). ♂: decondensing sperm head or male pronucleus (PN). Microtubules, actin filaments and chromosomes are shown by green, red and blue, respectively. a) In an egg at metaphase II before insemination, chromosomes are arranged at the equatorial plate and the long axis of the spindle is parallel to the nearest oolemma. b) At 2 h PI in 1.71 mM calcium, the chromosomes separate toward the two spindle poles. The spindle has oriented with its long axis perpendicular to the oolemma, and actin filaments start to form the contractile ring (arrowhead). c) At 3 h PI in 1.71 mM calcium, the PBII has already extruded and the contractile ring (arrowhead) has shrunk with the spindle located in the ring. d) At 2 h PI in 6.84 mM calcium, the egg has almost completed the second meiosis, while the spindle has located with its long axis parallel to the nearest oolemma. Actin filaments start to localize around the oolemma over the equatorial plate of the spindle (arrowhead). e) At 3 h PI in 6.84 mM calcium, the spindle is still located with its long axis parallel to the nearest oolemma and no sign of PBII extrusion is observed. A clump of actin enlarges compared with 2 h PI (d), but no ring structure is formed. f) At 4 h PI in 6.84 mM calcium, the PBII fails to extrude and two female PNs and a single male PN (out of focus) are observed. In this particular egg, actin filaments form the ring-like structure (arrowhead) in the cytoplasm without any sign of cytokinesis.

# Fukushima Project Headquarters

## Atsuro Ishida

*Deputy Director, Fukushima Project Headquarters*

E-mail: ishida.atsuro@qst.go.jp

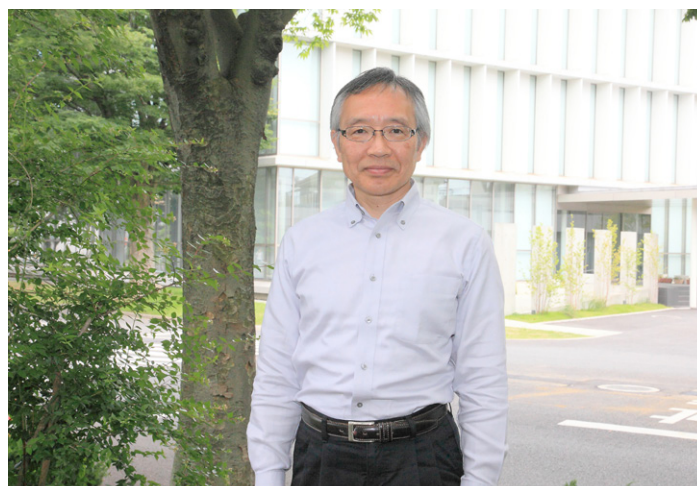
In order to support restoration and revitalization of Fukushima Prefecture following the nuclear accident at the Fukushima Daiichi Nuclear Power Plant (NPP), the Fukushima Project Headquarters was established in May 2012. The headquarters manages three research projects, Project for Human Health, Radiation Effect Accumulation and Prevention Project, and Project for Environmental Dynamics and Radiation Effects; these were chosen after consideration of the major concerns of people living in the prefecture.

### 1) Project for Human Health

This project started an epidemiological investigation with the cooperation of first responders who worked at Fukushima Daiichi NPP controlling the accident in the early stage. The project will monitor their health status by collecting relevant information. The database was developed with special attention to security of the collected information for long-term follow-up. More than 600 workers have been registered so far in the database along with the data of a baseline questionnaire survey on lifestyle, disease history, etc., and the data of annual medical check-up results. Preliminary analyses show that there are no demonstrable effects of radiation exposure on the workers' health status. The findings from the follow-up study are expected to be used for workers' health care, as well as for evaluating health effects of low dose radiation exposure.

The project also developed the NIRS external dose estimation system for Fukushima residents to estimate the external effective doses for the first four months after the Fukushima Daiichi NPP accident. This system has been adopted in the Fukushima Health Management Survey, which is a long-term health management survey for all people of Fukushima Prefecture, conducted by Fukushima Medical University, and the estimated results were provided to the Fukushima residents, individually. This task can be very useful as the first approximation of the external effective doses to Fukushima residents by the accident.

The results of the external dose estimations have been reported periodically in the Prefectural Oversight Committee Meeting for Fukushima Health Management Survey. According to the proceedings of the committee meeting held on 15 February 2016, the dose estimations for 547,380 residents among the entire population of Fukushima (about 2 million) have been performed. Among them, the doses of 468,748 residents were summarized, excluding the residents whose available survey data were for the period of less than four months. The doses of 62% of the residents were less than 1 mSv during



four months after the accident. The doses of 99.8% of the residents were less than 5 mSv. The maximum dose of the residents including radiation workers was 66 mSv. When excluding the workers, the maximum dose was 25 mSv.

### 2) Radiation Effect Accumulation and Prevention Project

This project aims at elucidating the effects of low-dose-rate radiation and its underlying mechanism, and then at providing possible measures to mitigate the risks based on findings using animal models. In order to answer the major questions determined from the concerns of Fukushima residents, the project conducts the following three research programs.

- i) Effects of the low-dose-rate radiation on life shortening and cancer induction are being examined for infant exposure in comparison with adult exposure, to confirm if the dose-rate effect for children is the same as that for adults.

The carcinogenic effect of the low-dose-rate radiation for the infant period was lower than that of the high-dose-rate radiation, resulting in an extension of the life span. In order to confirm the cancer incidence for every organ, pathological analyses are being continued.

- ii) Accumulation of radiation effects in the stem cells of the skin and mammary glands is being evaluated, to clarify if the dose-rate effect can be explained in part by the reduced accumulation of radiation-induced damage in stem cells or by the elimination of damaged stem cells.

It was shown that the accumulation of the radiation damage was low in a mammary stem cell culture model. In addition, it was clarified that the radiation effects on hair follicle stem cells increased in a dose-dependent manner and they last after cell proliferation.

- iii) Inhibitory effects of calorie restriction (CR) and antioxidant food ingredients on radiation-induced cancer are being investigated, to provide possible approaches to reduce the cancer risk after childhood exposure by subsequent control of diet.

The animal experiment to make 15% or 30% CRs from six months of age after irradiation at 1 week of age is being continued. Preliminary result showed that the inhibitory effect of CR was lower than that of CR from 7 weeks of age and there was no apparent difference between 15% and 30%.

### 3) Project for Environmental Dynamics and Radiation Effects

This project started the following two research programs related to the environmental contamination in Fukushima Prefecture.

- i) Estimation of radiation doses for Fukushima residents from surrounding ecosystems, and providing countermeasures to minimize the received dose. After coming back to their homes, many of the evacuees have been afraid of encountering high radiation doses from the contaminated environment and from the ingestion of radioactive materials from foods and water. In order to estimate long-term radiation doses of the residents from the surrounding environment during their daily life, the project started dose-estimation-oriented collection of environmental samples considering the migration of radioactive materials in the environment.

A highly precise analysis of Sr-90 concentration of 0.7 mBq has been achieved using TIMS. A survey of the radionuclide was carried out in migration studies on domestic animals and wildlife as well as for forest and coastal waters, and the activities tended to decrease year by year. The external exposure dose measurements of Fukushima inhabitants have been carried out, and an internal dose management tool has been developed.

- ii) Assessment of radiation effects on non-human biota in contaminated ecosystems. High contamination levels of the environment suggest possible effects of radiation on non-human biota. Although dramatic effects such as the "red forests" in contaminated Chernobyl areas have not

been observed, long-term studies are required to estimate the environmental effects. The project is collecting biological samples such as pine needles and pine cones, wild mice, and salamanders in heavily contaminated areas, and is estimating radiation effects using different endpoints (e.g. growth rate, reproduction and chromosome aberration).

Japanese fir populations near the Fukushima Daiichi NPP showed a significantly increased number of morphological defects, involving deletions of leader shoots of the main axis, compared to a control population far from the plant site. The frequency of the defects corresponded to the radioactive contamination levels of the observation sites.

The induction of chromosomal aberrations in splenic lymphocytes of small Japanese field mice (*Apodemus argenteus*) and house mice (*Mus musculus*) inhabiting the moderately and heavily contaminated areas of Fukushima Prefecture was significantly increased.

The highest dose rate to the Tohoku hynobiid salamanders, *Hynobius lichenatus*, was estimated to be 50  $\mu\text{Gy h}^{-1}$  in the most severely contaminated habitat in Fukushima Prefecture. The growth and survival of this amphibian were not affected at a dose rate of up to 490  $\mu\text{Gy h}^{-1}$  in the laboratory chronic gamma-irradiation experiment, suggesting that radioactive contamination would not severely affect *H. lichenatus* in Fukushima.

### 4) Other activities

In addition to the three projects, the headquarters manages telephone consultations in order to relieve the anxiety of people and to support research activities of the projects.

These consultations were operated by NIRS's staff members by turn for 24 hours a day, seven days a week for the first two weeks from March 17, 2011. The service continues to be run but with a reduced size, and a total of about 20,000 telephone calls have been received so far.

In the following highlight, four research topics are introduced from two research projects, the Project for Environmental Dynamics and Radiation Effects and the Radiation Effect Accumulation and Prevention Project.

## Highlight

# Research on characteristics of individual doses in Fukushima Prefecture after the Fukushima nuclear accident

**Kazuaki Yajima, Osamu Kurihara, Eunjoo Kim,  
Keiichi Akahane, Yasushi Ohmachi,  
Satoshi Yoshida**

E-mail: yajima.kazuaki@qst.go.jp

## Introduction

Huge amounts of radioactive materials were released into the environment as a result of the Fukushima nuclear accident. The radioactive contamination caused elevated ambient external dose rates in a wide area of Fukushima Prefecture. Evacuees in the whole of Fukushima Prefecture totaled 154,000 as of March 2014. Elevated ambient external dose rates have been decreasing due to physical decay, the weathering effect, and decontamination. In August 2013, the Japanese government finished reorganizing the three designated evacuation directive areas according to the projected radiation dose: the difficult-to-return area (>50 mSv), the restricted habitation area (20–50 mSv), and the evacuation-directive-lift-prepared area (<20 mSv). The lifting of the evacuation directive began first in Tamura City in April 2014. It is important that the level of the individual dose assumed after evacuees return home is substantially perceived. Aiming at investigating the relationship between individual doses based on a personal dosimeter measurements and ambient external dose by field measurements and experiments in an irradiation facility, and to estimate annual individual doses for representative lifestyles and occupations based on the ambient external dose rates at the measurement sites, a collaborative research study was carried out from August 2013 by the National Institute of Radiological Sciences (NIRS) and the Japan Atomic Energy Agency (JAEA) at the request of the Nuclear Emergency Response Headquarters, Cabinet Office [1][2]. In this report, an overview of the NIRS and JAEA research is given, with particular emphasis on estimation of the annual individual dose that mainly the NIRS was in charge of.

## Measurements

The field measurements were carried out during August and September 2013 in Kawauchi Village, Tamura City (Miyakoji District), and Iitate Village in Fukushima Prefecture. At the time the measurements were performed, the measurement sites were located mostly in either a restricted habitation area or an evacuation-directive-lift-prepared area. The 28 measurement sites were decided considering the likely lifestyles of residents in various occupations (e.g. private house, schools, farmlands, forests).

Ambient external dose rates at the sites were measured using NaI(Tl) scintillation survey meters (TCS-172B, Hitachi Aloka Medical) which were adjusted to give a response in the ambient external dose equivalent  $H^*(10)$  based on ICRP publication 74. The probes of the survey meters were set to an altitude of 1 m from the ground or floor. Individual doses were measured with Electric Personal Dosimeters (EPDs) (DOSE-e, Fuji Electric



Co.) worn by an NIRS staff member on the chest. The EPDs were modified by the manufacturer to display doses in personal dose equivalents  $H_p(10)$  based on ICRP publication 74. NIRS staff members carried portable global positioning system (GPS) data loggers and memo pads to record each action and event during the measurements. The measured individual doses integrated during a certain period were compared to the ambient external doses calculated from the ambient external dose rate measured at the same locations. A car-borne survey system "RADI-PROBE" was used to obtain the doses received while commuting a certain route. On the other hand, additional experiments for the response of several types of EPDs adhered to a 30 cm × 30 cm × 15 cm or 40 cm × 40 cm × 15 cm PMMA slab phantom set at several sites and at an irradiation facility were carried out by the JAEA.

## Relationship between the ambient external dose and individual dose

The relationship between the ambient external dose estimated from the ambient external dose rate measurement and individual doses measured with the EPDs worn by NIRS staff persons (A-E) is shown in Fig.1. The ratio of the measured individual dose to the ambient external dose was found to be 0.7 with 10% uncertainty for all the staff members excluding staff person B. This small difference is caused by the physical constitution of staff person B (170 cm tall and 145 kg in weight). The experiments for the EPDs response using PMMA slab phantoms by the JAEA showed similar results.

Thus, it was found that the ratio of the individual dose to ambient external dose was approx. 0.7 from the measurements in this work, and it was sufficient to estimate an individual dose by multiplying 0.7 by the ambient external doses in the investigated area.

## Estimation of the individual dose

Annual individual doses to adult residents living in Kawauchi Village, Tamura City (Miyakoji District), and Iitate Village

were calculated for some model cases under the following conditions.

- (1) Representative lifestyles and occupations (farmer, forest worker, office worker, school staff, and home-based individuals) were assumed. Time allocations for each place of residence were created for each occupation by referring to statistical data on Japanese lifestyles, and they are presented in Table 1.
- (2) The relationship between the ambient external dose and individual dose was taken into account: (individual dose) =  $0.7 \times$  (ambient external dose).
- (3) Living and working places were selected from the measurement sites assuming the lifestyle for each occupation and each investigated area. The calculation was based on the measured ambient external dose rates at the measurement site. The dose received during the commute between a private house and a workplace was also considered.
- (4) The dose rate of  $0.04 \mu\text{Sv/h}$  was used as a natural background dose rate.
- (5) The annual individual dose excluding natural background radiation was calculated for the 1 year just after the field measurements of this study. The predictable decrease of the ambient external dose rates was not taken into account.

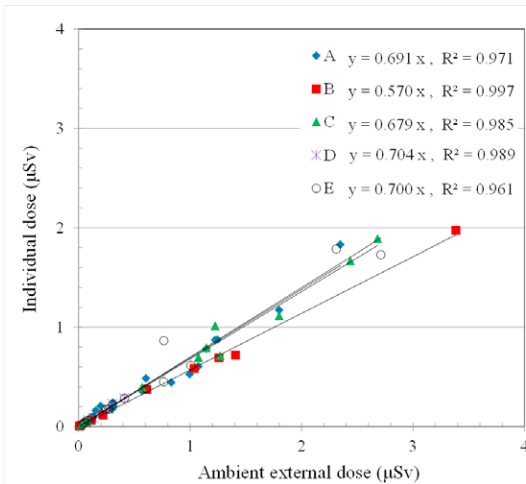


Fig.1 Relationship between the ambient external dose and individual dose for staff members A to E [1][2].

Figure 2 shows a conceptual diagram of the estimation method for a model case in which a school staff member commutes to a school located in a living area by car from a private house located in a restricted habitation area. The estimated annual individual doses according to various occupations in each area are summarized as follows.

- Tamura City: 0.6 mSv/y (Office) to 2.3 mSv/y (Forest)
- Kawauchi Village: 1.1 mSv/y (School) to 5.5 mSv/y (Forest)
- Iitate Village: 3.8 mSv/y (School) to 17.0 mSv/y (Forest)

The estimated doses of outdoor workers (forest workers) were higher than those of indoor workers (school staff member or office workers). This is caused by the fact that the ambient external dose rates in forests were higher than the surroundings regardless of decontamination, and the reinforced concrete construction of school buildings had a large shielding effect. It is thought that an easy and effective measure to reduce annual individual dose may be to reduce the time spent outdoors, for example, taking work breaks indoors.

### Conclusion

It was found that the ratio of the individual dose to ambient external dose was approx. 0.7 from the measurements performed in Tamura City, Kawauchi Village, and Iitate Village in Fukushima Prefecture. It was suggested that the estimation in the present work gives more realistic individual doses in response to each individual's radiation environment and lifestyle compared to the estimation based on the airborne survey and a certain lifestyle (e.g. 16 h for time spent indoors and 8 h for time spent outdoors). It is hoped that this research will contribute to the reconstruction and revitalization of Fukushima Prefecture.

Table 1 Time spent for each occupational category [1].

Occupational category	Time spent (h)			
	House *	Outdoor workplace	Indoor workplace	Commute *
Farmer	17.54	6.28	0	0.19
Forest worker				
Office worker	15.37	0.49	7.29	0.85
School staff				
Home-based individual	22.93	1.07	0	0

\* This calculation was performed using an actual commuting time based on the measurement.

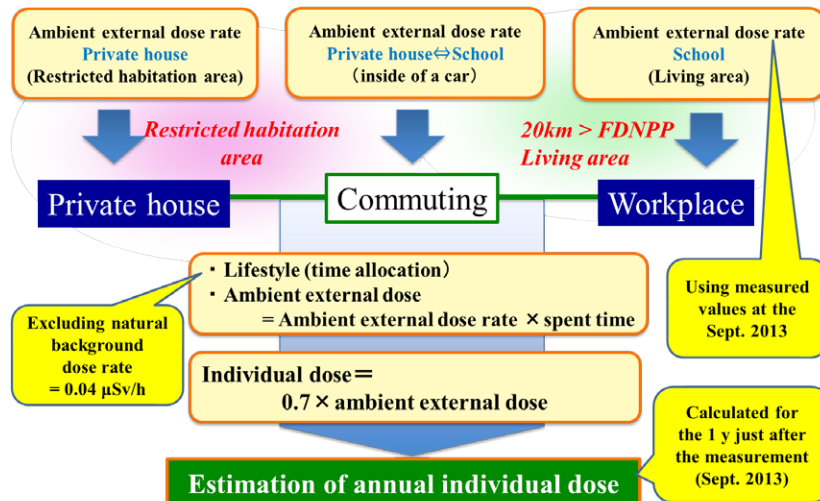


Fig.2 Conceptual diagram of the estimation method.

### References

- [1] Yajima K., et al., *Health Phys*, 109, 122, 2015.
- [2] NIRS and JAEA, NIRS-M-270, 2014.  
Available at <http://www.nirs.qst.go.jp/publication/irregular/index.html>

## Highlight

## Reconstruction of early internal doses to Fukushima residents after Fukushima Daiichi NPP accident

Eunjoo Kim, Osamu Kurihara

E-mail: kim.eunjoo@qst.go.jp

In FY 2012 we performed reconstruction of early internal doses to Fukushima residents living in the radiologically affected areas using a combination of the following three sources: thyroid measurement data ( $^{131}\text{I}$ ) for 1,080 children examined in the screening campaign, whole-body counter measurement data ( $^{134}\text{Cs}$ ,  $^{137}\text{Cs}$ ) for 3,000 adults, and atmospheric transport dispersion model simulations. This highlight describes the basics of the internal thyroid dose estimation and our subsequent attempts to improve the methodology for the most recent estimation.

### Internal dose estimation in FY 2012

Enormous amounts of radionuclides were released into the environment from the damaged reactor cores, exposing the public to radiation through several pathways. Dose estimation for people in the region is of great importance to assess the potential radiological risks to Fukushima residents in the future. Unfortunately, the number of human measurements available for directly estimating the thyroid equivalent dose (hereinafter, the "thyroid dose") due to the intake of  $^{131}\text{I}$  has been limited. The NIRS performed internal dose estimations for residents using a combination of the following three sources. The first was thyroid measurement data ( $^{131}\text{I}$ ) obtained from 1,080 children (under 15-y) examined in screening campaigns conducted in Kawamata Town, Iitate Village and Iwaki City by the Nuclear Emergency Response Local Headquarters at the end of March 2011 [1]; the second was the committed effective doses (CEDs) from radiocesium ( $^{134}\text{Cs}$ ,  $^{137}\text{Cs}$ ) of about 3,000 adult subjects examined in the WBC measurements by the Japan Atomic Energy Agency (JAEA) in the period between 11 July 2011 and 31 January 2012 [2] and the third was the time-series, ground-level air concentration maps ( $^{131}\text{I}$ ) generated by the Worldwide version of System for Prediction of Environmental Emergency Dose Information 2nd Version (WSPEEDI-II) with the latest source term at that time [3].

The thyroid measurement data among three sources are the most reliable data. In this estimation, two items were revised from those originally decided to determine the screening level. One was the age-dependent children factor converting the net readings from NaI(Tl) scintillation survey meter to the  $^{131}\text{I}$  radioactivity in the thyroid. This work used the modified factors that were calculated by the averages of the original factors used in the screening campaign and a previous study [4]. Another revised factor was the time of intake assumed in the intake scenario from chronic intake with a constant inhalation rate from 12 March to 23 March 2011 to acute intake on 15 March 2011. This change was considered reasonable in terms of conservative dose estimations because no significant elevation of the



ambient dose rate was observed before 15 March in the municipalities where the screening campaign was conducted.

CEDs obtained by the JAEA are human measurement data, but they were not directly linked to the intake of  $^{131}\text{I}$ . Moreover, only CEDs of adult subjects ( $\geq 18$ -y) of the WBC measurements could be used because of ethical issues at that time. The CEDs were evaluated based on the measured whole-body contents along with a common intake scenario, namely acute intake by inhalation of Type F compounds on 12 March 2011 [2]. Fortunately, no median CED value could be obtained from most of the municipalities because of non-detection for many subjects in the prolonged WBC measurements.

The intake ratio of  $^{131}\text{I}$  to  $^{137}\text{Cs}$  was derived from human measurement data of Iitate Village and Kawamata Town [5]. In these two municipalities, both the thyroid doses to children from  $^{131}\text{I}$  and the CEDs to adults from  $^{134}\text{Cs}$  and  $^{137}\text{Cs}$  were obtained. These two doses could be linked to each other on the assumption that adults and children inhaled air with the same intake ratio of the two radionuclides at different breathing volume rates (e.g., 5.16 m<sup>3</sup> per day for 1-y children, 22.2 m<sup>3</sup> per day for adult males [6]). This relationship is illustrated in Fig.1. The intake ratio of  $^{131}\text{I}$  to  $^{137}\text{Cs}$  was then derived by applying a thyroid dose and a CED at the same percentile to this relationship for the age group of 10-y children. The results are provided in Table 1.

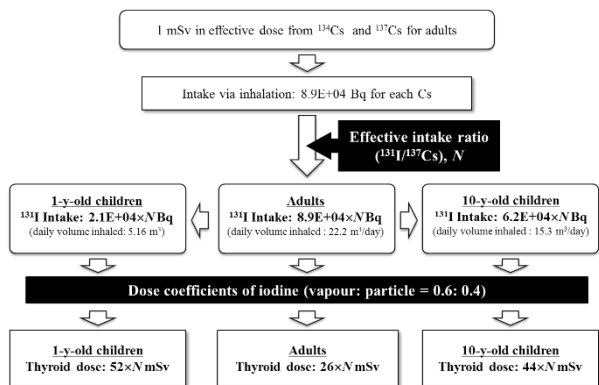


Fig.1 Relationship between the thyroid doses to children and the effective doses to adults.

Table 1 Derived intake ratios of <sup>131</sup>I to <sup>137</sup>Cs.

Municipality	95th percentile	90th percentile	80th percentile
Kawamata Town	3.3	2.4	2.7
Iitate Village	2.1	2.0	2.3

The third source was used to compensate for the shortage of human data. In this study, internal doses due to the inhalation of nuclides were calculated from time-series ground-level air concentration maps generated by WSPEESI-II [7]. The results demonstrated a tendency for the simulation to overestimate the doses in comparison to those determined using human measurements. This discrepancy would be minimized by incorporating individual behavior data containing the whereabouts of each person shortly after the accident and the time spent indoors/outdoors.

By combining the above three sources, the internal doses to Fukushima residents were estimated as shown in Table 2. The figures in the table are given as a 90th percentile value (rounded to the nearest 10%) of the internal thyroid doses to 1-y children and adults excluding the municipalities where the simulation was applied to the estimation. The internal thyroid dose was expected to be relatively higher in residents of Futaba Town, Iitate Village and Iwaki City than in the rest of the municipalities. Their thyroid doses were estimated to be mostly below 30 mSv, which was comparable to the estimations of other studies [8, 9]. Regarding Minami-soma City and Katsurao Village, the thyroid doses were assumed to be the same level as that for Namie Town neighboring these municipalities. Regarding Iwaki City, the simulation result was more heavily weighted in the estimation than the screening campaign result because the number of subjects in the latter was small in comparison to the population of youth (under 15-y) of Iwaki City.

Table 2 Internal thyroid doses to 1-y children and adults.

Municipality	1-y children	Adults	Method
Futaba Town	30	10	WBC
Okuma Town	20	< 10	WBC
Tomioka Town	10	< 10	WBC
Naraha Town	10	< 10	WBC
Hirono Town	20	< 10	WBC
Namie Town	20	< 10	WBC, Ref. [7]
Iitate village	30	20	Thyroid, WBC
Kawamata Town	10	< 10	Thyroid, WBC
Kawauchi Village	< 10	< 10	WBC
Katsurao Village	20	< 10	Same as Namie
Iwaki City	30	10	Simulation, Thyroid
Minami-soma City	20	< 10	Same as Namie
Other areas in Fukushima Pref.	< 10	< 10	Simulation

### New approach for the estimation

The internal thyroid dose estimation by the NIRS in FY 2012 showed only the upper dose levels for Fukushima residents. Needless to say, more detailed dose estimation has been needed, in particular, in order to clarify whether anyone in the area received significant radiation exposure. Figure 2 shows the proposed new method. As shown in the figure, the main feature of the proposed method is to characterize subject groups depending on their behavior patterns and internal dose levels and determine representative doses for each subject group. These representative doses could be assigned to persons who were not measured, but who acted in a similar way to those who were measured. The personal behavior data used in this method are basically the same as those used as input data for the NIRS external dose estimation system, which has been developed to perform the Basic Survey that is one of the main components of the Fukushima Health Management Survey [10]. These data include the whereabouts (the place-name and its latitude and longitude) and time spent indoors, outdoors or moving during the first four months after the accident. The behavior data for persons who were measured within one year after the accident became available through the approval of the research ethics committee of NIRS and Fukushima Medical University in 2013. To the present, NIRS has received 412 personal behavior data sets from FMU including 310 of the 1080 subjects of the screening campaign and 112 of 174 subjects of the pilot survey that was conducted by NIRS during the period between 27 June and 28 July 2011.

The internal dose estimations using the proposed method are ongoing for more detailed dose estimations based on the behavior data and these results will be reported in the future.

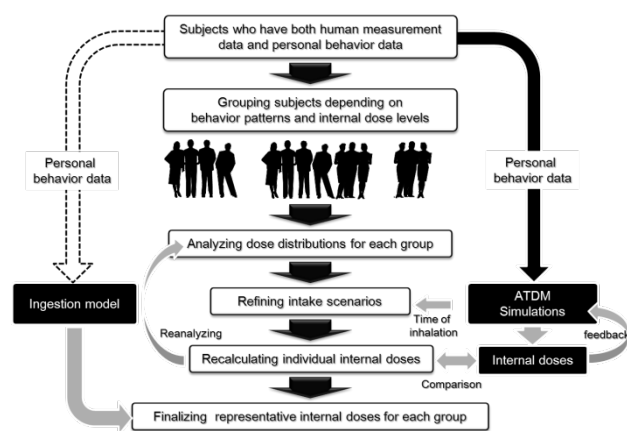


Fig.2 Proposed method for the internal dose estimation.

### References

- [1] Kim E. *et al. NIRS-M-252*, 59-66, 2012.
- [2] Momose T. *et al. NIRS-M-252*, 67-71, 2012.
- [3] Terada H. *et al. J Environ Radioact*, 112, 141, 2012.
- [4] Tanaka G and Kawamura H. *J Radiat Res*, 19, 78, 1978.
- [5] Kim E. *et al. Radiat Prot Dosim*, 168, 408, 2016.
- [6] International Commission on Radiological Protection. *ICRP Publication 71*. Pergamon, 1995.
- [7] Kim E. *et al. Radiat Prot Dosim* 2015. doi:10.1093/rpd/ncv385
- [8] Tokonami S. *et al. Sci Rep*, 2, 507, 2012.
- [9] Matsuda N. *et al. Radiat Res*, 179, 663, 2013.
- [10] Yasumura S. *et al. J Epidemiol*, 22, 375, 2012.

## Highlight

## Effects of age at exposure on the life shortening and tumor incidence after low-dose-rate irradiation in mice

**Yutaka Yamada, Takamitsu Morioka,  
Shunsuke Yamazaki, Shizuko Kakinuma,  
Yoshiya Shimada**

E-mail: yamada.yutaka@qst.go.jp

### Introduction

In the accident at TEPCO's Fukushima Daiichi Nuclear Power Plant, radioactive materials were released into the environment, and the radiation background level increased. Because some residents will be living in a high background area, attention is focused on health effects of a low-dose-rate radiation exposure for a long term. Especially, the protection of children to radiation effects has been of particular concern and parents are extremely worried about this.

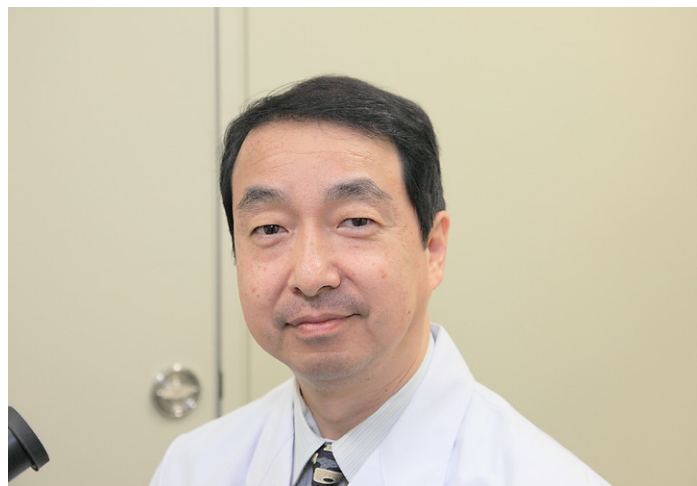
From animal experiments and epidemiological studies of inhabitants of high background areas, it is known that the risks of radiation exposure at the low-dose-rate for a long term become smaller than those of the single exposure to high-dose-rate radiation. With the current radiation protection system, the reduction factor (dose and dose-rate effectiveness factor: DDREF) of 2 is chosen by ICRP and NCRP [1],[2]. After that, the ICRP formally began discussions reexamining the basis for estimating risks due to low-dose exposure and to low-dose-rate exposure, and it established Task Group 91 to deal with the matter in 2013.

Generally, susceptibility of children to radiation is greater than that of adults, and it is known that the carcinogenic risk is high in children, but the effects caused by low-dose-rate radiation in children have not been examined to any extent. It remains unclear what the effects of low-dose-rate radiation exposure in children are and what the estimated risks are. (In other words, how large is the DDREF value in children?) It is an important matter for precise radiation protection to take measures to clarify the risks and the mechanism of the effects of low-dose-rate radiation in children.

The purpose of the study described here is to elucidate the effects of low-dose-rate radiation and its underlying mechanism using animal models. The effects of the low dose-rate radiation on life shortening and cancer induction are being examined for infant-juvenile exposure in comparison with adult exposure.

### Material and Method

A total of 1400 (700 per sex) specific-pathogen-free (SPF) B6C3F1 mice are being used in this study. The animals were divided into four groups of 100, three irradiated and one non-irradiated control (Table 1). The strain is a first generation hybrid (C57BL/6J and C3H/He) widely used in carcinogenicity studies. The mice in the infant (1 week old), young adult (7 weeks) and adult (15 weeks) stages were gamma (Cs 137) -irradiated at low-dose-rate for 4 consecutive weeks. The dose rates were 0.026 mGy/min and 0.105 mGy/min (total exposure doses of 1 Gy and 4 Gy, respectively) (Fig.1). The life shortening and incidence of leukemia and solid cancers are being investigated.



The dose-rate effectiveness factor (DREF) will be estimated in comparison with the data of single irradiation exposure in a previous study [3].

### Results

The survival of these animals is now being followed. In the preliminary results, the irradiated groups tend to have shorter life spans compared to the non-irradiated controls. The survival curve for groups (1-4, 7-10 and 15-18 weeks) irradiated to 4 Gy shifted toward the left compared to the groups irradiated to 1 Gy, indicating dose dependency. Comparisons of the life spans between ages at exposure have appeared to show no differences in the results to the present time.

The information obtained from the previous high-dose-rate study is being used in conjunction with the low-dose-rate information obtained in the present study to assess the influence of dose rate on life span after irradiation. In the case of exposure when 1 week old, preliminary results from the pathological studies suggested that the major cause of the life shortening at 4 Gy of high-dose-rate irradiation might be the appearance of thymic lymphoma in the early period, but 4 Gy of low-dose-rate irradiation might not have the same life shortening cause. The life shortening days per Gy of high-dose-rate and low-dose-rate irradiation were about 90 and 30 days, respectively, so that the DREF appeared to be around 3. All the data are being analyzed in detail.

The major neoplasms of the control group at the time of death have been lymphoma, liver tumor, lung tumor and hardenarian gland tumor in both sexes, and pituitary tumor and ovary tumor in female mice. The spectra of neoplasms observed in both the control and low-dose-rate irradiated mice appeared to be mostly similar to the present data.

It is necessary to continue the experiment to clarify the carcinogenic effect and age at exposure dependence caused by the low-dose-rate irradiation.

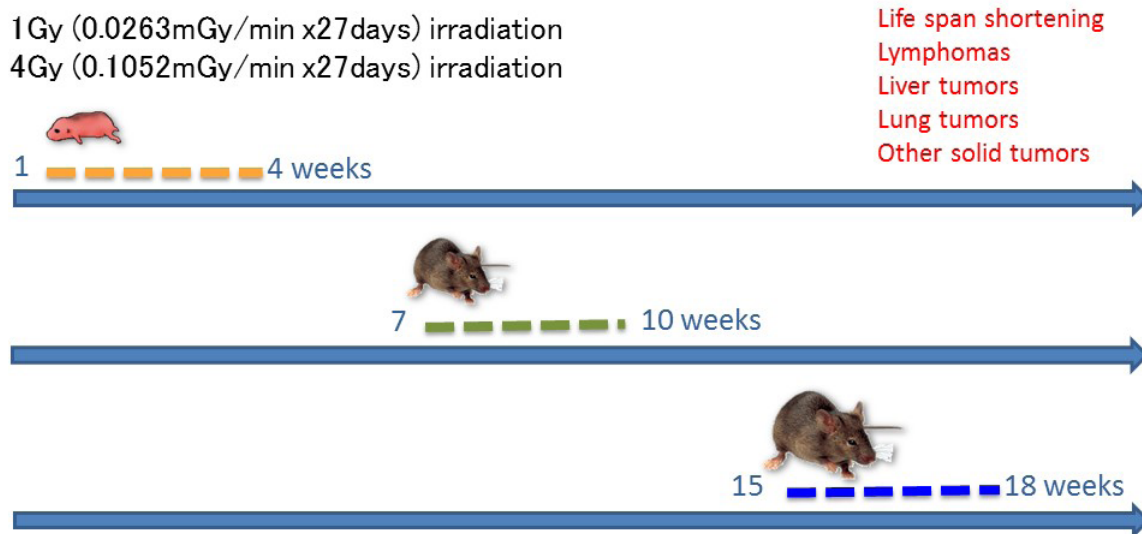


Fig.1 Experiment design of low-dose-rate exposure.

Table 1 Animal numbers of experimental groups.

	1 Gy		4Gy	
	female	male	female	male
Infant - juvenile (1-4 weeks)	100	100	100	100
Young adult (7-10 weeks)	100	100	100	100
Adult (15-18 weeks)	100	100	100	100

Control : female 100 male 100

**References**

- [1] ICRP, 1990 Recommendations of the International Commission on Radiological Protection. ICRP Publication 60. *Ann. ICRP* 21 (1-3), 1991.
- [2] NCRP Report No.116: Limitation of Exposure to Ionizing Radiation, 1993.
- [3] NIRS Annual Reports: Research for Radiation Protection. 2014.

# Research on Evaluation of Medical Exposure

## Yoshiya Shimada, Ph.D.

Director, Medical Exposure Research Project

E-mail: shimada.yoshiya@qst.go.jp

In this just-completed midterm plan at NIRS, the Medical Exposure Research Project (MER-project) has had a mission to investigate the frequencies and doses of Japanese medical radiation uses, both diagnostic and therapeutic. The data are being collected in collaboration with local hospitals and academic societies. These data will be stored in a national database of medical exposure (details for this are under contemplation) and used as scientific and practical purposes for the justification and optimization of radiation protection in medicine. They will also be provided for the UNSCEAR global survey project.

Five studies are being undertaken currently: (i) Estimations of examination frequencies and organ doses in X-ray CT, PET, and PET/CT in collaboration with local hospitals and academic societies; (ii) Organ dose estimations of patients for diagnosis and radiotherapy; (iii) Study of radiobiology in radiation use in medicine; (vi) Development of the method for risk-benefit communications in medicine; and (v) Running an organization (J-RIME: Japan Network for Research and Information on Medical Exposure) for the exchange of information on radiation protection in medicine. Their short descriptions follow.

### (1) Estimation of CT and PET doses

**CT dose.** WAZA-ARI is the web-based open system for the CT dose calculation, which has been developed by Oita University of Nursing and Health Sciences and the Japan Atomic Energy Agency (JAEA). From December 2012, it has been installed in the web server of NIRS, and is available to the public for trial use.

This year, using the improved WAZA-ARI "WAZA-ARlv2", we investigated CT doses in the NIRS hospital; we inputted the exposure conditions on about 500 CT examinations in cooperation with radiological technologists and calculated organ doses and effective doses. Those doses from devices with auto exposure control (AEC) were compared with doses without the AEC.

We also enhanced convenience of use for the functions of exposure conditions and statistical analysis and increased the information of dose coefficients corresponding to more CT scanner models. We held seminars in all over Japan to promote the expanded use of WAZA-ARI in medical settings. The number of registered users was increased to 700 (Fig.1).

**PET dose.** A physiologically based pharmacokinetics model (PBPK model) has been used to describe the kinetics of pharmaceuticals physiologically by using physiological parameters such as blood flow, organ volume, etc. in the pharmacokinetics field. For the internal dose estimation for FDG-PET examinations, we have modified and applied the PBPK-model, which can consider the differences among patients who have different body sizes and metabolisms (see the following highlight for details).

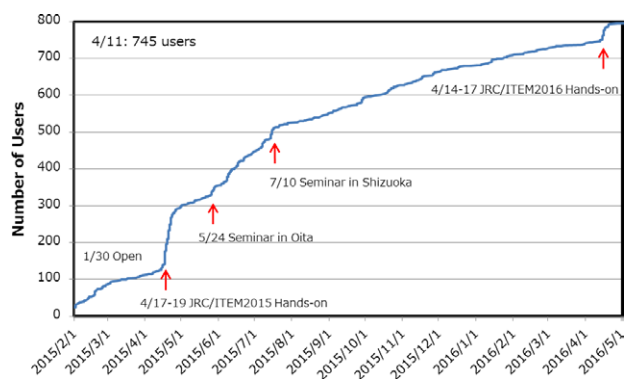
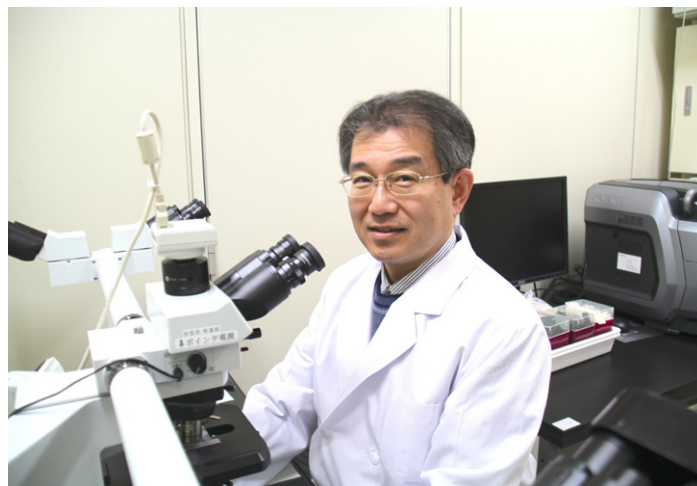


Fig.1 The number of registered users.

### (2) Estimation of organ dose in radiotherapy

Recent progresses in radiotherapy can provide benefits to patients with extended survival. On the other hand, the secondary cancer risk by undesired irradiation to non-target healthy tissue is of concern to the survivors.

In 2014, we developed the 3D dose map for estimation of non-target organ doses of the pelvic field using an anthropomorphic phantom and polymer gel dosimeter in radiotherapy for uterine cervical cancer. In 2015, we analyzed the 3D dose distributions of the organs of patients of uterine cervical cancer radiotherapy by using a typical treatment plan, in which irradiation conditions were determined based on the facts of the radiotherapy in the NIRS hospital.

Currently, we have estimated the organ doses of pediatric patients exposed to secondary neutrons after proton therapy using a Monte Carlo simulation code (PHITS); the photon beam line and 5-year-old voxel phantom were modeled (Fig.2). The secondary neutron doses of the non-target tissues were higher so as to be closer to the treatment target. The measurement techniques using an infant physics phantom were also verified to test the possible use of radio-activation of the phantom material for verification of the dose delivery distribution and to assess the doses of heterogeneous body materials (such as bones, muscles and fat) of the proton beam transmission area.

### (3) Dose Index Registry

The importance of tracking dose of patients with medical radiation exposure, which is the concept behind the IAEA's "Smart Card/SmartRadTrack project", has been acknowledged. We are developing an automatic dose collection system and database for CT examinations, which enables the transfer of DICOM data from devices of different manufacturers into one database (Fig.3). This system can collect CT radiation dose information in large quantities more correctly, compared to conventional questionnaire patterns. This makes it possible to compare the data of one medical institution with those of other medical institutions, so to reduce the variations of CT radiation doses among the institutions.

In 2015, the system became available for data collection from all CT makers. By December 2015, we had connected data acquisition tools to hospital PACS servers or CT devices of 30 medical institutions directly, and collected information on 80,000 CT examinations. These data can be shared among

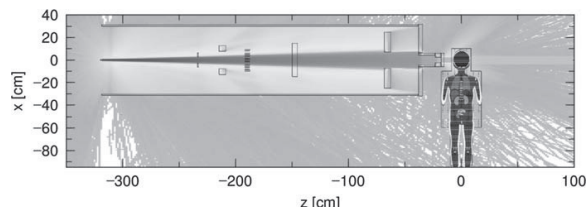


Fig.2 Dose estimation of pediatric patients exposed to secondary neutrons after proton therapy.

NIRS and cooperative institutions by using the VPN.

### (4) Development of the method for risk-benefit communications in medicine

Increasing awareness and knowledge about radiation protection in medicine is necessary to answer the public's concerns on health risks of low-dose radiation exposure including medical exposure.

Toward that end, we prepared materials explaining a risk assessment/management of radiological examinations. The main contents are global trends of medical exposure, dose assessment of medical exposure in Japan, radiation risk of diagnostic imaging in pediatric patients, improving radiation protection in pediatric imaging, creating better communications between medical staff members and parents of patients, and other related topics. The materials have been delivered into healthcare settings through the training courses hosted by NIRS, such as courses for young radiologists and for medical physicians.

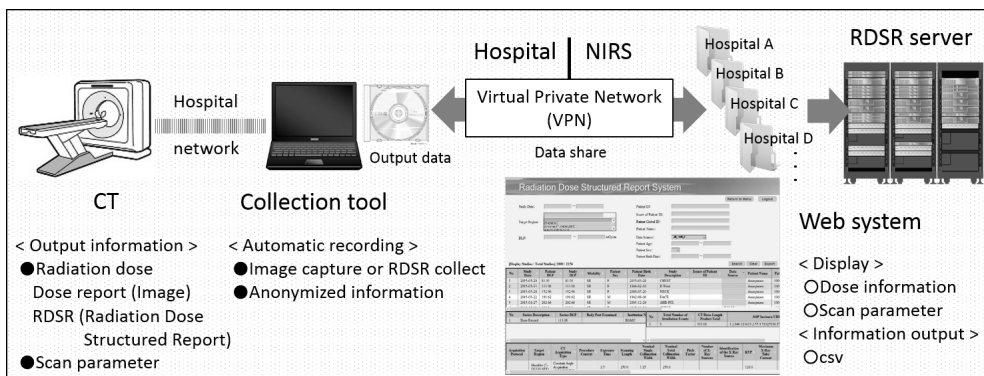


Fig.3 The automatic dose collection system and database for CT examinations.

### (5) J-RIME

For the nation-wide exchange of information on medical exposures, a general meeting of the Japan Network for Research and Information on Medical Exposure (J-RIME) was held in April 2014, and it was decided to establish a Working Group for diagnostic reference levels (DRLs) for each radiation examination.

J-RIME has discussed such topics as how to determine the DRLs of computed tomography, plain radiography, mammography, dental radiography, fluoroscopically-guided interventional procedures and nuclear medicine procedures. These "Japan DRLs 2015" were approved for publication by the J-RIME and its liaison organizations in June 2015 (Fig.4). This was the first attempt to establish national DRLs for radiation imaging in Japan, and it has brought favorable reactions from international bodies.

We have promoted better understanding, expanded use and deeper permeation of DRLs in medical settings in cooperation with J-RIME and its liaison organizations. We prepared standard manuals to explain DRLs for optimization of protection. There were authorized as official documents of J-RIME

and delivered to healthcare workers through liaison societies of J-RIME as well as to the public via the J-RIME homepage.

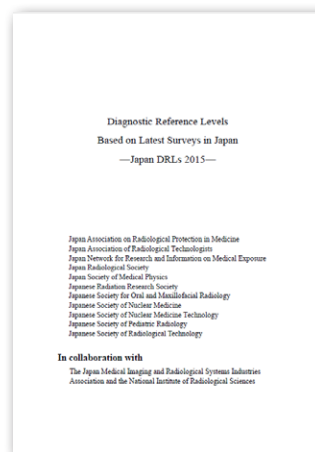


Fig.4 The report of "Japan DRLs 2015".

## Highlight

# Physiologically-based pharmacokinetic model for calculating internal doses in $^{18}\text{F}$ -FDG examinations

**Keiichi Akahane**

E-mail: akahane.keiichi@qst.go.jp

## Introduction

In nuclear medicine, positron emission tomography (PET) as well as other conventional imaging methods are well-established and performed as very useful methods in diagnoses for patients. Among the radiopharmaceuticals used in PET,  $^{18}\text{F}$ -fluoro-deoxy-glucose ( $^{18}\text{F}$ -FDG) is a typical and widely used compound. The medical exposures of patients in  $^{18}\text{F}$ -FDG examinations can be calculated based on the International Commission on Radiological Protection (ICRP) Publication 106 [1] in which the biokinetic data for the radiopharmaceutical and conversion factors of the organ doses (mGy) and effective doses (mSv) to the injected activities (MBq) of patients of 1, 5, 10, and 15 years of age and adult patients are shown in the publication tables. To determine these biokinetic parameters, compartment models have been used for calculating the cumulated activities in source organs. The compartment model can phenomenologically explain the kinetics of radiopharmaceuticals inside the body by setting the combination of organ or ideal compartments and movements of radiopharmaceuticals among them. On the other hand, a physiologically based pharmacokinetics model (PBPK model) has also been used to describe the kinetics of pharmaceuticals physiologically by using physiological parameters such as blood flow, organ volume, etc. in the pharmacokinetics field. The PBPK model is more realistic and provides better consideration for the physiological differences among individuals compared to the compartment models. In this study, the PBPK model was applied to estimate internal doses of the patients in  $^{18}\text{F}$ -FDG examinations to consider the differences among patients.

## Methods

In the PBPK model, the main organs are combined with blood flow lines among them. The parameters used in the model are organ volumes, blood flow rates, pharmaceutical concentrations, and partition coefficients of blood to organs as the physiological data for calculating the kinetics of the radiopharmaceuticals. However, the whole body PBPK model including all main organs is complicated and needs all parameter values determined (Fig.1). For the practical simplification in the dose calculation, the model was simplified (Fig.2) with source organs of  $^{18}\text{F}$ -FDG by referring to the ICRP publication data.

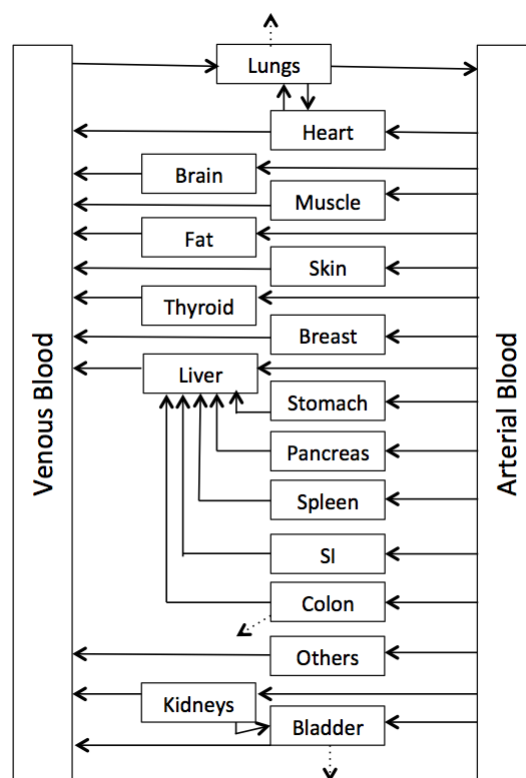


Fig.1 Physiologically based pharmacokinetics model (PBPK model) of the whole body.

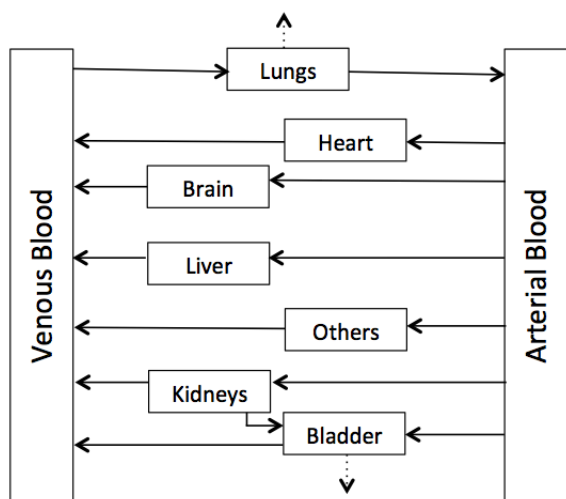


Fig.2 Physiologically based pharmacokinetics model (PBPK model) simplified for <sup>18</sup>F-FDG biokinetics calculations.

The time dependencies of the pharmaceutical concentrations in organs after injection can be described as a set of simultaneous differential equations. The concentrations of the pharmaceuticals were calculated by using a program implementing the Runge-Kutta method in the linux system. Physiological parameters of blood flow rates and volumes were determined by referring to data in the literature and papers on physiology. The rest of them were roughly assumed by considering the kinetics in the body.

### Results and discussion

The results of time dependencies of the concentrations and amounts of the activities of radiopharmaceuticals in organs depended on the settings of the physiological parameters in the PBPK model. Considering the characteristics of the <sup>18</sup>F-FDG radiopharmaceutical, some of the parameters were modified. By adjusting the parameters, concentrations of these organs were changed and the curves were reproduced to some degree (Fig.3).

The PBPK model has many physiological parameters and flexibility to fit the pharmacokinetics in the physiological conditions and anatomical components of the individual patient. For the same person, the differences of kinetics of radiopharmaceuticals depend not on the blood flow rate or organ volumes, but on the metabolisms of organs corresponding to the kinds of the nuclide and chemical forms. For the FDG kinetics, some parameters of the PBPK model were modified, and distribution patterns in organs showed differences compared to general conditions. Further consideration and remodeling of the movement and metabolism of the pharmaceuticals inside organs is necessary to reconstruct the kinetics of <sup>18</sup>F-FDG more accurately.

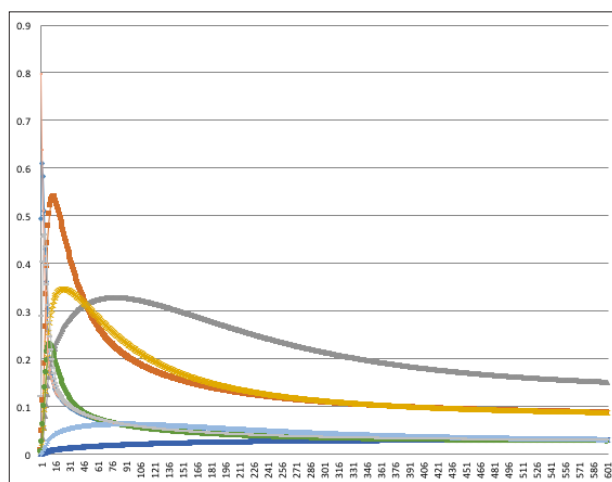
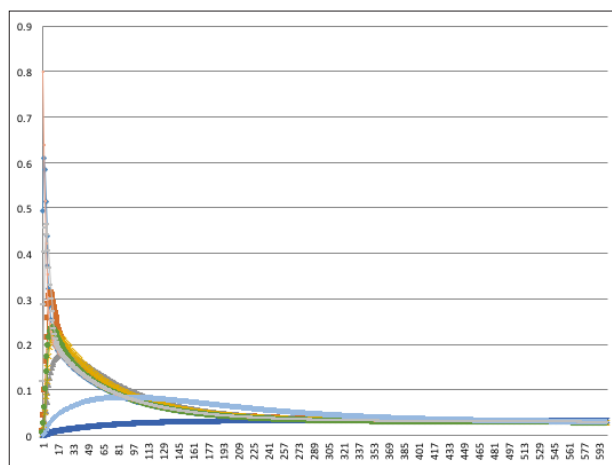


Fig.3 An example of the calculation results.

Adjusting parameters, in principle, the differences of patient body sizes and physiological conditions should be considered in the calculations not only for absorbed fractions of mathematical or voxel phantoms, but also the biokinetics of radiopharmaceuticals for dose estimations.

### References

- [1] ICRP. Radiation Dose to Patients from Radiopharmaceuticals - Addendum 3 to ICRP Publication 53. ICRP Publication 106. Ann. ICRP 38 (1-2), 2008.
- [2] M. T. Hays, *et al.* MIRD Dose Estimate Report No. 19: Radiation Absorbed Dose Estimates from <sup>18</sup>F-FDG, *J Nucl Med*, 43(2), 210, 2002.
- [3] M. T. Hays, *et al.* A Mathematical Model for the Distribution of Fluorodeoxyglucose in Humans, *J Nucl Med*, 40(8), 1358, 1999.

## Topic

## Collaboration with IAEA to develop a training package for medical physicists in support of nuclear and radiological emergencies

**Akifumi Fukumura, Shigekazu Fukuda  
Reiko Imai, Makoto Akashi**

E-mail: fukumura.akifumi@qst.go.jp

Medical physicists and radiological technologists have in-depth knowledge in radiation dosimetry, including dose estimation and dose measurements. Then they are expected to be potentially able to support and be involved in nuclear and radiological emergency (NRE) situations. However, in a major event such as Fukushima Dai-ichi Nuclear Power Plant accident, these professionals faced many kinds of difficulties that they had to deal with, without knowledge and experience in NRE situations.

The IAEA, in consultation with the World Health Organization (WHO), the International Organization for Medical Physics (IOMP) and the International Radiation Protection Association (IRPA), initiated a project to develop a specific training package to help prepare medical radiological physicists to support NRE situations. The training package was developed with the support of the Government of Japan and in collaboration with the National Institute of Radiological Sciences (NIRS) and Fukushima Medical University (FMU), and is endorsed by the Japan Society of Medical Physics (JSMP).

The first International Workshop to test the training package was held at FMU between 22 and 26 June 2015, with 22 clinical medical physicists participating in addition to lecturers from NIRS and FMU (Fig.1). This workshop has been designed to provide specific comprehensive training on NRE response for clinical radiation medical physicists. It also aims to:

- 1) Encourage and facilitate the embedding of medical physicists in NRE preparedness teams, in cooperation with other professions and organizations, at strategic and operational levels, both within hospitals and in the wider emergency planning structure;
- 2) Recognize the essential contributions of medical physics staff (technicians, dosimetrists etc.) in NRE preparedness programs and to ensure appropriate training;
- 3) Promote the interaction of medical physicists with other professional groups involved in NRE preparedness, including through participation in regular training and exercises; and
- 4) Encourage consideration of the potential of appropriately trained medical physicists to contribute to multidisciplinary NRE training of other professional groups, both within and outside health care settings.



The contents of the workshop were as follows.

- 1: Introduction
- 2: Nuclear and Radiological Emergencies
- 3: Radiation Measurements and Instrumentation
- 4: Dose Assessment and Dose Reconstruction
- 5: Monitoring and Decontamination of People – Scene and FMU
- 6: Monitoring and Decontamination of People – Hospital
- 7: Large Area Surveys – Monitoring of Food and Water
- 8: Biological Effects of Radiation – Cell and Tissue Effects
- 9: Biological Effects of Radiation – Stochastic Effects
- 10: Protection Strategies for the Public
- 11: Protection Strategies for Workers
- 12: Medical Management
- 13: Psychosocial Effects and Impacts on Mental Health
- 14: Effective Risk Communication

The International Workshop was evaluated by the participants and the lecturers. The results of the evaluation showed that the practical training sessions including decontamination of people were more popular than classroom lectures.

The Meeting on Lessons Learned from the International Workshop was held at NIRS between 20 and 22 October 2015 (Fig.2). The results of the workshop evaluation from the perspective of the participants and the lecturers were reviewed and used for revision of the workshop program and the contents of the handbook.

The updated training package is available at IAEA OPEN Learning Management System.  
(<http://olms-nkm.iaea.org/m2/enrol/index.php?id=348>)

The Second International Workshop will be held in the USA in 2016.



Fig.1 Participants in the IAEA "International Train the Trainers Workshop", held at Fukushima Medical University, Japan, on 22 - 26 June 2015.



Fig.2 Attendees of the IAEA Meeting on Lessons Learned from the "Train the Trainers Workshop on Medical Physics Support for Nuclear or Radiological Emergencies", held at NIRS, Japan, on 20 - 22 Oct. 2015.

# Program of Research on the Standardization and Clarification of Charged Particle Therapy

**Hiroshi Tsuji**

E-mail: tsuji.hiroshi@qst.go.jp

## Objectives

- To perform clinical research for clarifying usefulness of carbon ion therapy in order to establish new treatments for radioresistant tumors and to standardize the treatments for common cancers.
- To perform clinical research on utilization of the advanced technique of high-speed spot scanning irradiation of carbon ion beam not only in the treatment for head & neck or pelvic tumors but also for moving tumors in the chest and abdomen.
- To investigate the benefit of improving accuracy of imaging modalities, such as PET, MRI, and CT scanning for carbon ion therapy.
- To investigate the possibility of prediction or evaluation of effectiveness of carbon ion therapy using unique information obtained from imaging modalities.
- To develop and regulate a comprehensive database on radiotherapy, mainly carbon ion therapy in consideration of achieving evidence-based medicine. Additionally, to propose a national database available for multi-institutional research on particle therapy being carried out at domestic and foreign institutions.

## Progress of Research

The Program of Research on the Standardization and Clarification of Charged Particle Therapy consists of the Clinical Trial Research Team, Applied PET Research Team, Applied MRI Research Team, and Clinical Database Research Team. All the teams are performing research and development on charged particle therapy. Progress of research in each team is summarized below.

### 1) Clinical Trial Research Team

As of January 2016, a total of 9,716 patients had been treated with carbon ion beams at NIRS (Fig.1). Carbon ion radiotherapy of these patients was carried out as more than 60 different phase I/II or phase II clinical trials or advanced medicine (HAMT; highly advanced medical technology).

Six hundred and ninety-five patients were treated as new patients from April 2015 to January 2016. This number will be about 750 at the end of March 2016 and will be comparable to that of last year.

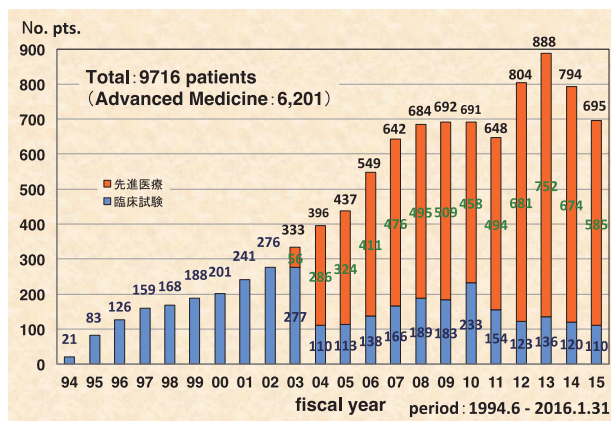


Fig.1 The yearly numbers of patients treated with carbon ion beams at NIRS.

Figure 2 lists the numbers of the patients for each tumor site. Prostate, bone & soft tissue, head & neck, lung, and liver are the leading 5 tumors sites. Recently the numbers of pancreatic tumor and recurrent rectal cancer patients have increased definitely.

Clinical trials for pancreas, esophagus, uterus, and kidney cancers are being conducted and patient enrollment has progressed. As advancements of the hypofractionation of carbon ion therapy, the single session treatment for lung cancer and 12-fraction treatment for prostate cancer could be established and their application as advanced medicine was started.

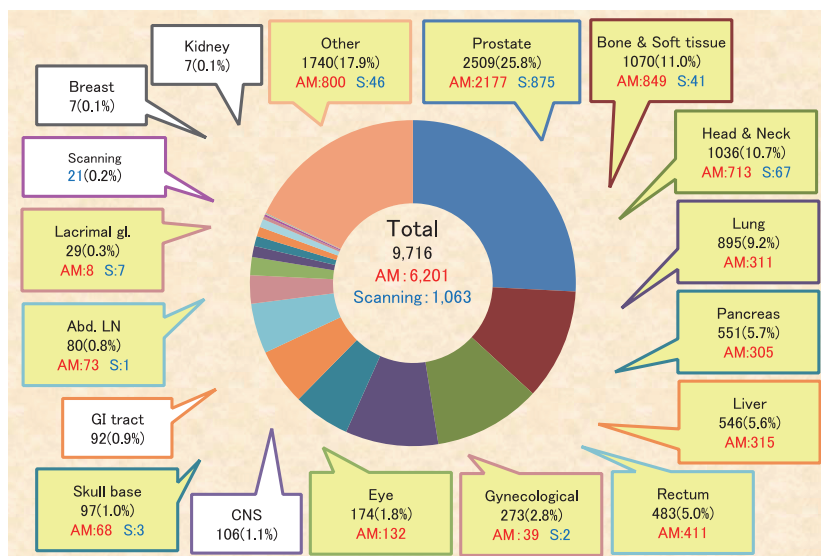


Fig.2 The numbers of patients for each tumor site treated with carbon ion beams.

Scanning irradiation became available for the routine treatment of less mobile targets in the head & neck or pelvic region. Actually more than one thousand patients could be safely and efficiently treated with scanning at the New Treatment Research Facility. In addition, the clinical trial aiming at verifying safety and steadiness of the respiratory-gated scanning system was carried out in 10 patients with a tumor in the chest or abdomen.

The new working group, named J-CROS (Japanese Carbon-ion Radiation Oncology Study Group), for the multi-institutional clinical trial of carbon ion therapy was established in 2014. Its members consist of four running carbon ion therapy facilities in Japan, the NIRS, the HIBMC in Hyogo, the GHMC in Gunma, and the HIMAT in Saga. A new institute i-ROCK in Kanagawa started carbon ion therapy and joined the active members of J-CROS last year. J-CROS performed data collection from the original four running institutes for a retrospective analysis (Table 1) and to plan a protocol for prospective clinical studies for major tumor sites.

Table 1 Retrospective studies conducted by J-CROS.

Tumor site	Institutes	Period	No. patients
Bone & Soft tissue	4	2003-2014	764
Head & Neck (non-SCC)	4	2003-2014	845
Liver	4	2005-2014	174
Lung (Stage I)	4	2003-2014	331
Lung (Advanced)	3	2003-2014	64
Prostate	3	2003-2014	2332
Rectum	3	2003-2014	224
Pancreas	3	2012-2014	66

## 2) Applied PET Research Team

In FY2015, we investigated whether PET could predict the therapeutic effect of charged particle radiotherapy soon after treatment by using clinical PET images. For head & neck melanoma and lung cancer, we analyzed the ratio of local

recurrence, distant metastasis and survival by PET images obtained before and after heavy particle radiotherapy. We compared the diagnostic accuracy of each quantitative method of PET accumulation. A correlation between PET accumulation and life prognosis was observed. PET studies may be useful in predicting the therapeutic effect of charged particle radiotherapy.

## 3) Applied MRI Research Team

To provide quantitative diagnostic information for heavy charged particle therapy, several MR methods have been applied to clinical diagnosis. A new robust method (eDKI) to estimate axial and radial diffusional-Kurtosis imaging maps was developed. Compared with the conventional way, the map quality was greatly improved without largely trading off its accuracy. The results can be seen on our website ([http://www.nirs.qst.go.jp/amr\\_diag/](http://www.nirs.qst.go.jp/amr_diag/)).

## 4) Clinical Database Research Team

It is essential to prepare a dedicated database system to perform multi-institutional trials by J-CROS and it is necessary to do this within a program that has a leading role in future trials. Thus, we developed a database system that can store the integrated information of patients treated at all the institutions of this study group. The data to be stored include pretreatment information, treatment data, and outcome information. In addition, a conversion tool was developed, which is available for the different types of medical information of the respective institutions. The carbon ion radiotherapy cases of craniocervical tumors, musculoskeletal tumors and prostate cancer were stored during FY 2015. The data management function of the database has been improved.

## References

- [1] Mizoguchi N, Tsuji H, et al., *Radiother Oncol*, 114, 373, 2015. doi:10.1016/j.radonc.2015.01.009
- [2] Takahashi W, Nakajima M, et al., *Cancer*, 121, 1321, 2015. doi:10.1002/cncr.29195
- [3] Kamada T, et al., *Lancet Oncology* 16; e93-e100, 2015.

## Cooperation with WHO-REMPAN in radiation emergency medicine

**Hideo Tatsuzaki, Yumiko Suto**

E-mail: tatsuzaki.hideo@qst.go.jp

Radiation emergency medicine including medical countermeasures in the case of a nuclear accident is one of the major missions of NIRS. Preparation for a domestic accident and creating an effective organizational system in Japan are required. NIRS implemented many projects along this line after the accident at the TEPCO Fukushima Daiichi Nuclear Power Station. In addition, reaction to an overseas accident is also considered to be an important mission of NIRS. Information exchanges with international organizations and individual researchers in foreign countries bring benefits to both sides. In this Topic section, cooperation in the fields between the World Health Organization (WHO) and NIRS is presented.

WHO is one of United Nations organizations that handles health or medical related issues. Among many subjects, medical countermeasures against radiation exposure, or radiation emergency medicine is handled by WHO. WHO's Radiation Emergency Medical Preparedness and Assistance Network (WHO-REMPAN) was established in 1987. As described by Carr [1]: "The primary purpose of the network is dual: (1) to provide technical assistance in radiation emergencies; and (2) to strengthen preparedness and response capability of the health sector in regions through technical guidance, information sharing, coordinated research, training, and exercise". REMPAN has two categories of members, namely Collaborating Centers (CC) and Liaison Institutes (LI). REMPAN members of the two categories, as of 2014, are listed in Tables 1 and 2.

NIRS has two functions in relation to the above mentioned purposes. In order to respond effectively to overseas nuclear and radiological accidents, NIRS established the Radiation Emergency Medical Assistance Team (REMAT) in January 2010. At this time, REMAT was composed of only part time members, in other words, they had their own primary mission apart from service in REMAT. To increase its effectiveness, REMAT had dedicated members of its own and became a standing division also called REMAT, in March 2013.

In order to strengthen the capability of the Asian region, NIRS has been conducting training courses together with WHO mainly for Asian professionals (Table 3). Additionally, NIRS received some middle term trainees.

NIRS was designated first as a WHO-LI in January 2004 and as a CC in September 2013. Out of five areas (or activities) of collaboration for CC, three areas are in the field of radiation emergency medicine and related to REMPAN activities.

The first activity is "Technical assistance to WHO in response to radiation emergencies". Under this activity, NIRS provides technical assistance and advice to WHO in the areas pertaining to medical management of over-exposed persons (subject to availability of resources).

The second activity is "Cooperation in the area of biodosimetry and BioDoseNet (cytogenetics and internal contamination monitoring)". Under this activity, NIRS cytogenetic laboratory is a key actor to develop and to strengthen cooperation of dose assessment in the region. The WHO BioDoseNet (network) was launched in 2008 for cooperation in this area. The NIRS cytogenetic laboratory is a core part of the network and its reference laboratories, and it is providing technical contributions to the BioDoseNet activities.



The third activity is "Cooperation in the area of strengthening preparedness to radiation emergencies and REMPAN activities". Under this activity, NIRS: provides education and training for emergency response personnel; participates in international exercises on radiation emergency in order to contribute to enhancement of the network's operation; participates and contributes to REMPAN meetings, seminars, workshops, etc. as required; and provides technical assistance on development of WHO technical reports, recommendations, and guidelines as required.

This year, NIRS organized the "NIRS Training Course on Radiation Emergency Medicine in Asia 2015" in cooperation with WHO and IAEA, from 7-9 December 2015. This course was for leaders in this specialty in Asia and was attended by 14 professionals from 13 Asian and Middle Eastern regions. It contributed to strengthening the capability in the region.

Additionally, NIRS sent experts to some WHO meetings during FY 2015. NIRS staff members attended "The 1st Face-to-Face Meeting of the REMPAN WG on Internal Contamination" in Bruges, Belgium, in April 2015. The attendees exchanged information for building international cooperation, and reported on the importance of preparing a manual for screening of children in a nuclear emergency. NIRS staff members also attended "The 2nd GDG meeting of the WHO project on development of WHO guidelines on KI Thyroid Blocking in Radiological and Nuclear Emergencies" in Pisa, Italy, in January 2016, and reported on workers' exposure after the TEPCO Fukushima NPP Accident.

In the biodosimetry field, together with other WHO BioDoseNet members, NIRS participated in two biodosimetry inter-laboratory comparison studies. NIRS results of the 2nd inter-laboratory comparison in the frame of RENEB were presented in ConRad 2015 (Munich, May 2015) and ICRR 2015 (Kyoto, May 2015). The quality of NIRS results of the KIRAMS (Korea)-AUB (Spain)-NIRS (Japan) inter-comparison study (February 2016) was certified based on the ISO standard (ISO 15189).

In addition to these activities, NIRS contributed to "WHO-REMPAN e-Newsletters" periodically and shared information.

NIRS is continuously preparing for radiological or nuclear accident overseas in cooperation with WHO-REMPAN.

### Reference

[1] Carr Z., *Health Phys.* 98(6), 773, 2010.

Table 1 Collaborating Centers as of June 2014 (Total number: 15).

Country	City	Institution
Australia	Yallambie, Victoria	Australian Radiation Protection and Nuclear Safety Agency (ARPANSA)
Brazil	Rio de Janeiro	Institute for Radioprotection and Dosimetry (IRD)
France	Fontenay-aux-Roses cedex	Institute for Radioprotection and Dosimetry (IRD) Radiological Protection and Human Health Division, Institute for Radiological Protection and Nuclear Safety (IRSN)
Germany	Wuerzburg	Clinic of Nuclear Medicine, University of Wurzburg
Japan	Hiroshima	Radiation Effects Research Foundation (REFR)
Japan	Nagasaki	Atomic Bomb Disease Institute Nagasaki University Graduate School of Biomedical Sciences
Japan	Chiba	National Institute of Radiological Sciences (NIRS)
Russian Federation	Moscow	Burnasyan Federal Medical Biophysical Center, FMBA
Russian Federation	Kaluga oblast	Medical Radiological Research Center (MRRC)
Russian Federation	St.-Petersburg	The Nikiforov Russian Center of Emergency and Radiation Medicine (NRCERM)
Russian Federation	Chelyabinsk	Urals Research Center for Radiation Medicine (URCRM)
Switzerland	Berne	Federal Office of Public Health, Radiological Protection
Ukraine	Kiev	National Research Center for Radiation Medicine
U.S.A.	Oak Ridge	Radiation Emergency Assistance Center/Training Site (REAC/TS)
U.S.A.	Atlanta	Centers for Disease Control and Prevention

Table 2 Liaison Institutions as of June 2014 (Total number: 30).

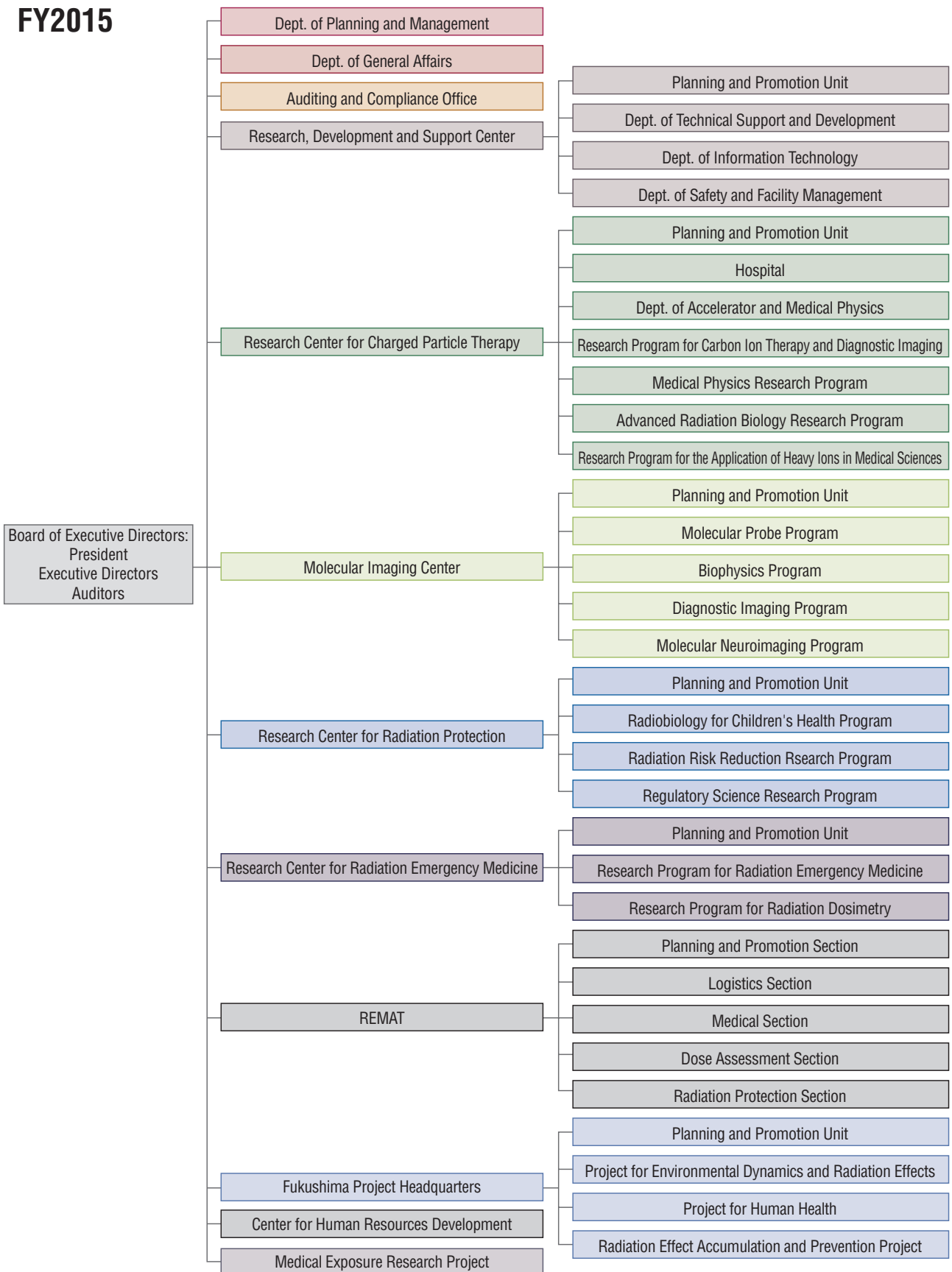
Country	City	Institution
Albania	Tirana	Radiation Protection Office, Ministry of Health
Argentina	Buenos Aires	Radiopathology Department - Nuclear Regulatory Authority
Armenia	Yerevan	Scientific Centre of Radiation Medicine and Burns, Ministry of Health, Republic of Armenia
Belarus	Gomel	Republican Research Center of Radiation Medicine and Human Ecology
Brazil	Rio de Janeiro	Electronuclear Medical Assistance Foundation (FEAM)
Bulgaria	Sofia	National Centre of Radiobiology and Radiation Protection (NCRPP)
Canada	Ottawa	Radiation Protection Bureau, Health Canada
China	Beijing	Chinese Centre for Medical Response to Radiation Emergency (CCMRRE) National Institute of Radiation Protection (NIRP), China CDC
China	Beijing	Beijing Institute for Radiation Medicine
Finland	Helsinki	STUK - Radiation and Nuclear Safety Authority
France	CLAMART CEDEX	French Defence Radiation Protection Service (SPRA)
Germany	Munich	Bundeswehr Institute of Radiobiology affiliated to the University of Ulm
Germany	EGGENSTEIN-LEOPOLDS-HAFEN	Karlsruhe Institute of Technology (KIT) Medical Services and KSM (KIT Safety Management)
Germany	Ulm	International Center for Advanced Studies in Health Sciences and Services (ICAS), Faculty of Medicine, Ulm University
Germany	Koln	Institute for Radiation Protection of the German Social Accident Insurance Institutions (IFS)
Hungary	Budapest	Frederic Joliot - Curie National Research Institute for Radiobiology and Radiohygiene
Japan	Hiroshima	Radiation Emergency Medicine Promotion Center, Hiroshima University
Japan	Hiroshima	Institute of Radiation Emergency Medicine, Hiroshima University (IREM/HU)
Japan	Fukushima	Fukushima Medical University
Norway	Ostera	Norwegian Radiation Protection Authority (NRPA)
Romania	Bucharest	National Institute of Public Health
Russian Federation	Ozyorsk	Southern Urals Biophysics Institute
South-Africa	Tygerberg	Radiation Emergency Medical Advisory Centre of South Africa (REMACSA)
South Korea	Seoul	National Radiation Emergency Medical Center (NREMC) Korea Institute of Radiological and Medical Sciences (KIRAMS)
South Korea	Seoul	Radiation Health Research Institute (RHRI) Korea Hydro & Nuclear Power Company
Sweden	Stockholm	Radiation Emergency Medicine Center and Dept of Hematology, Karolinska Institutet and Karolinska University Hospital
United Kingdom	Oxon	Public Health England (PHE) Centre for Radiation, Chemical and Environmental Hazards
United Kingdom	London	EBMT (European Group for Blood and Marrow Transplantation) Nuclear Accident Committee
U.S.A.	Bethesda	Radiation Nuclear Countermeasures Research and Product Development
U.S.A.	Minneapolis	Radiation Injury Treatment Network (RITN)

Table 3 Meetings in cooperation with WHO.

Year/month	Title of meetings
2006 Mar.	WHO-REMPAN Regional Workshop on Radiation Emergency Medical Preparedness and Response in the Western Pacific Asia co-organized by NIRS, WHO, WPRO (WHO-REMPAN)
2008 Nov.	Cytogenetic Biodosimetry for Asia and 46th IASTC Japan Workshop NIRS-IAEA Workshop on Cytogenetic Biodosimetry (IAEA & WHO)
2009 Feb.	NSC/NIRS Workshop on Medical Response to Nuclear Accidents in Asia organized by NIRS & NSC (in cooperation with WHO-SEARO)
2010 Jan.	NSC/NIRS Workshop on Medical Response to Nuclear Accidents in Asia (organized by NSC & NIRS, in cooperation with IAEA & WHO)
2011 Jan.	NIRS-IAEA Workshop on Cytogenetic Biodosimetry for Asia 2011 & NIRS-IAEA Workshop on Cytogenetic Biodosimetry (in cooperation with WHO)
2013 Mar.	NIRS Workshop on Medical Response to Nuclear Accidents in Asia 2013 -Interactive Training for Medical Professionals- (in cooperation with IAEA, WHO)
2014 Nov.	NIRS Workshop on Radiation Emergency Medicine in Asia 2014 (in cooperation with IAEA & WHO)

# Organization Chart

FY2015



# Board Members

Title		Name	Tenure	Mission
President		Yoshiharu YONEKURA	April 1, 2011- March 31, 2016	Represents the Institute and is responsible for managing its operations
Executive Director		Makoto AKASHI	April 1, 2015- March 31, 2016	Assists the President in managing the operations of the Institute in accordance with the directions of the President
Executive Director		Shinichi KUROKI	April 1, 2015- March 31, 2016	Assists the President in managing the operations of the Institute in accordance with the directions of the President
Auditor		Sanae AOKI	April 1, 2015- the approval of the financial statements in 2015	Audits the operations of the Institute
Auditor (part-time)		Masatoshi ARISAWA	April 1, 2015- the approval of the financial statements in 2015	Audits the operations of the Institute

# Activity of Center for Human Resources Development

NIRS has regarded Human Resources Development (HRD) as one of its most important missions since the time of its foundation. Therefore, NIRS established a training school in 1959 and developed it into Center for HRD in 2013 to expand its ability to carry out the mission. We have offered training courses to nurture specialists in radiation protection and workers handling radiation in the medical field such as medical doctors, nurses, and radiologists. Our training courses are characterized by lectures by various professionals and by hands-on practice using radiation sources and various measuring instruments.

## Our efforts in the first four years of the mid-term (from April 2011 to March 2015)

As this mid-term began just after the Fukushima Daiichi Nuclear Power Plant accident in March 2011, we had to greatly modify the original plan for it.

First of all, we increased the numbers of trainees in each training course and of the training courses in order to respond to demands after the accident. Secondly, we conducted new training courses to give lectures to public health nurses and school teachers. Persons in these occupations could play an important role in local communities by properly explaining about radiation to the general public and children, respectively, and they could be ambassadors to spread accurate knowledge to people efficiently. Thirdly, we offered lectures to high school, junior high school and elementary school students to directly provide accurate basic knowledge on radiation to the public. On the other hand, we also conducted new courses to enhance the essential capacities for radiologist and others.

As a result, the total number of trainees doubled in the first year (from April 2011 to March 2012), and tripled in the second after the accident (from April 2012 to March 2013). In the next two years from April 2013 to March 2015, the number remained high as can be seen in Fig.1.

## The final year of the mid-term (from April 2015 to March 2016)

Four years after the accident, the number of applications for the training courses did not decrease but remained steady in the final year of the mid-term. Thus, we were able to maintain the increased number of training courses. In addition, we had training courses for school teachers, students, policemen, and firefighters according to requests from local governments. These increasing demands are the likely result from the NIRS training courses becoming well known. Finally, we had almost 1,200 trainees from April 2015 to March 2016, which was more than in the previous year. We have emphasized hands-on practice, group discussions and table top exercises for efficient learning and promoted the introduction of IT using a tablet type portable terminal.

Table 1 Training courses from April 2015 to March 2016.

Training courses	Contents & target learners	No. of categories	Total courses
Radiation Experts	<ul style="list-style-type: none"> <li>• general radiation protection</li> <li>• radiobiology for nurses</li> <li>• medical physics</li> <li>• imaging diagnosis</li> <li>• etc.</li> </ul>	10	16
Radiation Emergency Medicine	<ul style="list-style-type: none"> <li>• medical workers</li> <li>• first responders</li> </ul>	10	13
Radiation Risk Communicators	<ul style="list-style-type: none"> <li>• public health nurses</li> <li>• school teachers</li> <li>• local government employees</li> </ul>	5	5
Education	<ul style="list-style-type: none"> <li>• students from elementary school to university</li> </ul>	8	10
Total		35	44

## Change in trainees' number

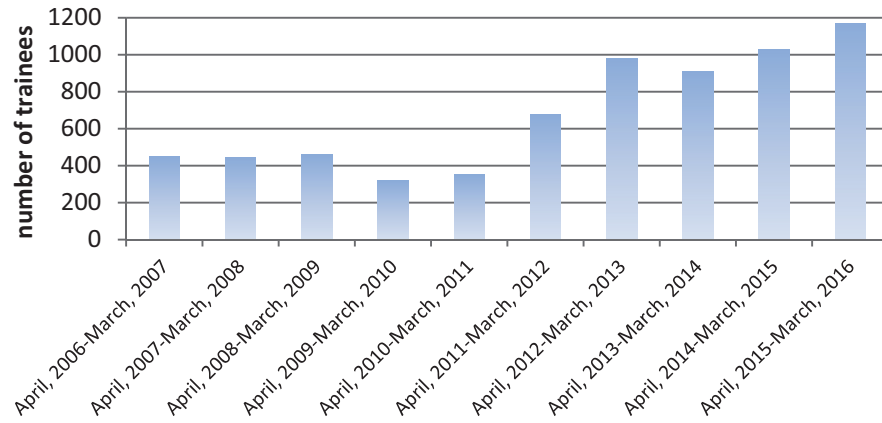


Fig.1 The number of trainees has been increasing since Fukushima Daiichi Nuclear Power Plant accident in 2011.



Trainees can learn efficiently through hands-on practice which is adjusted to their learning level.



We offered training courses for school students to provide basic knowledge on radiation.



The numbers of requests to provide training courses for radiation protection have been increasing from fire and police departments.

# International Collaboration

## Working with international organizations

### UNSCEAR

United Nations Scientific Committee on the Effects of Atomic Radiation  
Japan Expert Panel for UNSCEAR

### ICRP ICRP

International Commission on Radiological Protection  
Biological Effect, Medical Exposure Environment, Ethics

### ICRU

International Commission on Radiation Units and Measurements  
Charged Particle Therapy

### OECD/NEA

OECD/Nuclear Energy Agency  
Radiation Protection and its Framework for Public Health

### IAEA

International Atomic Energy Agency  
Collaborating Centre for Charged Particle Therapy, Molecular Imaging and Radiation Biology  
Radiation Emergency Medicine (RANET)

### WHO

World Health Organization  
Collaborating Centre for Radiation Emergencies, Biodosimetry, Indoor Radon Exposure and Medical Exposure

### IAEA/RCA

Radiotherapy, Nuclear Medicine Radiation Protection  
IAEA/Regional Cooperative Agreement for Research, Development and Training Related to Nuclear Science and Technology

### IAEA/WHO

Radiation Emergency Medicine Network System in Asia  
Asian Nuclear Safety Network

### FNCA FNCA

Forum for Nuclear Cooperation in Asia  
Radiotherapy

### ISO ISO

International Organization for Standardization  
Radiation Dosimetry

### GHSI

Global Health Security Initiative  
Anti-terrorism (Radiation)

### JICA

Japan International Cooperation Agency  
Radiology, Education and Training

### The meetings attended by NIRS Experts from April 2015 to March 2016 included:

#### FNCA

- FY2015 Workshop on Radiation Oncology (Hanoi, Vietnam)

#### IAEA

- 2015 Interim Meetings and Workshop of MODARIA WG 4 'Radioecological Data' and WG 8' Biota Modelling'
- Consultancy Meeting to Elaborate the Concept and Implementation of EPR Capacity Building Centres
- 2nd Consultancy Meeting on the Revision of the Emergency Preparedness and Response (EPR) Medical 2005
- IAEA Nuclear Energy Management School Abu Dhabi (UAE)
- 2015 Interim Meeting of MODARIA WG 3 'NORM and Legacy Sites'
- Final Research Coordination Meeting on CRP 'Production of Mo-99/Tc-99m'
- International Conference on Clinical PET-CT and Molecular Imaging: PET-CT in the Era of Multimodality Imaging and Image Guided Therapy
- International Conference on Global Emergency Preparedness and Response
- 4th Technical Meeting on Modelling and Data for Radiological Impact Assessments(MODARIA)
- Technical Meeting on Radiation Biology of Charged Particle Therapy
- IAEA/RCA Mid-Term Review Meeting on Strengthening the Effectiveness and Extent of Medical Physics Education and Training (Mumbai, India)

#### ICRP

- ICRP TG94 Draft Preparation Meeting (Paris, France)
- ICRP2015: 3rd International Symposium on the System of Radiological Protection (Seoul, Korea)

#### IEC

- IEC/SC62C/WG1 Meeting (Equipment for Radiotherapy, Nuclear Medicine and Radiation Dosimetry) (London, UK)

#### ISO

- ISO/TC85/SC2 and WG22/WG23 Meetings (Boras, Sweden)

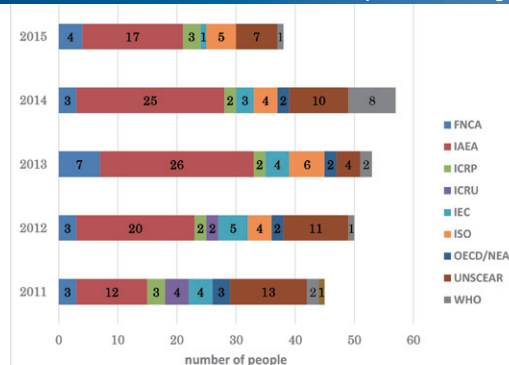
#### UNSCEAR

- 62nd Session of UNSCEAR
- UN General Assembly (New York, USA)

#### WHO

- 2nd Meeting of the WHO Guidelines Development Group for the Revision of 1999 WHO Guidelines on KI Thyroid Blocking in Nuclear Emergencies

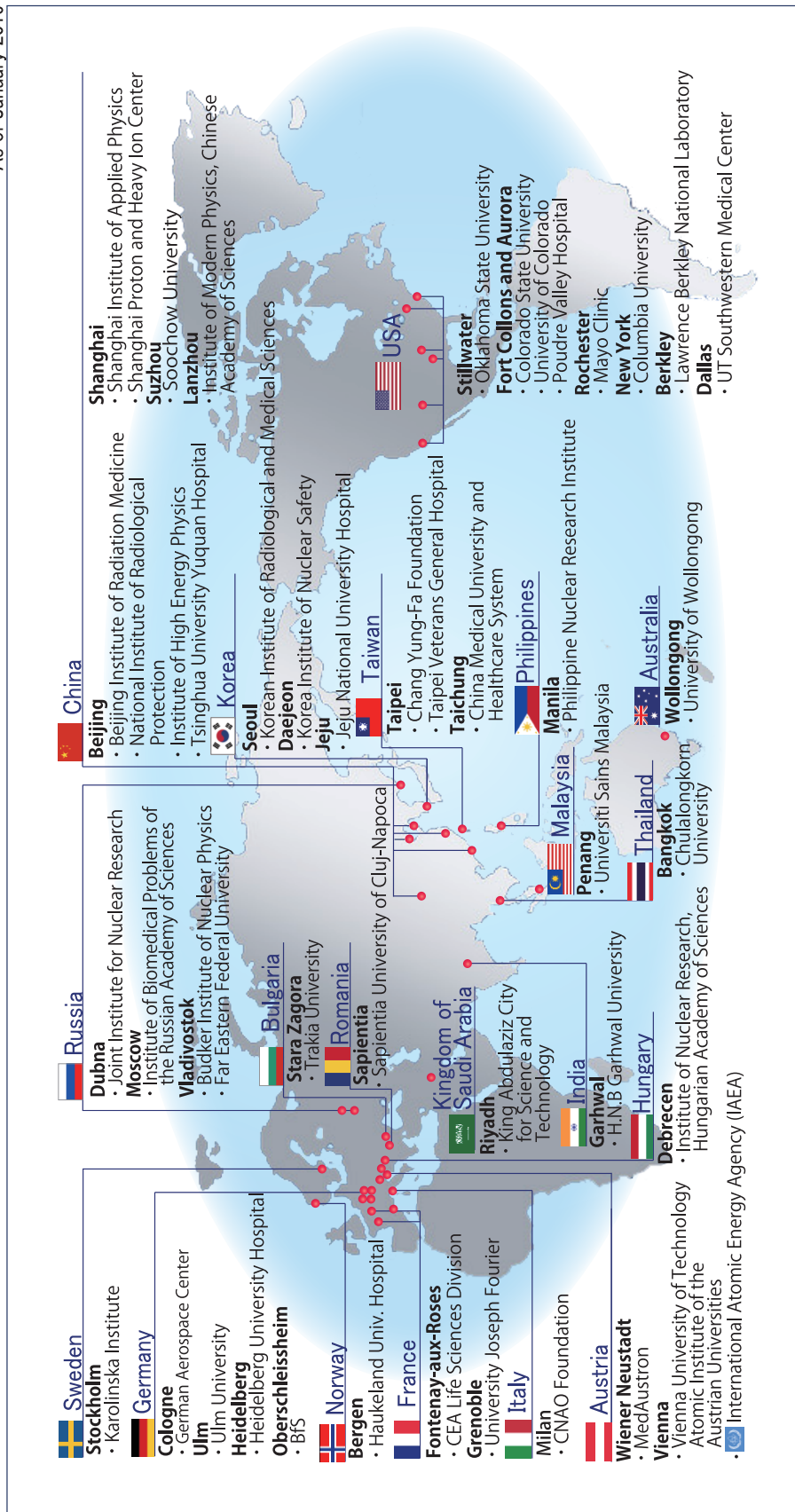
### 2011-2015 NIRS staff sent to the experts' meetings



\* The meetings were held at the organization's head office unless otherwise indicated.

## NIRS Overseas Partners through Memorandums

As of January 2016



# International Collaboration

## Year in Review — international meetings, training courses, etc.

2015

April

**1 April - 27 June**

IAEA-CC Intensive Training Course on Radiochemistry

June

**22-26 June**

IAEA Train the Trainers Workshop on Medical Physics Support for Nuclear or Radiological Emergencies (Fukushima, Japan)

**29-30 June**

NIRS-CEA/DSV Workshop on Treatment of Contamination and Dose Assessment (Fontenay-aux-Roses, France)

July

**27-30 July**

NIRS-KIRAMS Training Program on Radiation Emergency Medicine for Korean Medical Professionals

Sep.

**14-18 Sep.**

IAEA-NIRS Technical Meeting on the Future of Biodosimetry in Asia: Promoting a Regional Network



Oct.

**7 Oct.**

Visit by HE Dr.Pooda, Minister of Scientific Research and Innovation, Burkina Faso

**10 Oct.**

Visit by Colorado State Governor, Mr.Hickenlooper, *et al.*



**20-22 Oct.**

IAEA Consultancy Meeting on Lessons Learned from the Train the Trainers Workshop on Medical Physics Support for Nuclear or Radiological Emergencies



**26 Oct.**

Signing the Memorandum between LBNL and NIRS (Berkeley, CA,USA)



2015  
Nov.

8-9 Nov.

Japan-China Joint Seminar on Radiopharmaceutical Chemistry (JCSRC 2015)



9-14 Nov.

International Training Course on Carbon-Ion Radiotherapy (ITCCIR2015)

9-21 Nov.

IAEA-CC Workshop on Heavy Ion Radiotherapy



18-20 Nov.

IAEA Regional Meeting on Development of Action Plans for Potential Capacity Building Centres for Medical Response to Radiological Emergencies in Asia and the Pacific Region

Dec.

7-10 Dec.

NIRS Training Course on Radiation Emergency Medicine in Asia 2015 in Cooperation with IAEA and WHO



10-11 Dec.

SPHIC-NIRS Joint Symposium on Heavy Ion Radiotherapy (Shanghai, China)

16 Dec.

Symposium on 'Lifestyles and Radiation'



2016  
Jan.

9 Jan.

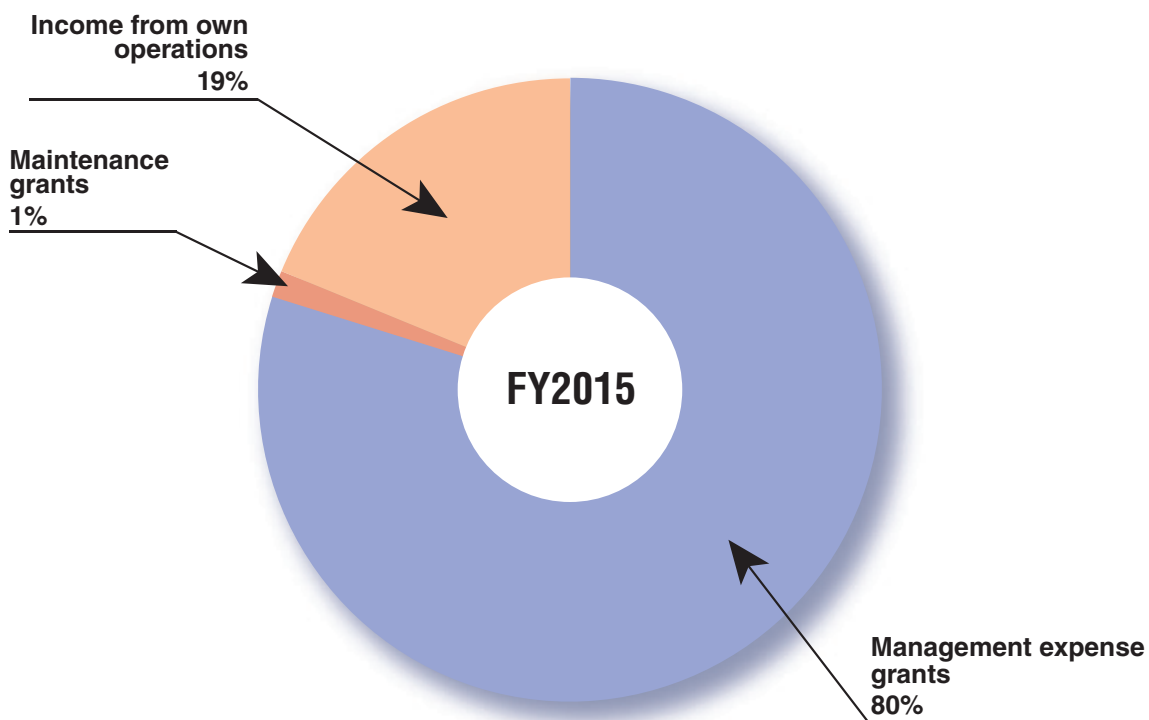
NIRS 2nd International Symposium on Heavy-Ion Radiotherapy and Advanced Technology



# Budget (FY2015)

(In million yen)

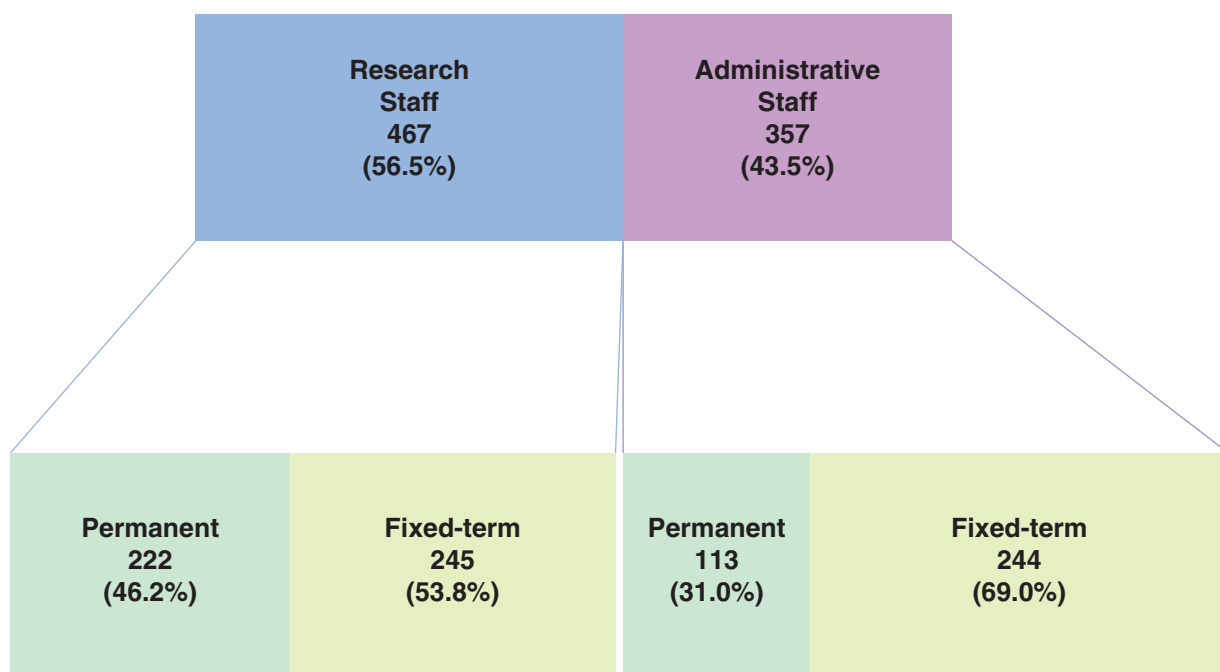
Total	11,838	Percent (%) of budget
Management expense grants	9,450	79.8%
Maintenance grants	162	1.4%
Income from own operations	2,226	18.8%
Income from operations ordered by government agencies, etc.	0	0.0%



(As of April 1, 2015)

## Personnel (FY2015)

<b>Research Staff</b>	<b>467 (56.5%)</b>
<b>Permanent</b>	<b>222 (46.2%)</b>
<b>Fixed-term</b>	<b>245 (53.8%)</b>
<b>Administrative Staff</b>	<b>357 (43.5%)</b>
<b>Permanent</b>	<b>113 (31.0%)</b>
<b>Fixed-term</b>	<b>244 (69.0%)</b>
<b>Total</b>	<b>816</b>



(As of April 1, 2015)

# Appendix

## List of Original Papers

This list includes the main publications by staff members that were registered with the NIRS Institutional Repository during the period from April 1, 2015 to March 31, 2016.

### ■ Research Center for Charged Particle Therapy

1. Phase II study of concurrent chemoradiotherapy with weekly cisplatin and paclitaxel in patients with locally advanced uterine cervical cancer: The JACCRO GY-01 trial. Kenji Umayahara, Munetaka Takekuma, Yasuyuki Hirashima, Shin-Ei Noda, Tatsuya Ohno, Etsuko Miyagi, Fumiki Hirahara, Eiji Hirata, Eiji Kondo, Tsutomu Tabata, Yutaka Nagai, Yoichi Aoki, Masaru Wakatuki, Masahiro Takeuchi, Takafumi Toita, Nobuhiro Takeshima, Ken Takizawa, *Gynecologic Oncology*, 140(2), 253-258, 2016, DOI:10.1016/j.ygyno.2015.12.008.
2. Concurrent chemoradiotherapy for T3-4 and N0-1 nasopharyngeal cancer: Asian multicenter trial of the Forum for Nuclear Cooperation in Asia. Tatsuya Ohno, Masaru Wakatsuki, Dang Huy Quoc Thinh, Ngo Thanh Tung, Dyah Erawati, Nana Supriana, C R Beena Devi, Shingo Kato, Kullathorn Thephamongkhon, Yaowalak Chansilpa, Miriam Joy C Calaguas, Xu Xiaoting, Cao Jianping, Parvin Akhter Banu, Chul-Koo Cho, Kumiko Karasawa, Takashi Nakano, Hirohiko Tsujii, *Journal of Radiation Research*, 57(1), 44-49, 2016, DOI:10.1093/jrr/rvv046.
3. Proposal for Bottom-up Hierarchical Task Analysis: Application to the Mammography Examination Process. A. Yagahara, H. Sato, Y. Yokooka, S. Tsuji, K. Kurowarabi, K. Ogasawara, *Journal of Medical Imaging and Health Informatics*, 5(7), 1429-1434, 2015.
4. Visualization of X-ray radiography technical process by hierarchical task analysis (HTA). Yuki Yokooka, Yasuo Okuda, Ayako Yagahara, Shintaro Tsuji, Naoki Nishimoto, Masahito Uesugi, Katsuhiko Ogasawara, *Journal of Medical Imaging and Health Informatics*, 6, 532-538, 2016.
5. Estimation of late rectal normal tissue complication probability parameters in carbon ion therapy for prostate cancer. Mai Fukahori, Naruhiro Matsufuji, Takeshi Himukai, Nobuyuki Kanematsu, Hideyuki Mizuno, Akifumi Fukumura, Hiroshi Tsuji, Tadashi Kamada, *Radiotherapy and Oncology*, 118(1), 136-140, 2016, DOI:10.1016/j.radonc.2015.11.023.
6. Single-Fraction Carbon-Ion Radiation Therapy for Patients 80 Years of Age and Older with Stage I Non-Small Cell Lung Cancer. Masataka Karube, Naoyoshi Yamamoto, Mio Nakajima, H. Yamashita, K. Nakagawa, Tadaaki Miyamoto, Hiroshi Tsuji, T. Fujisawa, Tadashi Kamada, *International Journal of Radiation Oncology Biology Physics*, 95(1), 542-548, 2016, DOI:10.1016/j.ijrobp.2015.11.034.
7. Carbon Ion Radiation Therapy for Unresectable Sacral Chordoma: An Analysis of 188 Cases. Reiko Imai, Tadashi Kamada, N. Araki, Working Group for Bone and Soft Tissue Sarcomas, *International Journal of Radiation Oncology Biology Physics*, 95(1), 322-327, 2016, DOI:10.1016/j.ijrobp.2016.02.012.
8. Comparison of clinical and functional outcome between surgical treatment and carbon ion radiotherapy for pelvic chondrosarcoma. Hidetatsu Outani, Kenichiro Hamada, Yoshinori Imura, Kazuya Oshima, Tsukasa Sotobori, Yusuke Demizu, Shigeki Kakunaga, Susumu Joyama, Reiko Imai, Tomoaki Okimoto, Norifumi Naka, Ikuo Kudawara, Takafumi Ueda, Nobuhito Araki, Tadashi Kamada, Hideki Yoshikawa, *International Journal of Clinical Oncology*, 21(1), 186-193, 2016, DOI:10.1007/s10147-015-0870-z.
9. Evaluation of the safety and efficacy of carbon ion radiotherapy for locally advanced adenoid cystic carcinoma of the tongue base. Masashi Koto, Azusa Hasegawa, Ryo Takagi, Hiroaki Ikawa, Kensuke Naganawa, Junetsu Mizoe, Keiichi Jingu, Hirohiko Tsujii, Hiroshi Tsuji, Tadashi Kamada, Yoshitaka Okamoto, *Head & Neck*, 38(S1), E2122-E2126, 2016, DOI:10.1002/hed.24397.
10. Carbon Ion Radiation Therapy with Concurrent Gemcitabine for Patients with Locally Advanced Pancreatic Cancer. Makoto Shinoto, Shigeru Yamada, Kotaro Terashima, Shigeo Yasuda, Yoshiyuki Shioyama, Hiroshi Honda, Tadashi Kamada, Hirohiko Tsujii, Hiromitsu Saisho, *International Journal of Radiation Oncology, Biology, Physics*, 2015, DOI:10.1016/j.ijrobp.2015.12.362.
11. Heavy ion (carbon ion) radiotherapy for skull base chordomas. Azusa Hasegawa, Masashi Koto, Ryo Takagi, Kensuke Naganawa, Hiroaki Ikawa, Riwa Kishimoto, Hiroshi Tsuji, Tadashi Kamada, *Japanese Journal of Neurosurgery*, 24(8), 528-534, 2015 (In Japanese with English abstract).
12. Adenovirus-mediated FIR demonstrated TP53-independent cell-killing effect and enhanced antitumor activity of carbon-ion beams. M. Kano, K. Matsushita, B. Rahmullulla, S. Yamada, H. Shimada, S. Kubo, T. Hiwasa, H. Matsubara, F. Nomura, *Gene Therapy*, 23(1), 50-6, 2016, DOI:10.1038/gt.2015.84.
13. Clinical trial of prophylactic extended-field carbon-ion radiotherapy for locally advanced uterine cervical cancer (protocol 0508). Masaru Wakatuki, Shingo Kato, Hiroki Kiyohara, Tatsuya Ohno, Kumiko Karasawa, Tomoaki Tamaki, Ken Ando, Hirohiko Tsujii, Takashi Nakano, Tadashi Kamada, Makio Syozu, *PLoS ONE*, 10(11), e0143301, 2015, DOI:10.1371/journal.pone.0127587.
14. Modeling Combined Chemotherapy and Particle Therapy for Locally Advanced Pancreatic Cancer. Marco Durante, Francesco Tommasino, Shigeru Yamada, *Frontiers in On-*

- cology, 5(145), 1-12, 2015, DOI:10.3389/fonc.2015.00145.
15. Analysis of normal-appearing white matter of multiple sclerosis by tensor-based two-compartment model of water diffusion. Yasuhiko Tachibana, Takayuki Obata, Tomio Inoue, Shigeki Aoki, *et al.*, *European Radiology*, 25(6), 1701-1707, 2015, DOI:10.1007/s00330-014-3572-4.
  16. Detection of pure ground-glass nodules in the lung by low-dose multi-detector computed tomography, with use of an iterative reconstruction method: a comparison with conventional image reconstruction by the filtered back-projection method. Shiho Akashita, Yasuhiko Tachibana, Kentaro Sakamaki, Keiji Sogawa, Tomio Inoue, *Japanese Journal of Radiology*, 33(3), 113-21, 2015.
  17. Progress of Fundamental Technology R&D Toward Accelerator Magnets Using Coated Conductors in S-Innovation Program. Naoyuki Amemiya, Zheming Zhang, Takuya Sano, Yusuke Sogabe, Toru Ogitsu, Kei Koyanagi, Tsutomu Kurusu, Yoshiharu Mori, Yoshiyuki Iwata, Koji Noda, Masahiro Yoshimoto, *IEEE Transactions on Applied Superconductivity*, 25(3), 4003505, 2015.
  18. Magnetization and field quality of a cosine-theta dipole magnet wound with coated conductors for rotating gantry for hadron cancer therapy. Naoyuki Amemiya, Yusuke Sogabe, Masaki Sakashita, Yoshiyuki Iwata, Koji Noda, Toru Ogitsu, Yusuke Ishii, Tsutomu Kurusu, *Superconductor Science and Technology*, 29(2), 024006, 2015.
  19. Design of superconducting magnets for a compact carbon gantry. Yoshiyuki Iwata, Toshiyuki Shirai, Koji Noda, *IEEE Transactions on Applied Superconductivity*, 26(4), 4400104, 2016.
  20. AFOMP Policy No 5: career progression for clinical medical physicists in AFOMP countries. W.H. Round, A.P. Stefanoylannis, K.H. Ng, L.V. Rodriguez, K. Thayalan, Y. Han, F. Tang, S. Fukuda, R. Srivastava, A. Krisanachinda, A.C. Shiao, X. Deng, *Australasian Physical & Engineering Sciences in Medicine*, 38(2), 217-221, 2015.
  21. Cryogenic molecular separation system for radioactive  $^{11}\text{C}$  ion acceleration. Ken Katagiri, Akira Noda, Koutarou Nagatsu, Masao Nakao, Satoru Houjou, Takashi Wakui, Kouji Noda, *Review of Scientific Instruments*, 86, 123303-1 - 123303-7, 2015, DOI:10.1063/1.4937593.
  22. A singly charged ion source for radioactive  $^{11}\text{C}$  ion acceleration. Ken Katagiri, Akira Noda, Koutarou Nagatsu, Masao Nakao, Satoru Hojo, Masayuki Muramatsu, Kazutoshi Suzuki, Takashi Wakui, Koji Noda, *Review of Scientific Instruments*, 87(2), 02B509, 2016.
  23. Electron string ion sources for carbon ion cancer therapy accelerators. A. Yu. Boytsov, D. E. Donets, E. D. Donets, E. E. Donets, K. Katagiri, K. Noda, D. O. Ponkin, A. Yu. Ramzdorf, V.V. Salnikov, V.B. Shutov, *Review of Scientific Instruments*, 86, 083308-1-083308-5, 2015.
  24. Carbon-ion Radiotherapy for Prostate Cancer: Analysis of Morbidities and Change in Health-related Quality of Life. Hitoshi Ishikawa, Hiroyuki Kato, Takuya Kaminuma, Hidemasa Kawamura, Kazuto Ito, Hiroshi Matsui, Junko Hirato, Nobuaki Shimizu, Yutaka Takezawa, Hiroshi Tsuji, Kazuhiro Suzuki, Tatsuya Ohno, Takashi Nakano, *Anticancer Research*, 35(10), 5559-5566, 2015.
  25. Carbon-ion radiotherapy for locally advanced primary or postoperative recurrent epithelial carcinoma of the lacrimal gland. Nobutaka Mizoguchi, Hiroshi Tsuji, Shingo Toyama, Tadashi Kamada, Hirohiko Tsujii, Yuko Nakayama, Atsushi Mizota, Yoshitaka Ohnishi, *Radiotherapy and Oncology: Journal of the European Society for Therapeutic Radiology and Oncology*, 114(3), 373-7, 2015, DOI:10.1016/j.radonc.2015.01.009.
  26. Magnetic resonance imaging appropriate for construction of subject-specific head models for diffuse optical tomography. Kazuki Kurihara, Hiroshi Kawaguchi, Takayuki Obata, Hiroshi Ito, Eiji Okada, *Biomedical Optics Express*, 6(9), 3197-3209, 2015, DOI:10.1364/BOE.6.003197.
  27. Chewing-induced regional brain activity in edentulous patients who received mandibular implant-supported overdentures: a preliminary report. Katsuhiko Kimoto, Yumie Ono, Atsumichi Tachibana, Yoshiyuki Hirano, Takero Otsuka, Akinori Ohno, Katsuhiko Yamaya, Takayuki Obata, Minoru Onozuka, *Journal of Prosthodontic Research*, 55(2), 89-97, 2011, DOI:10.1016/j.jpor.2010.09.006.
  28. Estimation of organ doses and effective doses in image-guided respiration-gated radiotherapy. Minoru Nakao, Satoshi Obara, Kuniaki Nabatame, Keiichi Akahane, Shigeru Sanada, Toshiyuki Shirai, *Radiation Protection Dosimetry*, 1-9, 2015, DOI:10.1093/rpd/hcv015.
  29. Range verification system using edge detection method for a scintillator and a CCD camera system. Naoya Saotome, Takuji Furukawa, Yousuke Hara, Kota Mizushima, Ryohei Tansho, Yuichi Saraya, Toshiyuki Shirai, Koji Noda, *Medical Physics* 43(4), 1754-1759, 2016, DOI:10.1118/1.4943955.
  30. High power test of an injector linac for heavy ion cancer therapy facilities. Liang Lu, Toshiyuki Hattori, Huanyu Zhao, Katsunori Kawasaki, Liangting Sun, Yuan He, Hongwei Zhao, *Physical Review Special Topics – Accelerators and Beams*, 18, 111002-1-111002-8, 2015.
  31. Experimental verification of gain drop due to general ion recombination for a carbon-ion pencil beam. Ryohei Tansho, Takuji Furukawa, Yousuke Hara, Kota Mizushima, Naoya Saotome, Yuichi Saraya, Toshiyuki Shirai, Koji Noda, *Medical Physics*, 43(2)635-642, 2016, DOI:10.1118/1.4939225.
  32. A dose calculation algorithm with correction for proton-nucleus interactions in non-water materials for proton radiotherapy treatment planning. Taku Inaniwa, Nobuyuki Kanematsu, Shinji Sato, R. Kohno, *Physics in Medicine and Biology*, 61(1), 67-89, 2016, DOI:10.1088/issn.0031-9155/61/1/67.
  33. Influence of nuclear interactions in body tissues on tumor dose in carbon-ion radiotherapy. Taku Inaniwa, Nobuyuki Kanematsu, Hiroshi Tsuji, Tadashi Kamada, *Medical Physics*, 42(12), 7132, 2015, DOI:10.1118/1.4936105.
  34. Effects of beam interruption time on tumor control probability in single-fractionated carbon-ion radiotherapy for non-small cell lung cancer. T. Inaniwa, N. Kanematsu, M. Suzuki, R.B. Hawkins, *Physics in Medicine and Biology*, 60(10), 4105-4121, 2015, DOI:10.1088/0031-9155/60/10/4105.
  35. Reformulation of a clinical-dose system for carbon-ion radiotherapy treatment planning at the National Institute of Radiological Sciences, Japan. Taku Inaniwa, Nobuyuki Kanematsu, Naruhiro Matsufuji, Tatsuaki Kanai, Toshiyuki Shirai, Koji Noda, Hiroshi Tsuji, Tadashi Kamada, Hirohiko Tsujii, *Physics in Medicine and Biology*, 60(8), 3271-3286, 2015, DOI:10.1088/0031-9155/60/8/3271.
  36. Objective assessment in digital images of skin erythema caused by radiotherapy. H. Matsubara, N. Matsufuji, H.

- Tsuji, N. Yamamoto, K. Karasawa, and M. Nakajima, W. Takahashi, M. Karube, *Medical Physics*, 42(9), 5568-5577, 2015, DOI:10.1118/1.4928890.
37. Nonquenched Isoscalar Spin- $M1$  Excitations in  $sd$ -Shell Nuclei. H. Matsubara, *et al.*, *Physical Review Letters*, 115(10), 102501-102506, 2015, DOI:10.1103/PhysRevLett.115.102501.
  38. DNA damage response proteins and oxygen modulate prostaglandin E2 growth factor release in response to low and high LET ionizing radiation. Christopher P. Allen, Walter Tinganelli, Sharma Neelam, Jingyi Nie, Cory Sicard, Francesco Natale, Maurice King III, Steven B. Keysar, Antonio Jimeno, Yoshiya Furusawa, Ryuichi Okayasu, Akira Fujimori, Marco Durante, Jac A. Nickoloff, *Frontiers in Oncology*, 5, 260, 2015, DOI:10.3389/fonc.2015.00260.
  39. Kill-painting of hypoxic tumours in charged particle therapy. Walter Tinganelli, Marco Durante, Ryoichi Hirayama, Michael Krämer, Andreas Maier, Wilma Kraft-Weyrather, Yoshiya Furusawa, Thomas Friedrich, Emanuele Scifoni, *Scientific Reports (Online Only URL:http://www.nature.com/srep/index.html)*, 5, 17016, 2015, DOI:10.1038/srep17016.
  40. Determination of the relative biological effectiveness and oxygen enhancement ratio for micronuclei formation using high-LET radiation in solid tumor cells: An in vitro and in vivo study. Ryoichi Hirayama, Akiko Uzawa, Maki Obara, Nobuhiro Takase, Kana Koda, Masakuni Ozaki, Miho Noguchi, Yoshitaka Matsumoto, Huizi Li, Kei Yamashita, Sachiko Koike, Koichi Ando, Toshiyuki Shirai, Naruhiro Matsufuji, Yoshiya Furusawa, *Mutation Research - Genetic Toxicology and Environmental Mutagenesis*, 793, 41-47, 2015, DOI:10.1016/j.mrgentox.2015.08.003.
  41. Carbon ions induce autophagy effectively through stimulating the unfolded protein response and subsequent inhibiting Akt phosphorylation in tumor cells. Xiaodong Jin, Feifei Li, Xiaogang Zheng, Yan Liu, Ryoichi Hirayama, Xiongxiang Liu, Ping Li, Ting Zhao, Zhongying Dai, Qiang Li, *Scientific Reports (Online Only URL:http://www.nature.com/srep/index.html)*, 5, 13815, 2015, DOI:10.1038/srep13815.
  42. Carbon Ion Beam Combined with Cisplatin Effectively Disrupts Triple Negative Breast Cancer Stem-Like Cells in Vitro. Sei Sai, Guillaume Vares, Eun Ho Kim, Kumiko Karasawa, Wang Bing, Mitsuru Neno, Yoshiya Horimoto, *Molecular Cancer (Online Only URL:http://www.molecular-cancer.com/)*, 14(166), 2015, DOI:10.1186/s12943-015-0429-7.
  43. Designing a ridge filter based on a mouse foot skin reaction to spread out Bragg-peaks for carbon-ion radiotherapy. Akiko Uzawa, Koichi Ando, Yuki Kase, Ryoichi Hirayama, Yoshitaka Matsumoto, Naruhiro Matsufuji, Sachiko Koike, Gen Kobashi, *Radiotherapy and Oncology: Journal of the European Society for Therapeutic Radiology and Oncology*, 115(2), 279-283, 2015, DOI:10.1016/j.radonc.2015.04.007.
  44. Pre-exposure to ionizing radiation stimulates DNA double strand break end resection, promoting the use of homologous recombination repair. Nakako Izumi Nakajima, Yoshihiko Hagiwara, Takahiro Oike, Ryuichi Okayasu, Takeshi Murakami, Takashi Nakano, Atsushi Shibata, *PLoS ONE*, 2016, DOI:10.1371/journal.pone.0122582.
  45. Movement of a small tumour in contact with the diaphragm - characterisation with four-dimensional CT. Motoki Kumagai, Shinichiro Mori, *Japanese Journal of Radiology*, 34, 154-157, 2016, DOI:10.1007/s11604-015-0509-z.
  46. Variation in patient position and impact on carbon-ion scanning beam distribution during prostate treatment. Shinichiro Mori, Taku Inaniwa, Kentaro Miki, Katsuyuki Tanimoto, Minoru Tajiri, Daigo Kuroiwa, Yurika Shiraishi, Kouichi Shibayama, Hiroshi Tsuji, *British Journal of Radiology*, 88, 20140623, 2015.
  47. Four-dimensional layer-stacking carbon-ion beam dose distribution by use of a lung numeric phantom. Shinichiro Mori, Motoki Kumagai, Kentaro Miki, *Radiological Physics and Technology*, 2015, DOI:10.1007/s12194-015-0312-7.
  48. Impact of treatment planning with deformable image registration on dose distribution for carbon-ion beam lung treatment using a fixed irradiation port and rotating couch. Motoki Kumagai, Shinichiro Mori, Naoyoshi Yamamoto, *British Journal of Radiology*, 88, 20140734, 2015, DOI:10.1259/bjr.20140734.
  49. XRCC1 Polymorphism Associated with Late Toxicity After Radiation Therapy in Breast Cancer Patients. Petra Seibold, Sabine Behrens, Peter Schmezer, Irmgard Helmbold, Gillian Barnett, Charlotte Coles, John Yarnold, Christopher J. Talbot, Takashi Imai, David Azria, C. Anne Koch, Alison M. Dunning, Neil Burnet, Judith M. Bliss, R Paul Symonds, Tim Rattay, Tomo Suga, Sarah L. Kerns, Celine Bourcier, Katherine A. Vallis, Marie-Luise Sautter-Bihl, Johannes Claßen, Juergen Debus, Thomas Schnabel, Barry S. Rosenstein, Frederik Wenz, Catharine M. West, Odilia Popanda, Jenny Chang-Claude, *International Journal of Radiation Oncology, Biology, Physics*, 92(5), 1084-1092, 2015, DOI:10.1016/j.ijrobp.2015.04.011.
  50. Irradiation induces diverse changes in invasive potential in cancer lines. Mayumi Fujita, Shigeru Yamada, Takashi Imai, *Seminars in cancer biology*, 35, 45-52, 2015, DOI:10.1016/j.semcancer.2015.09.003.
  51. Comparison of CD163+ Macrophages and CD206+ Cells in Lesional Skin of CD30+ Lymphoproliferative Disorders of Lymphomatoid Papulosis and Primary Cutaneous Anaplastic Large-cell Lymphoma. Aya Kakizaki, Taku Fujimura, Yumi Kambayashi, Sadanori Furudate, Mitsuko Kawano, Kouetsu Ogasawara, Setsuya Aiba, *Acta Dermato-venereologica*, 95(5), 600-602, 2015.
  52. Carbon-ion irradiation suppresses migration and invasiveness of human pancreatic carcinoma cells MIAPaCa-2 via Rac1 and RhoA degradation. Mayumi Fujita, Kaori Imadome, Yoshimi Shoji, Teturo Isozaki, Satoshi Endo, Shigeru Yamada, Takashi Imai, *International Journal of Radiation Oncology, Biology, Physics*, 93(1), 173-180, 2015, DOI:10.1016/j.ijrobp.2015.05.009.
  53. Effect of Alkyl Group on Transnitrosation of N-Nitrosothiazolidine Thiocarboxamides. Keiko Inami, Yuta Ono, Sonoe Kondo, Ikuo Nakanishi, Kei Ohkubo, Shunichi Fukuzumi, Masataka Mochizuki, *Bioorganic & Medicinal Chemistry*, 23(20), 6733-6739, 2015, DOI:10.1016/j.bmc.2015.09.008.
  54. Biliary excretion of essential trace elements in rats under oxidative stress caused by selenium deficiency. Kosuke Yamasaki, Yasunobu Sakuma, Junya Sasaki, Ken-ichiro Matsumoto, Kazunori Anzai, Keisuke Matsuoka, Chikako Honda, Masamichi Tsukada, Kazutoyo Endo, Shuichi Enomoto, *Analytical and Bioanalytical Chemistry*, 401(8), 2531-2538, 2011.
  55. Effect of Amifostine, a Radiation-Protecting Drug, on Oxy-

- gen Concentration in Tissue Measured by EPR Oximetry and Imaging. Megumi Ueno, Shingo Matsumoto, Atsuko Matsumoto, Sushma Manda, Ikuo Nakanishi, Ken-ichiro Matsumoto, James B. Mitchell, Murali C. Krishna, Kazunori Anzai, *Journal of Clinical Biochemistry and Nutrition*, in press, 2016.
56. Non-invasive Measurement of Melanin-Derived Radicals in Living Mouse Tail Using X-band EPR. Yukihiro Ogawa, Megumi Ueno, Emiko Sekine-Suzuki, Ikuo Nakanishi, Ken-ichiro Matsumoto, Shingo Fujisaki, *Journal of Clinical Biochemistry and Nutrition*, in press, 2016.
  57. Brain Contrasting Ability of Blood-Brain-Barrier-Permeable Nitroxyl Contrast Agents for Magnetic Resonance RedOx Imaging. Ken-ichiro Matsumoto, Toshihide Yamasaki, Mizuki Nakamura, Junji Ishikawa, Megumi Ueno, Ikuo Nakanishi, Aiko Sekita, Yoshikazu Ozawa, Tadashi Kamada, Ichio Aoki, Ken-ichi Yamada, *Magnetic Resonance in Medicine*, 2015, DOI:10.1002/mrm.25918.
  58. Solubilisation of a 2,2-Diphenyl-1-picrylhydrazyl Radical in Water by  $\beta$ -Cyclodextrin to Evaluate the Radical-Scavenging Activity of Antioxidants in Aqueous Media. Ikuo Nakanishi, Kei Ohkubo, Kohei Imai, Masato Kamibayashi, Yasuo Yoshihashi, Kenichiro Matsumoto, Kiyoshi Fukuhara, Katsuhide Terada, Shinobu Itoh, Toshihiko Ozawa, Shunichi Fukuzumi, *Chemical Communications*, 51(39), 8311-8314, 2015, DOI:10.1039/c5cc02236c.
  59. Radiation Therapy and Redox Imaging. Ken-ichiro Matsumoto, *Yakugaku Zasshi (Journal of the Pharmaceutical Society of Japan)*, 135(5), 719-724, 2015 (In Japanese with English abstract).
  60. Analysis of the Antioxidative Function of the Radioprotective Japanese Traditional (Kampo) Medicine, Hange-shashinto, in an Aqueous Phase. Chinami Matsumoto, Emiko Sekine-Suzuki, Minako Nyui, Megumi Ueno, Ikuo Nakanishi, Yuji Omiya, Masato Fukutake, Yoshio Kase, Ken-ichiro Matsumoto, *Journal of Radiation Research*, 56(4), 669-677, 2015.
  61. A laser-plasma-produced soft X-ray laser at 89 eV generates DNA double-strand breaks in human cancer cells. Katsutoshi Sato, Masaharu Nishikino, Tetsuya Kawachi, Takashi Shimokawa, Takashi Imai, Teruki Teshima, Hiroaki Nishimura, Masaki Kando, *Journal of Radiation Research*, 56(4), 633-638, 2015, DOI:10.1093/jrr/rrv015.
  62. Radiation chemical yields for the losses of typical functional groups in PADC films for high energy protons registered as unetchable tracks. Tamon Kusumoto, Yutaka Mori, Masato Kanasaki, Ryunosuke Ikenaga, Keiji Oda, Satoshi Kodaira, Hisashi Kitamura, Remi Barillon, Tomoya Yamauchi, *Radiation Measurements*, 87, 35-42, 2016, DOI:10.1016/j.radmeas.2016.01.029.
  63. Energy compensation of slow extracted beams with RF acceleration. Tetsuya Fujimoto, Hikaru Souda, Masami Torikoshi, Tatsuaki Kanai, Satoru Yamada, Koji Noda, *Nuclear Instruments and Methods in Physics Research A*, 812, 68-72, 2016, DOI:10.1016/j.nima.2015.12.044.
  64. Yields on the formation of OH groups and the loss of CH groups along nuclear tracks in PADC films. Tamon Kusumoto, Yutaka Mori, Masato Kanasaki, Takuya Ueno, Yuka Kameda, Keiji Oda, Satoshi Kodaira, Hisashi Kitamura, Remi Barillon, Tomoya Yamauchi, *Radiation Measurements*, 83, 59-62, 2015, DOI:10.1016/j.radmeas.2015.04.008.
  65. Parameters of 500 MeV/u  $^{56}\text{Fe}$  tracks in bubble detector (BD) T-15 – A new technique to estimate the number and diameter of superheated droplets in bubble detectors. S.-L. Guo, T. Doke, D.-H. Zhang, B.-L. Chen, L. Li, N. Hasebe, J. Kikuchi, N. Yasuda, T. Murakami, *Radiation Measurements*, 83, 5-11, 2015, DOI:10.1016/j.radmeas.2015.06.012.
  66. The Effect of p53 Status of Tumor Cells on Radiosensitivity of Irradiated Tumors with Carbon-Ion Beams Compared with  $\gamma$ -Rays or Reactor Neutron Beams. Shin-ichiro Masunaga, Akiko Uzawa, Ryoichi Hirayama, Yoshitaka Matsumoto, Yoshinori Sakurai, Hiroki Tanaka, Keizo Tano, Yu Sanada, Minoru Suzuki, Akira Maruhashi, Koji Ono, *World Journal of Oncology*, 6(4), 398-409, 2015, DOI:10.14740/wjon941w.
  67. Excess processing of oxidative damaged bases causes hypersensitivity to oxidative stress and low dose rate irradiation. Y. Yoshikawa, A. Yamasaki, K. Takatori, M. Suzuki, J. Kobayashi, M. Takao, Q.-M. Zhang-Akiyama, *Free Radical Research*, 49(10), 1239-1248, 2015, DOI:10.3109/10715762.2015.1061186.
  68. Radiosensitization of glioblastoma cells using a histone deacetylase inhibitor (SAHA) comparing carbon ions with X-rays. Lara Barazzuol, J. Charles G. Jeynes, Michael J. Merchant, Anne-Catherine Wéra, Miriam A Barry, Karen J. Kirkby, Masao Suzuki, *International Journal of Radiation Biology*, 91(1), 90-98, 2015.
  69. Genetic changes in progeny of bystander human fibroblasts after microbeam irradiation with X-rays, protons or carbon ions: the relevance to cancer risk. Narongchai Autsavapromporn, Ianik Plante, Cuihua Liu, Teruaki Konishi, Noriko Usami, Tomoo Funayama, Edouard I. Azzam, Takeshi Murakami, Masao Suzuki, *International Journal of Radiation Biology*, 91(1), 62-70, 2015.
  70. Metastable  $\text{Ar}^{17+}$  (2 s) production by Stark-assisted resonant coherent excitation. Y. Nakano, A. Sokolik, A.V. Stysin, Y. Nakai, K. Komaki, E. Takada, T. Murakami, T. Azuma, *Journal of Physics B: Atomic, Molecular and Optical Physics*, 48(14), 144026-1 - 144026-7, 2015, DOI:10.1088/0953-4075/48/14/144026.
  71. ESR spin trapping of radicals in methanol solution irradiated by heavy ion beams. Dependence on specific energy and LET. Seiko Nakagawa, Takeshi Murakami, *Nuclear Instruments and Methods in Physics Research Section B: Beam Interactions with Materials and Atoms*, 356-357, 108-113, 2015, DOI:10.1016/j.nimb.2015.04.040.

#### ■ Molecular Imaging Center

1. Anatomical and Functional Estimations of Brachial Artery Diameter and Elasticity using Oscillometric Measurements with Quantitative Approach. Keiichiro Yoshinaga, Satoshi Fujii, Yuuki Tominaga, Keisuke Takeuchi, Nagara Tamaki, *Pulse*, 4(1), 1-10, 2016, DOI:10.1159/000444368.
2. Feasibility of quantifying the myocardial blood flow with a shorter acquisition time using  $^{15}\text{O}$ -H $_2$ O PET. Ayaka Maruo, Osamu Manabe, Keiichiro Yoshinaga, Masanao Naya, Yuuki Tomiyama, Noriko Oyama-Manabe, Kenji Hirata, Keiichi Magota, Hiroyuki Tsutsui, Chietsugu Katoh, Nagara Tamaki, *Annals of Nuclear Cardiology*, 2(1), in press, 2016, DOI:10.17996/ANC.15002.
3. Comprehensive assessment of impaired peripheral and coronary artery endothelial functions in smokers using brachial artery ultrasound and oxygen-15-labeled water

- PET. Noriki Ochi, Keiichiro Yoshinaga, Yoichi M Ito, Yuuki Tomiyama, Mamiko Inoue, Mutsumi Nishida, Osamu Manabe, Hitoshi Shibuya, Chikara Shimizu, Eriko Suzuki, Satoshi Fujii, Chietsugu Katoh, Nagara Tamaki, *Journal of Cardiology*, in press, 2016, DOI:10.1016/j.jcc.2015.10.006.
4. Comparison of <sup>18</sup>F-fluorodeoxyglucose positron emission tomography (FDG PET) and cardiac magnetic resonance (CMR) in corticosteroid-naive patients with conduction system disease due to cardiac sarcoidosis. Hiroshi Ohira, David H. Birnie, Elena Pena, Jordan Bernick, Brian Mc Ardle, Eugene Leung, George A. Wells, Keiichiro Yoshinaga, Ichizo Tsujino, *European Journal of Nuclear Medicine and Molecular Imaging*, 43(2), 259-269, 2016.
  5. Administration of unfractionated heparin with prolonged fasting could reduce physiological <sup>18</sup>F-fluorodeoxyglucose uptake in the heart. Atsuro Masuda, Masanao Naya, Osamu Manabe, Keiichi Magota, Keiichiro Yoshinaga, Hiroyuki Tsutsui, Nagara Tamaki, *Acta Radiologica*, 57(6), 661-668, 2016, DOI:10.1177/0284185115600916.
  6. Quantitative measurements of brachial artery cross-sectional area and volume elastic modulus using automated oscillometric methods comparison with ultrasound. Yuuki Tomiyama, Yoshinaga Keiichiro, Satoshi Fujii, Noriki Ochi, Mamiko Inoue, Eriko Suzuki, Kumi Aziki, Hideo Nishibayashi, Chietsugu Katoh, Nagara Tamaki, *Hypertension Research*, 38(7), 478-484, 2015.
  7. Improved spillover correction model to quantify myocardial blood flow by 11C-acetate PET: comparison with 15O-H<sub>2</sub>O PET. Yuki Mori, Osamu Manabe, Masanao Naya, Yuuki Tomiyama, Keiichiro Yoshinaga, Keiichi Magota, Noriko Oyama-Manabe, Kenji Hirata, Hiroyuki Tsutsui, Nagara Tamaki, Chietsugu Katoh, *Annals of Nuclear Medicine*, 29(1), 15-20, 2015, DOI:10.1007/s12149-014-0904-z.
  8. Ethics and Quality Assurance in Investigator-Initiated Clinical Studies: The First Report-Experience from a Multi-center Clinical Study of Tau PET Imaging with [<sup>11</sup>C]PBB3-Chieko Kurihara, Takashi Horiguchi, Kazuko Suzuki, Tetsuya Suhara, *Japanese Journal of Clinical Pharmacology and Therapeutics*, 46(4), 211-224, 2015, DOI:10.3999/jscpt.46.211.
  9. Synthesis and Preliminary PET Imaging Studies of a FAAH Radiotracer ([<sup>11</sup>C]MPPO) Based on  $\alpha$ -Ketoheterocyclic Scaffold. Lu Wang, Joji Yui, Qifan Wang, Yiding Zhang, Wakana Mori, Yoko Shimoda, Masayuki Fujinaga, Katsushi Kumata, Tomoteru Yamasaki, Akiko Hatori, Benjamin H. Rotstein, Thomas Lee Collier, Chongzhao Ran, Neil Vasdev, Ming-Rong Zhang, Steven H. Liang, *ACS Chemical Neuroscience*, 7(1), 109-118, 2015, DOI:10.1021/acschemneuro.5b00248.
  10. Radiosynthesis and evaluation of 5-methyl-N-(4-[(<sup>11</sup>C)methylpyrimidin-2-yl]-4-(1H-pyrazol-4-yl)thiazol-2-amine ([<sup>11</sup>C]ADX88178) as a novel radioligand for imaging of metabotropic glutamate receptor subtype 4 (mGluR4). Masayuki Fujinaga, Tomoteru Yamasaki, Nobuki Nengaki, Masanao Ogawa, Katsushi Kumata, Yoko Shimoda, Joji Yui, Lin Xie, Yiding Zhang, Kazunori Kawamura, Ming-Rong Zhang, *Bioorganic & Medicinal Chemistry Letters*, 26(2), 370-374, 2016, DOI:10.1016/j.bmcl.2015.12.008.
  11. [<sup>18</sup>F]FPBMP: - a potential new positron emission tomography radioligand for imaging of translocator protein (18 kDa) in peripheral organs of rat. Anjani Tiwari, Joji Yui, Yiding Zhang, Masayuki Fujinaga, Tomoteru Yamasaki, Lin Xie, Yoko Shimoda, Katsushi Kumata, Akiko Hatori, Ming-Rong Zhang, *RSC Advances*, 5(123), 101447-101454, 2015, DOI:10.1039/C5RA22594A.
  12. N-(3,4-Dimethylisoxazol-5-yl)piperazine-4-[4-(2-fluoro-4-[(<sup>11</sup>C)methylphenyl]thiazol-2-yl)-1-carboxamide: A promising positron emission tomography ligand for fatty acid amide hydrolase. Yoko Shimoda, Masayuki Fujinaga, Akiko Hatori, Joji Yui, Yiding Zhang, Nobuki Nengaki, Yusuke Kurihara, Tomoteru Yamasaki, Lin Xie, Katsushi Kumata, Hideki Ishii, Ming-Rong Zhang, *Bioorganic & Medicinal Chemistry*, 24(4), 627-634, 2016, DOI:10.1016/j.bmc.2015.12.026.
  13. Utility of Translocator Protein (18 kDa) as a Molecular Imaging Biomarker to Monitor the Progression of Liver Fibrosis. Akiko Hatori, Joji Yui, Lin Xie, Katsushi Kumata, Tomoteru Yamasaki, Masayuki Fujinaga, Hidekatsu Wakizaka, Masanao Ogawa, Nobuki Nengaki, Kazunori Kawamura, Feng Wang, Ming-Rong Zhang, *Scientific Reports (Online Only URL:http://www.nature.com/srep/index.html)*, 5, 17327, 2015, DOI:10.1038/srep17327.
  14. Radiosynthesis and evaluation of N-(3,4-dimethylisoxazol-5-yl)piperazine-4-[4-(4-fluorophenyl)thiazol-2-yl]-1-[(<sup>11</sup>C)]carboxamide for in vivo positron emission tomography imaging of fatty acid amide hydrolase in brain. Yoko Shimoda, Joji Yui, Yiding Zhang, Akiko Hatori, Masanao Ogawa, Masayuki Fujinaga, Tomoteru Yamasaki, Lin Xie, Katsushi Kumata, Ming-Rong Zhang, *RSC Advances*, 5, 106122-106127, 2015.
  15. Synthesis and evaluation of 1-[2-(4-[(<sup>11</sup>C)methoxyphenyl]phenyl)piperazine for imaging of the serotonin 5-HT<sub>7</sub> receptor in the rat brain. Yoko Shimoda, Joji Yui, Lin Xie, Masayuki Fujinaga, Tomoteru Yamasaki, Masanao Ogawa, Nobuki Nengaki, Katsushi Kumata, Akiko Hatori, Kazunori Kawamura, Ming-Rong Zhang, *Bioorganic & Medicinal Chemistry*, 21(17), 5316-5322, 2013.
  16. Dynamic Changes in Striatal mGluR1 but not mGluR5 During Pathological Progression of Parkinson's Disease in Human Alpha-Synuclein A53T Transgenic Rats: A Multi-PET Imaging Study. Tomoteru Yamasaki, Masayuki Fujinaga, Kazunori Kawamura, Kenji Furutsuka, Nobuki Nengaki, Yoko Shimoda, Satoshi Shiomi, Makoto Takei, Hiroki Hashimoto, Joji Yui, Hidekatsu Wakizaka, Akiko Hatori, Lin Xie, Katsushi Kumata, Ming-Rong Zhang, *Journal of Neuroscience*, 36(2), 375-384, 2016.
  17. Development of 1-N-(<sup>11</sup>C)-Methyl-l- and -d-Tryptophan for pharmacokinetic imaging of the immune checkpoint inhibitor 1-Methyl-Tryptophan. Lin Xie, Jun Maeda, Katsushi Kumata, Joji Yui, Yiding Zhang, Akiko Hatori, Nobuki Nengaki, Hidekatsu Wakizaka, Masayuki Fujinaga, Tomoteru Yamasaki, Yoko Shimoda, Makoto Higuchi, Tetsuya Suhara, Feng Wang, Ming-Rong Zhang, *Scientific Reports (Online Only URL:http://www.nature.com/srep/index.html)*, 5, 16417, 2015, DOI:10.1038/srep16417.
  18. Manufacture and Utilization of a Low-level Radioactive <sup>68</sup>Ge/<sup>68</sup>Ga Generator in a Radiochemistry Laboratory Course. Kohshin Washiyama, Ryohei Amano, Tadashi Nozaki, Koji Ogawa, Kotaro Nagatsu, Minoru Sakama, Tatuo Ido, Hiroshi Yamaguchi, Nihon Ho'shasen Gijutsu Gakkai Zasshi (*Japanese Journal of Radiological Technology*), 71(10), 983-993, 2015.
  19. Identification of a major radiometabolite of [<sup>11</sup>C]PBB3. Hiroki Hashimoto, Kazunori Kawamura, Makoto Takei,

- Nobuyuki Igarashi, Tomoya Fujishiro, Satoshi Shiomi, Watanabe Ryuji, Masatoshi Muto, Kenji Furutsuka, Takehito Ito, Tomoteru Yamasaki, Joji Yui, Kazuyoshi Nemoto, Yasuyuki Kimura, Makoto Higuchi, Ming-Rong Zhang, *Nuclear Medicine and Biology*, 42(12), 905-910, 2015, DOI:10.1016/j.nucmedbio.2015.08.006.
20. In vivo imaging of blood-brain barrier permeability using positron emission tomography with 2-amino-[3-<sup>11</sup>C] isobutyric acid. Maki Okada, Tatsuya Kikuchi, Toshimitsu Okamura, Yoko Ikoma, Atsushi Tsuji, Hidekatsu Wakizaka, Ichio Aoki, Ming-Rong Zhang, Koichi Kato, Tomoo Kamakura, *Nuclear Medicine Communications*, 36(12), 1239-1248, 2015.
  21. Kinetic study of benzyl [1-<sup>14</sup>C]acetate as a potential probe for astrocytic energy metabolism in the rat brain: Comparison with benzyl [2-<sup>14</sup>C]acetate. Maki Okada, Kazuhiko Yanamoto, Tomohiko Kagawa, Keiko Yoshino, Rie Hosoi, Kohji Abe, Ming-Rong Zhang, Osamu Inoue, *Journal of Cerebral Blood Flow and Metabolism*, 36(2), 442-450, 2016, DOI:10.1177/0271678X15606144.
  22. Radiosynthesis and preliminary PET evaluation of glycogen synthase kinase 3 $\beta$  (GSK-3 $\beta$ ) inhibitors containing [(<sup>11</sup>C)methylsulfanyl], [(<sup>11</sup>C)methylsulfinyl] or [(<sup>11</sup>C)methylsulfonyl] groups. Katsushi Kumata, Joji Yui, Lin Xie, Yiding Zhang, Nobuki Nengaki, Masayuki Fujinaga, Tomoteru Yamasaki, Yoko Shimoda, Ming-Rong Zhang, *Bioorganic & Medicinal Chemistry Letters*, 25(16), 3230-3233, 2015, DOI:10.1016/j.bmcl.2015.05.085.
  23. A (<sup>11</sup>C)-labeled 1,4-dihydroquinoline derivative as a potential PET tracer for imaging of redox status in mouse brain. Toshimitsu Okamura, Maki Okada, Tatsuya Kikuchi, Hidekatsu Wakizaka, Ming-Rong Zhang, *Journal of Cerebral Blood Flow and Metabolism*, 35, 1930-1936, 2015, DOI:10.1038/jcbfm.2015.132.
  24. Improved Visualization and Specific Binding for Metabotropic Glutamate Receptor Subtype 1 (mGluR1) Using [<sup>11</sup>C]ITMM with Ultra-High Specific Activity in Small-Animal PET. Tomoteru Yamasaki, Masayuki Fujinaga, Joji Yui, Hidekatsu Wakizaka, Tomoyuki Ohya, Nobuki Nengaki, Masanao Ogawa, Yoko Ikoma, Akiko Hatori, Lin Xie, Kazunori Kawamura, Ming-Rong Zhang, *PloS ONE*, 10(6), e0130006, 2015, DOI:10.1371/journal.pone.0130006.
  25. [<sup>18</sup>F]FEBMP: Positron Emission Tomography Imaging of TSPO in a Model of Neuroinflammation in Rats, and in Vitro Autoradiograms of the Human Brain. Anjani Tiwari, Bin Ji, Joji Yui, Masayuki Fujinaga, Tomoteru Yamasaki, Lin Xie, Rui Luo, Yoko Shimoda, Katsushi Kumata, Yiding Zhang, Akiko Hatori, Jun Maeda, Makoto Higuchi, Feng Wang, Ming-Rong Zhang, *Theranostics*, 5(9), 961-969, 2015.
  26. Washout rate in rat brain irradiated by a <sup>11</sup>C beam after acetazolamide loading using a small single-ring OpenPET prototype. Yoshiyuki Hirano, Hiroyuki Takuwa, Eiji Yoshida, Fumihiko Nishikido, Yasunori Nakajima, Hidekatsu Wakizaka, Taiga Yamaya, *Physics in Medicine and Biology*, 61(5), 1875-1887, 2016, DOI:10.1088/0031-9155/61/5/1875.
  27. Development of a small single-ring OpenPET prototype with a novel transformable architecture. Hideaki Tashima, Eiji Yoshida, Naoko Inadama, Fumihiko Nishikido, Yasunori Nakajima, Hidekatsu Wakizaka, Tetsuya Shinaji, Munetaka Nitta, Shoko Kinouchi, Mikio Suga, Hideaki Haneishi, Taku Inaniwa, Taiga Yamaya, *Physics in Medicine and Biology*, 61(4), 1795-1809, 2016, DOI:10.1088/0031-9155/61/4/1795.
  28. Parameter Optimization of a Digital Photon Counter Coupled to a Four-Layered DOI Crystal Block with Light Sharing. Eiji Yoshida, Ian Somlai Schweiger, Hideaki Tashima, Sibylle I. Ziegler, Taiga Yamaya, *IEEE Transactions on Nuclear Science*, 62(3), 748-755, 2015, DOI:10.1109/TNS.2015.2420577.
  29. [<sup>11</sup>C]Raclopride binding in the striatum of minimally restrained and free-walking awake mice in a positron emission tomography study. Hiroyuki Takuwa, Jun Maeda, Yoko Ikoma, Masaki Tokunaga, Hidekatsu Wakizaka, Shouko Uchida, Iwao Kanno, Junko Taniguchi, Hiroshi Ito, Makoto Higuchi, *Synapse*, 69(12), 600-606, 2015, DOI:10.1002/syn.21864.
  30. Effects of point spread function-based image reconstruction on neuroreceptor binding in positron emission tomography study with [<sup>11</sup>C]FLB 457. Thongpraparn Thonnapong, Yoko Ikoma, Takahiro Shiraiishi, Taiga Yamaya, Hiroshi Ito, *Radiological Physics and Technology*, 9(1), 127-137, 2016, DOI:10.1007/s12194-015-0343-0.
  31. Vasodilation mechanism of cerebral microvessels induced by neural activation under high baseline CBF level results from hypercapnia in awake mice. Asuka Nishino, Hiroyuki Takuwa, Takuya Urushihata, Hiroshi Ito, Yoko Ikoma, Tetsuya Matsuura, *Microcirculation*, 22(8), 744-752, 2015, DOI:10.1111/micc.12250.
  32. Evaluation of semi-quantitative method for quantification of dopamine transporter in human PET study with <sup>18</sup>F-FE-PE2I. Yoko Ikoma, Takeshi Sasaki, Yasuyuki Kimura, Chie Seki, Yoshiro Okubo, Tetsuya Suhara, Hiroshi Ito, *Annals of Nuclear Medicine*, 29(8), 697-708, 2015, DOI:10.1007/s12149-015-0993-3.
  33. Development of radioiodine-labeled 4-hydroxyphenylcysteamine for specific diagnosis of malignant melanoma. Masato Kobayashi, Ryuichi Nishii, Naoto Shikano, Leo G Flores, Asuka Mizutani, Kazuhiro Ogai, Jyunko Sugama, Shigeki Nagamachi, Keiichi Kawai, *Nuclear medicine and biology*, 42(6), 536-540, 2015, DOI:10.1016/j.nucmedbio.2015.02.004.
  34. CT evaluation of acupuncture needles inserted into sacral foramina. Yuichi Katayama, Toyoharu Kamibeppu, Ryuichi Nishii, Shoichiro Mukai, Hironobu Wakeda, Toshiyuki Kamoto, *Acupuncture in Medicine*, 34(1), 20-6, 2016, DOI:10.1136/acupmed-2015-010775.
  35. Increase in [<sup>18</sup>F]-Fluoroacetate Uptake in Patients with Chronic Hemodynamic Cerebral Ischemia. Hiroshi Yamauchi, Shinya Kagawa, Yoshihiko Kishibe, Masaaki Takahashi, Ryuichi Nishii, Hiroshi Mizuma, Kazuhiro Takahashi, Hirotaka Onoe, Tatsuya Higashi, *Stroke*, 46(9), 2669-2672, 2015, DOI:10.1161/STROKEAHA.115.010080.
  36. The predictive value of preoperative <sup>18</sup>F-fluorodeoxyglucose PET for postoperative recurrence in patients with localized primary gastrointestinal stromal tumour. Kanae Kawai Miyake, Yuji Nakamoto, Yoshiki Mikami, Shiro Tanaka, Tatsuya Higashi, Eiji Tamamura, Tsuneo Saga, Shunsuke Minami, Kaori Togashi, *European Radiology*, in press, 2016, DOI:10.1007/s00330-016-4242-5.
  37. Prognostic value of PET/CT with <sup>18</sup>F-fluoroazomycin arabinoside for patients with head and neck squamous cell carcinomas receiving chemoradiotherapy. Tsuneo Saga, Masayuki Inubushi, Mitsuru Koizumi, Kyosan Yoshikawa, Ming-Rong Zhang, Takayuki Obata, Katsuyuki Tanimoto,

- Rintaro Harada, Takashi Uno, Yasuhisa Fujibayashi, *Annals of Nuclear Medicine*, 30(3), 217-224, 2016, DOI:10.1007/s12149-015-1048-5.
38. Prognostic value of <sup>18</sup>F-fluoroazomycin arabinoside PET/CT in patients with advanced non-small cell lung cancer. Tsuneo Saga, Masayuki Inubushi, Mitsuru Koizumi, Kyosan Yoshikawa, Ming-Rong Zhang, Katsuyuki Tanimoto, Atsushi Horiike, Noriko Yanagitani, Fumiyoshi Ohyanagi, Makoto Nishio, *Cancer Science*, 106(11), 1554-1560, 2015, DOI:10.1111/cas.12771.
  39. Development of the Fibronectin-Mimetic Peptide KSSPHSRN(SG)5RGDSP as a Novel Radioprobe for Molecular Imaging of the Cancer Biomarker  $\alpha 5\beta 1$  Integrin. Zhao-Hui Jin, Takako Furukawa, Katsushi Kumata, Lin Xie, Joji Yui, Hidekatsu Wakizaka, Yasuhisa Fujibayashi, Ming-Rong Zhang, Tsuneo Saga, *Biological & Pharmaceutical Bulletin*, 38(11), 1722-1731, 2015, DOI:10.1248/bpb.b15-00344.
  40. The effects of 18-h fasting with low-carbohydrate diet preparation on suppressed physiological myocardial <sup>18</sup>F-fluorodeoxyglucose (FDG) uptake and possible minimal effects of unfractionated heparin use in patients with suspected cardiac involvement sarcoidosis. Osamu Manabe, Keiichiro Yoshinaga, Hiroshi Ohira, Atsuro Masuda, Takahiro Sato, Ichizo Tsujino, Asuka Yamada, Noriko Oyama-Manabe, Kenji Hirata, Masaharu Nishimura, Nagara Tamaki, *Journal of Nuclear Cardiology*, 2015, DOI:10.1007/s12350-015-0226-0.
  41. Performance characteristics of a novel clustered multipinhole technology for simultaneous high-resolution SPECT/PET. Kenta Miwa, Masayuki Inubushi, Yasuto Takeuchi, Tetsuro Katafuchi, Mitsuru Koizumi, Tsuneo Saga, Masayuki Sasaki, *Annals of Nuclear Medicine*, 29(5), 460-466, 2015, DOI:10.1007/s12149-015-0966-6.
  42. Regorafenib as a potential adjuvant chemotherapy agent in disseminated small colon cancer: Drug selection outcome of a novel screening system using nanoimprinting 3-dimensional culture with HCT116-RFP cells. Yukie Yoshii, Takako Furukawa, Hironori Aoyama, Naoya Adachi, Ming-Rong Zhang, Hidekatsu Wakizaka, Yasuhisa Fujibayashi, Tsuneo Saga, *International Journal of Oncology*, 48(4), 1477-1484, 2016, DOI:10.3892/ijo.2016.3361.
  43. In Vivo Simultaneous Imaging of Vascular Pool and Hypoxia with a HT-29 Tumor Model: The Application of Dual-Isotope SPECT/PET/CT. Naoya Adachi, Yukie Yoshii, Takako Furukawa, Mitsuyoshi Yoshimoto, Yasuto Takeuchi, Masayuki Inubushi, Hidekatsu Wakizaka, Ming-Rong Zhang, Atsushi Tsuji, Masashi Takahashi, Yasuhisa Fujibayashi, Tsuneo Saga, *International Journal of Sciences: Basic and Applied Research*, 25(1), 26-39, 2016.
  44. Immunotargeting of Integrin  $\alpha 6\beta 4$  for Single-Photon Emission Computed Tomography and Near-Infrared Fluorescence Imaging in a Pancreatic Cancer Model. Aung U Winn, Atsushi Tsuji, Hitomi Sudo, Aya Sugyo, Takako Furukawa, Yoshinori Ukai, Yoshikazu Kurosawa, Tsuneo Saga, *Molecular Imaging*, 2015, DOI:10.1177/1536012115624917.
  45. Immuno-PET Imaging of HER3 in a Model in which HER3 Signaling Plays a Critical Role. Qinghua Yuan, Takako Furukawa, Takahiro Tashiro, Kouki Okita, Zhao-Hui Jin, Winn Aung, Aya Sugyo, Koutaro Nagatsu, Hiroko Endo, Atsushi B Tsuji, Ming-Rong Zhang, Takashi Masuko, Masahiro Inoue, Yasuhisa Fujibayashi, Tsuneo Saga, *PloS ONE*, 10(11), e0143076-1-e0143076-16, 2016, DOI:10.1371/journal.pone.0143076.
  46. Transcriptomic Signatures of Auger Electron Radioimmunotherapy Using Nuclear Targeting <sup>111</sup>In-Trastuzumab for Potential Combination Therapies. Huizi Keiko Li, Yukie Morokoshi, Kazuhiro Daino, Takako Furukawa, Tadashi Kamada, Tsuneo Saga, Sumitaka Hasegawa, *Cancer Biotherapy & Radiopharmaceuticals*, 30(8), 349-358, 2015.
  47. A limited overlap between intratumoral distribution of 1-(5-fluoro-5-deoxy- $\alpha$ -D-arabinofuranosyl)-2-nitroimidazole and copper-diacetyl-bis[N(4)-methylthiosemicarbazone]. Takako Furukawa, Qinghua Yuan, Zhao-Hui Jin, Winn Aung, Yukie Yoshii, Sumitaka Hasegawa, Hiroko Endo, Masahiro Inoue, Ming-Rong Zhang, Yasuhisa Fujibayashi, Tsuneo Saga, *Oncology Reports*, 34(3), 1379-1387, 2015, DOI:10.3892/or.2015.4079.
  48. Establishment and evaluation of a new highly metastatic tumor cell line 5a-D-Luc-ZsGreen expressing both luciferase and green fluorescent protein. Hitomi Sudo, Atsushi B Tsuji, Aya Sugyo, Hiroyuki Takuwa, Kazuto Masamoto, Yutaka Tomita, Norihiro Suzuki, Takeshi Imamura, Mitsuru Koizumi, Tsuneo Saga, *International Journal of Oncology*, 48(2), 525-532, 2016, DOI:10.3892/ijo.2015.3300.
  49. Polymeric Micelle Platform for Multimodal Tomographic Imaging to Detect Scirrhus Gastric Cancer. Yutaka Miura, Atsushi Tsuji, Aya Sugyo, Hitomi Sudo, Ichio Aoki, Masayuki Inubushi, Masakazu Yashiro, Kosei Hirakawa, Horacio Cabral, Nobuhiro Nishiyama, Tsuneo Saga, Kazunori Kataoka, *ACS Biomaterials Science & Engineering*, 1(11), 1067-1076, 2015, DOI:10.1021/acsbomaterials.5b00142.
  50. Preclinical evaluation of 2-amino-2-[<sup>11</sup>C]methyl-butanoic acid as a potential tumor-imaging agent in a mouse model. Chie Suzuki, Atsushi Tsuji, Koichi Kato, Hitomi Sudo, Ming-Rong Zhang, Tsuneo Saga, *Nuclear medicine communications*, 36(11), 1107-1112, 2015, DOI:10.1097/MNM.0000000000000364.
  51. Evaluation of Efficacy of Radioimmunotherapy with <sup>90</sup>Y-Labeled Fully Human Anti-Transferrin Receptor Monoclonal Antibody in Pancreatic Cancer Mouse Models. Aya Sugyo, Atsushi B Tsuji, Hitomi Sudo, Maki Okada, Mitsuru Koizumi, Hirokazu Satoh, Gene Kurosawa, Yoshikazu Kurosawa, Tsuneo Saga, *PloS ONE*, 10(4), e0123761-e0123761, 2015, DOI:10.1371/journal.pone.0123761.
  52. Liposomally formulated phospholipid-conjugated indocyanine green for intra-operative brain tumor detection and resection. Akiko Suganami, Yasuo Iwadate, Sayaka Shibata, Masamichi Yamashita, Tsutomu Tanaka, Natsuki Shinozaki, Ichio Aoki, Naokatsu Saeki, Hiroshi Shirasawa, Yoshiharu Okamoto, Yutaka Tamura, *International Journal of Pharmaceutics*, 2015, DOI:10.1016/j.ijpharm.2015.10.001.
  53.  $\gamma$ -PARCEL: Control of Molecular Release Using  $\gamma$ -Rays. Shuhei Murayama, Jun-Ichiro Jo, Kazutaka Arai, Fumihiko Nishikido, Rumiana Bakalova, Taiga Yamaya, Tsuneo Saga, Masaru Kato, Ichio Aoki, *Analytical Chemistry*, 87(23), 11625-11629, 2015, DOI:10.1021/acs.analchem.5b03030.
  54. 2-Deoxy-D-glucose Sensitizes Cancer Cells to Barasertib and Everolimus by ROS-independent Mechanism(s). Zhivko Zhelev, Donika Ivanova, Ichio Aoki, Tsuneo Saga, Rumiana Bakalova, *Anticancer Research*, 35(12), 6623-6632, 2015.

55. Passive and electro-assisted delivery of hydrogel nanoparticles in solid tumors, visualized by optical and magnetic resonance imaging in vivo. Rumiana Bakalova-Zheleva, Biliana Pancheva Nikolova-Lefterova, Shuhei Murayama, Severina Atanasova, Zhivko Zhelev, Ichio Aoki, Masaru Kato, Iana Tsoneva, Tsuneo Saga, *Analytical and Bioanalytical Chemistry*, 408(3), 905-914, 2016.
56. Magnetic resonance imaging of mitochondrial dysfunction and metabolic activity, accompanied by overproduction of superoxide. Rumiana Bakalova, Ekaterina Georgieva, Donika Ivanova, Zhivko Zhelev, Ichio Aoki, Tsuneo Saga, *ACS Chemical Neuroscience*, 6(12), 1922-1929, 2015, DOI:10.1021/acschemneuro.5b00220.
57. Sexual dimorphism of sulcal morphology of the ferret cerebrum revealed by MRI-based sulcal surface morphometry. Sawada K, Horiuchi-Hirose M, Saito S, Aoki I, *Frontiers in Neuroanatomy*, 9(55), 1-14, 2015, DOI:10.3389/fnana.2015.00055.
58. Male Prevalent Enhancement of Leftward Asymmetric Development of the Cerebellar Cortex in Ferrets (*Mustela putorius*). K. Sawada, M. Horiuchi-Hirose, S. Saito, I. Aoki, *Laterality: Asymmetries of Body, Brain and Cognition*, 20(6), 723-737, 2015.
59. Thermoactivatable Polymer-grafted Liposomes for Low-invasive Image-guided Chemotherapy. Ichio Aoki, Misao Yoneyama, Jun Hirose, Yuzuru Minemoto, Takayoshi Koyama, Daisuke Kokuryo, Shuhei Murayama, Rumiana Bakalova, Tsuneo Saga, Sadahito Aoshima, Kenji Kono, Yukihito Ishizaka, Kenji Kono, *Translational Research*, 166(6), 660-673, 2015.
60. Experimental model for evaluation of renal function using prototype of contrast substance and MRI. Rumiana Bakalova, George Hadjidekov, Zhivko Zhelev, Genoveva Zlateva, Lubomir Spasov, Ichio Aoki, *Radiology & Renology*, XLX(4), 197-201, 2011.
61. Image-guided Electro-assisted Drug Delivery: Comparison between Two Types of Electrodes. Biliana Nikolova, Severina Atanasova, Tsvetan Mudrov, Iana Tsoneva, Zhivko Zhelev, Rumiana Bakalova, Ichio Aoki, *International Journal of Bioautomation*, 19(2), 259-266, 2015.
62. Lymph node mapping using quantum dot-labeled polymersomes. Bakalova Rumiana, Zhivko Zhelov, Biliana Nikolova, Shuhei Murayama, Desislava Lazarova, Iana Tsoneva, Ichio Aoki, Tsuneo Saga, *General Physiology and Biophysics*, 34(4), 393-398, 2015.
63. Male prevalent enhancement of leftward asymmetric development of the cerebellar cortex in ferrets (*Mustela putorius*). Kazuhiko Sawada, Miwa Horiuchi-Hirose, Shigeyoshi Saito, Ichio Aoki, *Laterality: Asymmetries of Body, Brain and Cognition*, 20(6), 723-737, 2015, DOI:10.1080/1357650X.2015.1047379.
64. Hybrid Calcium Phosphate-Polymeric Micelles Incorporating Gadolinium Chelates for Imaging-Guided Gadolinium Neutron Capture Tumor Therapy. Peng Mi, Novriana Dewi, Hironobu Yanagie, Daisuke Kokuryo, Minoru Suzuki, Yoshinori Sakurai, Yanmin Li, Ichio Aoki, Hiroyuki Takahashi, Horacio Cabral, Nobuhiro Nishiyama, Kazunori Kataoka, *ACS Nano*, 9(6), 5913-5921, 2015, DOI:10.1021/acs.nano.5b00532.
65. Density-tunable conjugation of cyclic RGD ligands with polyion complex vesicles for the neovascular imaging of orthotopic glioblastomas. Wataru Kawamura, Yutaka Miura, Daisuke Kokuryo, Kazuko Toh, Naoki Yamada, Takahiro Nomoto, Yu Matsumoto, Daiki Sueyoshi, Xueying Liu, Ichio Aoki, Nobuhiro Nishiyama, Tsuneo Saga, Akihiko Kishimura, Kazunori Kataoka, *Science and Technology of Advanced Materials*, 16(035004), 2015, DOI:10.1088/1468-6996/16/3/035004.
66. Amyloid  $\beta$  accumulation assessed with  $^{11}\text{C}$ -Pittsburgh compound B PET and postmortem neuropathology. Hiroyuki Hatsuta, Masaki Takao, Kenji Ishii, Kiichi Ishiwata, Yuko Saito, Kazutomi Kanemaru, Tomio Arai, Tetsuya Suhara, Hitoshi Shimada, Hitoshi Shinotoh, Akira Tamaoka, Shigeo Murayama, *Current Alzheimer Research*, 12(3), 278-286, 2015.
67. Correlation of frontal atrophy with behavioral changes in amyotrophic lateral sclerosis. Tatsuhiro Terada, Tomokazu Obi, Jun Miyata, Manabu Kubota, Miho Yoshizumi, Toshiya Murai, Kinya Yamazaki, Kouichi Mizoguchi, *Neurology and Clinical Neuroscience*, 4(3), 85-92, 2016, DOI:10.1111/ncn3.12046.
68. A new method to quantify tau pathologies with  $^{11}\text{C}$ -PBB3 PET using reference tissue voxels extracted from brain cortical gray matter. Yasuyuki Kimura, Hironobu Endo, Masanori Ichise, Hitoshi Shimada, Chie Seki, Yoko Ikoma, Hitoshi Shinotoh, Makiko Yamada, Makoto Higuchi, Ming-Rong Zhang, Tetsuya Suhara, *EJNMMI Research*, 6(1), 24, 2016, DOI:10.1186/s13550-016-0182-y.
69. [ $^{11}\text{C}$ ]TASP457, a novel PET ligand for histamine H3 receptors in human brain. Yasuyuki Kimura, Chie Seki, Yoko Ikoma, Masanori Ichise, Kazunori Kawamura, Keisuke Takahata, Sho Moriguchi, Tomohisa Nagashima, Tetsuya Ishii, Soichiro Kitamura, Fumitoshi Niwa, Hironobu Endo, Makiko Yamada, Makoto Higuchi, Ming-Rong Zhang, Tetsuya Suhara, *European Journal of Nuclear Medicine and Molecular Imaging*, 43(9), 1653-1663, 2016, DOI:10.1007/s00259-016-3332-6.
70. Association of IQ Changes and Progressive Brain Changes in Patients with Schizophrenia. Manabu Kubota, Neeltje E.M. van Haren, Sander V. Hajjma, Hugo G. Schnack, Wiepke Cahn, Hilleke E. Hulshoff Pol, René S. Kahn, *JAMA Psychiatry*, 72(8), 803-812, 2015, DOI:10.1001/jamapsychiatry.2015.0712.
71. Structural MRI Differences between Patients with and without First Rank Symptoms: A Delusion? Henriette D. Heering, Godefridus J.C. Koevoets, Laura Koenders, Marise W.J. Machielsen, Carin J. Meijer, Manabu Kubota, Jessica de Nijs, Wiepke Cahn, Hilleke E. Hulshoff Pol, Lieuwe de Haan, Rene S. Kahn, Neeltje E.M. van Haren, *Frontiers in Psychiatry*, 6(107), 1-8, 2015, DOI:10.3389/fpsy.2015.00107.
72. Insular Gray Matter Volume and Objective Quality of Life in Schizophrenia. Teruhisa Uwatoko, Miho Yoshizumi, Jun Miyata, Shiho Ubukata, Hironobu Fujiwara, Ryosaku Kawada, Manabu Kubota, Akihiko Sasamoto, Genichi Sugihara, Toshihiko Aso, Shinichi Urayama, Hidenao Fukuyama, Toshiya Murai, Hidehiko Takahashi, *PLoS ONE*, 10(11), e0142018, 2015, DOI:10.1371/journal.pone.0142018.
73. Discrepancy between explicit judgement of agency and implicit feeling of agency: Implications for sense of agency and its disorders. Naho Saito, Keisuke Takahata, Toshiya Murai, Hidehiko Takahashi, *Consciousness and Cognition*, 37, 1-7, 2015, DOI:10.1016/j.concog.2015.07.011.

74. Functional connectivity of the striatum in experts of stenography. Takehito Ito, Tetsuya Matsuda, Shinsuke Shimojo, *Brain and Behavior*, 5(5), e00333, 2015, DOI:10.1002/brb3.333.
75. FDG-PET improves diagnosis in patients presenting with focal onset dementias. Carl Taswell, Victor L Villemagne, Paul Yates, Hitoshi Shimada, Cristian E Leyton, Kirrie J Ballard, Olivier Piguet, James R Burrell, John R Hodges, Christopher C Rowe, *Journal of Nuclear Medicine*, 56(10), 1547-1553, 2015, DOI:10.2967/jnumed.115.161067.
76. PET Quantification of Tau Pathology in Human Brain with <sup>11</sup>C-PBB3. Yasuyuki Kimura, Masanori Ichise, Hiroshi Ito, Hitoshi Shimada, Yoko Ikoma, Chie Seki, Harumasa Takano, Soichiro Kitamura, Hitoshi Shinotoh, Kazunori Kawamura, Ming-Rong Zhang, Naruhiko Sahara, Tetsuya Suhara, Makoto Higuchi, *Journal of Nuclear Medicine*, 56(9), 1359-1365, 2015, DOI:10.2967/jnumed.115.160127.
77. Dementia with Lewy bodies can be well-differentiated from Alzheimer's disease by measurement of brain acetylcholinesterase activity - A [<sup>11</sup>C]MP4A PET study -. Hitoshi Shimada, Hitoshi Shinotoh, Tsuneyoshi Ota, Koichi Sato, Makiko Yamada, Kiyoshi Fukushi, Toshiaki Irie, Ming-Rong Zhang, Makoto Higuchi, Satoshi Kuwabara, Tetsuya Suhara, *International Journal of Geriatric Psychiatry*, 30(11), 1105-1113, 2015, DOI:10.1002/gps.4338.
78. Neurosteroidogenesis today: Novel targets for neuroactive steroid synthesis and action and their relevance for translational research. Patrizia Porcu, Anna Barron, Cheryl Anne Frye, Alicia A. Walf, Song-Yu Yang, Xue-Ying He, A Leslie Morrow, Gian Carlo Panzica, Roberto C. Melcangi, *Journal of Neuroendocrinology*, 28(2), 2016, DOI:10.1111/jne.12351.
79. Development of TASP0410457 (TASP457), a novel dihydroquinolinone derivative as a PET radioligand for central histamine H3 receptors. Kazumi Koga, Jun Maeda, Masaki Tokunaga, Masayuki Hanyu, Kazunori Kawamura, Mari Ohmichi, Toshio Nakamura, Yuji Nagai, Chie Seki, Yasuyuki Kimura, Takafumi Minamimoto, Ming-Rong Zhang, Toshimitsu Fukumura, Tetsuya Suhara, Makoto Higuchi, *EJNMMI Research*, 6(1), 11, 2016, DOI:10.1186/s13550-016-0170-2.
80. Imaging the role of TLR4 on cell proliferation and inflammation after cerebral ischemia by PET. Ana Moraga, Vanessa Gómez-Vallejo, María Isabel Cuartero, Boguslaw Szczupak, Eneko San Sebastián, Irati Markuerkiaga, Jesús M. Pradillo, Makoto Higuchi, Jordi Llop, María Ángeles Moro, Abraham Martín, Ignacio Lizasoain, *Journal of Cerebral Blood Flow and Metabolism*, 36(4), 702-708, 2016, DOI:10.1177/0271678X15627657.
81. Brain-targeted co-delivery of therapeutic gene and peptide by multifunctional nanoparticles in Alzheimer's disease mice. Yang Liu, Sai An, Jianfeng Li, Yuyang Kuang, Xi He, Yubo Guo, Haojun Ma, Yu Zhang, Bin Ji, Chen Jiang, *Biomaterials*, 80, 33-45, 2016, DOI:10.1016/j.biomaterials.2015.11.060.
82. Chemogenetic disconnection of monkey orbitofrontal and rhinal cortex reversibly disrupts reward value. Mark A G Eldridge, Walter Lerchner, Richard C Saunders, Hiroyuki Kaneko, Kristopher W Krausz, Frank J Gonzalez, Bin Ji, Makoto Higuchi, Takafumi Minamimoto, Barry J Richmond, *Nature Neuroscience*, 19(1), 37-39, 2016, DOI:10.1038/nn.4192.
83. Imaging Multimodalities for Dissecting Alzheimer's Disease: Advanced Technologies of Positron Emission Tomography and Fluorescence Imaging. Masafumi Shimojo, Makoto Higuchi, Tetsuya Suhara, Naruhiko Sahara, *Frontiers in Neuroscience*, 9, 482, 2015, DOI:10.3389/fnins.2015.00482.
84. Development of Novel PET Probes for Central 2-Amino-3-(3-hydroxy-5-methyl-4-isoxazolyl)propionic acid (AMPA) Receptors. Norihito Oi, Masaki Tokunaga, Michiyuki Suzuki, Yuji Nagai, Yosuke Nakatani, Noboru Yamamoto, Jun Maeda, Takafumi Minamimoto, Ming-Rong Zhang, Tetsuya Suhara, Makoto Higuchi, *Journal of Medicinal Chemistry Manuscript*, 58(21), 8444-8462, 2015, DOI:10.1021/acs.jmedchem.5b00712.
85. Distinct Binding of Amyloid Imaging Ligands to Unique Amyloid- $\beta$  Deposited in the Presubiculum of Alzheimer's Disease. Bin Ji, Chun-Jen Chen, Kazunori Bando, Hiroki Ashino, Hideaki Shiraiishi, Hiroaki Sano, Hiroyuki Kasahara, Takao Minamizawa, Kazutaka Yamada, Maiko Ono, Ming-Rong Zhang, Chie Seki, Lars Farde, Tetsuya Suhara, Makoto Higuchi, *Journal of Neurochemistry*, 135(5), 859-866, 2015.
86. Age-related changes in neuroactive steroid levels in 3xTg-AD mice. Donatella Caruso, Anna Barron, Meghan A Brown, Federico Abbiati, Paloma Carrero, Christian J Pike, Luis M Garcia-Segura, Roberto C Melcangi, *Neurobiology of Aging*, 34(4), 1080-1089, 2013, DOI:10.1016/j.neurobiolaging.2012.10.007.
87. Prognostic indicators of six-month mortality in elderly people with advanced dementia: A systematic review of the literature. Meghan Brown, Elizabeth Sampson, Louise Jones, Anna Barron, *Palliative Medicine*, 27(5), 389-400, 2013, DOI:10.1177/0269216312465649.
88. The impact of luteinizing hormone and testosterone on beta amyloid (A $\beta$ ) accumulation: Animal and human clinical studies. Giuseppe Verdile, Prita Asih, Anna Barron, Eka J. Wahjoepramono, Lars M. Ittner, Ralph N. Martins, *Hormones and Behavior*, 76, 81-90, 2015, DOI:10.1016/j.yhbeh.2015.05.020.
89. SNAREs Controlling Vesicular Release of BDNF and Development of Callosal Axons. Masafumi Shimojo, Julien Courchet, Simon Pieraut, Nina Torabi-Rander, Richard Sando, Franck Polleux, Anton Maximov, *Cell Reports*, 11(7), 1054-1066, 2015, DOI:10.1016/j.celrep.2015.04.032.
90. In Vivo PET Imaging of the  $\alpha_4\beta_2$  Nicotinic Acetylcholine Receptor as a Marker for Brain Inflammation after Cerebral Ischemia. Abraham Martin, Boguslaw Szczupak, Vanessa Gomez-Vallejo, Maria Domercq, Ainhoa Cano, Daniel Padro, Clara Munoz, Makoto Higuchi, Carlos Matute, Jordi Llop, *Journal of Neuroscience*, 35(15), 5998-6009, 2015, DOI:10.1523/JNEUROSCI.3670-14.2015.
91. A primary role for nucleus accumbens and related limbic network in vocal tics. Kevin William McCairn, Yuji Nagai, Yukiko Hori, Erika Kikuchi, Taihei Ninomiya, Tetsuya Suhara, Ju-Young Lee, Atsushi Iriki, Takafumi Minamimoto, Masahiko Takada, Masaki Isoda, Masayuki Matsumoto, *Neuron*, 89(2), 300-307, 2016.
92. Top-Down Regulation of Laminar Circuit via Inter-Area Signal for Successful Object Memory Recall in Monkey Temporal Cortex. Masaki Takeda, Kenji W Koyano, Toshiyuki Hirabayashi, Yusuke Adachi, Yasushi Miyashita, *Neuron*, 86(3), 840-852, 2015, DOI:10.1016/j.neuron.2015.03.047.

### Research Center for Radiation Protection

1. Induction of Non-Targeted Stress Responses in Mammary Tissues by Heavy Ions. Tony J. C. Wang, Cheng-Chia Wu, Yunfei Chai, Roy K. K. Lam, Nobuyuki Hamada, Yukio Uchihori, Shizuko Kakinuma, Peter K. N. Yu, Tom K. Hei, *et al.*, PLoS ONE, 10(8), e0136307, 2015, DOI:10.1371/journal.pone.0136307.
2. The effect of age at exposure on the inactivating mechanisms and relative contributions of key tumor suppressor genes in radiation-induced mouse T-cell lymphomas. Masaaki Sunaoshi, Yoshiko Amasaki, Shinobu Hirano-Sakairi, Benjamin J. Blyth, Takamitsu Morioka, Mutsumi Kaminishi, Yi Shang, Mayumi Nishimura, Yoshiya Shimada, Akira Tachibana, Shizuko Kakinuma, Mutation Research/Fundamental and Molecular Mechanisms of Mutagenesis, 779, 58-67, 2015, DOI:10.1016/j.mrfmmm.2015.06.004.
3. Genetic Analysis of T Cell Lymphomas in Carbon Ion-Irradiated Mice Reveals Frequent Interstitial Chromosome Deletions: Implications for Second Cancer Induction in Normal Tissues During Carbon Ion Radiotherapy. Benjamin J. Blyth, Shizuko Kakinuma, Masaaki Sunaoshi, Yoshiko Amasaki, Shinobu Hirano-Sakairi, Kanae Ogawa, Ayana Shirakami, Yi Shang, Chizuru Tsuruoka, Mayumi Nishimura, Yoshiya Shimada, PLoS ONE, 10(6): e0130666, 2015, DOI:10.1371/journal.pone.0130666.
4. Biological measures to minimize the risk of radiotherapy-associated second cancer: A research perspective. Tatsuhiko Imaoka, Nobuyoshi Ishii, Isao Kawaguchi, Shino Homma-Takeda, Kazutaka Doi, Kazuhiro Daino, Ikuo Nakanishi, Keiko Tagami, Toshiaki Kokubo, Takamitsu Morioka, Ayaka Hosoki, Masaru Takabatake, Shinji Yoshinaga, International Journal of Radiation Biology, 29(6), 289-301, 2016, DOI:10.3109/09553002.2016.1152413.
5. Chronic Intake of Japanese Sake Mediates Radiation-Induced Metabolic Alterations in Mouse Liver. Tetsuo Nakajima, Guillaume Vares, Bing Wang, Mitsuru Neno, PLoS ONE, 11(1), e0146730-1-e0146730-18, 2016, DOI:10.1371/journal.pone.0146730.
6. Roles of Sulfur Metabolism and Rhodanese in Detoxification and Anti-Oxidative Stress Functions in the Liver: Responses to Radiation Exposure. Tetsuo Nakajima, Medical Science Monitor, 21, 1721-1725, 2015, DOI:10.12659/MSM.893234.
7. Dietary Modification of Mouse Response to Total-Body-Irradiation. Bing Wang, Kaoru Tanaka, Takanori Katsube, Kouichi Maruyama, Yasuharu Ninomiya, Mitsuru Neno, Evolution of Ionizing Radiation Research, Chapter 3, 2015, <http://dx.doi.org/10.5772/60653>.
8. Chronic restraint-induced stress has little modifying effect on radiation hematopoietic toxicity in mice. Bing Wang, Kaoru Tanaka, Takanori Katsube, Yasuharu Ninomiya, Guillaume Vares, Qiang Liu, Akinori Morita, Tetsuo Nakajima, Mitsuru Neno, Journal of Radiation Research, 56(5), 760-767, 2015, DOI:10.1093/jrr/rrv030.
9. The Parapineal Is Incorporated into the Habenula during Ontogenesis in the Medaka Fish. Y. Ishikawa, K. Inohaya, N. Yamamoto, K. Maruyama, M. Yoshimoto, M. Iigo, T. Oishi, A. Kudo, H. Ito, Brain, Behavior and Evolution, 85(4), 257-270, 2015, DOI:10.1159/000431249.
10. Nuclear localization of ubiquitin-activating enzyme Uba1 is characterized in its mammalian temperature-sensitive mutant. Kimihiko Sugaya, Yoshie Ishihara, Sonoe Inoue, Genes to Cells, 20(8), 659-666, 2015, DOI:10.1111/gtc.12257.
11. A comprehensive analysis of radiosensitization targets: functional inhibition of DNA methyltransferase 3B radiosensitizes by disrupting DNA damage regulation. Hiroaki Fujimori, Akira Sato, Sota Kikuhara, Junhui Wang, Takahisa Hirai, Yasufumi Murakami, Yuka Sasaki, Ryuichi Okayasu, Mitsuko Masutani, Scientific Reports, 5, 18231, 2016, DOI:10.1038/srep18231.
12. VE-821, an ATR inhibitor, causes radiosensitization in human tumor cells irradiated with high LET radiation. Hiroshi Fujisawa, Nakako Izumi Nakajima, Shigeaki Sunada, Younghyun Lee, Hirokazu Hirakawa, Hirohiko Yajima, Akira Fujimori, Mitsuru Uesaka, Ryuichi Okayasu, Radiation Oncology (Online only URL:<http://www.royournal.com/>), 10, 175, 2015, DOI:10.1186/s13014-015-0464-y.
13. Survey of Radioactive Contamination along Mt. Fuji's Climbing Routes Following TEPCO's Fukushima Daiichi Nuclear Power Plant Accident. Kazuki Iwaoka, Kazuaki Yajima, Hiroshi Yasuda, Masahiro Hosoda, Shinji Tokonami, Hidenori Yonehara, Radiation Emergency Medicine, 4(2), 21-24, 2015.
14. Diurnal variation of atmospheric electric field at the summit of Mount Fuji, Japan, distinctly different from the Carnegie curve in the summertime. Masashi Kamogawa, Yoko Suzuki, Rikuma Sakai, Hironobu Fujiwara, Tatsuo Torii, Yoshihiro Kakinami, Yasuyuki Watanabe, Ryo Sato, Satoshi Hashimoto, Hiroshi Okochi, Kazuhiko Suzuki, Hiroshi Yasuda, Yoshiaki Orihara, Tomoyuki Miura, Geophysical Research Letters, 42(8), 3019-3023, 2015.
15. A pilot study for dose evaluation in high-level natural radiation areas of Yangjiang, China. Y. Omori, S. Tokonami, T. Ishikawa, S.K. Sahoo, A. Akata, A. Sorimachi, M. Hosoda, C. Pornnumpa, P. Wanabongse, H. Kudo, Y. Hu, Y. Ao, X. Li, Y. Fu, Q. Sun, S. Akiba, Journal of Radioanalytical and Nuclear Chemistry, 306(1), 317-323, 2015, DOI:10.1007/s10967-015-4286-z.
16. Characteristics of the Environmental Radon and Thoron in Minamidaito-jima, a Comparatively High Background Radiation Island in Japan. Y. Shiroma, M. Hosoda, T. Ishikawa, S.K. Sahoo, S. Tokonami, M. Furukawa, Radiation Emergency Medicine, 4(1), 27-33, 2015.
17. Comparative dosimetry for radon and thoron in high background radiation areas in China. H. Kudo, S. Tokonami, Y. Omori, T. Ishikawa, K. Iwaoka, S.K. Sahoo, N. Akata, M. Hosoda, Radiation Protection Dosimetry, 167(1-3), 155-159, 2015.
18. Estimation of radon emanation coefficient for representative soils in Okinawa, Japan. Y. Shiroma, M. Hosoda, T. Ishikawa, S.K. Sahoo, S. Tokonami, M. Furukawa, Radiation Protection Dosimetry, 167(1-3), 147-150, 2015, DOI:10.1093/rpd/ncv233.
19. Comparative study of various techniques for environmental radon, thoron and progeny measurements. R.C. Ramola, M. Prasad, M. Rawat, A. Dangwal, G.S. Gusain, R. Mishra, S.K. Sahoo, S. Tokonami, Radiation Protection Dosimetry, 167(1-3), 22-28, 2015.
20. An intercomparison done at NIRS, Japan on continuous monitors for measuring <sup>220</sup>Rn concentration. Atsuyuki Sorimachi, Janik Mirosław, Shinji Tokonami, Applied Radiation and Isotopes, 107, 145-151, 2016, DOI:10.1016/

- j.apradiso.2015.10.007.
21. Optimization of the Timepix chip to measurement of radon, thoron and their progenies. Janik Miroslaw, Ondrej Ploc, Michael Fiederle, Simon Procz, Kavasi Norbert, Applied Radiation and Isotopes, 107, 220-224, 2016, DOI:10.1016/j.apradiso.2015.10.023.
  22. Radon-Thoron discriminative measurements in the high natural radiation areas of Southwestern Cameroon. Saidou, Shinji Tokonami, Janik Miroslaw, B.G. Samuel, Abdourahimi, N.N. Joseph Emmanuel, Journal of Environmental Radioactivity, 150, 242-246, 2015, DOI:10.1016/j.jenvrad.2015.09.006.
  23. Novel method for estimation of the indoor-to-outdoor airborne radioactivity ratio following the Fukushima Daiichi Nuclear Power Plant accident. Yanliang Tan, Tetsuo Ishikawa, Janik Miroslaw, Shinji Tokonami, Masahiro Hosoda, Atsuyuki Sorimachi, Science of the Total Environment, 536, 25-30, 2015.
  24. The most recent international intercomparisons of radon and thoron monitors with the NIRS radon and thoron chambers. Janik Miroslaw, Hidenori Yonehara, Radiation Protection Dosimetry, 164(4), 595-600, 2015, DOI:10.1093/rpd/ncv318.
  25. Distribution of uranium, thorium and some stable trace and toxic elements in human hair and nails in Niska Banja Town, a high natural background radiation area of Serbia (Balkan Region, South-East Europe). S.K. Sahoo, Z.S. Zunic, R. Kritsanawanat, P. Zagrodzki, P. Bossew, N. Veselinovic, S. Mishra, H. Yonehara, Journal of Environmental Radioactivity, 145, 66-77, 2015, DOI:10.1016/j.jenvrad.2015.03.020.
  26. Estimation of External Dose by Car-Borne Survey in Kerala, India. M. Hosoda, S. Tokonami, Y. Omori, S.K. Sahoo, S. Akiba, A. Sorimachi, T. Ishikawa, R. Nair, P.A. Jayalekshmi, P. Sebastin, K. Iwaoka, N. Akata, H. Kudo, PLoS ONE, 10(4), e0124433, 2015, DOI:10.1371/journal.pone.0124433.
  27. Public Health Concerns on Radiation Exposure after the Fukushima Daiichi Nuclear Power Plant Accident. Reiko Kanda, Satsuki Tsuji, Hidenori Yonehara, Masami Torikoshi, Journal of Disaster Research, 10(Sp), 716-717, 2015, DOI:10.20965/jdr.2015.p0716.
  28. A new approach to evaluate factors controlling elemental sediment-seawater distribution coefficients ( $K_d$ ) in coastal regions, Japan. Hyoe Takata, Tatsuo Aono, Keiko Tagami, Shigeo Uchida, Science of the Total Environment, 543, 315-325, 2016, DOI:10.1016/j.scitotenv.2015.11.034.
  29. Consideration on the Long Ecological Half-life Component of  $^{137}\text{Cs}$  in Demersal Fish Based on Field Observation Results Obtained after the Fukushima Accident. Keiko Tagami, Shigeo Uchida, Environmental Science and Technology, 50(4), 1804-1811, 2016.
  30. Radionuclide biological half-life values for terrestrial and aquatic wildlife. N.A. Beresford, K. Beaugelin-Seiller, J. Burgos, M. Cujic, S. Fesenko, A. Kryshev, N. Pachal, A. Real, B.S. Su, Keiko Tagami, *et al.*, Journal of Environmental Radioactivity, 150, 270-276, 2015.
  31. Determination of carbon species formed by decomposition of acetate in Japanese paddy soil. N. Ishii, H. Koiso, S. Uchida, Radioprotection, 46(6), S483-S486, 2011, DOI:10.1051/radiopro/20116693s.
  32. Newly derived transfer factors for Th, Am, Pu and Ci after IAEA TRS No. 472's publication: A review. Zhongtang Wang, Jian Zheng, Keiko Tagami, Shigeo Uchida, Journal of Radioanalytical and Nuclear Chemistry, 306(1), 11-20, 2015, DOI:10.1007/s10967-015-4260-9.
  33. Biological proliferation of  $^{137}\text{Cs}$  to forest bird species in a forest ecosystem. Masashi Murakami, Takao Suzuki, Nobuhito Ohte, Nobumasa Ishii, Japanese Journal of Ornithology, 64(1), 55-61, 2015, DOI:10.3838/jjo.64.55 (In Japanese with English abstract).
  34. Pu distribution in seawater in the near coastal area off Fukushima after the Fukushima Daiichi Nuclear Power Plant accident. W. T. Bu, J. Zheng, T. Aono, J. W. Wu, K. Tagami, S. Uchida, Q. J. Guo, M. Yamada, Journal of Nuclear and Radiochemical Sciences, 15(1), 1-6, 2015.
  35. Effect of ashing temperature on accurate determination of plutonium in soil samples. Zhongtang Wang, Guosheng Yang, Jian Zheng, Liguang Cao, Haijun Yu, Yanbei Zhu, Keiko Tagami, Shigeo Uchida, Analytical Chemistry, 87(11), 5511-5515, 2015, DOI:10.1021/acs.analchem.5b01472.
  36. Pu isotopes in soils collected downwind from Lop Nor: Regional fallout vs. global fallout. Wenting Bu, Youyi Ni, Qiuju Guo, Jian Zheng, Shigeo Uchida, Scientific Reports, 5, 12262, 2015, DOI:10.1038/srep12262.
  37. Bromine and iodine in Japanese soils determined with polarizing energy dispersive X-ray fluorescence spectrometry. Shin-ichi Yamasaki, Akira Takeda, Takahiro Watanabe, Keiko Tagami, Shigeo Uchida, Hyoe Takata, Yuji Maejima, Nobuharu Kihou, Noriyoshi Tsuchiya, Soil Science and Plant Nutrition, 61(5), 751-760, 2015, DOI:10.1080/00380768.2015.1054773.
  38. Evaluation of a new sector-field ICP-MS with Jet Interface for ultra-trace determination of Pu isotopes: from femto-gram to attogram levels. Jian Zheng, Journal of Nuclear and Radiochemical Sciences, 15(1), 7-13, 2015.
  39. Plutonium concentration and isotopic ratio in soil samples from central-eastern Japan collected around the 1970s. Guosheng Yang, Jian Zheng, Keiko Tagami, Shigeo Uchida, Scientific Reports, 5(9636), 2015, DOI:10.1038/srep09636.
  40. Measurement of air dose rate change with time in Shinkansen super express train between Tokyo and Shin-Aomori stations with a handheld radiation monitor. Keiko Tagami, Shigeo Uchida, Nobuyoshi Ishii, Houshakagaku (Radiochemistry), 31, 2-6, 2015 (In Japanese with English abstract).
  41. Measurement of air dose rate change with time in Shinkansen super express train between Tokyo and Niigata stations with a handheld radiation monitor. Keiko Tagami, Shigeo Uchida, Nobuyoshi Ishii, Houshakagaku (Radiochemistry), 31, 7-11, 2015 (In Japanese with English abstract).
  42. Radiological Dose Rates to Marine Fish from the Fukushima Daiichi Accident: The First Three Years Across the North Pacific. Mathew P. Johansen, Elizabeth Ruedig, Keiko Tagami, Shigeo Uchida, Kathryn Higley, Nicholas A. Beresford, Environmental Science & Technology, 49(3), 1277-1285, 2015, DOI:10.1021/es505064d.
  43. Effective half-lives of  $^{137}\text{Cs}$  in giant butterbur and field horsetail, and the distribution differences of potassium and  $^{137}\text{Cs}$  in aboveground tissue parts. Keiko Tagami, Shigeo Uchida, Journal of Environmental Radioactivity, 141, 138-145, 2015, DOI:10.1016/j.jenvrad.2014.12.013.

44. Effect of Sludge Particle Size on Uptake of Cs-137 by Two Leaf Vegetables. Nobumasa Ishii, Keiko Tagami, Shigeo Uchida, Journal of Residuals Science & Technology, 12(2), 61-65, 2015.

#### ■ Research Center for Radiation Emergency Medicine

1. Regression of diffuse large B-cell lymphoma in sphenoid and ethmoid sinuses following treatment with loxoprofen. Yuki Hiroshima, Takeo Kato, Katsushi Tajima, Leukemia & Lymphoma, 57(3), 721-723, 2016, DOI:10.3109/10428194.2015.1070154.
2. An isolated myeloid blast crisis presenting as optic nerve sarcoma in a patient with chronic myeloid leukemia treated with imatinib. Hisashi Yamamoto, Masakazu Yamamoto, Eijiro Omoto, Takeo Kato, Katsushi Tajima, British Journal of Haematology, 170(3), 290, 2015, DOI:10.1111/bjh.13503.
3. A prospective analysis of clinical efficacy and safety in chronic myeloid leukemia-chronic phase patients with imatinib resistance or intolerance as evaluated using European LeukemiaNet 2013 criteria. Kazunori Murai, Tomoaki Akagi, Kenji Shimosegawa, Tomohiro Sugawara, Kenichi Ishizawa, Shigeki Ito, Keiko Murai, Mutsuhito Motegi, Hisayuki Yokoyama, Hideyoshi Noji, Katsushi Tajima, Jun Kimura, Takaaki Chou, Kazuei Ogawa, Hideo Harigae, Kohmei Kubo, Koji Oba, Junichi Sakamoto, Yoji Ishida, European Journal of Haematology, 95(6), 558-565, 2015, DOI:10.1111/ejh.12536.
4. NCYM promotes calpain-mediated Myc-nick production in human MYCN-amplified neuroblastoma cells. Wataru Shoji, Yusuke Suenaga, Yoshiaki Kaneko, S.M. Rafiqul Islam, Jennifer Alagu, Sana Yokoi, Masaki Nio, Akira Nakagawara, Biochem Biophys Res Commun., 461(3), 501-506, 2015, DOI:10.1016/j.bbrc.2015.04.050.
5. Functional interplay between MYCN, NCYM, and OCT4 promotes aggressiveness of human neuroblastomas. Yoshiaki Kaneko, Yusuke Suenaga, S.M. Rafiqul Islam, Daisuke Matsumoto, Yohko Nakamura, Miki Ohira, Sana Yokoi, Akira Nakagawara, Cancer Science, 106(7), 840-847, 2015, DOI:10.1111/cas.12677.
6. NCYM, a Cis-antisense gene of MYCN, encodes a de novo evolved protein that inhibits GSK3 $\beta$  resulting in the stabilization of MYCN in human neuroblastomas. Yusuke Suenaga, S.M. Rafiqul Islam, *et al.*, PLoS Genetics, 10(1), e1003996, 2014, DOI:10.1371/journal.pgen.1003996.
7. Sendai virus-mediated expression of reprogramming factors promotes plasticity of human neuroblastoma cells. S.M. Rafiqul Islam, Y. Suenaga, A. Takatori, *et al.*, Cancer Science, 106(10), 1351-1361, 2015, DOI:10.1111/cas.12746.
8. Cytotoxicity of synthetic cannabinoids on primary neuronal cells of the forebrain: the involvement of cannabinoid CB1 receptors and apoptotic cell death. Ken-ichi Tomiyama, Masahiko Funada, Toxicology and Applied Pharmacology, 274(1), 17-23, 2014, DOI:10.1016/j.taap.2013.10.028.
9. Mammalian Bcnt/Cfdp1, a potential epigenetic factor characterized by an acidic stretch in the disordered N-terminal and Ser250 phosphorylation in the conserved C-terminal regions. Shintaro Iwashita, Takehiro Suzuki, Takeshi Yasuda, Kentaro Nakashima, Taiichi Sakamoto, Toshiyuki Kohno, Ichiro Takahashi, Takayasu Kobayashi, Yoshiko Ohno-Iwashita, Shinobu Imajoh-Ohmi, Si Young Song, Bioscience Reports, 35(4), e00228, 2015, DOI:10.1042/BSR20150111.
10. Comparison of Absorbents and Drugs for Internal Decorporation of Radiocesium: Advances of Polyvinyl Alcohol Hydrogel Microsphere Preparations Containing Magnetite and Prussian Blue. Izumi Tanaka, Hiroshi Ishihara, Haruko Yakumaru, Mika Tanaka, Kazuko Yokochi, Katsushi Tajima, Makoto Akashi, Biological and Pharmaceutical Bulletin, 39(3), 353-360, 2016, DOI:10.1248/bpb.b15-00728.
11. Quantification of damage due to low-dose radiation exposure in mice: construction and application of a biodosimetric model using mRNA indicators in circulating white blood cells. Hiroshi Ishihara, Izumi Tanaka, Haruko Yakumaru, Mika Tanaka, Kazuko Yokochi, Kumiko Fukutsu, Katsushi Tajima, Mayumi Nishimura, Yoshiya Shimada, Makoto Akashi, Journal of Radiation Research, 57(1), 25-34, 2016.
12. Practical Self-absorption Correction Method for Various Environmental Samples in a 1000cm<sup>3</sup> Marinelli Container to Perform Accurate Radioactivity Determination with HP Ge Detectors. Hidesuke Itadzu, Osamu Kurihara, Tetsuo Iguchi, Radioisotopes, 64(11), 661-671, 2015, DOI:http://doi.org/10.3769/radioisotopes.64.661.
13. GHSI emergency radionuclide bioassay laboratory network: Summary of a recent exercise. Chunsheng Li, Armin Ansari, Christine Bartizel, Paolo Battisti, Didier Franck, Udo Gerstmann, Isabella Giardina, Claude Guichet, Derek Hammond, Martina Hartmann, Robert L. Jones, Eunjoo Kim, Raymond Ko, Ryan Norhard, Deborah Quayle, Baki Sadi, David Saunders, Radiation Protection Dosimetry, 2015, DOI:10.1093/rpd/ncv386.
14. Estimation of early internal doses to Fukushima residents after the nuclear disaster based on the atmospheric dispersion simulation. Eunjoo Kim, Kotaro Tani, Naoaki Kunishima, Osamu Kurihara, Kazuo Sakai, Makoto Akashi, Radiation Protection and Dosimetry, 2015, DOI:10.1093/rpd/ncv385.
15. Implementation of iodine biokinetic model for interpreting I-131 contamination in breast milk after the Fukushima nuclear disaster. Kotaro Tani, Osamu Kurihara, Eunjoo Kim, Satoshi Yoshida, Kazuo Sakai, Makoto Akashi, Scientific Reports, 5, 12426-1 - 12426-9, 2015, DOI:10.1038/srep12426.
16. Intake ratio of I-131 to Cs-137 derived from thyroid and whole-body doses to Fukushima residents. Eunjoo Kim, Osamu Kurihara\*, Kotaro Tani, Yasushi Ohmachi, Kumiko Fukutsu, Kazuo Sakai, Makoto Akashi, Radiation Protection Dosimetry, 2015, DOI:10.1093/rpd/ncv344.
17. Sodium bicarbonate protects uranium-induced acute nephrotoxicity through uranium-decorporation by urinary alkalization in rats. Yasushi Ohmachi, Tomomi Imamura<sup>1</sup>, Mizuyo Ikeda, Eriko Shishikura, Eunjoo Kim, Osamu Kurihara, and Kazuo Sakai, Journal of Toxicologic Pathology, 28(2), 65-71, 2015.
18. Chromothripsis-like chromosomal rearrangements induced by ionizing radiation using proton microbeam irradiation system. Maki Morishita, Tomoki Muramatsu, Yumiko Suto, Momoki Hirai, Teruaki Konishi, Shin Hayashi, Daichi Shigemizu, Tatsuhiko Tsunoda, Keiji Moriyama, Johji Inazawa, Oncotarget, 7(9), 10182-92, 2016, DOI:10.18632/oncotarget.7186.
19. Construction of a cytogenetic dose-response curve for low-dose range gamma-irradiation in human peripheral blood

- lymphocytes using three-color FISH. Yumiko Suto, Miho Akiyama, Takashi Noda, Momoki Hirai, *Mutation Research/Genetic Toxicology and Environmental Mutagenesis*, 794, 32-38, 2015.
20. Model-based verification of hypotheses on the origin of modern Japanese revisited by Bayesian inference based on genome-wide SNP data. Shigeki Nakagome, Takehiro Sato, Hajime Ishida, Tsunehiko Hanihara, Tetsutaro Yamaguchi, Ryosuke Kimura, Shuhei Mano, Hiroki Oota, Keiichi Omoto, Katsushi Tokunaga, Naruya Saitou, Shoji Kawamura, Hideyuki Tanabe, Kazuo Umetsu, Atsushi Tajima, Naoki Osada, Toshimitsu Yamamoto, Jun Ohashi, Yumiko Suto, Nao Nishida, Ryuichi Sakate, Hiromi Sawai, *Molecular Biology and Evolution*, 32(6), 1533-1543, 2015.
- Research, Development and Support Center**
1. Analysis of elemental content and map of beech leaves by PIXE and micro-PIXE. Katsumi Saitoh, Koichiro Sera, Masakazu Oikawa, Hideyuki Shimizu, *International Journal of PIXE*, 24(3-4), 177-188, 2015, DOI:10.1142/S0129083514400105.
  2. G2-M phase-correlative bystander effects are co-mediated by DNA-PKcs and ATM after carbon ion irradiation. Wenzhi Tu, Chen Dong, Teruaki Konishi, Alisa Kobayashi, Yoshiya Furusawa, Yukio Uchihori, Yuexia Xie, Bingrong Dang, Wenjian Li, Chunlin Shao, *Mutation Research/Genetic Toxicology and Environmental Mutagenesis*, (795), 1-6, 2016, DOI:10.1016/j.mrgentox.2015.11.001.
  3. ATR signaling cooperates with ATM in the mechanism of low dose hypersensitivity induced by carbon ion beam. Lian Xue, Yoshiya Furusawa, Dond Yu, *DNA Repair*, 34, 1-8, 2015, DOI:10.1016/j.dnarep.2015.07.001.
  4. Dependence of the bystander effect for micronucleous formation on dose of heavy-ion radiation in normal human fibroblasts. Yoshitaka Matsumoto, Nobuyuki Hamada, Mizuho Aoki-Nakano, Tomoo Funayama, Tetsuya Sakashita, Seiichi Wada, Takehiko Kakizaki, Yasuhiko Kobayashi, Yoshiya Furusawa, *Radiation Protection Dosimetry*, 166(1-4), 152-156, 2015, DOI:doi:10.1093/rpd/ncv177.
  5. In vivo radiobiological assessment of the new clinical carbon ion beams at CNAO. Angelica Facchetti, Vischioni Barbara, M. Ciocca, M. Ferrarini, Y. Furusawa, A. Mairani, Y. Matsumoto, A. Mirandola, S. Molinelli, A. Uzawa, Freixas G. Vilches, R. Orecchia, *Radiation Protection Dosimetry*, 166(1-4), 379-382, 2015, DOI:10.1093/rpd/ncv145.
  6. The differential role of human macrophage in triggering secondary bystander effects after either gamma-ray or carbon beam irradiation. Chen Dong, Mingyuan He, Wenzhi Tu, Teruaki Konishi, Weili Liu, Yuexia Xie, Bingrong Dang, Wenjian Li, Yukio Uchihori, Tom K. Hei, Chunlin Shao, *Cancer Letters*, 363(1), 92-100, 2015, DOI:10.1016/j.canlet.2015.04.013.
  7. Relative clinical effectiveness of carbon ion radiotherapy: theoretical modelling for H&N tumours. Laura Antonovic, Alexandru Dasu, Yoshiya Furusawa, Iuliana Toma-Dasu, *Journal of Radiation Research*, 56(4), 639-645, 2015, DOI:10.1093/jrr/rrv016.
  8. Role of isolated and clustered DNA damage and the post-irradiating repair process in the effects of heavy ion beam irradiation. Yuka Tokuyama, Yoshiya Furusawa, Hiroshi Ide, Akira Yasui, Hiroaki Terato, *Journal of Radiation Research*, 56(3), 446-455, 2015, DOI:10.1093/jrr/rru122.
  9. Low-dose neutron dose response of zebrafish embryos obtained from the Neutron exposure Accelerator System for Biological Effect Experiments (NASBEE) facility. C.Y.P. Ng, E.Y. Kong, Teruaki Konishi, Alisa Kobayashi, Noriyoshi Suya, S.H. Cheng, K N. Yu, *Radiation Physics and Chemistry*, 114, 12-17, 2015, DOI:10.1016/j.radphyschem.2015.05.020.
  10. Fragmentation Cross Section of 800 A MeV Silicon Ions on Carbon Target. Hui-Hui Ao, Man-Man Tian, Zhen Feng, Ya-Qin Sun, Jun-Sheng Li, Dong-Hai Zhang, Satoshi Kodaira, Nakahiro Yasuda, *Physics Procedia*, 80, 46-49, 2016, DOI:10.1016/j.phpro.2015.11.091.
  11. Projectile Fragment Emission in the Fragmentation of Silicon on Carbon and Polyethylene Targets at 800 A MeV. Zhen Feng, Hui-Hui Ao, Ya-Qin Sun, Man-Man Tian, Dong-Hai Zhang, Jun-Sheng Li, Satoshi Kodaira, Nakahiro Yasuda, *Physics Procedia*, 80, 36-40, 2016, DOI:10.1016/j.phpro.2015.11.085.
  12. Two-stage Development of the Lunar Farside Highlands Crustal Formation. Keiko Yamamoto, Junichi Haruyama, Shingo Kobayashi, Makiko Ohtake, Takahiro Iwata, Yoshiaki Ishihara, Nobuyuki Hasebe, *Planetary and Space Science*, 120, 43-47, 2016, DOI:10.1016/j.pss.2015.11.002.
  13. Polysulfone as a scintillation material without doped fluorescent molecules. Hidehito Nakamura, Hisashi Kitamura, Nobuhiro Sato, Masaya Kanayama, Yoshiyuki Shirakawa, Sentaro Takahashi, *Nuclear Instruments and Methods in Physics Research Section A: Accelerators, Spectrometers, Detectors and Associated Equipment*, 797, 206-209, 2015, DOI:10.1016/j.nima.2015.06.049.
  14. A model survey meter using undoped poly (ether sulfone). Hidehito Nakamura, Yoshiyuki Shirakawa, Masaya Kanayama, Nobuhiro Sato, Hisashi Kitamura, Sentaro Takahashi, *Nuclear Instruments and Methods in Physics Research Section A: Accelerators, Spectrometers, Detectors and Associated Equipment*, 780, 127-130, 2015, DOI:10.1016/j.nima.2015.01.068.
  15. Enhancement of critical current density and mechanism of vortex pinning in H<sup>+</sup>-irradiated FeSe single crystal. Yue Sun, Sunseong Pyon, Tsuyoshi Tamegai, Ryo Kobayashi, Tatsuya Watashige, Shigeru Kasahara, Yuji Matsuda, Takasada Shibauchi, Hisashi Kitamura, *Applied Physics Express*, 8(11), 113102-1-113102-4, 2015, DOI:10.7567/APEX.8.113102.
  16. Validation of <sup>64</sup>Cu-ATSM damaging DNA via high-LET Auger electron emission. Dayton D. McMillan, Junko Maeda, Bell Justin, Matthew D. Genet, Garrett Phoonswadi, Kelly A. Mann, Susan L. Kraft, Hisashi Kitamura, Akira Fujimori, Yukie Yoshii, Takako Furukawa, Yasuhisa Fujibayashi, Takamitsu Kato, *Journal of Radiation Research*, 56(5), 784-791, 2015, DOI:10.1093/jrr/rrv042.
  17. Characteristic X-ray detector: In-situ imaging of radioactive contaminant distribution. Shingo Kobayashi, Takayuki Shinomiya, Toru Yoshida, Hisashi Kitamura, Yoshiyuki Shirakawa, Kazuyoshi Kurita, Yukio Uchihori, *Radiation Measurements*, 82, 26-30, 2015.
  18. Application of Al<sub>2</sub>O<sub>3</sub>:C+ fibre dosimeters for 290 MeV/n carbon therapeutic beam dosimetry. L.F. Nascimento, F. Vanhavere, Satoshi Kodaira, Hisashi Kitamura, D. Verellen, Y. De Deene, *Radiation Physics and Chemistry*, 115, 75-80, 2015, DOI:10.1016/j.radphyschem.2015.06.001.
  19. Critical current density and vortex dynamics in pristine

- and proton-irradiated Ba<sub>0.6</sub>K<sub>0.4</sub>Fe<sub>2</sub>As<sub>2</sub>. Toshihiro Taen, Fumiaki Ohtake, Sunseong Pyon, Tsuyoshi Tamegai, Hisashi Kitamura, *Superconductor Science and Technology*, 28(8), 085003-1-085003-8, 2015, DOI:10.1088/0953-2048/28/8/085003.
20. Application of CR-39 plastic nuclear track detectors for quality assurance of mixed oxide fuel pellets. S. Kodaira, M. Kurano, T. Hosogane, F. Ishikawa, T. Kageyama, M. Sato, M. Kayano, N. Yasuda, *Review of Scientific Instruments*, 86, 056103-1-056103-3, 2015, DOI:10.1063/1.4919904.
  21. Histone methyltransferase Smyd3 regulates early embryonic lineage commitment in mice. Shinnosuke Suzuki, Yusuke Nozawa, Satoshi Tsukamoto, Takehito Kaneko, Hiroshi Imai, Naojiro Minami, *Reproduction (Cambridge, England)*, 150(1), 21-30, 2015, DOI:10.1530/REP-15-0019.
  22. CHD1 acts via the Hmgpi pathway to regulate mouse early embryogenesis. Shinnosuke Suzuki, Yusuke Nozawa, Satoshi Tsukamoto, Takehito Kaneko, Ichiro Manabe, Hiroshi Imai, Naojiro Minami, *Development (Cambridge, England)*, 142(13), 2375-84, 2015, DOI:10.1242/dev.120493.
  23. Deficiencies in extrusion of the second polar body due to high calcium concentrations during in vitro fertilization in inbred C3H/He mice. Yuki Ohta, Yoshikazu Nagao, Naojiro Minami, Satoshi Tsukamoto, Seiji Kito, *Zygote*, 2015, DOI:10.1017/S096719941500060X.
  24. Autophagic activity as an indicator for selecting good quality embryos. Satoshi Tsukamoto, *Reproductive Medicine and Biology*, 2015(14), 57-64, 2015, DOI:10.1007/s12522-014-0197-x.
  25. Induced pluripotent stem cell generation-associated point mutations. R. Araki, M. Sugiura, Y. Hoki, M. Sunayama, M. Nakamura, Y. Kasama, M. Abe, *Inflammation and Regeneration*, 35(5), 226-232, 2015.
  26. Generation of mouse pluripotent stem cell-derived proliferating myeloid cells as an unlimited source of functional antigen-presenting cells. Rong Zhang, Tian-Yi Liu, Satoru Senju, Miwa Haruta, Narumi Hirose, Motoharu Suzuki, Minako Tatsumi, Norihiro Ueda, Hiroyuki Maki, Ryusuke Nakatsuka, Yoshikazu Matsuoka, Yutaka Sasaki, Shinobu Tsuzuki, Hayao Nakanishi, Ryoko Araki, Masumi Abe, Yoshiki Akatsuka, Yasushi Sakamoto, Yoshiaki Sonoda, Yasuharu Nishimura, Kiyotaka Kuzushima, Yasushi Uemura, *Cancer Immunology Research*, 3(6), 668-77, 2015, DOI:10.1158/2326-6066.CIR-14-0117.
  27. Changes in radiological imaging frequencies in children before and after the accident at the Fukushima Daiichi Nuclear Power Plant in Fukushima Prefecture, Japan. Koji Yoshida, Naomi Hayashida, Yoshiko Fukushima, Akira Ohtsuru, Takashi Ohba, Arifumi Hasegawa, Hisashi Sato, Fumio Shishido, Kiyotake Yasui, Atsushi Kumagai, Takashi Yusa, Takashi Kudo, Shunichi Yamashita, Noboru Takamura, *Japanese Journal of Radiology*, 33(10), 619-626, 2015.
  28. Radiology nursing after the Fukushima Daiichi nuclear power plant accident: A nationwide questionnaire survey of nurse administrators and practice nurses. Toshiko Tomizawa, Chieko Itaki, Keiko Aizu, Ayako Ohgino, Maiko Kitajima, Noriko Ogura, Yoshiko Fukushima, Yoichiro Hosokawa, Yuka Noto, Hideaki Yamabe, Yoshiko Nishizawa, *Journal of the Radiological Nursing Society of Japan*, 3(1), 10-19, 2015 (In Japanese with English abstract).
  29. Bipolarization of Risk Perception about the Health Effects of Radiation in Residents after the Accident at Fukushima Nuclear Power Plant. M. Orita, N. Hayashida, Y. Nakayama, T. Shinkawa, H. Urata, Y. Fukushima, Y. Endo, S. Yamashita, N. Takamura, *PLoS ONE*, 10(6), e0129227, 2015.
  30. Internal radiation exposure dose in Iwaki City, Fukushima Prefecture after the accident at Fukushima Dai-ichi Nuclear Power Plant. Makiko Orita, Naomi Hayashida, Hiroshi Nukui, Naoko Fukuda, Takashi Kudo, Naoki Matsuda, Yoshiko Fukushima, Noboru Takamura, *PLoS ONE*, 9(12), e11407, 2014.
  31. The framework and future prospects of radiological nursing as advanced practice nursing care. Yoshiko Nishizawa, Yuka Noto, Tomoko Ichinohe, Hideko Urata, Yuko Matsunari, Chieko Itaki, Toshiko Tomizawa, Tetsuko Shinkawa, Ruriko Kidachi, Rika Yatsushiro, Yoshiko Fukushima, Emiko Konishi, *Journal of the Radiological Nursing Society of Japan*, 3(1), 2-9, 2015 (In Japanese with English abstract).
  32. Measurement of individual doses of radiation by personal dosimeter is important for the return of residents from evacuation order areas after nuclear disaster. Makiko Orita, Naomi Hayashida, Yasuyuki Taira, Yoshiko Fukushima, Juichi Ide, Yuuko Endo, Takashi Kudo, Shunichi Yamashita, Noboru Takamura, *PLoS ONE*, 10(3), e0121990, 2015.
  33. Factors associated with nurses' intention to leave their jobs after the Fukushima Daiichi Nuclear Power Plant accident. Yoshinobu Sato, Naomi Hayashida, Makiko Orita, Hideko Urata, Tetsuko Shinkawa, Yoshiko Fukushima, Yumiko Nakashima, Takashi Kudo, Shunichi Yamashita, *PLoS ONE*, 10(3), e0122389, 2015.
  34. A method to visualize transdermal nickel permeation in mouse skin using a nickel allergy patch. Tomoko Sugiyama, Motohiro Uo, Takahiro Wada, Toshio Hongo, Daisuke Omagari, Kazuo Komiyama, Masakazu Oikawa, Mikio Kusama, *Bio-Medical Materials and Engineering*, 26(1-2), 1-8, 2015, DOI:10.3233/BME-15154.
  35. Neutron induced bystander effect among zebrafish embryos. C.Y.P. Ng, E.Y. Kong, Alisa Kobayashi, Noriyoshi Suya, Yukio Uchihori, S.H. Cheng, Teruaki Konishi, K.N. Yu, *Radiation Physics and Chemistry*, 117, 153-159, 2015, DOI:10.1016/j.radphyschem.2015.08.009.
  36. Rescue of Targeted Nonstem-Like Cells from Bystander Stem-Like Cells in Human Fibrosarcoma HT1080. Yu Liu, Alisa Kobayashi, Qibin Fu, Gen Yang, Teruaki Konishi, Yukio Uchihori, Tom K. Hei, Yugang Wang, *Radiation Research*, 184(3), 334-340, 2015, DOI:10.1667/RR14050.1.
- **Fukushima Project Headquarters**
1. Evolutionary pathway of pseudogenization of globin genes,  $\alpha 5$  and  $\beta 5$ , in genus *Oryzias*. Kouichi Maruyama, Bing Wang, Yuji Ishikawa, Shigeki Yasumasu, Ichiro Iuchi, *Development Genes and Evolution*, 225, 305-311, 2015, DOI:10.1007/s00427-015-0509-0.
  2. Study on long-term radiation exposure analysis after the Fukushima Dai-ichi nuclear power plant accident: validation of the EU long-term radiation exposure model (ERMIN). Minsik Kim, Ryohji Ohba, Masamichi Oura, Shinsuke Kato, *Journal of Nuclear Science and Technology*, 53(6), 2016, DOI:10.1080/00223131.2015.1077170.
  3. Measurement of <sup>90</sup>strontium in contaminated Fukushima soils using liquid scintillation counter. N. Kavasi, S.K.

- Sahoo, H. Arae, S. Yoshida, A. Sorimachi, S. Tokonami, *Radiation Protection Dosimetry*, 167(1-3), 376-379, 2015.
4. Variability of radiocaesium inventory in Fukushima soil cores from one site measured at different times. S. Mishra, S.K. Sahoo, H. Arae, A. Sorimachi, M. Hosoda, S. Tokonami, T. Ishikawa, *Radiation Protection Dosimetry*, 167(1-3), 344-347, 2015.
  5. Morphological defects in native Japanese fir trees around the Fukushima Daiichi Nuclear Power Plant. Yoshito Watanabe, Kouichi Maruyama, Yoshihisa Kubota, Shoichi Fuma, Isao Kawaguchi, Satoshi Yoshida, *et al.*, *Scientific Reports*, 5, 13232, 2015, DOI:10.1038/srep13232.
  6. The *Staurotypos* turtles and aves share the same origin of sex chromosomes but evolved different types of heterogametic sex determination. Taiki Kawagoshi, Yoshinobu Uno, Chizuko Nishida, Yoichi Matsuda, *PLoS One*, 2014, DOI:10.1371/journal.pone.0105315.
  7. Terrestrial radioisotopes in black shale hosted Mn-carbonate deposit Urkut, Hungary. Vight Tamas, Kovacs Tibor, Somlai Janos, Kavasi Norbert, Polgari Marta, Biro Lorant, *Acta Geophysica*, 61(4), 831-847, 2015, DOI:10.2478/s11600-013-0124-2.
  8. Natural radioactivity survey on soils originated from southern part of Thailand as potential sites for nuclear power plants from radiological viewpoint and risk assessment. R. Kritsanuwat, H. Arae, M. Fukushi, S.K. Sahoo, S. Chan-ayotha, *Journal of Radioanalytical and Nuclear Chemistry*, 305(2), 487-499, 2015, DOI:10.1007/s10967-015-3994-8.
  9. Chromosomal Aberrations in Wild Mice Captured in Areas Differentially Contaminated by the Fukushima Dai-Ichi Nuclear Power Plant Accident. Yoshihisa Kubota, Hideo Tsuji, Taiki Kawagoshi, Naoko Shiomi, Hiroyuki Takahashi, Yoshito Watanabe, Shoichi Fuma, Kazutaka Doi, Isao Kawaguchi, Masanari Aoki, Masahide Kubota, Yoshiaki Furuhashi, Yusaku Shigemura, Masahiko Mizoguchi, Fumio Yamada, Morihiko Tomozawa, Shinsuke H. Sakamoto, Satoshi Yoshida, *Environmental Science and Technology*, 49, 10074-10083, 2015, DOI:10.1021/acs.est.5b01554.
  10. Estimating annual individual doses for evacuees returning home to areas affected by the Fukushima nuclear accident. Kazuaki Yajima, Osamu Kurihara, Yasushi Ohmachi, Masashi Takada, Yasutaka Omori, Keiichi Akahane, Kim Eunjo, Masami Torikoshi, Hidenori Yonehara, Satoshi Yoshida, Kazuo Sakai, Makoto Akashi, *Health Physics*, 109(2), 122-133, 2015, DOI:10.1097/HP.0000000000000308.
  11. A Study of a Development of Internal Exposure Management Tool Suited for Japanese Diet Behavior. Shin Hasegawa, Shinya Oku, Daisuke Fujise, Yuki Yoshida, Kazuaki Yajima, Yasuo Okuda, Thierry Schneider, Jacques Lochard, Isao Kawaguchi, Osamu Kurihara, Masaki Matsumoto, Tatsuo Aono, Katsuhiko Ogasawara, Shinji Yoshinaga, Satoshi Yoshida, *Radiological Issues for Fukushima's Revitalized Future*, 221-232, 2016, DOI:10.1007/978-4-431-55848-4.
  12. Secondary cancers after a childhood cancer diagnosis: a nationwide hospital-based retrospective cohort study in Japan. Yasushi Ishida, Dongmei Qiu, Miho Maeda, Junichiro Fujimoto, Hisato Kigasawa, Ryoji Kobayashi, Maho Sato, Jun Okamura, Shinji Yoshinaga, Takeshi Rikiishi, Hiroyuki Shichino, Chikako Kiyotani, Kazuko Kudo, Keiko Asami, Hiroki Hori, Hiroshi Kawaguchi, Hiroko Inada, Souichi Adachi, Atsushi Manabe, Tatsuo Kuroda, *International Journal of Clinical Oncology*, 21(3), 506-516, 2016, DOI:10.1007/s10147-015-0927-z.
  13. Research on medical radiation exposure and children's health: Results from questionnaire survey for a large-scale follow-up study in future. Hidenori Otake, Masahiko Kuraishi, Hiroyuki Takei, Yoshito Tsushima, Shinji Yoshinaga, Michiaki Kai, Keigo Endo, *The Japanese Society of Education for Radiological Technology*, 3(1), 23-32, 2015.
  14. The effects of gamma rays on the regeneration of hair follicles are carried over to later hair cycles. Kimihiko Sugaya, Yoshie Ishihara, Sonoe Inoue, Tomohisa Hirobe, *International Journal of Radiation Biology*, 91(12), 957-963, 2015, DOI:10.3109/09553002.2015.1101647.
  15. Expression of a rice glutaredoxin in aleurone layers of developing and mature seeds: subcellular localization and possible functions in antioxidant defense. Shigeto Morita, Yuki Yamashita, Masayoshi Fujiki, Rie Todaka, Yuri Nishikawa, Ayaka Hosoki, Chisato Yabe, Jun'ichi Nakamura, Kazuyoshi Kawamura, I Nengah Suastika, Masa H. Sato, Takehiro Masumura, Yasunari Ogihara, Kunisuke Tanaka, Shigeru Satoh, *Planta*, 242(5):1195-1206, 2015, DOI:10.1007/s00425-015-2354-9.

■ **Other research themes**

1. Comparison of cosmic rays radiation detectors on-board commercial jet aircraft. Jan Kubancak, Iva Ambrozova, Katerina Pachnerova Brabcova, Jan Jakubek, Dagmar Kyselova, Ondrej Ploc, Julius Bems, Vaclav Stepan, Yukio Uchihori, *Radiation Protection Dosimetry*, 164(4), 484-488, 2015, DOI:10.1093/rpd/ncv332.
2. Calibration of modified Liulin detector for cosmic radiation measurements on-board aircraft. D. Kyselova, I. Ambrozova, P. Krist, Y. Uchihori, H. Kitamura, O. Ploc, *et al.*, *Radiation Protection Dosimetry*, 164(4), 489-492, 2015, DOI:10.1093/rpd/ncv332.

# Access Map



NIRS Home Page (English)  
You can access our website  
by scanning the QR code.



<http://www.nirs.qst.go.jp>

